

Role of Hyperpolarization-activated  
and Cyclic Nucleotide-gated (HCN) Channels  
in Hippocampal Neurons

Inaugural-Dissertation

zur

Erlangung des Doktorgrades

der Mathematisch-Naturwissenschaftlichen Fakultät

der Universität zu Köln

vorgelegt von

Matthias Deutsch

aus Trier

Jülich, 2019

Berichtersteller/in: Prof. Dr. Arnd Baumann

Prof. Dr. Guenter Schwarz

Tag der letzten mündlichen Prüfung: 22.01.2020

*„Frischkäse hält unser Hirn munter“*

Erwin Neher, 2009



## Zusammenfassung

Um ihre Funktionen in der Verarbeitung und Weiterleitung von Informationen wahrnehmen zu können, sind Neurone auf die adäquate Ausstattung mit Ionen-leitenden Kanälen angewiesen. Zu diesen Kanälen gehören, unter anderem, auch die hyperpolarisationsaktivierten und zyklisch Nukleotid-gesteuerten (HCN) Kanäle. Sie leiten den in seinen biophysikalischen Eigenschaften einzigartigen  $I_h$ -Strom, der maßgeblich an verschiedenen zellulären elektrischen Prozessen beteiligt ist.

Um den spezifischen Einfluss der HCN-Kanäle auf die elektrischen Eigenschaften von Neuronen zu untersuchen, wurden zwei Werkzeuge (CRISPRi und RNAi) zur Beeinflussung der HCN-Kanal-Genexpression etabliert und analysiert. Durch die Verwendung rekombinanter Adeno-assoziiierter Viren (rAAV) als Genfähren wurden diese Werkzeuge in post-mitotische Neuronen eingebracht. Die Validierung beider Knock-Down-Techniken zeigte, dass CRISPRi und RNAi die *hcn* Expression spezifisch reduzierten. Dabei erwies sich jedoch die RNAi-vermittelte Reduktion der *hcn*-Transkripte als robuster und effizienter als die der CRISPRi-vermittelte Strategie.

Bei Säugetieren entstanden, im Laufe der phylogenetischen Entwicklung, vier verschiedene HCN-Kanal-Isoformen (HCN1-4). Um den Beitrag einzelner HCN-Kanal-Untereinheiten zu neuronalen Funktionen zu untersuchen, wurde der Untereinheiten-spezifische RNAi-vermittelte Knock-down in Primärkulturen hippocampaler Neurone angewandt. Elektrophysiologische Experimente zeigten, dass die Isoform-spezifische Reduktion zu Subtyp-spezifischen Veränderungen der  $I_h$ -Strom-Eigenschaften führte. Dies zeigt, dass die einzelnen HCN-Kanal-Isoformen aufgrund ihrer unterschiedlichen molekularen und biophysikalischen Beschaffenheit letztlich die Eigenschaften des  $I_h$ -Stroms auf unterschiedliche Art und Weise prägen. Somit haben Neurone die Möglichkeit, sich durch regulierte Expression der einzelnen HCN-Kanal-Untereinheiten an ständig wechselnde Anforderungen, sowohl während der Entwicklung als auch in der Aufrechterhaltung neuronaler Funktionen, anzupassen.

Neurone funktionieren jedoch nicht als eigenständige Einheiten, sondern sind in neuronale Netzwerke eingebunden. Um die Folgen der Reduktion der HCN2-Isoform für die neuronale Übertragung und Integration von Informationen zu untersuchen, wurden exzitatorische synaptische Ereignisse in Primärkulturen hippocampaler Neurone gemessen. Diese Experimente implizierten, dass die HCN2-Untereinheit sowohl an der

präsynaptischen Freisetzung von Neurotransmittern als auch an der postsynaptischen Integration des Signals beteiligt ist. Um die Rolle der HCN2-Untereinheit in der Gestaltung der Netzwerkeigenschaften des Hippocampus zu untersuchen, wurden stereotaktische rAAV-Injektionen durchgeführt. Die Injektion in den dorsalen Hippocampus erwachsener Mäuse führte unerwarteterweise zu einer Degeneration der CA1-Pyramidalzellschicht. Ob für diese Degeneration der Verlust der HCN2-Untereinheit ursächlich ist oder aber durch Nebeneffekte hervorgerufen wurde, kann nicht abschließend beantwortet werden.

## Abstract

To fulfill their functions in processing and transmitting information by electrical potentials, neurons heavily rely on proper equipment with membrane-bound ion-conducting channels. Among these, the unique properties of hyperpolarization-activated and cyclic nucleotide-gated (HCN) channels and the corresponding  $I_h$ -current contribute to various electrical properties of neurons.

To elaborate on the specific role of HCN channels in shaping electrical properties of neurons, two gene-expression interfering tools, i.e. RNAi and CRISPRi, were established and evaluated. By using Adeno-associated viruses (AAVs) as gene ferries, these tools were delivered to post-mitotic neurons. Validation of both knock-down techniques showed that RNAi and CRISPRi were capable to reduce *hcn*-transcript levels. However, RNAi-mediated HCN-channel knock-down was more robust and efficient than CRISPRi-mediated knock-down.

During phylogenetic development, four different HCN channel isoforms (HCN1-4) emerged in mammals. In order to elaborate on the contribution of the individual HCN channel subunits to neuronal functions, the subunit-specific RNAi-mediated knock-down was utilized in primary hippocampal neurons. Electrophysiological experiments showed that the isoform-specific knock-downs were capable of inducing subtype-specific changes in  $I_h$ -current properties. Thus, due to their different biophysical identities, the differential expression pattern of the individual HCN channel isoforms ultimately shapes the  $I_h$ -current properties to adapt to the requirements of neurons.

Because neurons are incorporated into neural networks *in vivo* they do not function as individual units. To examine the consequences of HCN2 isoform knock-down on neuronal transmission and information integration, excitatory synaptic events were measured in primary hippocampal neurons. These experiments indicated that the HCN2 subunit might participate in both, presynaptic neurotransmitter release and postsynaptic signal integration. Furthermore, stereotaxic AAV injections and subsequent behavioral and biochemical analyses were performed to investigate the role of HCN2 in influencing hippocampal network properties. Unexpectedly, injection of AAVs in the dorsal hippocampus of adult mice resulted in severe degeneration of the CA1 pyramidal cell layer. It is unclear whether this degeneration can be attributed to the loss of HCN2 or by unacknowledged side effects.



---

**Table of Content**


---

Zusammenfassung .....	V
Abstract .....	VII
Table of Content.....	1
List of Abbreviations.....	3
<b>Chapter 1 Introduction.....</b>	<b>7</b>
1.1 Hyperpolarization-activated and cyclic nucleotide-gated (HCN) channels .....	8
1.1.1 Structure of HCN channels.....	8
1.1.2 Function and properties of HCN channels.....	10
1.1.3 HCN channels and the Hippocampus.....	13
1.2 Gene-expression interfering techniques .....	15
1.2.1 RNA interference (RNAi).....	15
1.2.2 CRISPR interference (CRISPRi) .....	17
1.3 Aim of the Thesis .....	20
<b>Chapter 2 Material and Methods .....</b>	<b>21</b>
2.1 Chemicals, kits and consumables .....	21
2.2 Cloning of constructs.....	21
2.3 Validation of knock-down efficiencies for shRNAs/sgRNAs.....	22
2.4 Production and purification of recombinant Adeno-associated viruses (rAAVs) .....	23
2.5 Heterologous expression of proteins in HEK293 cells.....	24
2.6 Primary hippocampal neuron (PHN) cultures .....	24
2.7 Organotypic hippocampal slice culture (OHSC) .....	25
2.8 Immunocytochemistry.....	25
2.8.1 Colocalization analysis .....	26
2.9 Stereotaxic injections of rAAV vectors .....	26
2.10 Behavioral animal experiments.....	27
2.10.1 Elevated zero maze test .....	28
2.10.2 Open field test.....	28
2.10.3 Spatial object recognition .....	28
2.10.4 Fear conditioning .....	29
2.11 Preparation of tissue .....	29
2.12 Immunohistochemistry.....	30
2.13 Quantification of gene expression by real-time PCR.....	30
2.13.1 RNA isolation and cDNA synthesis .....	30
2.13.2 Standard fragment generation for qPCR .....	31
2.13.3 Real-time PCR.....	31

2.13.4 Agarose gel electrophoresis .....	32
2.14 Protein analysis.....	33
2.14.1 Protein preparation from tissue .....	33
2.14.2 Electrophoretic protein separation and western blotting.....	33
2.14.3 Protein detection on western blots .....	34
2.15 Calcium-imaging.....	34
2.16 Whole-cell patch-clamp recordings .....	35
2.17 Data analysis.....	36
2.18 Figures and Tables of Materials and Methods.....	37
<b>Chapter 3 Results .....</b>	<b>43</b>
3.1 Knock-down of HCN channel expression in vitro .....	43
3.1.1 Generation of AAV-based gene-interfering tools .....	43
3.1.2 Functional expression of knock-down constructs in HEK293 cells .....	46
3.1.3 Validation of knock-down in HEK293 cells .....	48
3.1.4 Functional expression of knock-down constructs in PHNs.....	52
3.1.5 Validation of knock-down in PHNs.....	54
3.1.6 Functional expression and validation of knock-down constructs in OHSCs .....	56
3.2 Electrophysiological characterization of HCN channels.....	60
3.2.1 Electrophysiological characterization of HCN channels in HEK293 cells.....	60
3.2.2 Electrophysiological characterization of HCN channels in PHNs of wildtype and HCN1 <sup>-/-</sup> mice.....	61
3.2.3 Electrophysiological characterization of HCN-channel function in RNAi treated PHNs .....	64
3.2.4 Consequences of HCN channel reduction on basic properties of PHNs.....	66
3.2.5 Consequences of HCN channel reduction on I <sub>h</sub> -current properties.....	68
3.2.6 Effects of HCN channel blocker ZD7288 on PHNs.....	74
3.2.7 Consequences of HCN2-channel knock-down for neuronal signaling.....	78
3.3 In vivo HCN2-channel knock-down by stereotaxic intrahippocampal rAAV injections ...	86
3.3.1 Analysis of behavioral changes upon stereotaxic intrahippocampal rAAV injections .....	87
3.3.2 Biochemical and molecular-biological analyses of injected animals .....	93
3.3.3 Immunohistochemical analysis of changes upon stereotaxic intrahippocampal rAAV injections .....	97
<b>Chapter 4 Discussion.....</b>	<b>107</b>
4.1 Knock-down of HCN-channel isoforms in vitro .....	108
4.2 Electrophysiological characterization of HCN-channel knock-down in vitro .....	111
4.3. In vivo HCN2-channel knock-down.....	117
4.4 Summary and Outlook.....	121
<b>Chapter 5 Bibliography .....</b>	<b>122</b>
Danksagung .....	CXXXIII
Erklärung.....	CXXXIV
Lebenslauf .....	CXXXV

**List of Abbreviations**

---

4-AP	4-Aminopyridine
AAV	Adeno-associated virus
aCSF	artificial Cerebrospinal Fluid
AGO2	Argonaut 2
AMPA	$\alpha$ -amino-3-hydroxy-5-methyl-4-isoxazolepropionic acid
Amp <sup>r</sup>	Ampicillin resistance
AP	anteroposterior
AP	Action potential
BDNF	Brain-derived Neurotrophic Factor
BLAST	Basic Local Alignment Search Tool
CA	Cornu ammonis
CaMKII	Ca <sup>2+</sup> /calmodulin-dependent protein kinase II
cAMP	cyclic adenosine monophosphate
cDNA	complementary DNA
cGMP	cyclic guanosine monophosphate
CHO	chinese hamster ovary
CMV	Cytomegalovirus
CNBD	cyclic nucleotide binding domain
CNG	cyclic nucleotide-gated
CNQX	cyanquixaline
CNS	central nervous system
CP	crossing point
CRISPR	Clustered Regularly Interspaced Short Palindromic Repeats
CRISPRi	CRISPR interference
D-AP5	D-(-)-2-amino-5-phosphonopentanoic acid
dCas9	dead Cas9
DG	dentate gyrus
DHC	dorsal hippocampus
DMEM	Dulbecco's Modified Eagle Medium
DNA	deoxyribonucleic acid
DR	discrimination ratio
dsRNA	double-stranded RNA
DV	dorsoventral
E	efficiency
e.g.	<i>exempli gratia</i>
EAG-like	ether-à-go-go-like
EC	entorhinal cortex
ECL	enhanced chemiluminescence

---

EDTA	ethylenediaminetetraacetic acid
eEPSC	evoked EPSC
eGFP	enhanced GFP
EGTA	ethylene glycol-bis( $\beta$ -aminoethyl ether)- <i>N,N,N,N</i> -tetraacetic acid
EM	Electron microscopy
EPD	Eukaryotic Promoter Database
EPSC	excitatory postsynaptic current
ERT2	mutant estrogen receptor
Exp5	Exportin-5
EZM	elevated zero maze
FBS	fetal bovine serum
FC	fear conditioning
FCS	fetal calf serum
GABA	$\gamma$ -Aminobutyric acid
GAPDH	glyceraldehyde 3-phosphate dehydrogenase
GFAP	glial fibrillary acidic protein
GFP	green fluorescent protein
HA	human influenza hemagglutinin
HBSS	Hanks' Balanced Salt Solution
HCN	Hyperpolarization-activated and cyclic nucleotide-gated
HCN1 <sup>-/-</sup>	HCN1-channel knock-out genotype
hDop1	human dopamine D1
HEK293	human embryonic kidney 293
HEPES	4-(2-hydroxyethyl)-1-piperazineethanesulfonic acid
HRP	horseradish peroxidase
hU6	human U6
IB4	isolectin B4
I <sub>f</sub> ; I <sub>q</sub> ; I <sub>h</sub>	HCN channel-mediated current
ITR	inverted terminal repeat
Kan <sup>r</sup>	Kanamycin resistance
KRAB	Krüppel-associated box motif
LAMP-1	lysosomal-associated membrane protein 1
LANUV	Landesamt für Natur, Umwelt und Verbraucherschutz
MAP2	microtubule-associated protein 2
MCS	multiple cloning site
mEPSC	miniature EPSC
MiRP1	MinK-related peptide 1
ML	mediolateral
M-MLV-RT	Moloney Murine Leukemia Virus Reverse Transcriptase
MOI	multiplicity of infection
mRNA	messenger RNA
mTOR	mechanistic Target of Rapamycin
NBA	Neurobasal A Medium
NEX	neuronal basic helix-loop-helix protein
NLS	nuclear localization signal

NMDA	N-Methyl-d-aspartic acid
OF	open field
OHSC	organotypic hippocampal slice culture
Ori	origin of replication
p.i.	post injection
PA	paraformaldehyde
PAGE	polyacrylamide gel electrophoresis
PBS	phosphate buffered saline
PCR	polymerase chain reaction
PEI	polyethylenimine
PHN	primary hippocampal neuron
PP	perforant path
PTFE	polytetrafluoroethylene
PVDF	polyvinylidene fluoride
qPCR	quantitative PCR
qRT-PCR	quantitative reversed-transcription PCR
rAAV	recombinant AAV
RACE	rapid extension of cDNA ends
RISC	RNA induced silencing complex
RNA	ribonucleic acid
RNAi	RNA interference
RNaseIII	Ribonuclease III
RT	room temperature
s.d.	standard deviation
Sa	<i>Staphylococcus aureus</i>
SC	schaffer collateral
Scr	scrambled
SDS	sodium dodecyl sulfate polyacrylamide
sEPSC	spontaneous EPSC
sgRNA	short-guidance RNA
shRNA	short-hairpin RNA
siRNA	short-interfering RNA
slm	stratum lacunosum-moleculare
so	stratum oriens
SOR	spatial object recognition
Sp	<i>Streptococcus pyogenes</i>
sp	stratum pyramidale
TAE	Tris-acetate-EDTA
TALE	transcription activator-like effector
TRIP8b	tetratricopeptide repeat-containing Rab8b-interacting protein
TrkB	tropomyosin receptor kinase B
TSS	transcriptional start site
TTX	tetrodotoxin
TVA	Tierversuchsantrag
V <sub>1/2</sub>	half-maximal activation potential

VHC	ventral hippocampus
WB	Westernblot
WPRE	Woodchuck Hepatitis Virus (WHP) posttranscriptional regulatory element
wt	wildtype

---

# Chapter 1

## Introduction

---

Hyperpolarization-activated and cyclic nucleotide-gated (HCN) channels are known to control important electrical properties of neurons, for example by determining and stabilizing the resting membrane potential (Kase and Imoto, 2012). Due to their unique activation and gating properties, these channels play crucial roles in generating rhythmic activities and thus participate, e.g. in cardiac pacemaking (DiFrancesco, 1986), as well as in modulating the sleep and wake cycle in the thalamocortical system (McCormick and Pape, 1990). In contrast to these well characterized properties, the roles of HCN channels in other brain regions are still elusive. Thus, the aim of this thesis was to investigate the consequences of specific HCN channel knock-down in hippocampal neurons both, *in vitro* and *in vivo*.

### 1.1 Hyperpolarization-activated and cyclic nucleotide-gated (HCN) channels

HCN channel currents have been first described in motoneurons (Araki et al., 1961) and later in sinoatrial node cells (Noma and Irisawa, 1976) and photoreceptors (Fain et al., 1978). Because of its unique and unusual physiological appearance, the current was initially named funny-current ( $I_f$ ) (Brown et al., 1979) or queer-current ( $I_q$ ) (Halliwell and Adams, 1982). In this thesis, the term ‘inward current activated by hyperpolarization’ ( $I_h$ ) (Yanagihara and Irisawa, 1980) will be used to describe this current.

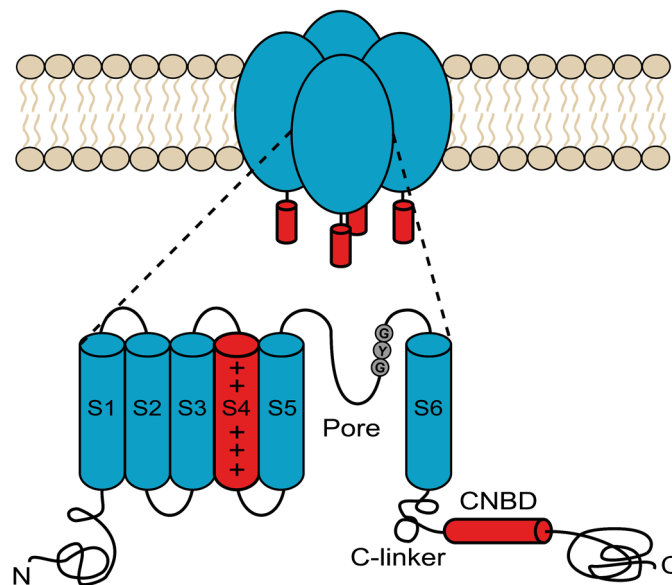


**Figure 1.1: Structure and topology of HCN channels**

Top: Schematic representation of the tetrameric structure of HCN channels. Bottom: Transmembrane and cytoplasmic arrangements of a single HCN channel monomer. One monomer is composed of six transmembrane segments including the voltage sensor (S4), the selectivity filter harboring the GYG motif, the pore forming helices (S5 and S6), and the C-terminal domain harboring the cyclic nucleotide binding domain (CNBD) attached via a C-linker to the S6 helix.

#### 1.1.1 Structure of HCN channels

Molecular cloning of HCN channel subunits finally led to the identification of the molecular basis for the previously described currents (Santoro et al., 1997, Gauss et al., 1998, Ludwig et al., 1998, Santoro et al., 1998, Ludwig et al., 1999). In mammals, the family of HCN channel genes comprises four different isoforms (HCN1-4) (Sunkara et al., 2018). These channels, together with cyclic nucleotide-gated (CNG) (Biel and Michalakakis, 2007) and ether-à-go-go-like (EAG-like) channels (Meyer and Heinemann, 1998), form the subgroup of cyclic nucleotide-regulated channels within the large superfamily of pore-loop cation channels (Yu et al., 2005). The four HCN channel genes

encode for polypeptides of ~800 – 1200 amino acids. Each isoform contains six highly conserved (80 – 90 %)  $\alpha$ -helical segments (S1-S6) with an ion-conducting pore between S5 and S6 (Biel et al., 2009). Similar to all voltage-dependent pore-loop cation channels, a positively charged S4 helix forms the voltage sensor of HCN channels (Fig. 1.1) (Vaca et al., 2000).

In contrast to other voltage gated channels, inward movement of S4 triggers opening of HCN channels, while it leads to the closure of depolarization activated voltage-dependent potassium channels (Männikkö et al., 2002). A recent study based on cryo-EM structures of the human HCN1 channel, showed that the reversed voltage-dependent gating might be explained by several unique structural features of these channels. First, HCN1 channels harbor an unusually long S4 helix, which contacts the C-linker in the cytoplasm. Second, the S4, S5 and S6 helices are in a packing arrangement. Third, an HCN channel specific domain was described. These structural features altogether might stabilize a closed ion channel gate when the S4 voltage sensor is in a ‘depolarized’ state. The authors suggested, that a voltage-driven inward displacement of the S4 helix upon membrane hyperpolarization might disrupt these stabilizing interactions, thus allowing the ion conducting pore to open (Lee and MacKinnon, 2017).

Notably, the amino acid sequences of the pore region of all HCN channel isoforms, which are located between the S5 and S6 helices, contain the selectivity filter motif GYG (Glycine-Tyrosine-Glycine), which is a hallmark of  $K^+$ -selective voltage gated channels (Fig. 1.1) (Doyle et al., 1998). Thus, based on primary structure comparisons, HCN channels were thought to exclusively conduct  $K^+$  ions and to exclude  $Na^+$  ions or divalent ions from being conducted through the pore. However, HCN channels conduct both,  $Na^+$ - and  $K^+$ -ions with permeability ratios of about 1:4, leading to a depolarizing  $Na^+$ -driven current at physiological conditions (Gauss et al., 1998, Ludwig et al., 1998, Santoro et al., 1998, Robinson and Siegelbaum, 2003). Additionally, they also display a small but physiological relevant permeability for  $Ca^{2+}$  ions (Yu et al., 2004). Attempts to solve these rather surprising observations at the molecular level by site-directed mutagenesis approaches were quite unsuccessful in identifying residues in the pore region of HCN channels that may confer the permeation properties (Macri et al., 2002, Azene et al., 2003, Macri et al., 2012). Again, cryo-EM structures of the human HCN1 channel provided a structure-based explanation for these unique HCN channel properties. Potassium selectivity in  $K^+$ -selective voltage gated channels originates from the precise geometry of the selectivity filter, in which bound  $K^+$  ions are coordinated by backbone (=carbonyl)

oxygen atoms of certain amino acid residues located in the selectivity filter (Lee and MacKinnon, 2017). While for  $K^+$ -selective channels binding of 2  $K^+$ -ions in the pore region is essential to increase the probability that a  $Na^+$  ion is hindered to pass through the conduction pathway (Doyle et al., 1998), HCN channels bind only a single  $K^+$ -ion, leading to an increased probability that an entering  $Na^+$  ion can exit on either side and thus might permeate the channel pore. This mechanism of nonselective ion conduction in HCN channels is thought to originate from surrounding amino acids, leading to a reorientation of the selectivity filter compared to  $K^+$ -selective channels (Lee and MacKinnon, 2017).

In addition to the voltage dependence of HCN channel gating, the open state probability and activation kinetics of these channels are modulated by cyclic nucleotides (DiFrancesco and Tortora, 1991). Responsible for the direct modulatory effect of cyclic AMP (cAMP) or cyclic GMP (cGMP) is their binding to the highly conserved cyclic nucleotide binding domain (CNBD) (Fig. 1.1) (Kaupp and Seifert, 2001). In contrast to CNG channels, binding of cyclic nucleotides is not required to open HCN channels (Kaupp and Seifert, 2002, Craven and Zagotta, 2006). Instead, cAMP or cGMP binding induces local conformational changes at the CNBD that are propagated to the ion conducting pore via the C-linker. However, these binding events induce only small displacements of the S6 helix, consistent with the observation that cyclic nucleotide binding alone is insufficient for channel opening (Lee and MacKinnon, 2017).

### ***1.1.2 Function and properties of HCN channels***

Although the four HCN channel isoforms found in mammals (HCN1-4) show a high degree of sequence similarity (Tanguay et al., 2019), basic biophysical features of the different HCN channel subtypes differ remarkably from each other, especially when homomeric channels are examined in heterologous expression systems. Within the HCN channel family, the HCN1 subtype activates at the most positive membrane potentials, with half maximal activation voltages ( $V_{1/2}$ ) of -70 to -90 mV (Altomare et al., 2003). In addition, HCN1 shows the fastest activation kinetics with  $\tau$  values ranging from 30 to 300 ms (Ishii et al., 2001). However, compared to the other members, HCN1 steady-state activation curves show only weak depolarizing shifts in the presence of saturating cAMP concentration (+2 to +7 mV) (Altomare et al., 2003, Stieber et al., 2005). While HCN1 is the fastest activating HCN channel subtype, HCN4 activates the slowest, with  $\tau$  values ranging from a few hundred milliseconds to seconds (Ludwig et al., 1999, Stieber et al.,

2005). Furthermore, HCN4 activates at the most hyperpolarized membrane potentials with  $V_{1/2}$  of around -100 mV (Ludwig et al., 1999, Altomare et al., 2003, Stieber et al., 2005) and its steady-state activation curves are very sensitive to the presence of cAMP, inducing a depolarizing shift of about 20 mV (Stieber et al., 2005). HCN2 and HCN3 adopt intermediate biophysical current properties with  $V_{1/2}$  values of -70 and -80 to -95 mV, respectively (Altomare et al., 2003, Mistrik et al., 2005, Stieber et al., 2005). Moreover, HCN2 activation kinetics range from 150 ms to 1s (Ludwig et al., 1999, Stieber et al., 2005), while HCN3 activation kinetics range from 250 to 400 ms (Mistrik et al., 2005, Stieber et al., 2005). Remarkably, the human HCN2 subtype was found to be very sensitive for cAMP, leading to a depolarizing shift in  $V_{1/2}$  values of around -25 mV, cyclic nucleotides did not induce a shift of  $V_{1/2}$  of the hHCN3 subtype (Stieber et al., 2005) which might be explained by structural difference in the HCN3 channel domains (Biel et al., 2009).

The biophysical properties of the different HCN channel subtypes make them favorable in participating in oscillatory electrical processes, extensively studied in pacemaker cells of the sinoatrial node, responsible for generating the heart beat (Brown et al., 1979, DiFrancesco, 1981, DiFrancesco and Tortora, 1991).

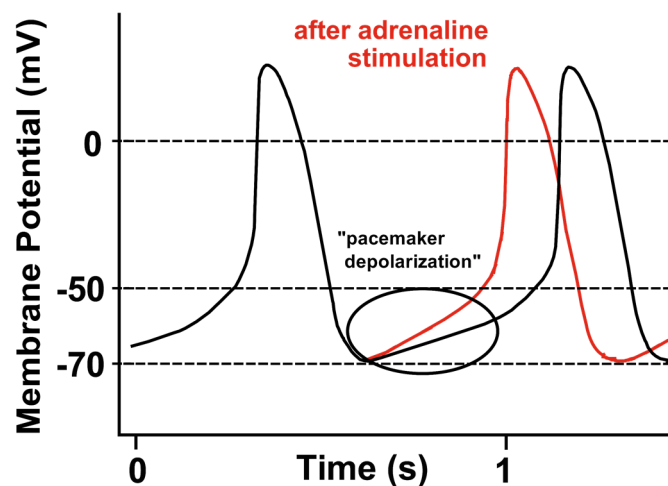


**Figure 1.2: Role of HCN channels and  $I_h$ -currents in cardiac automaticity**

Idealized pacemaker potentials of the sinoatrial node in the absence (black trace) and presence (red trace) of adrenergic stimulation. Modified from (Biel et al., 2009).

Action potentials of pacemaker cells are characterized by a pacemaker depolarization, occurring after the repolarization phase. This depolarization drives the membrane potential back toward the threshold of voltage-gated  $Ca^{2+}$  ion channels, thereby maintaining action potential firing of the sinoatrial node cells (Figure. 1.2) (Mangoni and

Nargeot, 2008). Among others,  $I_h$ -currents are thought to participate in the pacemaker depolarization, since they are activated at hyperpolarized membrane potentials. Furthermore, the direct modulatory effect of cAMP on  $I_h$ -current properties might account for the regulation of the heart beat by sympathetic stimulation. An increased cAMP production due to  $\beta$ -adrenergic stimulation facilitates  $I_h$ -current activation. In contrast, vagal stimulation lowers cAMP levels thus preventing HCN modulation (Brown et al., 1979, DiFrancesco, 1981, DiFrancesco and Tortora, 1991, DiFrancesco, 2019). However, HCN channel currents are not solely responsible for generating the pacemaker depolarization, but might serve as its initiators (Biel et al., 2009).

In addition to the central contribution of HCN channels in heart physiology,  $I_h$ -current contributions were also reported in oscillatory processes of the thalamocortical network during sleep (McCormick and Pape, 1990, Pape, 1996). Due to channel activation close to resting membrane potentials around -70 mV and its non-inactivating properties, HCN channels are thought to exert a depolarizing effect on resting membrane potentials in many cell types (Pape, 1996). Thus, HCN channels might serve to stabilize resting membrane properties against both, hyperpolarizing and depolarizing inputs (Kase and Imoto, 2012). This function of  $I_h$ -currents is thought to influence dendritic integration properties in hippocampal CA1 pyramidal neurons by modulating the kinetics of excitatory and inhibitory postsynaptic potentials (Wahl-Schott and Biel, 2009).

Since the biophysical properties of HCN channel isoforms are strikingly different, the individual subtypes might be expressed differentially and/or complementary. Strengthening this hypothesis, hetero-oligomerization of HCN subunits to heterotetrameric ion channels was observed in various tissues (Bender et al., 2001, Brewster et al., 2007). With exception of HCN2-HCN3 oligomers, all dual combinations of HCN subunits form heteromeric complexes in the plasma membrane (Much et al., 2003). Because the various combinations of heterotetrameric channels result in a multitude of biophysical  $I_h$ -current properties, neurons possess a powerful mechanism to generate specific  $I_h$ -currents to fulfill their physiological requirements. The existence of a plethora of  $\beta$ -subunits, scaffolding proteins, and regulatory proteins, i.e. TRIP8b, Caveolin-3 or MiRP1, even increases the variability of functional HCN channels and may add further variability to their biophysical properties (Sartiani et al., 2017).

### 1.1.3 HCN channels and the Hippocampus

HCN channel expression has been described in numerous cell types throughout the mammalian central nervous system (CNS) (Monteggia et al., 2000). Especially in the hippocampus, a region known to play a critical role in learning and memory (Jarrard, 1993), HCN channels are highly expressed in developing and adult animals (Seo et al., 2015). The hippocampus, together with the adjacent amygdala, forms the central axis of the limbic system of mammals.

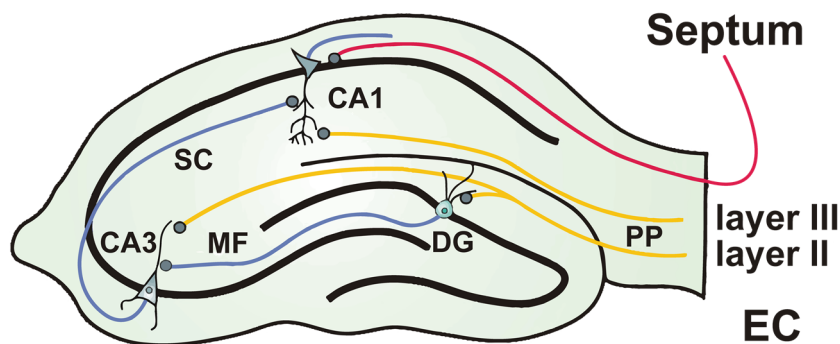


**Figure 1.3: Anatomy of the hippocampal formation**

The hippocampal formation forms a unidirectional network with input from the *entorhinal cortex* (EC) forming connections with the *dentate gyrus* (DG) and *cornu ammonis* (CA) CA3 pyramidal neurons via the *perforant path* (PP) (layer II). DG neurons send axons to CA3 pyramidal cells via the *Mossy fiber* pathway (MF), whereas CA3 neurons send axons to CA1 pyramidal cells via the *Schaffer collateral* pathway (SC). CA1 neurons also receive direct input from the PP (layer III) and from the medial septum-diagonal band of Broca connecting the midbrain to the hippocampus. Modified from (Wahl-Schott and Biel, 2009).

The hippocampal formation is composed of the *cornu ammonis* (CA) subfields CA1, CA2 and CA3 together with the *dentate gyrus* (DG). The synaptic transmission within the hippocampal formation resembles a trisynaptic circuit organization. (1) The information enters the hippocampus from superficial layers (mostly layer II and III) of entorhinal cortex (EC) neurons. Axons originating from layer II neurons project to granule cells of the DG and pyramidal neurons of CA3. This pathway is called the *perforant path* (PP). (2) Additionally, granule cells of the DG send descending axons, forming the so-called mossy fiber, to the pyramidal neurons of CA3. (3) Axons of CA3 pyramidal cells form both, recurrent connections onto other pyramidal cells in CA3, and projections to pyramidal cells located in CA1. This pathway is called the *Schaffer collateral* (SC). Subsequently, pyramidal cells in CA1 project to the subiculum and to deep layers of the entorhinal cortex (Fröhlich, 2016).

Notably, both electrophysiological and immunohistochemical studies revealed that the HCN-current  $I_h$  and the HCN1 and HCN2 subunits are enriched in the distal dendrites of hippocampal pyramidal neurons (Magee, 1998, Lörincz et al., 2002, Notomi and Shigemoto, 2004, Huang et al., 2009). Although at lower densities, HCN channels are also located in the soma of some pyramidal neurons (Robinson and Siegelbaum, 2003). Impairing the  $I_h$ -current by pharmacological blockade or genetic ablation results in augmented dendritic excitability due to an increase in membrane resistance (Magee, 1998, Magee, 1999, Robinson and Siegelbaum, 2003, Huang et al., 2009). These changes in membrane resistance ultimately affect synaptic potential shapes and thus also the dendritic integration properties of the pyramidal neurons (Shah, 2014). Furthermore, especially HCN1 subunits are also localized in hippocampal axons and synaptic terminals of inhibitory and excitatory neurons (Notomi and Shigemoto, 2004, Boyes et al., 2007, Brewster et al., 2007). By regulating calcium entry through T-type voltage gated  $Ca^{2+}$  channels, HCN channels participate thereby also in synaptic transmission within the hippocampal network (Huang et al., 2011). Moreover, HCN channel gene-expression undergoes developmental changes during aging (Seo et al., 2015). Hence, native HCN channels are differently expressed and diversely regulated and thus, the biophysical properties of the  $I_h$ -current contribute to various cellular and network functions within the hippocampal formation. To elucidate the specific role of an individual HCN channel subunit, manipulation of the subunit's expression pattern in a temporally and spatially controlled manner is required.

## ***1.2. Gene-expression interfering techniques***

Despite the success to uncover the functional properties of individual proteins, gaining knowledge on how proteins modulate multicellular networks or animal behavior is still a challenging task. Thus, a central question of this thesis was to examine the biological role of individual HCN channel subtypes and how quantitative differences in their expression levels contribute to mono- and multicellular functions.

The generation and usage of transgenic animals emerged as a key approach for elucidating gene regulation and function. The technology of gene transfer into early developing embryos paved the way for establishing transgenic animals and thus enabled the generation of HCN channel knock-out mouse models (Cho et al., 2009). Although these models provided valuable insights into HCN channel physiology and function, the consequences of altered HCN channel expression were often difficult to interpret as HCN channels are involved in various processes within a single organism. Knock-out of some genes, among them the *hcn4* gene, lead to embryonic lethality (Stieber et al., 2003). The lack of adult mice therefore makes it difficult to determine variable gene functions during certain phases of the life-cycle. Furthermore, most HCN knock-out mouse models result in a global loss of HCN channel subtype expression (Ludwig et al., 2003, Nolan et al., 2004, Stieglitz et al., 2017). These models might be insufficient for evaluating the details of how HCN channels behave in certain tissues and to study the consequences of HCN channel impairment for local cellular or network functions.

### ***1.2.1 RNA interference (RNAi)***

In addition to transgenic approaches, gene expression can be manipulated by impairment of the mRNA level using a mechanism called RNA interference (RNAi) (Chang et al., 2006, Shan, 2010, Boettcher and McManus, 2015).

By combining RNAi with viral vector systems, a temporally and spatially controlled knock-down of a gene of interest can be achieved. Among these viral vector systems, AAVs have proven their potential to deliver genomic material into target cells, both *in vitro* and *in vivo* (Hermonat and Muzyczka, 1984, Lipkowitz et al., 1999, Günther et al., 2019). Until now, AAVs have not been associated with any human disease, even though most of the human population (>70%) are seropositive for one or more AAV serotypes (Calcedo et al., 2011). Due to their broad tissue tropism, non-pathogenic nature

and low immunogenicity, an AAV-based vector approach has been used for the first human gene therapy approved in western nations (Kotterman and Schaffer, 2014).

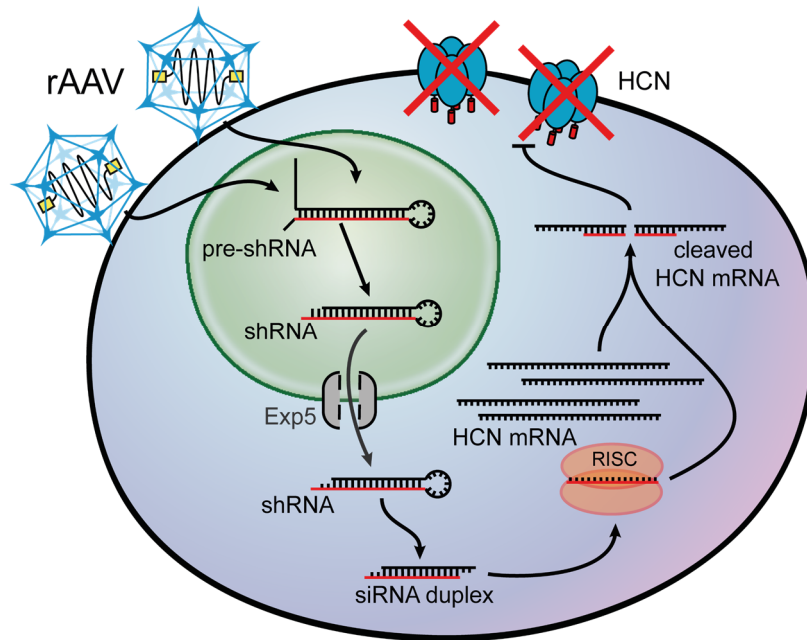


**Figure 1.4: Mechanism of AAV-mediated RNAi induced gene silencing**

Upon transduction of cells with shRNA encoding rAAVs, pre-short hairpin RNA (shRNA) is processed in the nucleus, followed by Exportin-5 (Exp5) dependent export of shRNA to the cytoplasm. After removal of the loop structure, double stranded short-interfering RNA (siRNA) is incorporated into the RNA induced silencing complex (RISC) and one of the RNA strands is removed. The mature shRNA hybridizes to the target mRNA which subsequently becomes cleaved and thereby degraded.

The principle of RNAi is based on a double-stranded RNA (dsRNA)-mediated homology mechanism leading to degradation of targeted mRNA. The cell autonomous RNAi mechanism evolved to regulate eukaryotic gene expression and largely contributes to host immunity against foreign, e.g. viral, gene expression (Unniyampurath et al., 2016). The core component of this mechanism is the expression of small interfering RNAs (siRNAs). These molecules are complementary to the target RNA which shall be attacked. Under (normal) cellular conditions siRNAs are generated by processing long double-stranded RNAs to 21 nt double-stranded RNA molecules. One strand of the siRNA then hybridizes to the mRNA of the target gene. This process is mediated by several proteins that assemble to a complex called “RNA induced silencing complex” (RISC) by which finally the mRNA of the target gene is cleaved.

This mechanism has been adapted and implemented for the use of RNAi as an experimental tool. Vector based systems have been developed, allowing to constitutively express short hairpin RNAs (shRNAs). ShRNA molecules consist of two 19-22 nt long

complementary parts, connected by a loop structure, thus protecting them from degradation by endonucleases. They are processed by the ribonuclease III (RNaseIII)-like enzyme Dicer, to produce siRNAs (Yu et al., 2002, Rao et al., 2009). When processed by Dicer into linear 19-22 nt double stranded siRNA molecules, a characteristic two nucleotide overhang at each 3' end remains (Elbashir et al., 2001). Incorporation of the siRNA into RISC forms the activated RISC complex, which is guided to the complementary target mRNA (Meister and Tuschl, 2004, Leung and Whittaker, 2005). Upon binding to the target mRNA, the RNase H-like endonuclease Argonaut 2 (AGO2) is activated, cleaves the phosphodiester bonds of the target mRNA molecule and thereby induces subsequent degradation of the molecule by other cellular mechanisms (Unniyampurath et al., 2016). Finally, the still activated RISC relieves the cleaved mRNA, and enters the degradation cycle again. Thus, substantial amounts of mRNA are degraded. Consequently, the protein level will be decreased due to the impaired *de novo* protein biosynthesis (Hommel et al., 2003, Siolas et al., 2005, McCaffrey et al., 2008). Although it is widely used, RNAi is prone for induction of inflammatory immune responses as a result of siRNA expression (Meng and Lu, 2017) and also for binding non-targeted mRNA leading to unspecific off-target effects (Qiu et al., 2005).

### ***1.2.2 CRISPR interference (CRISPRi)***

As alternative strategies, programmable genome engineering techniques such as zinc finger and transcription activator-like effector (TALE) nucleases emerged, allowing to impair the expression of target genes at the DNA level (Klug, 2010, Gaj et al., 2013, Joung and Sander, 2013). Unfortunately, all these techniques suffer from off-target effects as well as from technically demanding and sophisticated requirements, resulting in low throughput and limited specificity.

In the last few years the 'Clustered Regularly Interspaced Short Palindromic Repeat' (CRISPR) technique emerged as an extremely successful and efficient tool for introducing targeted mutations into the genome in a variety of cell lines (Jinek et al., 2012, Cong et al., 2013, Liang et al., 2015) and model organisms (Friedland et al., 2013, Jiang et al., 2013, Mali et al., 2013). The CRISPR/Cas9 technique consists of two components: (1) the protein Cas9, an RNA-guided endonuclease naturally integrated in type II CRISPR-Cas bacterial adaptive immune system acting as a helicase and a nuclease to unwind and cut the target DNA; (2) a single-chimeric short guide RNA (sgRNA) which specifies binding of Cas9 to a target sequence (Jinek et al., 2012, Doudna and Charpentier,

2014). This system attracted much attention due to the ease of use, its versatility and reduced off-target effects.

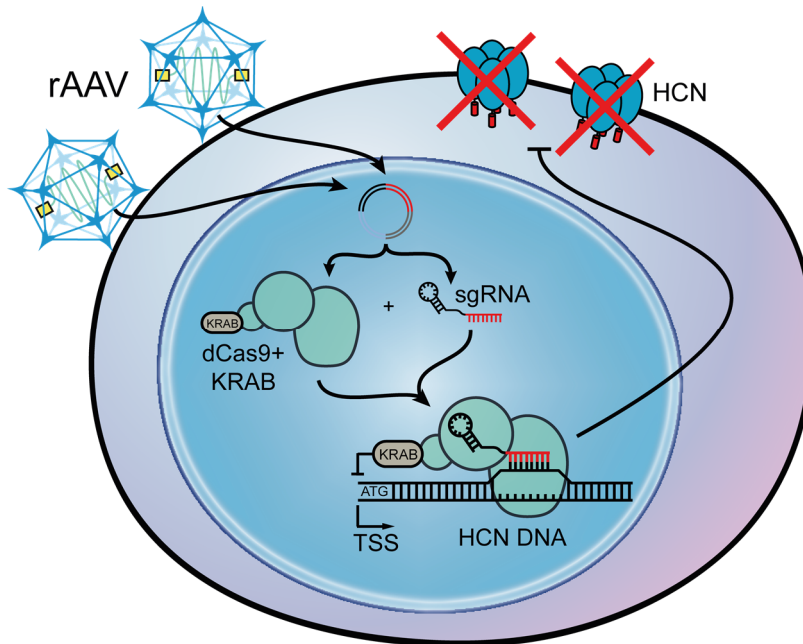


**Figure 1.5: Mechanism of AAV-mediated CRISPRi induced gene silencing**

Mechanism of ‘Clustered Regularly Interspaced Short Palindromic Repeats’ interference (CRISPRi) induced gene silencing. The simultaneous rAAV-mediated expression of enzymatically inactive Cas9+KRAB and a sequence specific sgRNA causes a ‘physical’ block of the promoter region of a target gene. Thereby, transcription and subsequently *de novo* protein biosynthesis are inhibited.

Depending on the experimental design, a complete knock-out mediated by the CRISPR/Cas9 technique may still have some disadvantages, especially when interfering with essential genes participating in cell cycle regulation, metabolism, or cellular signaling in general. To overcome these drawbacks, Qi and colleagues implemented the benefits of RNAi into the methodology of CRISPR and presented a technique called CRISPR interference (CRISPRi) (Gilbert et al., 2013, Larson et al., 2013, Qi et al., 2013). CRISPRi is based on a mutation in the Cas9 gene, leading to a loss of the nuclease activity in the Cas9 protein. The enzymatically inactive molecule is called dead Cas9 (dCas9). Moreover, dCas9 was fused to the Krüppel-associated box (KRAB) repression domain, to produce an efficient transcriptional interference protein complex (Gilbert et al., 2013). In the nucleus, the dCas9-KRAB fusion protein binds to the endogenous DNA and interferes with the transcription machinery without cutting the DNA sequence. Because CRISPRi is designed to prevent transcription by binding to the gene’s promoter, the dCas9-KRAB protein is targeted to the transcriptional start site (TSS) of a gene of interest by a sgRNA. Typically, CRISPRi is effective in a gene’s promoter encompassing residues

-50 to +300 bps of the TSS (Gilbert et al., 2014). This strategy almost abolishes the likelihood of off-target effects (Mandegar et al., 2016).

Beside the enormous potential of CRISPR and CRISPRi in controlling and regulating gene expression, these tools are challenging to deliver into postnatal cells or animals. Again, rAAVs have the potential to overcome these limitations. Nevertheless, rAAVs possess a restricted cargo size of 4.5 kb (excluding the inverted terminal repeats) (Grieger and Samulski, 2005, Wu et al., 2010), which limits the success of packaging the commonly used *Streptococcus pyogenes* Cas9 (SpCas9, 4.2 kb) (Jinek et al., 2013) and its sgRNA with suitable control elements. To overcome this drawback, Ran and colleagues characterized smaller Cas9 orthologs from different species and identified the 3.2 kb large Cas9 enzyme from *Staphylococcus aureus* (SaCas9) as a potential candidate to substitute for SpCas9 (Ran et al., 2015). Finally, an enzymatically inactive (dSaCas9-KRAB) fusion construct was generated that can be expressed together with specific sgRNAs and suitable control elements by rAAVs *in vitro* and *in vivo* (Thakore et al., 2018).

### ***1.3 Aim of the Thesis***

The main focus of this thesis is to contribute to the understanding of HCN channel function in neurons in general and in hippocampal neuronal signal processing in particular. In order to elaborate on the functions of individual HCN channel subunits to neuronal and systemic functions, strategies are required to specifically interfere with HCN channel subunit expression in a temporally and spatially controlled fashion. Consequently, one goal of this thesis is to establish an AAV-delivered form of CRISPRi and comparing it with the previously established AAV-delivered form of RNAi, to identify the most suitable technique for HCN subunit-specific knock-down *in vivo* and *in vitro*.

With a suitable technique on hand, the consequences of HCN subunit-specific knock down in primary hippocampal neuron cultures will be determined. By incorporating electrophysiological and Calcium imaging experiments, the function of individual HCN channel subtypes in controlling electrical neuronal properties will be examined. To elaborate on the participation of the HCN2 subunit in neuronal signaling, excitatory synaptic events will be measured in neurons where the HCN2 subunit is specifically downregulated.

In a recent study, the group of Arnd Baumann could show that HCN4 in the dorsal hippocampal network contributes to emotion-related memory formation (Günther et al., 2019). By choosing a similar experimental approach, hence, stereotaxic viral injections and subsequent behavioral and biochemical analysis, the role of HCN2 in influencing hippocampal network properties will be examined.

---

# Chapter 2

## Material and Methods

---

### *2.1 Chemicals, kits and consumables*

Chemicals were purchased from: AppliChem (Darmstadt, Germany), Merck Millipore (Hohenbrunn, Germany), Serva (Heidelberg, Germany) and Sigma-Aldrich (Taufkirchen, Germany). Consumables were purchased from: BD Biosciences (Franklin Lakes, NJ, USA), Greiner (Frickenhausen, Germany), Ibidi (Martinsried, Germany), Menzel (Braunschweig, Germany), Millipore (Hohenbrunn, Germany), Eppendorf (Hamburg, Germany) and VWR (Langenfeld, Germany).

### *2.2 Cloning of constructs*

All molecular biological techniques were performed, if not stated otherwise, according to (Green, 2012). For targeting *hcn* genes by RNAi, several shRNA-encoding recombinant plasmids were purchased from Merck Millipore (Darmstadt, Germany). Individual fragments were cloned into pENN-CaMKIIeGFP vector provided by the University of Pennsylvania Vector Core (Philadelphia, PA, USA) containing the human U6 (hU6) promoter 5' upstream to the shRNA-encoding fragment (see Table 2). For calcium-imaging in primary hippocampal neurons, the eGFP reporter gene was replaced by a GCaMP6f-WPRE encoding cassette, isolated from Addgene (Watertown, MA, USA) plasmid #100834 (pENN.AAV.CamKII.GCaMP6f.WPRE.SV40), which was a gift from James M. Wilson. For generating a CRISPRi vector, a custom designed backbone including Adeno-associated virus (AAV) serotype 2 wildtype (wt) inverted terminal repeats (ITRs), a human influenza hemagglutinin (HA)-tag, and a KRAB (Krüppel-associated box motif) element was purchased from Thermo Fisher Scientific. The sgRNA scaffold including the hU6 promoter and a dSaCas9-encoding construct were

gifts from Feng Zhang (Addgene plasmid #61591 for the sgRNA scaffold and the SaCas9; and plasmid #61594 for the dSaCas9) (Ran et al., 2015). For subcellular localization experiments, the sgRNA scaffold was replaced by an eGFP reporter gene, or the HA-tag was replaced by a miniSOG fluorescent reporter (Shu et al., 2011). *Hcn*-gene specific sgRNA sequences (see Table 3) were designed using E-CRISP, a CRISPR target-site identification online tool (Heigwer et al., 2014). Complementary single-stranded oligonucleotides were purchased from Eurofins (Ebersberg, Germany). Complementary pairs of oligonucleotides were incubated at 95°C for 5 min in 50 mM NaCl, 1 mM EDTA, 10 mM Tris/HCl, pH 7.5, and annealed while cooling the samples to RT. Double-stranded fragments were cloned into the sgRNA scaffold of the vector backbone by restriction digest (BsaI) followed by ligation. For analyzing specificity and efficacy of CRISPRi mediated gene knock-down in HEK293 cells, human dopamine D1 receptor (NM\_000794) promoter was purchased from GeneCopoeia (HPRM30728) (Rockville, MD, USA) and cloned into a pcDNA3.1 expression vector, thereby substituting for the CMV promoter to drive expression of a mCherry fluorescent reporter in cells constitutively expressing dopamine D1 receptors.

### ***2.3 Validation of knock-down efficiencies for shRNAs/sgRNAs***

For validation of RNAi mediated knock-down in HEK293 cell lines constitutively expressing individual HCN channel subunits (HCN1, 2, 4), hU6-shRNA+CMV-eGFP encoding constructs were transfected by the calcium phosphate co-precipitation method described by Chen and Okayama (Chen and Okayama, 1987). For each target gene, up to five different shRNA sequences (see Table 2) were examined independently. For validation of CRISPRi mediated knock-down in HEK293 cells, hU6-sgRNA and CMV-dSaCas9-KRAB encoding constructs were transfected by calcium phosphate co-precipitation in a cell line constitutively expressing mCherry reporter under the control of the human dopamine D1 (hDop1) receptor promoter. Five different sgRNA sequences (see Table 3) were examined independently. For validation of RNAi in primary hippocampal neurons (PHNs), hU6-shRNA+ CKII-eGFP encoding recombinant Adeno-associated viral particles (rAAVs) were produced (see Chapter 2.4). PHNs were transduced with a multiplicity of infection (MOI) of  $2 \times 10^4$  viral particles per neuron. For validation of CRISPRi in PHNs, hU6-sgRNA+ CKII-dSaCas9-KRAB encoding constructs were packaged into viral particles of serotype 2 and 9 and PHNs were

transduced with a MOI of  $2 \times 10^4$  viral particles per neuron. For each target gene, up to 4 different sgRNA sequences were examined independently (see Table 3). Total RNA was isolated from HEK293 cells and PHNs using the RNeasy Mini Kit (Qiagen) according to the supplier's protocol. Quantification of knock-down efficiencies was done as described in chapter 2.13. Those constructs which induced a robust and reproducible knock-down were chosen for further analysis (Table 4).

#### ***2.4 Production and purification of recombinant Adeno-associated viruses (rAAVs)***

Recombinant Adeno-associated viral (rAAV) particles were prepared by triple-transfection of HEK293 cells (ATCC; #CRL-1573), using a modified calcium phosphate coprecipitation method (Chen and Okayama, 1987) or PEI transfection (Longo et al., 2013). HEK293 cells were cultivated in DH10 medium (DMEM + Glutamax<sup>TM</sup>, 10 % (v/v) FBS, 1 % (v/v) antibiotics/antimycotics (all from Gibco/Thermo Fisher Scientific)) at 37°C, 5 % CO<sub>2</sub>, and 95 % relative humidity. After 24 h, cells were triple transfected with vectors flanked by AAV2 (wt) inverted terminal repeats (ITRs) containing the transgenic viral genome and the helper plasmids pXX6-80 and pRC2 or pRC9 (R.J. Samulski, University of Florida, Gainesville, USA) providing the proteins for DNA replication and capsid assembly of rAAVs (see Table 5). 24 h after transfection the medium was exchanged for hunger medium (DH10, 2 % (v/v) FBS, and 1% (v/v) antibiotics/antimycotics (all from Gibco/Thermo Fisher Scientific)). 72 h after transfection cells were harvested in PBS-M/K (130 mM NaCl, 2.5 mM KCl, 1 mM MgCl<sub>2</sub>, 70 mM Na<sub>2</sub>HPO<sub>4</sub>, 30 mM NaH<sub>2</sub>PO<sub>4</sub>, pH 7.4) and centrifuged (200xg, 4°C, 5min). Cell pellets were re-suspended in lysis buffer (150 mM NaCl, 50 mM Tris/HCl, pH 8.5) and cells were lysed by five freeze/thaw-cycles. Free nucleic acids were digested with benzonase (50 U/ml; Merck Millipore, Darmstadt, Germany) for 30 min at 37°C. After a centrifugation step (5000xg, 4°C, 30 min) the rAAV suspension was sub-layered with iodixanol solutions (for details see Table 6) and centrifuged (rotor Ti 70; 264,000xg, 4°C, 2 h). Viral particles were collected in the 40 % iodixanol phase, sterile filtered (0.2 µm pore size) and further purified using Amicon Ultra Centrifugal Filters (Ultracel-100k, 15 ml; Merck Millipore). For determination of genomic titers, viral genomes were isolated using the DNeasy Blood & Tissue Kit (Qiagen) according to the supplier's protocol and quantitative PCR (see Chapter 2.13) was performed using primers framing

either a segment of the eGFP-encoding sequence or the dSaCas9-encoding sequence (Table 12).

### ***2.5 Heterologous expression of proteins in HEK293 cells***

Human embryonic kidney cells (HEK293; #85120602) were obtained from ECACC/Sigma Aldrich (Taufkirchen, Germany) and grown in a low glucose containing medium (M10, MEM+Glutamax™, 10% (v/v) fetal calf serum (FCS), 1% antibiotics/antimycotics, and 1% (v/v) non-essential amino acids (all from Gibco/Thermo Fisher Scientific)). Cells were propagated in 9 cm petri dishes at 37°C, 5% CO<sub>2</sub> and ~95% relative humidity. Twice a week, when cells reached approximately 90% confluency, they were trypsinized and seeded at densities of 10 - 14 x 10<sup>5</sup> cells onto new petri dishes. To establish cell lines constitutively expressing individual HCN channel subunits (HCN1, 2, 4) or the human dopamine D1 receptor promoter-mCherry construct, transfections were performed with a modified calcium phosphate co-precipitation method. Cell clones were selected in the presence of Geneticin (G418; 0.8 – 1 mg/mL in M10 medium). Functional expression of HCN channels or mCherry and homogeneity of cell clones was examined by immunological staining.

### ***2.6 Primary hippocampal neuron (PHN) cultures***

Hippocampi were prepared from 1 - 3 days-old wildtype mice (C57BL/6 strain obtained from an in-house animal facility) or a transgenic 129/Sv-based mouse line that does not express functional HCN1 channel proteins (Nolan et al., 2003). Animals of the transgenic strain were kindly provided by Dr. E. R. Kandel (Center for Neurobiology and Behavior, Columbia University, USA). Brains were dissected in ice-cold Hanks' balanced salt solution (HBSS; Gibco/Thermo Fisher Scientific). Hippocampi were incubated in papain solution (DMEM (Gibco/Thermo Fisher Scientific), 25 U/mL papain, 1.6 mM L-cysteine, 1 mM CaCl<sub>2</sub>, 0.5 mM EDTA) at 37°C for 20 min and subsequently transferred to inactivating solution (2.5% (w/v) trypsin inhibitor, 2.5% (w/v) albumin in FCS solution consisting of DMEM, 100 U/mL penicillin, 100 µg/mL streptomycin, 10% (v/v) FCS; all from Gibco/Thermo Fisher Scientific), and 0.1% (v/v) MITO+ serum extender (Corning/Thermo Fisher Scientific, Darmstadt, Germany)) at 37°C for 5 min. Cells were then triturated in FCS solution. PHNs were counted and plated on coverslips in 4-well plates (Ibidi, Martinsried, Germany) pre-coated with poly-D-lysine (0.2 mg/mL

poly-D-lysine, 50 mM H<sub>3</sub>BO<sub>3</sub>, 25 mM Na<sub>2</sub>B<sub>4</sub>O<sub>7</sub>, pH 8.5). PHNs were plated with a density of 300 cells/mm<sup>2</sup> and maintained in 500 µL NBA medium (Neurobasal A Medium (Gibco/Thermo Fisher Scientific), 100 U/ml penicillin, 100 µg/ml streptomycin, 2% (v/v) B27-supplement (Invitrogen/Thermo Fisher Scientific, Darmstadt, Germany) and 1% (v/v) Glutamax (Gibco/Thermo Fisher Scientific)) at 37°C, 5% CO<sub>2</sub> and 95% relative humidity for 15 days. Medium was partially exchanged every 2 - 3 days. For transduction, rAAVs were added with a MOI of  $2 \times 10^4$  per neuron, 2 - 3 days after plating (days *in vitro*, d.i.v.).

### **2.7 Organotypic hippocampal slice culture (OHSC)**

Hippocampi from 2 - 3 days-old mice (C57BL/6 strain from an in-house animal facility) were dissected in ice-cold oxygenated dissection buffer (aCSF: 124 mM NaCl, 2.5 mM KCl, 1.25 mM NaH<sub>2</sub>PO<sub>4</sub>, 26 mM NaHCO<sub>3</sub>, 5 mM MgSO<sub>4</sub>, 0.5 mM CaCl<sub>2</sub>, 25 mM D-glucose). Hippocampi were placed on a PTFE membrane (Merck, Darmstadt, Germany) and cut into 300 µm coronal slices using a custom-made tissue chopper. Slices were washed three times in pre-warmed HBSS without Ca<sup>2+</sup>- and Mg<sup>2+</sup>-ions (Gibco/Thermo Fisher Scientific). Three slices were collected and positioned on Millicell cell culture inserts (30 mm, hydrophilic PTFE, 0.4 µm; Merck, Darmstadt, Germany) in 6 well culture plates (Corning/Merck, Darmstadt, Germany) containing 1 mL of a well-established slice culture medium according to Stoppini et al. (Stoppini et al., 1991) with slight modifications (80% (v/v) MEM, 20% (v/v) heat inactivated horse serum (Gibco/Thermo Fisher Scientific) containing (in final concentrations) 20 mM HEPES, 14.5 mM NaCl, 2 mM MgSO<sub>4</sub>, 1 mM CaCl<sub>2</sub>, 1 mM L-glutamine, 80 µM ascorbic acid, 13 mM D-glucose, 0.033 % (v/v) insulin, 50 U/mL penicillin, 50 µg/mL streptomycin). Plates were kept in a humidified CO<sub>2</sub> incubator (5% CO<sub>2</sub>, 95 % relative humidity) at 37°C and cultures were maintained for a maximum of 15 days. Medium was partially exchanged every 2 - 3 days. For transduction, a total of  $1 \times 10^8$  rAAVs were added on top of a slice at d.i.v. 1 - 2.

### **2.8 Immunocytochemistry**

Primary and secondary antibodies used for immunocytochemistry (ICC) are listed in Table 7 and 8. HEK293 cells, PHNs, or OHSCs were rinsed with PBS (NaCl 140.3 mM;

KCl 3.68 mM; Na<sub>2</sub>HPO<sub>4</sub> 9.89 mM; KH<sub>2</sub>PO<sub>4</sub> 1.76 mM; pH 7.3) and fixed in PFA (4% (w/v) paraformaldehyde in PBS) for 10 min at room temperature (RT). After several rinses with PBS, unspecific binding sites were blocked for 1 h at RT in blocking solution (CT: ChemiBLOCKER (Merck, Darmstadt, Germany) 5 % (v/v), Triton X-100 0.5% (v/v) in PBS). Subsequently, samples were incubated with primary antibodies (Table 7) in CT at 4 °C over night or at RT for 4 h, rinsed for several times with PBS and then incubated with secondary antibodies (Table 8) in CT at RT for 1 h. Finally, samples were washed with PBS, before mounting the coverslips containing cells or PTFE membranes containing slices in Aqua-Poly/Mount (Polysciences, Eppelheim, Germany) on microscopy slides. Fluorescent images were obtained with an inverted confocal laser scanning microscope (TCS SP5II; Leica, Wetzlar, Germany).

### ***2.8.1 Colocalization analysis***

HEK293 cell lines constitutively expressing individual HCN channel subunits (HCN1, 2, 4) were transfected with shRNA encoding plasmids using PEI transfection (Longo et al., 2013). Cells were plated on coverslips in 24-well plates (Greiner) pre-coated with poly-L-lysine (0.1 mg/mL) with a density of 300 cells/mm<sup>2</sup>. Plates were kept in a humidified CO<sub>2</sub> incubator (5% CO<sub>2</sub>, 95% relative humidity) at 37°C and cultures were maintained for two days before fixation. After immunocytochemistry and image acquisition using an inverse confocal laser scanning fluorescence microscope (TCS SP5II, Leica), images were analyzed using the ImageJ Coloc 2 analysis plugin (Schindelin et al., 2012).

### ***2.9 Stereotaxic injections of rAAV vectors***

All experimental procedures were approved by the LANUV (Landesamt für Natur, Umwelt und Verbraucherschutz Nordrhein-Westfalen, Germany), TVA #81-02.04.2018.A309. Animals (4 weeks old male mice, *Mus musculus*, C57BL/6J (Charles River, MA, USA)) were kept in groups of 4 animals in greenline cages (Tecniplast, Germany) under an inverted 12:12 light:dark cycle at 21 ± 2 °C, 50-70% relative humidity, food and water ad libitum, and nesting material available. For stereotaxic injection, the stereotaxic setup from World Precision Instruments, Inc. (Sarasota, FL, USA) was used. The setup included a Stereotaxic Frame with 45° zygomatic bars for fixation of the cranium on two axes, an UltraMicroPump III (UMP3)

with SYS-Micro4 MicroSyringe pump controller for controlled microinjection, and a NanoFil 10  $\mu$ L syringe with a 33G beveled replacement NanoFil needle for minimal intrusion (see Figure 2.1 A). Animals were kept for 4 weeks for habituation before they underwent stereotaxic injection of rAAV suspensions. Animals were deeply anesthetized with 2.5 % isoflurane prior to and during surgery. Additionally, animals received analgetic treatment with an intraperitoneal injection of 200 mg/kg Novalgine and local injection of Bupivacaine (80  $\mu$ L, 2.5 mg/ml). During surgery an animal temperature controller with a heating plate and a temperature probe (World Precision Instruments, Inc.) was used to keep the body temperature of the anesthetized animals constant. The fur at the surgical site was removed, skin was cleaned and finally prepared with Kodan Tinktur forte (Schülke, Hamburg, Germany). An incision was made to expose the top of the cranium. Bilateral holes were drilled into the cranium according to the injection coordinates with a micro driller (Ideal Micro Drill, Stoelting, Wood Dale, IL, USA). Injections were performed bilaterally in the CA1 region of the dorsal hippocampus at stereotaxic coordinates -1.9 mm anteroposterior (AP) relative to the bregma,  $\pm$ 1.5 mm mediolateral (ML), and -1.4 mm dorsoventral (DV) (see Fig 2.1 B). Wildtype mice were randomly assigned to receive suspensions of rAAV9 (pENN-hU6-shScr-CaMKII-eGFP) or rAAV9 (pENN-hU6-sh2-CaMKII-eGFP). Animals were injected with 1  $\mu$ L viral suspension ( $2.5 \times 10^9$  virus particles in total) per hippocampus with a rate of 0.2  $\mu$ L/min. After injection of both hippocampi, the incision was sutured with Ethilon Monofil (Ethicon, Somerville, NJ, USA). The skin was cleaned and treated with Octenisept (Schülke). Four hours, 24 hours, and 48 hours post injection, mice received analgetic treatment with intraperitoneal injections of Carprofen (5 mg/kg) and were scored according to the experimental procedures approved by the LANUV. Animals were kept for 4 weeks before behavioral experiments were performed. One week before starting behavioral experiments mice were single housed and control (shScr injected) or knock-down (sh2 injected) mice were handled for 2 min per day for 3 consecutive days, before the first behavioral experiments were performed.

### ***2.10 Behavioral animal experiments***

Behavioral testing and tissue collection were performed during the morning of the light phase. Data collection and analysis of behavioral experiments were performed automatically using the ANY-maze (Stoelting) video tracking system.

### ***2.10.1 Elevated zero maze test***

At day one, naive single housed control (shScr injected) or knock-down (sh2 injected) mice were exposed to a custom made zero maze with a height of 70 cm, a boardwalk width of 5 cm and an outside circumference of 200 cm. It consisted of two open quadrants and two closed quadrants. In this test each mouse was allowed to investigate the apparatus for 5 min. Sessions were scored for the time spent in open and closed quadrants, distance moved, velocity of movement, as well as the number of transitions between quadrants. Transitions were scored when the center point of the body left the former quadrant. Time spent in the open quadrants vs. the closed quadrants was calculated.

### ***2.10.2 Open field test***

At day two, control (shScr injected) or knock-down (sh2 injected) mice were exposed to a custom-made open field arena consisting of a rectangular open field (30.5 cm x 38.5 cm) for 6 min. Quadrants were defined as central (inner area more than 5 cm distant from apparatus wall) and peripheral (within 5 cm distance of apparatus wall) zones. Sessions were scored for the time spent in the central and peripheral zones, the number of transitions between central and peripheral zones, as well as distance moved, and velocity of movement. Transitions were scored when the center point of the body left the former zone. Time spent in the central zone vs. time spent in the peripheral zone was calculated.

### ***2.10.3 Spatial object recognition***

On day three, control (shScr injected) or knock-down (sh2 injected) mice were exposed to a custom-made open field arena consisting of the rectangular open field (30.5 cm x 38.5 cm). The experimental apparatus now included an internal visual cue placed on one of the four arena walls and three distinct objects, *i.e.* a glass bottle, a rectangular metal column, and a half round shaped plastic cylinder, which were placed in the arena at specified locations. During three training sessions on the same day, mice were allowed to freely explore the environment and objects for 6 min in each session. Mice were placed back to their home cage for 3 minutes between the training sessions. After 24 h, mice were placed back in this arena for the testing phase. The same three objects were present in the arena, but one of the three objects (the half round shaped plastic cylinder) was displaced to a novel spatial location. Mice were allowed to freely explore the environment

and the objects for 6 min. The third training sessions and the testing sessions were scored for exploratory behavior in which the animal's snout was within approximately 1 cm distance of an object. Discrimination between the objects was calculated using a discrimination ratio (DR), calculated as the absolute difference in the time spent exploring the novel and familiar objects divided by the total time spent exploring the objects, which takes into account individual differences in the total amount of exploration (Barker and Warburton, 2011). Test sessions were additionally scored for the distance moved and velocity of movement.

### ***2.10.4 Fear conditioning***

Contextual fear conditioning was performed using the ugo basile fear conditioning system (Stoelting). On the eighth day, animals received three training sessions in enclosed rectangular conditioning chambers. Control (shScr injected) or knock-down (sh2 injected) animals were exposed to the conditioning context for 148 s, followed by a 2 s 0.75 mA footshock. Animals were removed from the chambers 30 s after receiving a footshock and were placed back to their home cage for 3 minutes between the training sessions. After 24 h, animals were tested for memory retention by returning them to the conditioning chamber for a single 5 min context test. Training and testing sessions were recorded and freezing behavior as well as distance moved, and velocity of movement was measured using automated scoring software (ANY-maze).

### ***2.11 Preparation of tissue***

For tissue preparation, newborn animals were cooled on ice and decapitated. Adult animals were anesthetized with 5% isoflurane and decapitated. Fur, muscle, and the lower jaw were removed. The cranium was opened along the main fissure using scissors and forceps, and the brain was removed. For western blotting or RNA isolation, the hippocampi were isolated in ice-cold Hanks' balanced salt solution (HBSS; Gibco/Thermo Fisher Scientific) and stored at -80 °C. For immunohistochemistry, the whole brain was fixed in 4% (w/v) paraformaldehyde (PA) for 30 min. Subsequently, the tissue was washed in PBS for 30 min at RT.

### ***2.12 Immunohistochemistry***

For immersion fixation, whole brains were fixed in 4% (w/v) PA for 30 min and washed for 30 min in PBS. For cryo-protection, tissue was incubated in 10% (w/v) sucrose (in PBS) for 1 h at RT and subsequently in 30% (w/v) sucrose (in PBS) for 2 d at 4 °C. For cryo-sectioning, brains were trimmed by removing the olfactory bulbs and the cerebellum. Tissue was embedded in freezing medium (Tissue Tek, Sakura Finetek, Zouterwoude, NL) and frozen at -20 °C. Tissue was cut in 18 – 22 µm thick sections at -22 °C using a cryostat (Microm HM550, Thermo Fisher Scientific). After transfer onto microscope slides (SuperForst Plus, Menzel), slices were air-dried and subsequently stored at -20 °C. For immunohistochemistry, samples were thawed, dried at RT, and encircled with a hydrophobic marker (ImmEdge™ Pen, Vector Laboratories, CA, USA). Immunological staining was performed in a damp chamber to avoid drying of samples. After several rinses with PBS, unspecific binding sites were blocked for 1 h at RT in CT blocking solution. Subsequently, samples were incubated with primary antibodies (Table 9) in CT and 0.75% (v/v) Triton X-100 at 4 °C over night, rinsed for several times with PBS and then incubated with secondary antibodies (Table 10) in CT and 0.75% (v/v) Triton X-100 at RT for 1 h. Finally, samples were washed with PBS, before embedding samples on mounting slides with Aqua-Poly/Mount (Polysciences, Eppelheim, Germany) under coverslips. Fluorescent images were obtained with an inverted confocal laser scanning microscope (TCS SP5II; Leica, Wetzlar, Germany).

### ***2.13 Quantification of gene expression by real-time PCR***

The transcript numbers of individual target genes expressed in cells and/or tissue were determined using quantitative PCR (qPCR).

#### ***2.13.1 RNA isolation and cDNA synthesis***

Total RNA from PHNs or OHSCs was isolated after 14 - 15 d.i.v.. Total RNA from HEK293 cells was isolated 2 – 3 days after transfection using the RNeasy Mini Kit (Qiagen) according to the supplier's protocol. Total RNA from whole hippocampi was isolated by grinding the frozen tissue to a powder using a Teflon bar, followed by adding 200 µL of RLT+ Buffer (Qiagen) to the frozen powder. Further homogenization was achieved by passing the lysate 5 – 10 times through a 25-gauge needle attached to a 1 ml

syringe until a homogeneous lysate was achieved. To minimize RNA loss, the syringe was washed with 150  $\mu\text{L}$  of RLT+ Buffer (Qiagen). First-strand cDNA synthesis was performed using Oligo-dT primers (Qiagen) and Moloney Murine Leukemia Virus reverse transcriptase (M-MLV-RT, Life Technologies/Thermo Fisher Scientific) according to the supplier's protocol. Briefly, cDNA synthesis was performed in a final volume of 25  $\mu\text{L}$ . 1  $\mu\text{g}$  of RNA was mixed with 0.5  $\mu\text{g}$  Oligo-dT Primers and denatured at 65  $^{\circ}\text{C}$  for 10 min. Samples were transferred quickly to 4  $^{\circ}\text{C}$  for 2 min for hybridization of Oligo-dT primers to mRNA. Synthesis of cDNA was performed in First-Strand Buffer (1x), 1 mM dNTPs, 40 U RNaseOUT™ (Invitrogen), 10 mM DTT, 400 U M-MLV-RT at 37  $^{\circ}\text{C}$  for 1 h. The enzyme was inactivated at 65  $^{\circ}\text{C}$  for 10 min and cDNA samples were aliquoted and stored at -80  $^{\circ}\text{C}$ .

### 2.13.2 Standard fragment generation for qPCR

Specific primer pairs targeting the genes of interest were designed to amplify standard fragments (see Table 11). Specificity of primer pairs was confirmed by BLAST analysis. For quantification, defined molecule numbers of standard fragments were used as PCR templates in the light cycler reaction to establish calibration curves. The concentration of purified standard fragments was determined and molecule numbers were calculated based on equation 1. An ubiquitously expressed gene (housekeeping gene), here a component of the glycolysis cascade, the glyceraldehyde-3-phosphate dehydrogenase (*gapdh*), served as control and to normalize data. Amplicon sizes of *gapdh* fragments are 150 bp for amplification on cDNA and 284 bp for amplification on genomic DNA.

#### Equation 1:

$$DNA \text{ molecules in sample} = \frac{\text{amount of DNA} \left[ \frac{\text{ng}}{\mu\text{L}} \right] \times 6.022 \times 10^{23}}{\text{fragment length (bp)} \times 10^9 \times 660 \text{ g/mol}}$$

### 2.13.3 Real-time PCR

Thermocycling was performed in a LightCycler 1.5 (Roche, Mannheim, Germany) using the QuantiTect SYBR Green PCR Kit (Qiagen). QPCR reactions were performed in a final volume of 20  $\mu\text{L}$  in 1x SYBR green reaction buffer on 2  $\mu\text{L}$  aliquots of first-strand cDNA samples and 100 nM of each primer (see Table 11). Melting curves were assessed at the end of each experiment to test for the specificity of the generated DNA fragments.

During each qPCR run (for details see Table 12), three standard fragment probes containing fragment numbers covering at least five orders of magnitude were amplified in duplicate. QPCR reactions of samples were performed in duplicate on first-strand cDNA samples and a water control was run in parallel. Data were analyzed using the second derivative maximum of the exponential amplification reaction to determine the crossing point (CP) of each sample. CP values of the standard probes were assigned to defined fragment numbers and thus could be used to calculate a calibration curve. The amplification efficiency (E) was calculated from the slope ( $m$ ) of the calibration curve using equation 2. To analyze the expression of a target gene in comparison to *gapdh*, different methods were used: (1) for relative expression levels the delta-delta Ct-method (Equation 3) was used. (2) If necessary, efficiency-corrected relative expression values of the target gene in treated and non-treated samples was determined, as qPCR runs may deviate from optimal, i.e. 2-fold, amplification efficiency (Equation 4).

**Equation 2:**

$$E = 10^{-1/m}$$

**Equation 3:**

$$\text{relative expression} = 2^{-(\text{Mean CP of target gene}) - (\text{Mean CP of reference gene})}$$

**Equation 4:**

$$E \text{ corrected expression} = \frac{E(\text{target gene})^{\Delta CP(\text{target gene})}}{E(\text{reference gene})^{\Delta CP(\text{reference gene})}}$$

**2.13.4 Agarose gel electrophoresis**

Size separation of DNA fragments was performed by gel electrophoresis in horizontal agarose gels. Visualization of DNA fragments was achieved by staining with SYBR Safe (Invitrogen). This dye can be excited at 509 nm and emits fluorescence at 534 nm. For agarose gel electrophoresis a TAE-based buffer (40 mM Tris, 1 mM EDTA, 10 mM acetic acid, pH 8.0) system was used. Depending on the DNA fragment sizes agarose concentrations ranged from 0.75 % to 2 % (w/v). Agarose was heat-dissolved in TAE buffer prior to addition of SYBR safe (1:10,000). Samples were mixed with 1/10 volume sample buffer (50 % (v/v) glycerol, 0.1 % (w/v) xylene cyanole, 10 x TAE).

Electrophoresis was performed at 90 mV. A DNA ladder was run in parallel for identification of DNA fragment sizes.

### ***2.14 Protein analysis***

Protein expression in hippocampal tissue was examined by western blotting.

#### ***2.14.1 Protein preparation from tissue***

Protein preparation was done according to S. Baghirova et al., (Baghirova et al., 2015) unless specified otherwise. To study protein expression in tissue, 100  $\mu$ L ice-cold buffer A (150 mM NaCl, 50 mM HEPES, 25  $\mu$ g/ml Digitonin (Sigma-Aldrich), 1 M Hexylene glycol (Sigma-Aldrich) and 1% (v/v) Protease inhibitor cocktail (Sigma-Aldrich)), was added to 5 mg of tissue. Samples were homogenized with a pestle on ice and additionally passed 5 – 10 times through a 25-gauge needle attached to a 1 ml syringe until a homogeneous lysate was obtained. The lysate was incubated for 10 min at 4 °C in a shaker, before it was centrifuged at 4000xg for 10 min at 4 °C. The supernatant containing the cytosolic proteins was collected and stored at -80 °C for further analysis. The pellet was resuspended in 200  $\mu$ L of ice-cold buffer B (150 mM NaCl, 50 mM HEPES, 15% (v/v) Igepal (Sigma-Aldrich), 1 M Hexylene glycol, 1% (v/v) Protease inhibitor cocktail). The suspension was incubated for 30 min at 4 °C in a shaker, before it was centrifuged at 6000xg for 10 min at 4 °C. The supernatant, containing membrane proteins, was collected and stored at -80 °C for further analysis.

#### ***2.14.2 Electrophoretic protein separation and western blotting***

Electrophoretic separation of proteins was performed based on a protocol described by Laemmli (Laemmli, 1970). Sodium dodecylsulfate polyacrylamide gel electrophoresis (SDS-PAGE) was performed in ‘Minigel Twin’ chambers (Biometra). Protein concentrations were determined with the amido-black assay. Proteins (25  $\mu$ g) were separated in 10% polyacrylamide gels. Electrophoresis was performed with 25 mA/gel for approx. 60 min in running buffer (0.1% (w/v) SDS, 192 mM glycine, 25 mM Tris/HCl). Proteins were transferred for 45 min at 2.5 mA/cm<sup>2</sup> onto PVDF membranes (polyvinylidene fluoride; Immobilon P, Millipore) in transfer buffer (20% (v/v) methanol,

25 mM Tris, pH 10.4). Membranes were stored at 4°C in PBS-Tween (PBS, 0.05% (v/v) Tween) before protein detection.

### ***2.14.3 Protein detection on western blots***

For antibody staining, western blot membranes were blocked with blocking solution (5% (w/v) milk powder in PBS-Tween) for 1 hour at room temperature. Afterwards, primary antibodies (see Table 13) were applied in incubation solution (1% (w/v) milk powder in PBS-Tween) and incubated overnight at 4 °C. After washing the membranes in PBS-Tween once shortly and 3 x 5 min at room temperature, HRP-coupled secondary antibodies (see Table 14) were applied in incubation solution. The membrane was washed 3 x 5 min in PBS-Tween and once with PBS, followed by application of ECL (enhanced chemiluminescence)-based detection. The Chemiluminescence Detection Kit for HRP (AppliChem) was used according to the supplier's protocol. Detection of specifically bound antibodies was performed by exposing the membranes to X-ray film (Amersham Hyperfilm™ ECL™, GE Healthcare) for 30 s to 1 h.

For re-probing of western blots, membranes were incubated in stripping buffer (200 mM glycine, 0.1% (w/v) SDS, 1% (v/v) Tween-20, pH 2.2) twice for 10 min at RT. Buffer was discarded and membranes were washed with PBS-Tween twice for 10 min. Afterwards, membranes were washed with PBS-Tween twice for 5 min before they were used for additional immunostaining experiments.

### ***2.15 Calcium-imaging***

To monitor intracellular Ca<sup>2+</sup>-fluctuations in PHNs, Ca<sup>2+</sup>-responses in rAAV9 (pENN-hU6-shRNA-CaMKII-GCaMP6f-WPRE) transduced neurons were triggered by voltage step stimulations of varying intensities. Therefore, coverslips carrying PHNs were placed in a custom-made recording chamber, surrounded by platinum wires (diameter of 0.5 mm) attached to an external stimulation unit (NIHON Electronic Stimulator 1001, NIHON KOHDEN, Rosbach, Germany). Cells were superfused constantly with extracellular saline solution containing 150 mM NaCl, 4 mM KCl, 2 mM MgCl<sub>2</sub>, 2 mM CaCl<sub>2</sub>, 10 mM HEPES, pH 7.4. Live cell imaging was performed using an Olympus BX50WI microscope body (Olympus, Tokyo, Japan) and an ANDOR-TM camera (iXONEM+ DU-897D-CS0BV, Andor Solis, Oxford Instruments, Abingdon, UK) for signal detection. For excitation, a 470 nm LED (THORLABS, M00462613) was used. The light was guided

through a dichroic mirror reflecting wavelengths  $\leq 498$  nm onto the sample. The excitation light was focused on the sample via the objective and the emitted light was guided through the dichroic mirror which passed wavelengths  $\geq 498$  nm. Photons were collected by the camera. The system was operated with an ANDOR SOLIS software (Andor Solis X-2747). During measurements, exposure time and acquisition rate was automatically adjusted. The time units were recalculated to seconds based on the number of frames taken per second.

### ***2.16 Whole-cell patch-clamp recordings***

Whole-cell patch-clamp recordings were performed at RT following the methods described by Hamill et al. (Hamill et al., 1981). Patch pipettes with tip resistances between 2.5 and 4 M $\Omega$  were fashioned from borosilicate glass with an inner diameter of 0.86 mm and an outer diameter of 1.5 mm (Harvard Apparatus, Holliston, MA, USA) using a temperature-controlled pipette puller (P1000, Sutter Instrument, Novato, CA, USA). For HEK293 cells and PHNs, the pipettes were filled with intracellular saline solution containing 10 mM KCl, 10 mM NaCl, 120 mM KGluconate, 10 mM EGTA, 10 mM HEPES, 4 mM MgATP and 0.3 mM NaGTP, adjusted to pH 7.3 with KOH and an osmolality of  $\sim 310$  mOsm/L. During the experiments, the cells were superfused constantly with extracellular saline solution containing 150 mM NaCl, 4 mM KCl, 2 mM CaCl<sub>2</sub>, 2 mM MgCl<sub>2</sub> and 10 mM HEPES, adjusted to pH 7.4 with NaOH and adjusted to 330 mOsm/L with glucose. To isolate HCN-mediated I<sub>h</sub>-currents in primary hippocampal neurons, glutamate receptor (AMPA/kainate receptor) mediated currents were blocked by 10  $\mu$ M CNQX (Tocris Bioscience, Ellisville, MI, USA) and NMDA-mediated currents were blocked by 50  $\mu$ M D-APV (Tocris Bioscience), GABA<sub>A</sub> receptor-mediated currents were blocked by 25  $\mu$ M Bicuculline (Tocris Bioscience), inwardly rectifying potassium currents were blocked by 0.5 mM BaCl<sub>2</sub> (Sigma-Aldrich, Schnellendorf, Germany), voltage-dependent potassium channels were blocked by 3 mM 4-AP (Tocris Bioscience), and voltage-dependent sodium channels were blocked by 2  $\mu$ M TTX (Tocris Bioscience). To isolate action potentials in primary hippocampal neurons, AMPA/kainate receptor-mediated currents were blocked by 10  $\mu$ M CNQX, NMDA-mediated currents were blocked by 50  $\mu$ M D-APV, and GABA<sub>A</sub> receptor-mediated currents were blocked by 25  $\mu$ M Bicuculline. To isolate miniature EPSCs, voltage-dependent sodium channels were blocked by 2  $\mu$ M TTX, and GABA<sub>A</sub> receptor-mediated currents were blocked by

25  $\mu\text{M}$  Bicuculline. To isolate spontaneous and evoked EPSCs, GABA<sub>A</sub> receptor-mediated currents were blocked by 25  $\mu\text{M}$  Bicuculline. To determine mEPSC properties with reasonable fidelity and to prevent detection of “false events” (due to random noise fluctuations), spontaneous mEPSCs with peak amplitudes of  $>15$  pA and a charge criterion of  $>25$  fC (Guzman et al., 2010) were analyzed using a commercial software (Mini Analysis, Synaptosoft, Version 6.0.3). Evoked EPSCs were triggered by 0.5 mA/1 ms current injection at a frequency of 0.2 Hz via a bipolar electrode (PI2CEA3 concentric bipolar electrode, tip diameter 2–3  $\mu\text{m}$ , platinum/iridium, Hofheim, Germany) placed at a distance of 200–250  $\mu\text{m}$  from the patched cell. Peak current amplitudes were measured from baseline current amplitudes determined before the stimulation (Guzman et al., 2014). Whole-cell voltage-clamp and current-clamp recordings were performed using an EPC10 patch-clamp amplifier (HEKA-Elektronik, Lambrecht, Germany) that was controlled by the program Patch Master (version 2.5; HEKA-Elektronik). Electrophysiological data were sampled at 20 kHz and low pass filtered at 2.9 kHz with a four-pole Bessel-filter. Offset potentials, electrode capacity and membrane capacity were compensated manually. PHNs were voltage-clamped at -70 mV. The liquid junction potential between intracellular and extracellular solutions was calculated and also compensated by adjusting the offset potential. Series resistance was compensated between 60 and 80 % with a time constant ( $\tau$ ) of 100  $\mu\text{s}$ .

### ***2.17 Data analysis***

The software used for data recording and analysis is listed in Table 1. Data are represented as mean  $\pm$  s.d. (standard deviation) or as box and whisker plots. The two-tailed unpaired Student's t test was applied for calculation of p values using GraphPad Prism (version 5; Graphpad Software Inc., La Jolla, CA, USA). A p value of  $<0.05$  was considered significant (\* $p<0.05$ , \*\* $p<0.01$ , \*\*\* $p<0.001$ ).

## 2.18 Figures and Tables of Materials and Methods

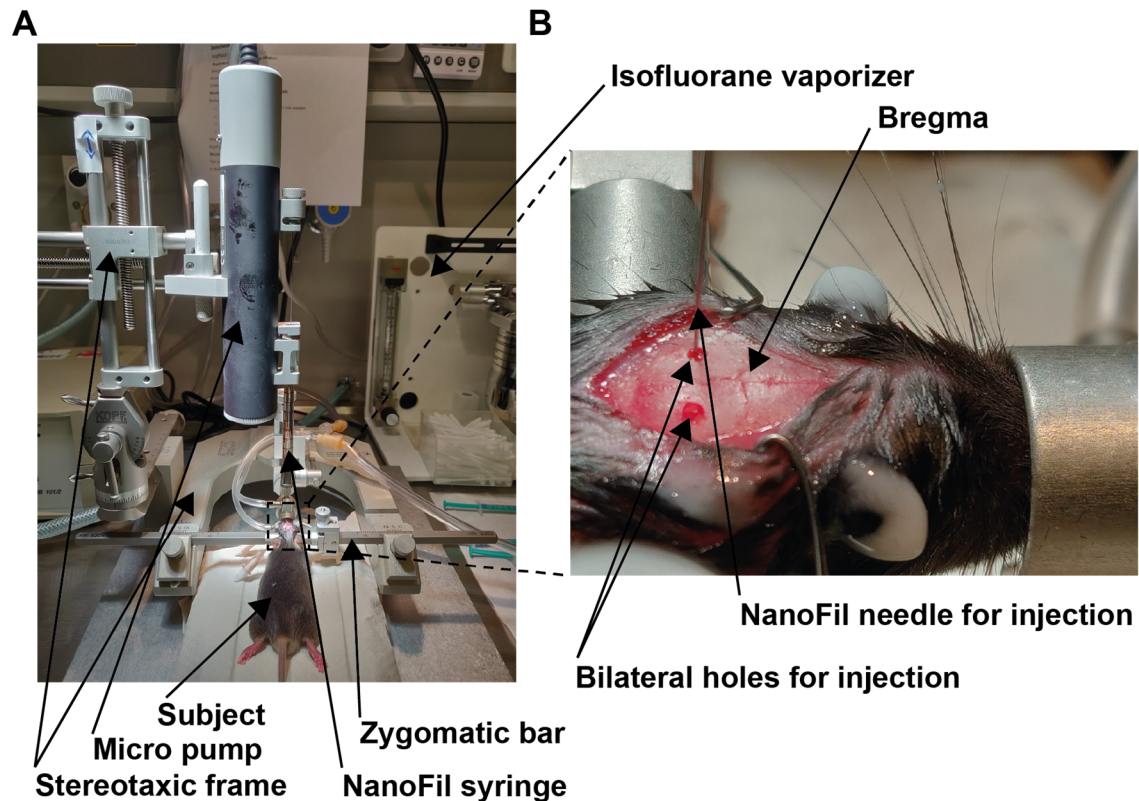


**Figure 2.1: Equipment for stereotaxic rAAV delivery into the mouse hippocampus**

(A) Picture showing the isofluorane vaporizer, the stereotaxic frame with micro pump, NanoFil syringe, zygomatic bars and a mounted subject. (B) Picture showing the mounted head of a subject. The skin was removed and two bilateral holes were drilled, according to positions determined via the bregma, into the cranium to facilitate access for the Nanofil injection needle.

**Table 1: Software used in this study**

Software	Task	Developer
Adobe Illustrator	image/data processing	Adobe
Andor Solis X-2747	data acquisition	Oxford Instruments
ANZ-maze	data acquisition/ data analysis	Stoelting
EndNote	reference management	Clarivate Analytics
Excel	data analysis	Microsoft
Fitmaster	data analysis	HEKA
GENTle	data analysis	Magnus Manske, University of Cologne, DE
IGOR Pro	image processing	Wavemetrics
ImageJ	image processing	Wayne Rasband, NIH, USA
ImageLab	data acquisition	Bio-Rad Laboratories
LAS-AF	data acquisition	Leica Microsystems
MiniAnalysis	data analysis	Synaptosoft
NanoDrop 2000	data acquisition	Thermo Fisher Scientific
Origin	data analysis	OriginLab
Patchmaster	data acquisition	HEKA
pClamp 10	data acquisition/ data analysis	Molecular Devices

Prism 5.0	data analysis	GraphPad Software
Windows XP, NT, and 7	operating system	Microsoft
Word	text processing	Microsoft

**Table 2: Sequences and binding positions of examined shRNAs**

Sequences of individual shRNAs and their target positions relative to the ATG start codon are summarized in Table 2. Target sequences for shRNAs are based on the murine mRNA sequences NM\_010408.3 for HCN1, NM\_008226.2 for HCN2, and NM\_001081192.1 for HCN4.

Target gene	Name	Sequence	Position (bp)
	shScr	F: CAACAAGATGAAGAGCACCAA R: TTGGTGCTCTTCATCTTGTTG	
HCN1	sh1.1	F: GTGGCCTACATGCAAATGTAA R: TTACATTTGCATGTAGGCCAC	2862 – 2882
HCN1	sh1.2	F: GCTGGGTTTCTCTGAATGAAA R: TTTCATTCAGAGAAACCCAGC	957 – 977
HCN1	sh1.3	F: CCTCCAATCAACTATCCTCAA R: TTGAGGATAGTTGATTGGAGG	1876 – 1896
HCN1	sh1.4	F: GCGCCAGAAGATACATGATTA R: TAATCATGTATCTTCTGGCGC	1252 – 1272
HCN1	sh1.5	F: GCACTTCGTATCGTGAGGTTT R: AAACCTCACGATACGAAGTGC	728 – 748
HCN2	sh2.1	F: CCATGCTGACAAAGCTCAAAT R: TTTGAGCTTTGTCAGCATGG	1583 – 1603
HCN2	sh2.2	F: CTGTTGTTTCATGGTGGGAAAT R: ATTTCCACCATGAACAACAG	574 - 594
HCN2	sh2.3	F: GCATTGTTATTGAGGACAACA R: TGTTGTCCTCAATAACAATGC	713 – 733
HCN2	sh2.4	F: CCGCATTGTTATTGAGGACA R: TGTCTCAATAACAATGCCGG	716 – 736
HCN4	sh4.1	F: GAGAGGAGATCATCAACTTTA R: TAAAGTTGATGATCTCCTCTC	1733 – 1753
HCN4	sh4.2	F: CTCCAAACTGCCGTCTAATTT R: AAATTAGACGGCAGTTTGGAG	3582 – 3602
HCN4	sh4.3	F: AGCGCATCCATGACTACTATG R: CATAGTAGTCATGGATGCGCT	1646 – 1666
HCN4	sh4.4	F: AGCGTCAGAGCGGATACTTAT R: ATAAGTATCCGCTCTGACGCT	2014 – 2034
HCN4	sh4.5	F: GAAGACATCCTCAGGTTCTTT R: AAAGAACCTGAGGATGTCTTC	3453 – 3473

**Table 3: Sequences and binding positions of examined sgRNAs**

Sequences of individual sgRNAs and their target positions relative to the transcriptional start site (TSS). Target sequences of sgRNAs were chosen according to the predicted TSS listed in the Eukaryotic Promoter Database (EPD) (Dreos et al., 2015), or the promoter nucleotide sequence provided by GeneCopoeia for the hDOP1 receptor promoter.

Target gene	Name	Sequence	Position (bp)
	sgScr	F: CAACAAGATGAAGAGCACCAA R: TTGGTGCTCTTCATCTTGTTG	
HCN1	sg1.1	F: CGTCCAACAGCCGCGACGATGC R: GCATCGTCGCGGCTGTTGGACG	232 – 252
HCN1	sg1.2	F: CTCCGCGTCCAACAGCCGCGAC R: GTCGCGGCTGTTGGACGCGGAG	227 – 248
HCN1	sg1.3	F: GCTCCTGGCTTCGAGCCCCGGCGAGT	139 – 166

		R: ACTCGCCGGGGGCTCGAAGCCAAGGAGC	
HCN2	sg2.1	F: TCGCACCCGGAGTCGGCGGAC R: GTCCGCCGACTCCGGGTGCGA	162 – 182
HCN2	sg2.2	F: GACTGCCCCGGCGCCGCTCGCCATGGAT R: ATCCATGGCGAGGCGCGCCGGGCAGTC	0 – 27
HCN2	sg2.3	F: GCGGCCAAGGGCGGCGCGAATG R: CATTGCGCCGCCCTTGCCCGC	238 - 259
HCN2	sg2.4	F: AGTCGGCGGACGAGCCCGGCC R: GGCCGGGCTCGTCCCGGACT	173 - 193
HCN4	sg4.1	F: GTAGAGGAGGCAAAGCGAGAAC R: GTTCTCGCTTTGCCTCCTCTAC	139 – 1159
HCN4	sg4.2	F: GAGCTGCGGCGGCTTCATGAAT R: ATTCATGAAGCCGCCGAGCTC	-17 – 4
HCN4	sg4.3	F: CGGCTGGGCTCAGCTAGAGGC R: GCCTCTAGCTGAGCCCAGCCG	125 – 144
hDop1	sgDop1.1	F: GACCAGCAAGCGCACAGGCCGGCGGGGT R: CCCC GCCGGCCTGTGCGCTTGCTGGTC	-45 – -18
hDop1	sgDop1.2	F: GCTGCCCAGGTGACCAGTCCTGGGAGT R: CTCCAGGACTGGTCACCTGGGCAGC	133 – 159
hDop1	sgDop1.3	F: CTGATGTGCTTTCTCTTAGGAAGAT R: TCTTCCTAAGAGAAAGCACATCAGG	-24 – 1
hDop1	sgDop1.4	F: GTCTGCCATGGACGGGACTGGGCTGGT R: CCAGCCCAGTCCCGTCCATGGCAGAC	18 – 44
hDop1	sgDop1.5	F: AGCGCCCAGGAGCCCTTAGCCGGGGT R: CCCC GGCTAAGGGCTCCTGGGCGCT	182 – 208

**Table 4: Sequences and binding positions of functional sgRNAs and shRNAs**

Sequences of individual sgRNAs and their target positions relative to the transcriptional start site (TSS) and sequences of individual shRNAs and their target positions relative to the ATG start codon. Target sequences of sgRNAs were chosen according to the predicted TSS listed in the Eukaryotic Promoter Database (EPD). Target sequences for shRNAs are based on murine mRNA sequences NM\_010408.3 (HCN1), NM\_008226.2 (HCN2), and NM\_001081192.1 (HCN4).

Target gene	Name	Sequence	Position (bp)
HCN1	sg1	F: CTCCGCGTCCAACAGCCGCGAC R: GTCGCGGCTGTTGGACGCGGAG	227 – 248
HCN2	sg2	F: TCGCACCCGGAGTCGGCGGAC R: GTCCGCCGACTCCGGGTGCGA	162 – 182
HCN4	sg4	F: GTAGAGGAGGCAAAGCGAGAAC R: GTTCTCGCTTTGCCTCCTCTAC	135 – 159
	sgScr	F: CAACAAGATGAAGAGCACCAA R: TTGGTGCTCTTCATCTTGTTG	
HCN1	sh1	F: CCTCCAATCAACTATCCTCAA R: TTGAGGATAGTTGATTGGAGG	1876 – 1896
HCN2	sh2	F: CCATGCTGACAAAGCTCAAAT R: TTGAGCTTTGTCAGCATGG	1583 – 1603
HCN4	sh4	F: CTCCAAACTGCCGTCTAATTT R: AAATTAGACGGCAGTTTGAG	3582 – 3602
	shScr	F: CAACAAGATGAAGAGCACCAA R: TTGGTGCTCTTCATCTTGTTG	

**Table 5: Plasmids to generate rAAVs used in this study**

Plasmid	Application
pCKII-dSaCas9KRAB-eGFP	Visualization of dSaCas9 expression
pCKII-dSaCas9KRAB-hU6- sgScr/1.1/1.2/1.3/2.1/2.2/2.3/2.4/4.1/4.2/4.3/4.4	CRISPRi mediated knockdown
pENN-hU6-shScr/1/2/4-CKII-eGFP	RNAi mediated knockdown
pENN-hU6-shScr/2-CKII-GCaMP6f-WPRE	RNAi mediated knockdown/calcium imaging
pRC2	Generation of rAAV serotype2
pRC9	Generation of rAAV serotype9
pXX6-80	Helper plasmid for generation of rAAVs

**Table 6: Iodixanol gradient-solutions for rAAV purification:** (for 50 ml solution)

10 x PBS/K is composed of KCl (50 mM), KH<sub>2</sub>PO<sub>4</sub> (14 mM), NaCl (1379.3 mM), Na<sub>2</sub>HPO<sub>4</sub> (80.6 mM); pH 7.4

	15 %	25%	40%	60%
10 x PBS / K (50 mM)	5 ml	5 ml	5 ml	
MgCl <sub>2</sub> (50 mM)	1 ml	1 ml	1 ml	1 ml
NaCl (5 M)	10 ml			
Optiprep (60 % iodixanol)	12.5 ml	20.83 ml	33.33 ml	49 ml
H <sub>2</sub> O	22.5 ml	24.17 ml	11.67 ml	
Phenolred	375 µL	500 µL		125 µL

**Table 7: Primary antibodies used for immunocytochemistry**

List of primary antibodies applied for immunocytochemistry. Abbreviations: gp, guinea pig; rb, rabbit; rt, rat; ms, mouse; ch, chicken.

Antigen	Source	Dilution	Supplier
GFP	ch	1:1000	Chemicon (ab16901)
HA	rt	1:100	Roche/Merck
HCN1	gp	1:500	in house
HCN2	rb	1:500	in house
HCN4	rb	1:500	in house
IB4		1:1000	ThermoFisher (I21414)
LAMP-1	ms	1:1000	Santa Cruz (sc-20011)
MAP2	rb	1:1000	Synaptic Systems (188 002)
mCherry	ms	1:500	Clontech (632543)
TOPRO-3		1:1000	Invitrogen (T3605)

**Table 8: Secondary antibodies used for immunocytochemistry**

List of secondary antibodies applied for immunocytochemistry. Abbreviations: gp, guinea pig; rb, rabbit; ms, mouse; rt, rat; ch, chicken; dk, donkey.

Antibody	Source	Dilution	Supplier
α ch Cy2	dk	1:200	Dianova (703-225-155)
α gp Cy3	dk	1:500	Dianova (706-165-148)
α ms Cy3	dk	1:200	Dianova (715-165-150)
α rb Cy3	dk	1:500	Dianova (711-165-152)
α rb Dy488	dk	1:500	Dianova (711-485-152)

$\alpha$ rt Cy5	dk	1:500	Dianova (712-175-153)
$\alpha$ rt Dy488	gt	1:500	Invitrogen (A11006)
$\alpha$ ms Cy5	dk	1:400	Dianova (715-175-151)
Streptavidin-Cy3		1:1000	Dianova (016-160-084)

**Table 9: Primary antibodies used for immunohistochemistry of tissue sections**

List of primary antibodies applied for immunocytochemistry. Abbreviations: rb, rabbit; rt, rat; ms, mouse; ch, chicken.

Antigen	Source	Dilution	Supplier
Caspase-3	rb	1:50	Abcam (ab2302)
GFAP	ms	1:500	Sigma (G3893)
GFP	ch	1:1000	Chemicon (ab16901)
HCN1 7C3	rt	1:5	in house
HCN2 3G7	rt	1:10	in house
HCN4 PG2-1A4	rt	1:2	in house
NeuN	rb	1:500	Abcam (ab104225)
TOPRO-3		1:1000	Invitrogen (T3605)

**Table 10: Secondary antibodies used for immunohistochemistry of tissue sections**

List of secondary antibodies applied for immunocytochemistry. Abbreviations: rb, rabbit; ms, mouse; rt, rat; ch, chicken; dk, donkey.

Antibody	Source	Dilution	Supplier
$\alpha$ ch Cy2	dk	1:200	Dianova (703-225-155)
$\alpha$ ms Cy3	dk	1:400	Dianova (715-165-150)
$\alpha$ rb Cy3	dk	1:400	Dianova (711-165-152)
$\alpha$ rt Cy3	dk	1:400	Dianova (712-165-153)

**Table 11: Sequences of qPCR primer pairs**

Primer sequences, accession numbers, melting temperatures, and amplicon sizes for target and reference genes used in qPCR experiments.

Target gene	Sequence	$T_m$ ( $^{\circ}$ C)	Fragment length (bp)
BDNF NM_001048139.1	F: TGCAGGGGCATAGACAAAAGG R: CTTATGAATCGCCAGCCAATTCTC	62	110
<i>c-fos</i> NM_010234	F: CTGTCAACACACAGGACTTTT R: AGGAGATAGCTGCTCTACTTTG	62	274
GFP JQ064510.1	F: GACGTAAACGGCCACAAGTTC R: GAAGTCGTGCTGCTTCATGTG	60	189
hDop1 NM_000794.3	F: GACCTTGTCTGTACTCATCTCCT R: GTCACAGTTGTCTATGGTCTCAG	60	118
hGAPDH NM_002046.5	F: GGTATCGTGGAAGGACTCATG R: GCCACAGCCTTGGCAGC	63	150
mCherry KJ567138	F: GAACGGCCACGAGTTCGAGA R: CTTGGAGCCGTACATGAACTGAGG	63	145
mGAPDH NM_008084.2	F: GGCATTGTGGAAGGGCTCATG R: GCCACAGCCTTGGCAGC	62	150
mHCN1	F: CTCAGTCTCTTGCGGTTATTACG	62	91

NM_010408.3	R: TGGCGAGGTCATAGGTCATG		
mHCN2 NM_008226.2	F: ATCGCATAGGCAAGAAGAAGACTC R: CAATCTCCTGGATGATGGCATT	60	102
mHCN4 NM_001081192.1	F: GCATGATGCTTCTGCTGTGT R: GCTTCCCCCAGGAGTTATTC	60	123
mTOR NM_020009.2	F: CTCCGATTGTGAAATTGTTTGA R: TGCTGGTAAATCAAAGGGTCTT	60	355
SaCas9 HE980450.1	F: CAGATTCAAGACCAGCGACTAC R: GTCGATGTAGGTGTCGATGAAG	62	103
TrkB NM_001025074.2	F: TGACGCAGTCGCAGATGCTG R: TTTCTGTACATGATGCTCTCTGG	62	274

**Table 12: qPCR program sequence**

Program	Process	Temperature (°C)	Duration	Iteration	Detection
Pre-incubation	Denaturation	95	10 min	1	-
Amplification	Denaturation	95	20 s	40-50	-
	Annealing	$T_m$ of primer	20 s		-
	Elongation	72	20 s		single
Melting	Denaturation	95	1 s	1	-
	Annealing	60	15 s		-
	Melting	65 to 95	0.1 °C/s		continuously
Cooling	Cooling	40	30 s	1	-

**Table 13: Primary antibodies used for western blot analyses.**

List of various primary antibodies applied for specific detection of proteins on western blots: [rb] rabbit; [ms] mouse;

Antigen	Name	Source	Dilution	Supplier
$\beta$ -tubulin	tubulin	ms	1:5000	Sigma-Aldrich (T4026)
green fluorescent protein	GFP	rb	1:5000	Abcam (ab290)
HCN2	HCN2 3G7	rb	1:50	In-house

**Table 14: Secondary antibodies used for western blot analyses.**

List of various secondary antibodies applied for specific detection of proteins on western blots: [HRP] horse radish peroxidase; [rb] rabbit; [ms] mouse; [gt] goat; [dk] donkey;

Antibody	Characteristics	Source	Dilution	Supplier
$\alpha$ -rb	HRP-coupled	gt	1:10,000	Sigma-Aldrich (A6154)
$\alpha$ -ms	HRP-coupled	dk	1:1000	Santa Cruz (sc-2318)

---

# Chapter 3

## Results

---

### *3.1 Knock-down of HCN channel expression in vitro*

To examine the functional role of proteins, transgenic strategies, e.g., knock-in or knock-out approaches emerged as frequently used and extremely powerful tools. Typically, these strategies aim to achieve a complete loss-of-function phenotype by modification of the genomic DNA.

#### *3.1.1 Generation of AAV-based gene-interfering tools*

A recently developed method to manipulate gene expression is the “Clustered Regularly Interspaced Short Palindromic Repeats” (CRISPR) technique. CRISPR typically introduces targeted mutations into the genomic DNA that further cause a loss of function phenotype by generating deletions or insertions into a gene’s coding sequence. The core component of this technique is an enzymatically active Cas9 protein, which has the inherent ability to cut the genomic DNA. The DNA double strand break triggers cellular repair mechanisms, which eventually cause gain or loss of nucleotides that ultimately disturb a genes’ open reading frame (Jinek et al., 2012, Wiedenheft et al., 2012, Cong et al., 2013, Wang et al., 2013, Doudna and Charpentier, 2014).

To broaden the versatility of the CRISPR toolbox, CRISPR interference (CRISPRi) has been developed recently. With CRISPRi, the genomic DNA is no longer affected, instead, RNA synthesis is blocked by occupation of the target gene’s promoter. Thereby protein *de novo* biosynthesis is impaired (Gilbert et al., 2013, Larson et al., 2013, Dominguez et al., 2016). The main component of CRISPRi is a nuclease-deficient version of *Staphylococcus aureus* Cas9 (dSaCas9). Additionally, to increase the efficiency of

CRISPRi, the dSaCas9 protein is fused to the Krüppel-associated box (KRAB) repression domain, resulting in a transcriptional interference protein complex (dSaCas9-KRAB; see Figure 3.1 B) (Gilbert et al., 2013, Gilbert et al., 2014), which is guided to the promoter region of a gene of interest.

To make use of this technique in different model systems and to examine the experimental potential of the method, a modular all-in-one vector was designed providing the core components necessary to induce CRISPRi-mediated knock-down (Fig. 3.1 BI).

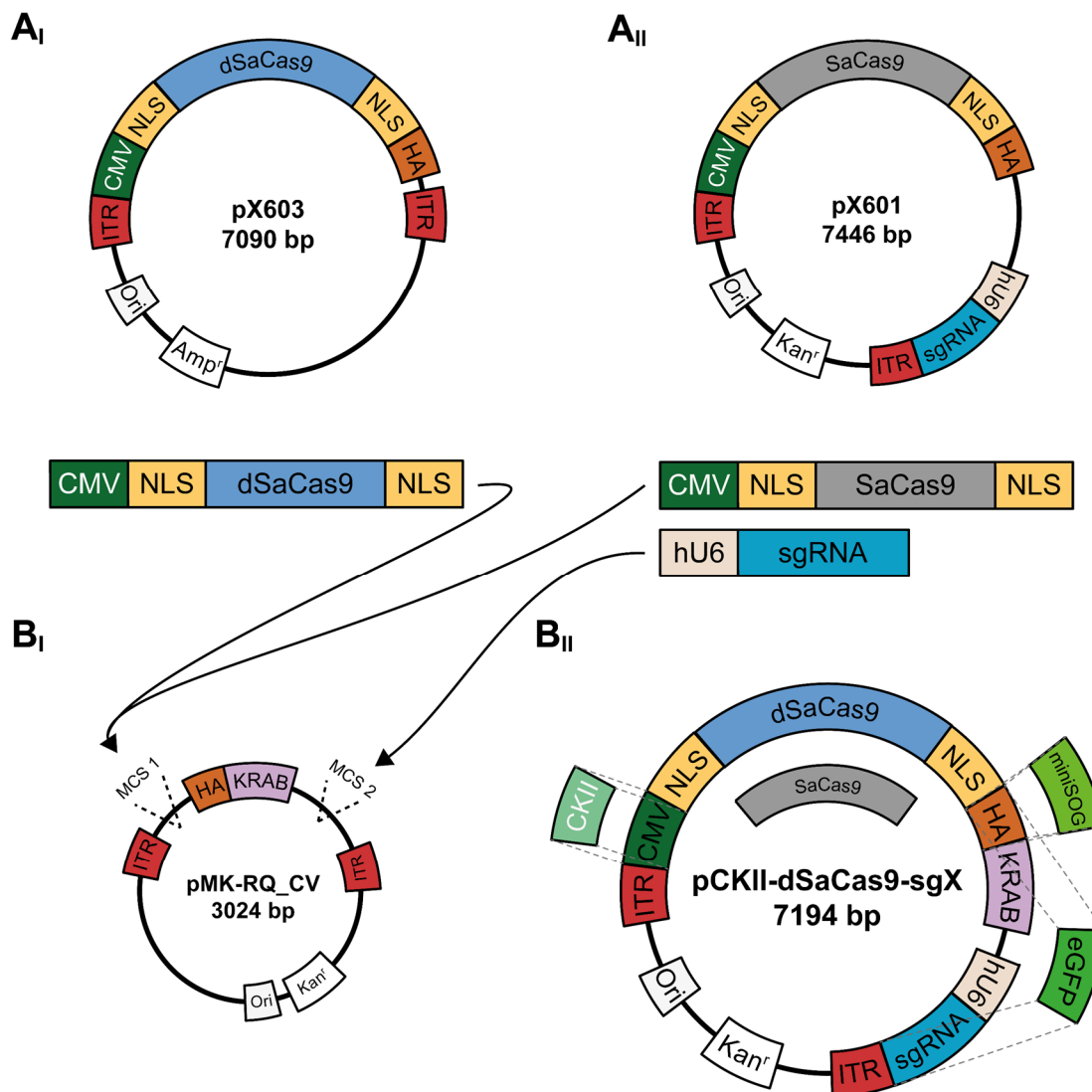


**Figure 3.1: Cloning strategy for constructs mediating gene knock-down by CRISPRi**

Schematic representation of plasmids used for generating the vector-backbone to mediate CRISPRi. (AI) Schematic representation of Addgene plasmid #61594 (pX603) containing elements encoding nuclease deficient *Staphylococcus aureus* Cas9 (dSaCas9) flanked by nuclear localization signals (NLS). The dSaCas9 is expressed under the control of a cytomegalovirus promoter (CMV). (AII) Schematic representation of Addgene plasmid #61591 (pX601) containing the gene encoding nuclease active *Staphylococcus aureus* Cas9 (SaCas9) flanked by NLS. The construct is expressed under the control of a CMV promoter. In addition, the plasmid encodes a short guidance RNA (sgRNA) expression cassette

controlled by the human U6 (hU6) promoter. (BI) Schematic representation of the vector backbone used to incorporate the CMV-NLS-dSaCas9-NLS or CMV-NLS-SaCas9-NLS cassette in multiple cloning site #1 (MCS 1) and the hU6-sgRNA cassette in MCS #2. For visualization of expression, an HA-tag (human influenza hemagglutinin A) is fused in frame and 5' to the Krüppel associated box motif (KRAB). For production of recombinant Adeno-associated viruses (rAAVs), inverted terminal repeats (ITRs) were incorporated into the vector backbone. (BII) Schematic representation of the dSaCas9 and sgRNA expression plasmid. The modulatory design of the vector also allows to exchange the CMV promoter for, e.g., a CaM kinase II promoter (CKII) and the dSaCas9 for SaCas9. For localization experiments, variants with dSaCas9 fused to eGFP or miniSOG were generated.

Initially, the dSaCas9 gene, flanked by nuclear localization sites (NLS) and the CMV promoter, were isolated by restriction digest (BamHI/AgeI) from the pX603 plasmid (Figure 3.1 AI) (Ran et al., 2015) and cloned into the multiple cloning site #1 (MCS 1) of the custom designed pMK-RQ\_CV vector backbone. Thereby, the dSaCas9 gene was directly fused to a human influenza hemagglutinin (HA) tag necessary for localization experiments and to the KRAB transcriptional repression motif. To retain the possibility for performing classical CRISPR knock-out experiments, the NLS-flanked, enzymatically active form of SaCas9 and the corresponding CMV promoter were isolated by restriction digest (BamHI/AgeI) from the pX601 plasmid (Fig. 3.1 AII) (Ran et al., 2015) and alternatively cloned into the multiple cloning site #1 (MCS 1) of pMK-RQ\_CV. Expression of these fusion proteins can be driven either by the ubiquitously active CMV promoter or by tissue-specific promoters, like the neuron specific CKII promoter. Due to the NLS, the dSaCas9-KRAB protein complex translocates into the nucleus where, targeted by short guidance RNAs (sgRNAs), it binds to the transcriptional start site (TSS) of the target gene to interfere with the transcription machinery. To co-express sgRNAs from the same vector backbone, an sgRNA expression cassette comprising the human U6 (hU6) promoter and the insertion site for sgRNAs was isolated by restriction digest (EcoRI/NotI) from the pX601 plasmid (Fig. 3.1 AII) (Ran et al., 2015) and cloned into the MCS #2 (Fig. 3.1 BI) of pMK-RQ\_CV. To achieve more flexibility and to allow direct proof of SaCas9-/dSaCas9-expression without performing immunostaining, the HA-tag was exchanged by a miniSOG fluorescent reporter (Shu et al., 2011). If another fluorescent label is required the sgRNA expression scaffold, the HA-tag, and the KRAB motif were exchanged for an eGFP-encoding cassette that was directly fused to the Cas9-encoding element (Fig. 3.1 BII). For delivering the CRISPRi core components to a variety of cell-types, the vector allows production of recombinant Adeno-associated viruses (rAAVs) due to the flanking inverted terminal repeats (ITRs).

In addition to the CRISPRi strategy, the widely used cell-autonomous defense mechanism of RNA inhibition (RNAi) (Shan, 2010) was used to knock-down the expression of target genes. By formation of complementary RNA double strands, cellular defense processes are initiated, leading to a degradation of the targeted mRNA. Consequently, the protein level decreases due to impairment of *de novo* protein biosynthesis. The core component necessary for RNAi is a short hairpin RNA (shRNA) expressed, e.g., under the control of a constitutively active hU6 promoter. For identification of transduced cells, an eGFP-reporter was expressed either under the control of the ubiquitously active CMV promoter or the neuron-specific CKII promoter (Fig. 3.2 A). For delivering the RNAi components to a variety of cell-types, the vector is also suited to produce rAAVs due to the flanking inverted terminal repeats (ITRs).

### ***3.1.2 Functional expression of knock-down constructs in HEK293 cells***

To examine the functionality of the different knock-down constructs (Fig. 3.2 A and B), HEK293 cells were transfected and the expression of reporter genes was monitored (Fig 3.2 C). Figure 3.2 CI shows CMV-mediated expression of the eGFP reporter. From the same construct, shRNAs were co-expressed driven by the hU6 promoter. Notably, localization of eGFP was not restricted to specific cellular compartments. Figure 3.2 CII, CIII, and CIV show the expression of dSaCas9 either fused to an HA-tag (CII), to an eGFP (CIII) or to a miniSOG fluorescent reporter (CIV). The protein was preferentially located in the nucleus, as expected due to the NLS flanking the dSaCas9 cassette. However, the miniSOG fusion protein was preferentially localized in sub-compartments of the nucleus, thus resulting in spot-like fluorescence signals.

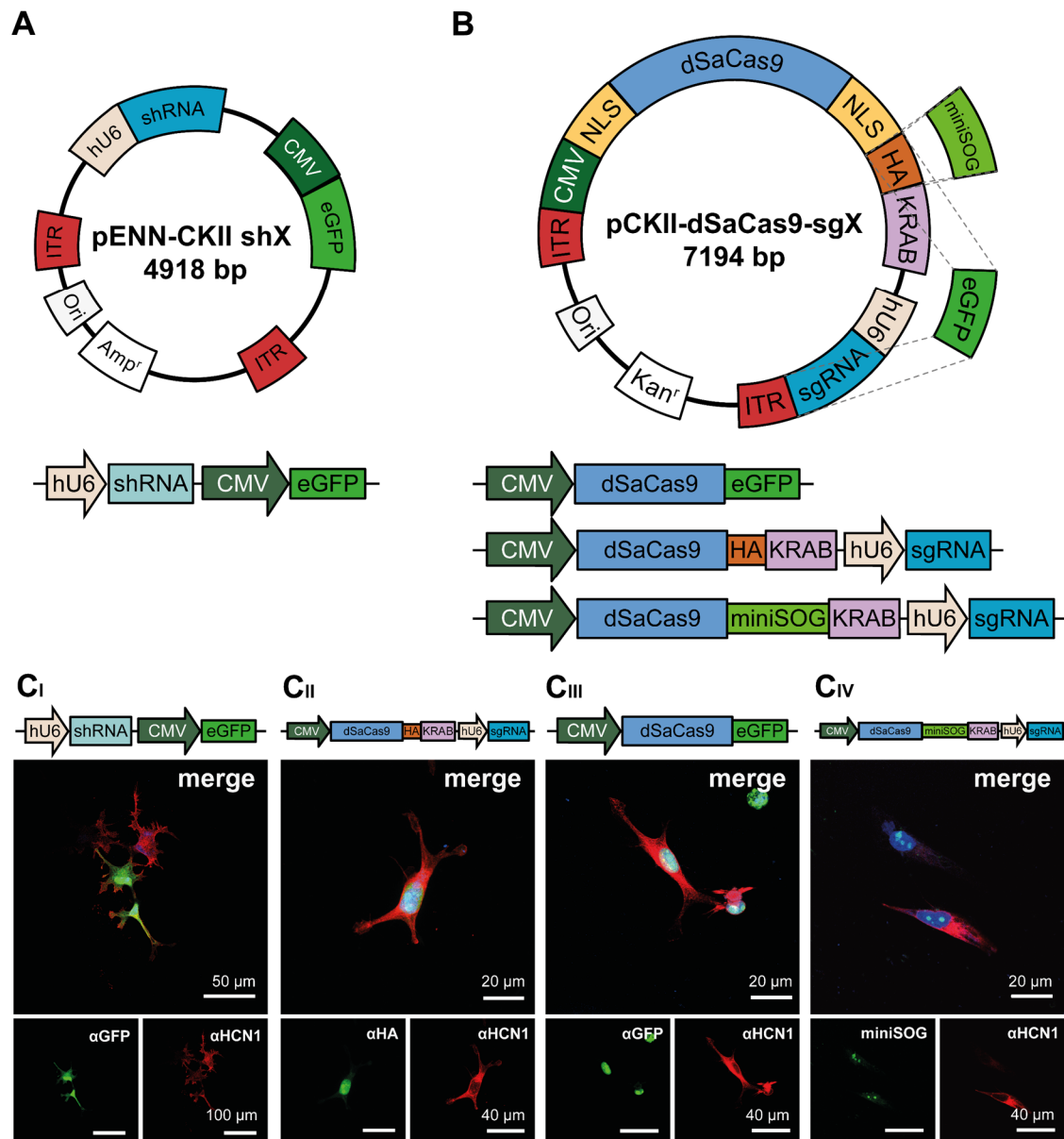


**Figure 3.2: Expression of RNAi- and CRISPRi-mediated constructs in HEK293 cells**

(A) Schematic representation of the RNAi-mediated plasmid for expression in HEK293 cells. Expression of the short-hairpin RNA (shRNA) is controlled by the hU6 promoter. Expression of eGFP is controlled by the CMV promoter. (B) Schematic representation of CRISPRi-mediated plasmid for expression in HEK293 cells. (C) Representative immunofluorescence images showing the expression of the (CI) eGFP reporter of the RNAi construct, (CII) HA-tagged dSaCas9 protein including the KRAB domain and the sgRNA expression scaffold, (CIII) eGFP-tagged dSaCas9 and, (CIV) miniSOG-tagged dSaCas9 protein including the KRAB domain and the sgRNA expression scaffold in HEK293 cells constitutively expressing HCN-channel subunit 1 (HCN1). Schematic representation of constructs is shown above the images. Staining was performed with specific anti ( $\alpha$ )-eGFP,  $\alpha$ -HA-tag, and  $\alpha$ -HCN1 antibodies combined with fluorescently labeled secondary antibodies (green and red). MiniSOG was detected by autofluorescence (green). Nuclei were labeled with TOPRO (blue).

### ***3.1.3 Validation of knock-down in HEK293 cells***

To validate the specificity of CRISPRi in HEK293 cells, a cell-line was generated which constitutively expressed a mCherry fluorescent reporter under the control of the human dopamine D1 receptor (hDop1) promoter (Fig. 3.3 A and B). Because HEK293 cells endogenously express hDop1 receptors (Huang and Li, 2009), expression of the mCherry-construct also occurred in these cells. To knock-down the expression of mCherry in this cell-line, sgRNAs were designed to guide dSaCas9 to a region ranging from -50 to +300 bps relative to the predicted transcriptional-start site (TSS) of the hDop1 receptor promoter. Individual sgRNAs were cloned into the CRISPRi-vector backbone by restriction digest (BsaI). The CRISPRi vector and an eGFP fluorescent reporter encoding vector were co-expressed in the HEK293 cell-line. Subsequently, confocal images of mCherry fluorescence and eGFP fluorescence were captured and Pearson R values were calculated for colocalization of mCherry and eGFP signals. The mCherry signal should decrease in those cells in which mCherry expression is downregulated by CRISPRi. In contrast, the eGFP fluorescence signal should remain rather constant. Consequently, the Pearson R value decreases as a measure for colocalization of both signals.

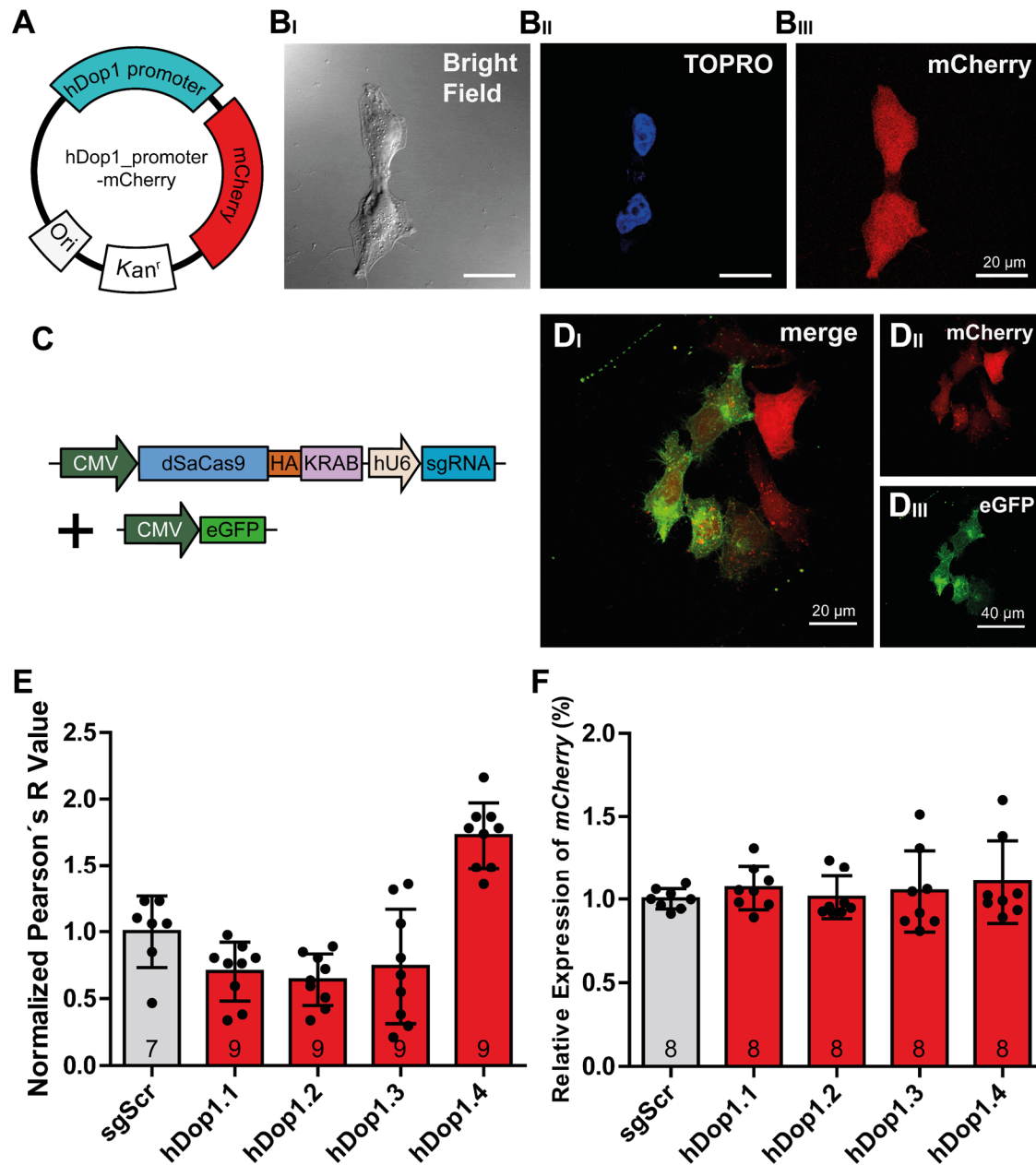


**Figure 3.3: CRISPRi-mediated knock-down of hDop1-promoter driven mCherry expression in HEK293 cells**

(A) Schematic representation of the construct for generating HEK293 cells constitutively expressing mCherry under control of the human dopamine D1 (hDop1) receptor promoter. (B) Representative bright-field and immunofluorescence images showing (B<sub>I</sub>) HEK293 cells in bright field, (B<sub>II</sub>) nuclei stained with TOPRO, and (B<sub>III</sub>) expression of mCherry. (C) Schematic representation of constructs used for mCherry knock-down, as well as colocalization analysis of mCherry and eGFP expression. (D) Representative immunofluorescent images showing (D<sub>I</sub>) the merged image of (D<sub>II</sub>) expression of mCherry under the control of hDop1 promoter and (D<sub>III</sub>) eGFP reporter expression in HEK293 cells. (E) Colocalization analysis by comparison of Pearson's R values for HEK293 cells expressing mCherry, co-transfected with the eGFP reporter and different CRISPRi constructs targeting dSaCas9 to the hDop1 promoter by sgRNAs (sgScr = control, sghDop1.1, 1.2, 1.3; and 1.4). Data were obtained from indicated numbers of fluorescent images from at least 3 independent transfections. Pearson's R values were normalized to sgScr values and depicted as mean  $\pm$  standard deviation. (F) qRT-PCR analysis of mCherry expression levels in HEK293 cells expressing mCherry under the control of hDop1 promoter and different CRISPRi constructs targeting dSaCas9 to the hDop1 promoter by sgRNAs (sgScr, sghDop1.1, 1.2, 1.3; and 1.4). cDNA was prepared

from indicated numbers of coverslips from 3 independent transfections. Results are depicted as mean  $\pm$  standard deviation.

Normalized colocalization analyses are shown in Figure 3.3 E. The knock-down efficacies of the sgRNAs were compared to a scrambled sgRNA (sgScr), which was designed not to bind to the hDop1 promoter or any other endogenous promoter. Some of the CRISPRi-sgRNA constructs showed a moderate reduction in the Pearson R value (sgScr:  $1.0 \pm 0.268$ ; sghDop1.1:  $0.72 \pm 0.22$ ; sghDop1.2:  $0.641 \pm 0.193$ ; sghDop1.3  $0.74 \pm 0.43$ ). Notably, sghDop1.4 even showed an increase of the Pearson R value ( $1.725 \pm 0.25$ ). To corroborate these changes in mCherry expression levels, quantitative reversed transcription PCR (qRT-PCR) experiments were performed. The qRT-PCR experiments revealed no changes in mCherry transcript levels, independent of the sgRNA construct tested (sgScr:  $1.0 \pm 0.061$ ; sghDop1.1:  $1.07 \pm 0.133$ ; sghDop1.2:  $1.01 \pm 0.128$ ; sghDop1.3  $1.05 \pm 0.246$ ; sghDop1.4:  $1.01 \pm 0.039$ ). Possible explanations for the insufficient knock-down of mCherry might arise from the experimental design. On the one hand, expression of mCherry under control of the hDop1 receptor promoter competed with the endogenous hDop1 receptor expression in HEK293 cells. Thus, dSaCas9 proteins most likely were targeted to both, the introduced promoter from the mCherry construct and the endogenous hDop1 receptor promoter, which may have led to a low knock-down efficiency when targeting the reporter construct. On the other hand, expression of eGFP, which was used for the colocalization analysis, originated from co-transfected eGFP-encoding construct and not from the dSaCas9-encoding construct. Thus, the colocalization experiment might suffer from an overestimation of eGFP signals.

In an independent series of experiments, the specificity and efficacy of RNAi-mediated knock-down for hyperpolarization-activated and cyclic nucleotide-gated (HCN) channels was tested. Therefore, shRNA-encoding constructs targeting individual HCN channel isoforms were transfected in HEK293 cells constitutively expressing homomeric HCN channels 1, 2 or 4. The RNAi-inducing constructs and the corresponding shRNAs were previously designed and tested in our group (Günther, 2016). Two days after transfecting HEK293 cells with RNAi-inducing constructs, cells were fixed and stained with specific antibodies (Fig. 3.4 A). Capturing confocal images of immunolabeled HCN channels and eGFP fluorescence was used to calculate Pearson R values for colocalization of fluorescence signals. Similar to the experiment described above, HCN immunofluorescence signals should decrease in those cells, in which HCN channel

expression was downregulated, whereas the eGFP fluorescence signal should remain almost constant. Consequently, the Pearson R value decreases as a measure for colocalization of both signals.

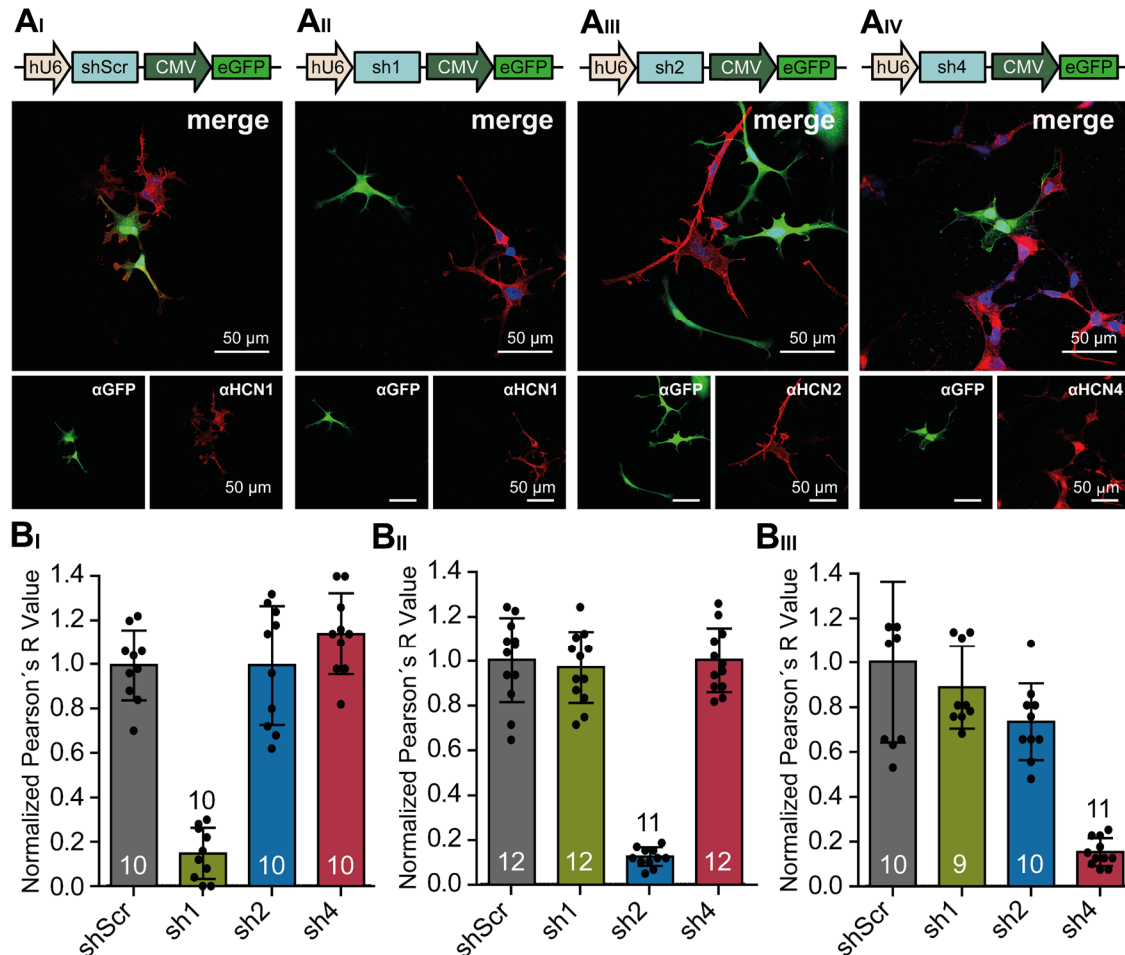


**Figure 3.4: RNAi-mediated HCN-channel knock-down in HEK293 cells**

(AI) Representative immunofluorescence images showing the expression of (AI) the eGFP reporter of shScr-expressing, (AII) sh1-expressing, (AIII) sh2-expressing, or (AIV) sh4-expressing variants in HEK293 cells constitutively expressing HCN channel isoforms 1, 2 or 4, respectively. Schematic representation of constructs is shown above the images. Stainings were performed with specific anti ( $\alpha$ -eGFP,  $\alpha$ -HA-tag, and  $\alpha$ -HCN antibodies combined with fluorescently labeled secondary antibodies (green and red). Nuclei were labeled with TOPRO (blue). (B) Colocalization analysis by comparison of Pearson's R values for HEK293 cells (BI) constitutively expressing HCN1 channels and transfected with different shRNA-encoding constructs (shScr = control, sh1, sh2 and sh4), (BII) constitutively expressing HCN2 channels and the same series of constructs, and (BIII) constitutively expressing HCN4 channels and the same series of constructs. Data were obtained from indicated numbers of fluorescence images from at least five independent transfections. Pearson's R values were normalized to shScr controls and results are depicted as mean  $\pm$  standard deviation.

Normalized colocalization analyses are shown in Figure 3.4 B. Only shRNA1 (sh1), which binds to *hcn1* mRNA, downregulated HCN1 channel protein expression (Fig. 3.4 BI). In contrast, a control shRNA (shScr), which was designed not to bind to endogenous

mRNA, and shRNAs binding to *hcn2* (sh2) or *hcn4* (sh4) mRNAs did not interfere with HCN1 channel expression (shScr:  $1.0 \pm 0.159$ ; sh1:  $0.149 \pm 0.115$ ). Similarly, only shRNA2 (sh2) which binds to *hcn2* mRNA (shScr:  $1.0 \pm 0.189$ ; sh2:  $0.122 \pm 0.042$ ) (Fig. 3.4 BII) and shRNA4 (sh4), which binds to *hcn4* mRNA (shScr:  $1.0 \pm 0.361$ ; sh4:  $0.152 \pm 0.062$ ) (Fig. 3.4 BIII), induced specific downregulation of either HCN2 or HCN4 channel proteins, respectively.

#### ***3.1.4 Functional expression of knock-down constructs in PHNs***

To assess the functional role of individual HCN channel subunits in their physiological environment, RNAi- and CRISPRi-inducing constructs were expressed in primary hippocampal neurons (PHNs). Recombinant Adeno-associated viruses (rAAVs) were generated and served as gene ferries to deliver the constructs (Fig. 3.5 A and B) to these neurons (Fig. 3.5 C and D).

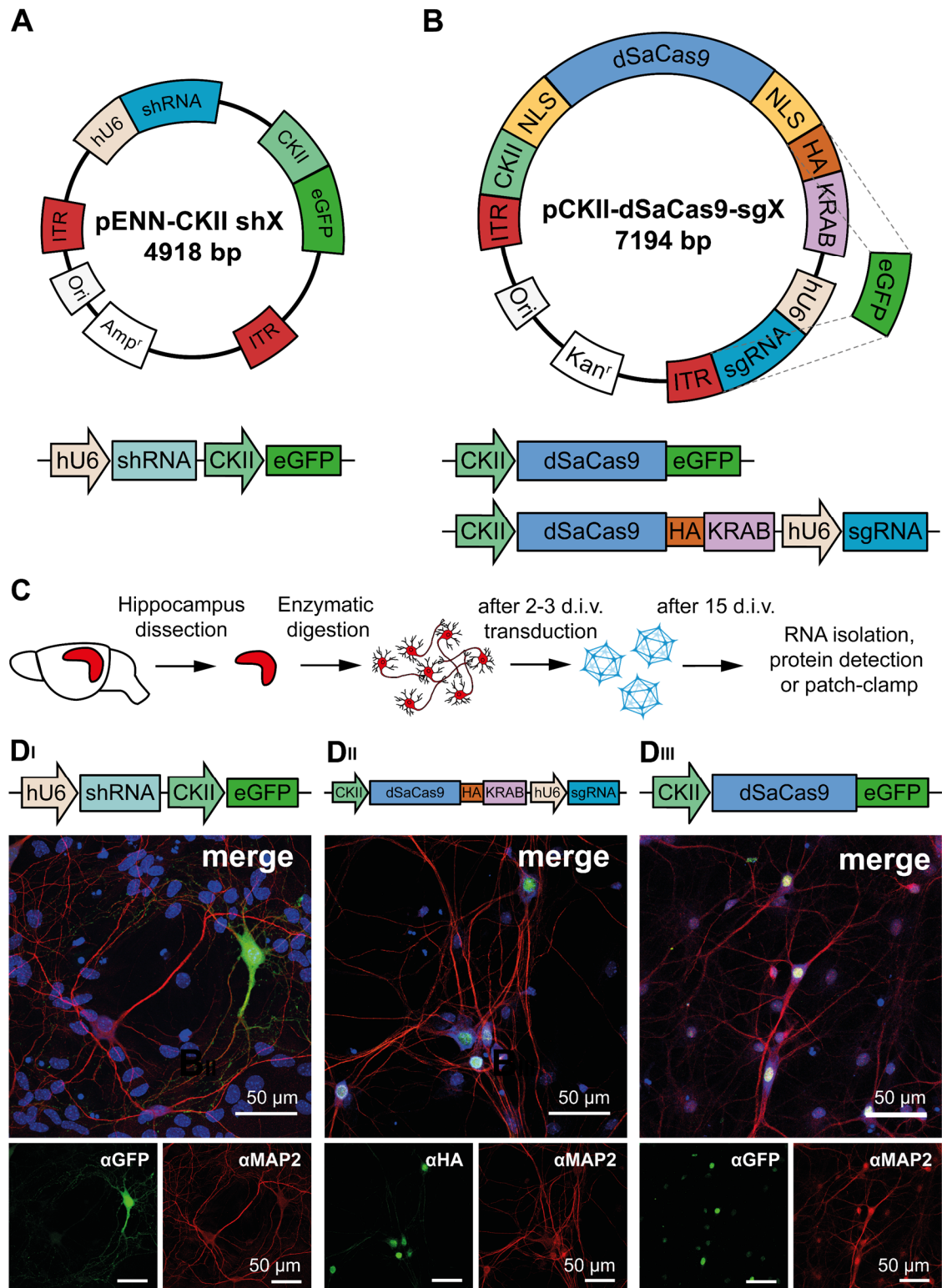


**Figure 3.5: Expression of RNAi- and CRISPRi-mediated constructs in primary hippocampal neurons**

(A) Schematic representation of the RNAi-mediated plasmid for expression in neurons. Expression of the short-hairpin RNA (shRNA) is controlled by the hU6 promoter. Expression of eGFP is controlled by a CKII promoter. (B) Schematic representation of CRISPRi-mediated plasmid for expression in neurons. Expression of dSaCas9-HA or dSaCas9-eGFP is controlled by a CKII promoter. (C) Schematic representation of the preparation and transduction procedure of primary hippocampal neurons (PHNs). For details see Material and Methods section 2.6. (D) Representative immunofluorescent images of

rAAV9-transduced PHNs expressing the (DI) eGFP reporter of the RNAi-inducing construct, (DII) HA-tagged dSaCas9, and (DIII) eGFP-tagged dSaCas9 of CRISPRi-inducing constructs. The eGFP, HA-tag, and the neuron-specific microtubule-associated protein 2 (MAP2) were immunostained with specific anti ( $\alpha$ -GFP,  $\alpha$ -HA, and  $\alpha$ -MAP2) antibodies combined with fluorescently labeled secondary antibodies (eGFP and HA-tag, green; MAP2, red). Nuclei were labeled with TOPRO (blue). Cartoons of the AAV-delivered constructs are displayed above the merged immunofluorescent images.

PHNs were prepared from C57BL/6J mice (see Chapter 2.6) and subsequently incubated with rAAVs encoding shRNA and eGFP (Fig. 3.5 DI), dSaCas9-HA (Fig. 3.5 DII), or dSaCas9-eGFP (Fig. 3.5 DIII). Twelve days after transduction, neurons were fixed and expression of reporter proteins was studied by immunocytochemistry. Figure 3.5 DI shows a single PHN in which expression of the eGFP fluorescent reporter was mediated by the neuron specific CKII promoter. Distribution of eGFP was not restricted to specific cellular compartments. The fluorescent signal was visible in the soma of the neuron as well as in the cellular extensions. Figure 3.5 DII and DIII shows detection of the HA-tag (DII) and of the eGFP reporter (DIII) directly fused to the dSaCas9 protein. Both fusion proteins were preferentially located in the nuclei of the neurons, due to the NLS flanking the dSaCas9 cassette (Fig. 3.5 DII and DIII).

### ***3.1.5 Validation of knock-down in PHNs***

Cultured PHNs express at least three HCN channel isoforms which can be detected by immunohistochemistry. Notably, even individual neurons express all three of these isoforms (Fig. 3.6 A). A central goal of this thesis was to downregulate channel isoforms specifically and independently by RNAi or CRISPRi, in order to identify the best suited strategy for HCN-channel knock-down in postmitotic cells. For RNAi-mediated knock-down, shRNA sequences were chosen, which demonstrated high specificity and efficacy in previous, cell-culture based experiments (Kaschuba, 2010, Günther, 2016). Recombinant AAVs were generated and the knock-down efficacies of individual shRNAs were compared to a scrambled shRNA (shScr) control construct. For CRISPRi-mediated knock-down, sgRNAs were designed binding in regions between -50 and +300 bps relative to the predicted TSS of the different HCN channel genes. The knock-down efficacies of these sgRNAs were again compared to a scrambled control sgRNA (sgScr), which was designed not to bind to any endogenous promoters. For delivering the constructs, recombinant rAAVs representing serotype 2 and 9 were generated. While rAAV2 is considered to transduce a broad range of cell-types and tissues, rAAV9 is more likely in transducing neurons (Aschauer et al., 2013).

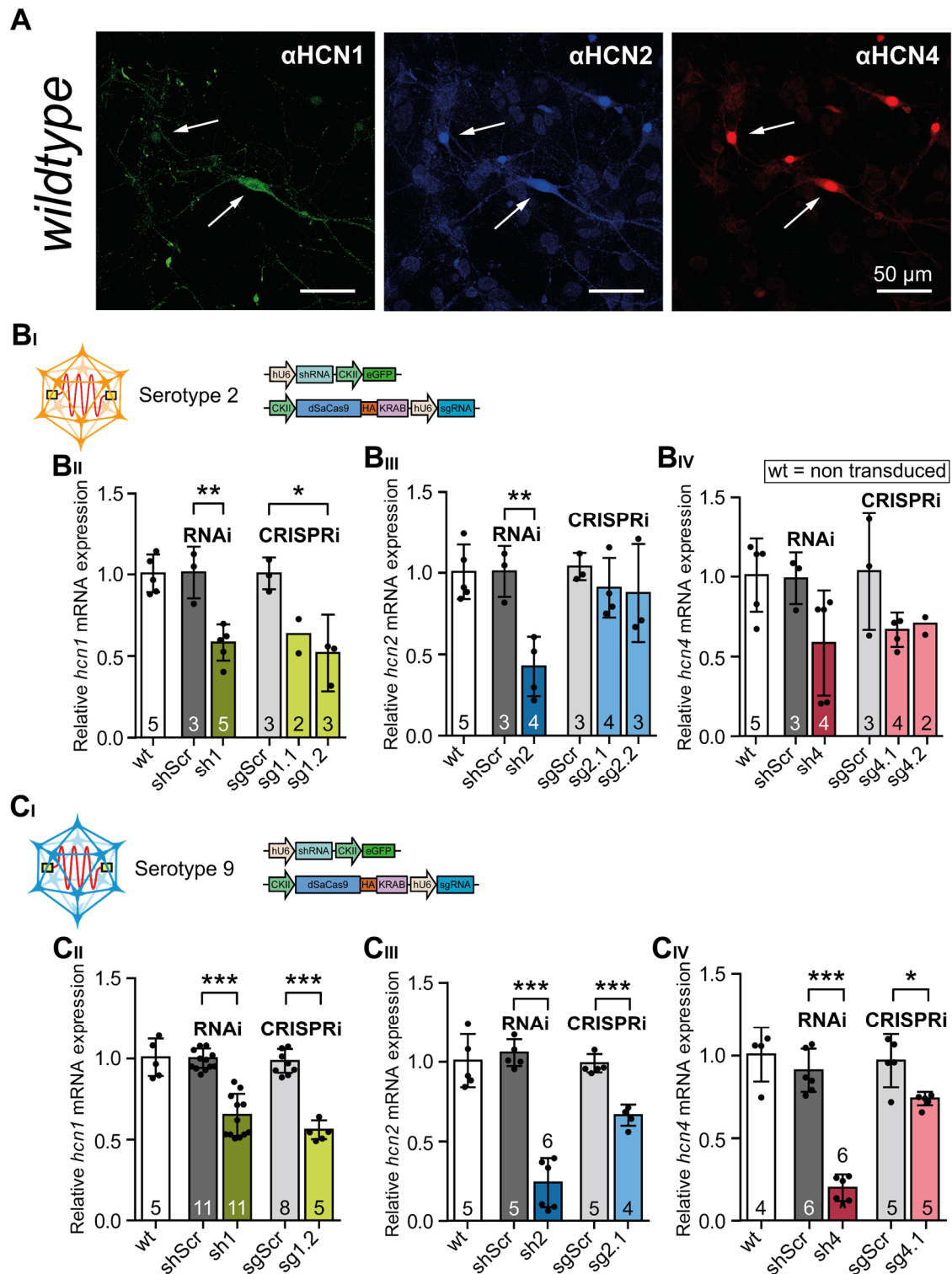


**Figure 3.6: RNAi and CRISPRi reduce the amount of HCN channel transcripts in primary hippocampal neurons**

(A) Representative immunofluorescent images showing expression of HCN-channel isoforms 1 (green), 2 (blue) and 4 (red) in wildtype, i.e. non-treated, hippocampal neurons. Isoforms were stained using subunit-specific antibodies combined with fluorescently labeled secondary antibodies. (B<sub>i</sub>) Schematic representation of constructs delivered by rAAV2 to PHNs. (B<sub>ii</sub> to B<sub>iv</sub>) qRT-PCR analysis of *hcn1*, *hcn2* and *hcn4* mRNA levels in hippocampal neurons after transduction with shRNA or sgRNA/dSaCas9 expressing rAAV2s. (C<sub>i</sub>) Schematic representation of constructs delivered by rAAV9 to PHNs. (C<sub>ii</sub> to C<sub>iv</sub>) qRT-PCR analysis of *hcn1*, *hcn2* and *hcn4* mRNA levels in hippocampal neurons after transduction

with shRNA or sgRNA/dSaCas9 expressing rAAV9s. Complementary DNA was obtained from indicated numbers of transduced coverslips. Results are depicted as mean  $\pm$  standard deviation. Statistical significance was assessed using the unpaired two-tailed Student's t test, \* $p < 0.05$ , \*\* $p < 0.01$ , \*\*\* $p < 0.001$ .

In neurons transduced with rAAV2 virions (Fig. 3.6 B), each of the previously identified shRNAs reduced the mRNA levels of the target gene in comparison to untreated wildtype and shScr-treated controls (Fig. 3.6 BII-BIV). Sh1, designed to knock-down the expression level of the HCN1 channel subunit, reduced *hcn1* transcripts to  $58.3 \pm 11.2\%$  of the shScr control. Similarly, sh2, designed to knock-down the expression level of the HCN2 channel subunit, reduced *hcn2* transcripts to  $42.3 \pm 18.3\%$  of the shScr control and sh4, designed to knock-down the expression level of the HCN4 channel subunit, reduced *hcn4* transcripts to  $60.1 \pm 32.9\%$  of the shScr control. Neither of the shRNA constructs affected expression of the other HCN channel subunits (Günther, 2016). Notably, in CRISPRi experiments, only sg1.2, designed to knock-down the expression level of the HCN1 channel subunit, caused a robust reduction of *hcn1* mRNA to  $51.8 \pm 23.6\%$  of the sgScr control (Fig. 3.6 BII). Using rAAV9 virions for transduction (Fig. 3.6 C), knock-down efficiencies of shRNAs were similar to the values obtained with rAAV2 virions (sh1:  $65.2 \pm 13\%$  of the shScr control; sh2:  $24 \pm 15.5\%$  of the shScr control; sh4:  $25.2 \pm 8.1\%$  of the shScr control). Interestingly, the knock-down efficiencies of sg1.2 targeting the HCN1 gene promoter (Fig. 3.6 CII), sg2.1 targeting the HCN2 gene promoter (Fig. 3.6 CIII), and sg4.1 targeting the HCN4 gene promoter (Fig. 3.6 CIII), were markedly improved when delivered by rAAV9 virions (sg1:  $71.1 \pm 21.5\%$  of the sgScr control; sg2:  $66.3 \pm 6.6\%$  of the sgScr control; sg4:  $83.9 \pm 4.1\%$  of the sgScr control). In comparison to RNAi, however, CRISPRi-mediated knock-down inhibited the expression of *hcn1*, 2, and 4 mRNA less efficiently.

### **3.1.6 Functional expression and validation of knock-down constructs in OHSCs**

While primary hippocampal neurons are perfectly suited to study a neurons' physiology on the single cell level, organotypic hippocampal slice cultures (OHSCs) are widely used to study network properties. Therefore, the effects of HCN-channel knock-down in OHSCs prepared from C57BL/6J mice (Fig. 3.7) was examined.

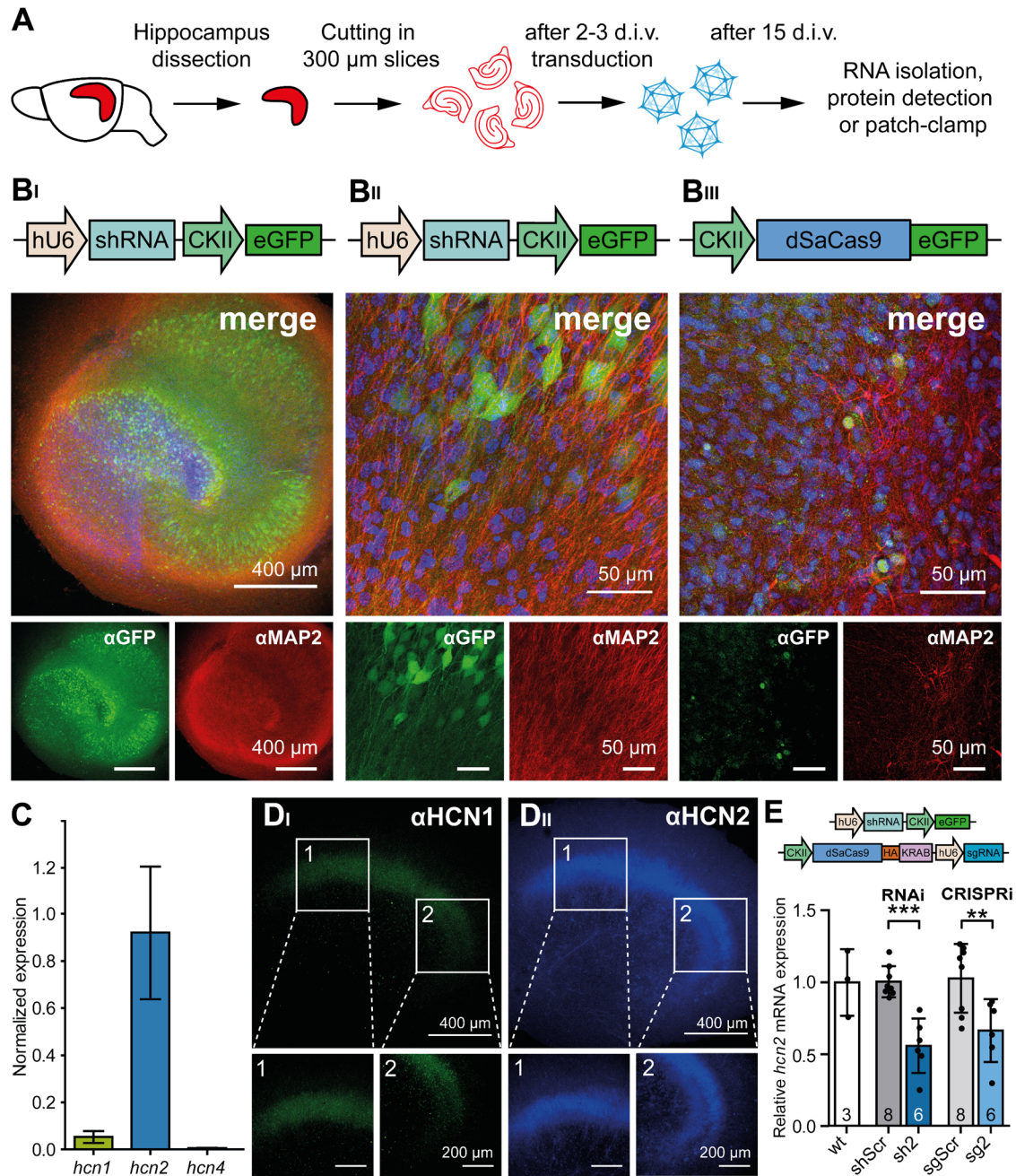


**Figure 3.7: RNAi and CRISPRi reduce the amount of HCN2 channel transcripts in organotypic hippocampal slice cultures.**

(A) Schematic representation of the preparation and transduction procedure for organotypic hippocampal slice cultures (OHSCs). For details see Material and Methods section 2.7. (B) Representative immunofluorescent images showing rAAV9-transduced OHSCs expressing the (B<sub>i</sub> and B<sub>ii</sub>) eGFP (green) reporter of the RNAi-inducing construct, or (B<sub>iii</sub>) eGFP-tagged dSaCas9 of the CRISPRi-inducing construct. The eGFP and the neuron-specific MAP2 protein (red) were immunostained with specific anti ( $\alpha$ )-GFP and  $\alpha$ -MAP2 antibodies combined with fluorescently labeled secondary antibodies (eGFP green; MAP2, red). Nuclei were labeled with TOPRO (blue). Cartoons of the AAV-delivered constructs are displayed above the merged immunofluorescent images. (C) qRT-PCR analysis of transcript levels of HCN isoforms 1, 2 and 4 in OHSCs. Transcript levels were normalized to *gapdh* and values shown are calculated to the sum of all *hcn* transcripts. cDNA was prepared from 5 culture inserts, each containing 3 individual slices. In total, slices were obtained from 3 different animals. (D<sub>i</sub> and D<sub>ii</sub>) Representative immunofluorescent images showing expression of HCN-channel isoforms 1 (green), and 2 (blue). Isoforms were stained using specific antibodies and fluorescently labeled secondary antibodies. Enlargements show

HCN-isoform expression in hippocampal cornu ammonis (CA) regions CA1 (1) and CA3 (2) subfields. (E) qRT-PCR analysis of *hcn2* mRNA levels in organotypic slices after transduction with shRNA or sgRNA/dSaCas9 expressing rAAV9. Complementary DNA was obtained from indicated numbers of culture inserts, each containing 3 individual slices. In total, slices were obtained from at least 3 different animals. Results are depicted as mean  $\pm$  standard deviation. Statistical significance was assessed using the unpaired two-tailed Student's t-test, \*\* $p < 0.01$ , \*\*\* $p < 0.001$ .

After two weeks of cultivation and 12-13 days after transduction with rAAV9 expressing shRNA constructs (Fig. 3.7 BI and BII) or CRISPRi-inducing dSaCas9-eGFP constructs (Fig. 3.7 BIII), samples were fixated and expression of reporter proteins was examined immunohistochemically. In agreement with the previous experiments performed on HEK293 cells and PHNs, transduction with rAAV9 virions of OHSCs yielded a high number of transduced neurons, especially for rAAVs encoding shRNAs. Furthermore, rAAVs inducing RNAi and rAAVs inducing CRISPRi both reproduced the localization pattern of reporter proteins previously observed in HEK293 cells and PHNs. The eGFP reporter encoded by shRNA containing constructs was homogeneously distributed in the cell soma and cellular extensions, whereas dSaCas9-eGFP fluorescence was restricted to the nucleus (Fig. 3.7 BII and BIII).

Expression of *hcn1*, *hcn2* and *hcn4* transcripts (Fig. 3.7 C) as well as the corresponding proteins (Fig. 3.7 DI and DII) was examined in OHSCs. Both, qRT-PCR and immunohistochemistry indicated that HCN2 is the most abundant channel isoform in OHSCs (qRT-PCR quantification: *hcn1*  $5.3 \pm 2.5$  %; *hcn2*  $92.1 \pm 28.4$  %; *hcn4*  $5.5 \pm 1.3$  %). Based on this finding, further RNAi and CRISPRi experiments were intended to only manipulate HCN2 channel expression in OHSCs. Both, sh2 and sg2 (sg2.1) reduced *hcn2* mRNA levels compared to untreated wildtype and shScr- or sgScr-treated controls (sh2:  $52.1 \pm 18.9$  %; sg2:  $62.7 \pm 21.9$  %) (Fig. 3.7 F). Taken together, these experiments strongly suggest that both techniques are suitable to manipulate expression levels of HCN-encoding transcripts and channel proteins in a variety of culture systems.

---

The results of construction, functional expression, and validation of both knock-down techniques showed that both techniques, i.e. CRISPRi and RNAi, specifically reduced *hcn* transcript levels in transgenic cell-lines, primary hippocampal neurons (PHNs), and organotypic hippocampal slice cultures (OHSCs) for each of the three targeted HCN isoforms.

However, RNAi-mediated HCN-channel knock-down was more robust and efficient, compared to CRISPRi-mediated knock-down in recombinant cell-lines, PHNs as well as OHSCs

In addition, rAAV9 virions were better suited than rAAV2 virions for delivering the cargo into PHNs or OHSCs.

---

### 3.2 Electrophysiological characterization of HCN channels

To gain insight into the basic biophysical properties of the different HCN-channel subtypes expressed in PHNs, the cation currents through HCN channels, known as  $I_h$ -currents, were examined by whole-cell patch-clamp electrophysiology.

#### 3.2.1 Electrophysiological characterization of HCN channels in HEK293 cells

By recording current-voltage relationships and extracting the half-maximal activation voltages from HEK293 cells constitutively expressing HCN channel subtypes (HCN1, HCN2 and HCN4; see Fig. 3.8 A), differences in activation potentials of HCN channel subtypes were confirmed (Altomare et al., 2003, Baruscotti et al., 2005).

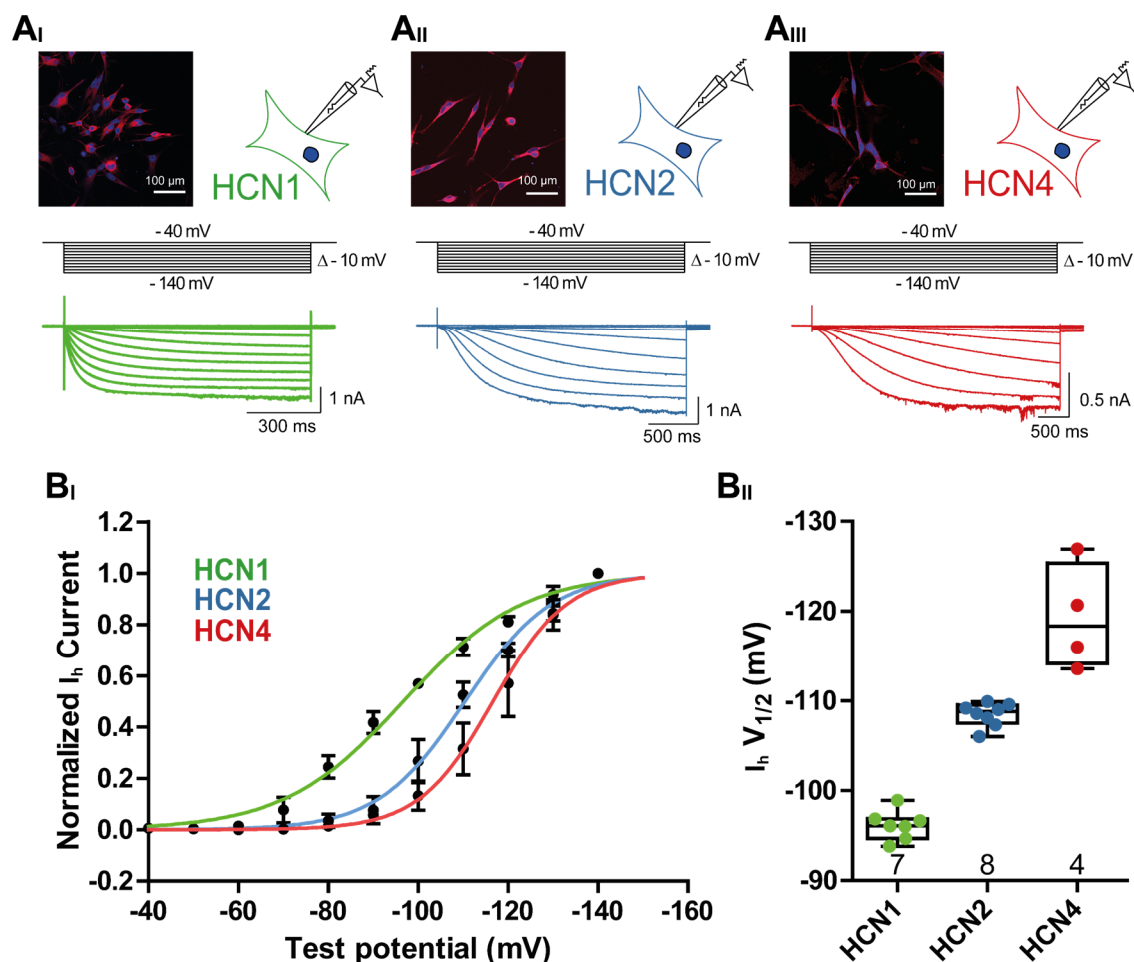


Figure 3.8: Whole-cell patch-clamp recordings of  $I_h$ -currents in HEK293 cell-lines constitutively expressing HCN channel subunits 1, 2 or 4.

(A) Upper panel: Representative immunofluorescent images showing HEK293 cell-lines constitutively expressing HCN channel subunit 1 (A<sub>I</sub>), 2 (A<sub>II</sub>), and 4 (A<sub>III</sub>). Stainings were performed with subunit specific HCN channel antibodies combined with fluorescently labeled secondary antibodies (red). Nuclei

were labeled with TOPRO (blue). Lower panel: Representative voltage stimulation protocols and corresponding current traces of whole-cell patch-clamp recordings derived from HEK293 cell-lines constitutively expressing HCN channel subunit 1 (AI), 2 (AII), and 4 (AIII). (BI) Current-voltage relationships recorded from HEK293 cell-lines constitutively expressing HCN channel subunits 1, 2 or 4. Currents were calculated from the difference of the instantaneous current and the steady-state current. The continuous lines represent fitted Boltzmann functions of the data. (BII) Half-maximal activation voltages of the different homomeric HCN-channels were calculated from the fitted Boltzmann functions of the whole-cell currents. Results are depicted as boxplots.

Homomeric HCN1 channels activate at more positive membrane potentials in comparison to HCN2 and HCN4 homomeric channels which activate at more negative membrane potentials (HCN1:  $-96.14 \pm 1.63$  mV; HCN2:  $-108.5 \pm 1.3$  mV; HCN4:  $-119.3 \pm 5.86$  mV). This results in an activation sequence of HCN1 > HCN2 > HCN4 from more depolarized to very hyperpolarized potentials (Fig. 3.8 B).

### ***3.2.2 Electrophysiological characterization of HCN channels in PHNs of wildtype and HCN1<sup>-/-</sup> mice***

To examine the effects of a complete loss of the HCN1-channel protein on basic neuronal properties and I<sub>h</sub>-channel current properties, recordings from wildtype (untreated) PHNs (Fig. 3.9) served as controls for recordings from PHNs derived from HCN1-channel knock-out (HCN1<sup>-/-</sup>) mice (Nolan et al., 2003). Cultured wildtype PHNs expressed at least three HCN channel isoforms which were quantified by qRT-PCR (Fig. 3.9 B).

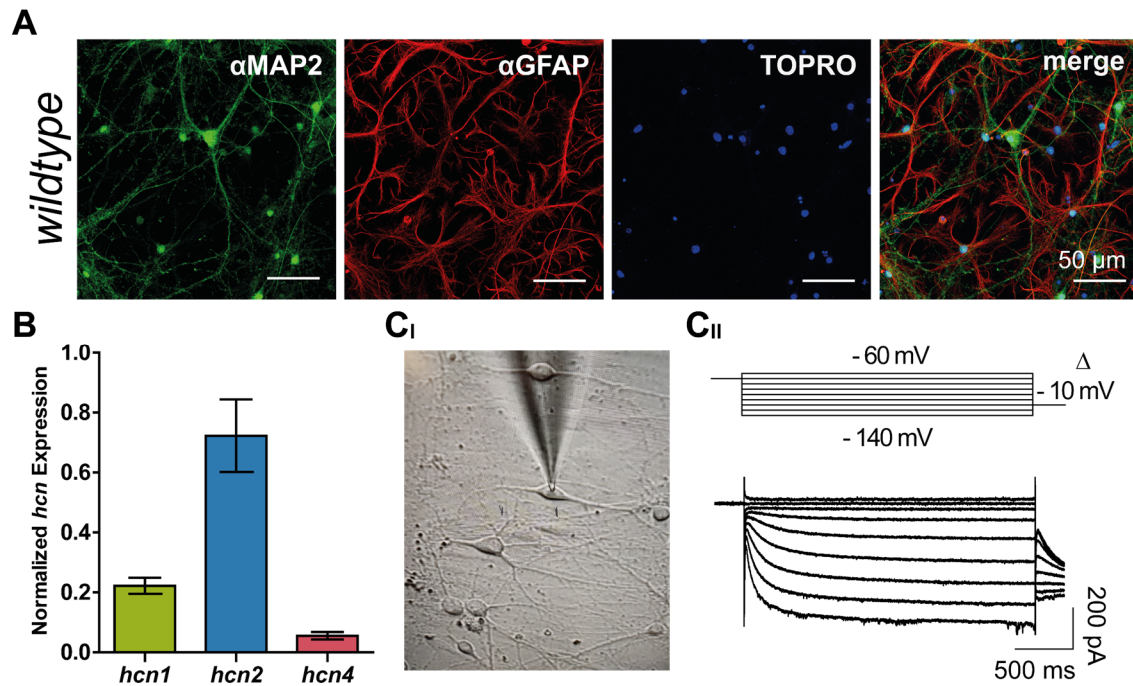


**Figure 3.9: Whole-cell patch-clamp recordings of pharmacologically isolated  $I_h$ -currents in PHNs**

(A) Representative immunofluorescent images of cultured wildtype primary hippocampal neurons (PHNs). Neurons were stained using a MAP2 antibody and glia cells were stained using an antibody against glial fibrillary acidic protein (GFAP). Primary antibodies were combined with fluorescently labeled secondary antibodies (MAP2 green; GFAP, red). Nuclei were labeled with TOPRO (blue). (B) qRT-PCR analysis of transcript expression levels for HCN isoforms 1, 2 and 4 in PHNs. Transcript levels were normalized to *gapdh* and values shown are calculated to 1 as the sum of all *hcn* transcripts. cDNA was prepared from 5 coverslips with PHNs from at least 3 different animals. (CI) Representative image showing the patch-clamp analysis of a PHN. (CII) Representative voltage stimulation protocol and corresponding current traces of whole-cell patch-clamp recordings derived from a PHN after 15 days *in vitro* (d.i.v.). Results are depicted mean  $\pm$  standard deviation.

Examination of transcript numbers showed, that *hcn2* transcripts were most abundant ( $72 \pm 12.3\%$ ), followed by *hcn1* and *hcn4* transcripts (*hcn1*:  $22 \pm 2.6\%$ ; *hcn4*:  $6 \pm 0.9\%$ ) (Fig. 3.9 B).

To check for compensatory changes of HCN channel expression levels upon ablation of the HCN1 channel subtype, HCN channel transcript numbers were also quantified in PHNs derived from HCN1<sup>-/-</sup> mice (Fig. 3.10 BI).

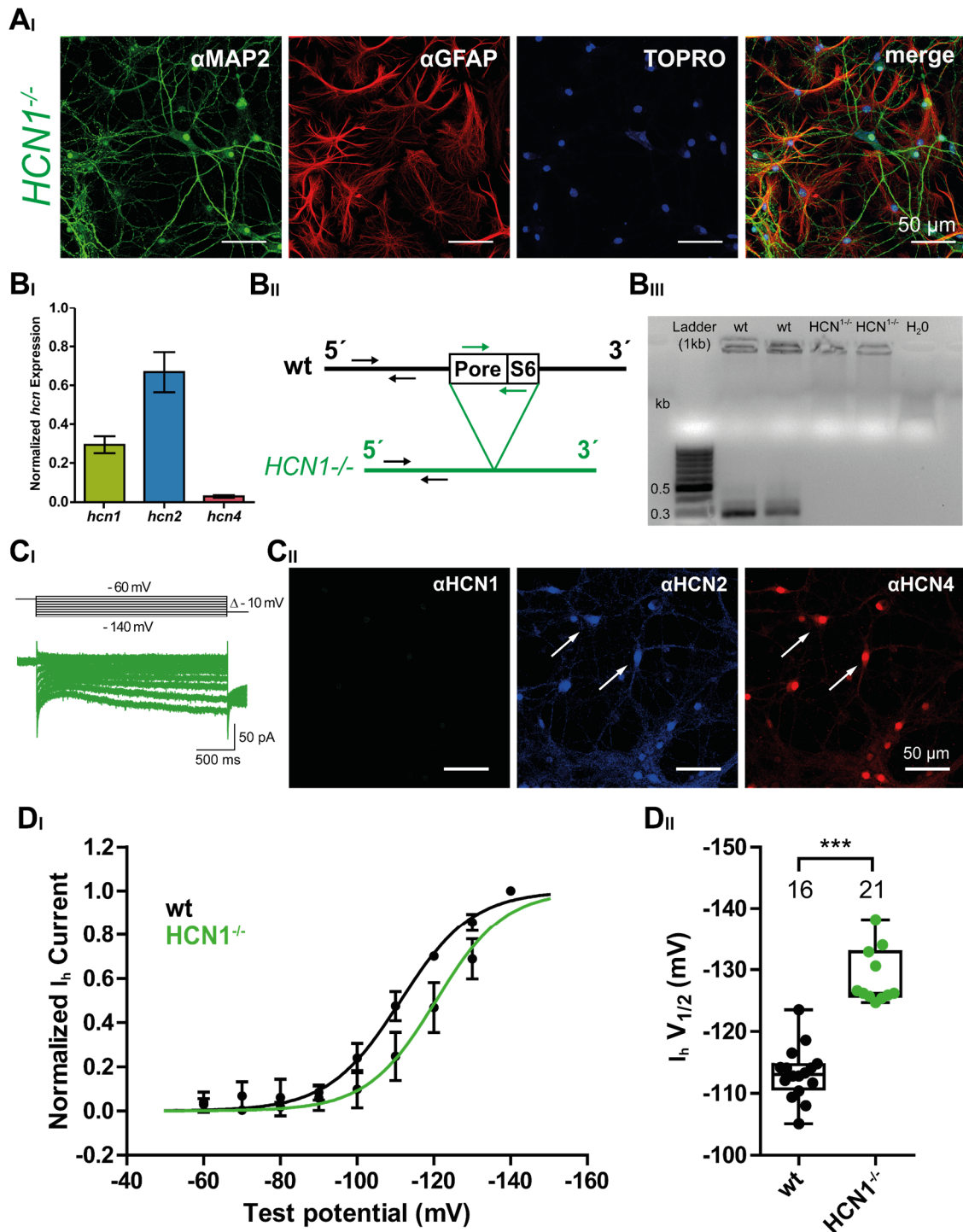


**Figure 3.10: Whole-cell patch-clamp recordings of pharmacologically isolated  $I_h$ -currents in PHNs derived from *HCN1* knock-out (*HCN1*<sup>-/-</sup>) mice**

(A) Representative immunofluorescent images of PHNs derived from a *HCN1* channel knock-out mouse (*HCN1*<sup>-/-</sup>). Neurons were stained using a MAP2 antibody and glia cells were stained using an antibody against GFAP. Primary antibodies were combined with fluorescently labeled secondary antibodies (MAP2 green; GFAP, red). Nuclei were labeled with TOPRO (blue). (B<sub>i</sub>) qRT-PCR analysis of transcript levels for HCN isoforms 1, 2 and 4 in PHNs derived from *HCN1*<sup>-/-</sup> mice. Transcript levels were normalized to *gapdh* and values shown were calculated to 1 as the sum of all *hcn* transcripts. cDNA was prepared from 6 coverslips with PHNs from at least 3 different animals. (B<sub>ii</sub>) Transcript structure encoding the HCN1 channel subunit in wt and *HCN1*<sup>-/-</sup> mice. The black primer pair was used for qRT-PCR analysis and the green primer pair was used for the PCR reaction shown in B<sub>iii</sub>. (B<sub>iii</sub>) Agarose gel showing fragments of a

PCR reaction using the primer pair (green) binding in the deleted genomic region of HCN1<sup>-/-</sup> mice. (CI) Representative voltage stimulation protocol and corresponding current traces of whole-cell patch-clamp recordings derived from HCN1<sup>-/-</sup> PHN after 15 days *in vitro* (d.i.v.). (CII) Representative immunofluorescent images showing expression of HCN-channel isoforms 1 (green), 2 (blue) and 4 (red) in PHNs derived from HCN1<sup>-/-</sup> mice. Isoforms were stained using subunit-specific antibodies combined with fluorescently labeled secondary antibodies. (DI) Current-voltage relationships recorded from PHNs of wildtype and HCN1<sup>-/-</sup> mice. Currents were calculated from the difference of the instantaneous current and the steady-state current. The continuous lines represent fitted Boltzmann functions of the data. (DII) Half-maximal activation voltages of recordings from PHNs of wildtype and HCN1<sup>-/-</sup> mice, calculated from the fitted Boltzmann functions of the whole-cell currents. Results are depicted as boxplots. Statistical significance was assessed using the unpaired two-tailed Student's t-test, , \*\*\*p<0.001.

The quantification showed that, similar to wildtype neurons, HCN2-encoding transcripts were most abundant ( $67 \pm 10.4$  %), followed by HCN1- and HCN4-encoding transcripts (*hcn1*:  $30 \pm 4.4$  %; *hcn4*:  $3 \pm 0.6$  %) in PHNs derived from HCN1<sup>-/-</sup> mice. Because the knock-out of the HCN1 channel subtype was generated by a deletion of exons coding for the pore and S6 transmembrane domain (Fig. 3.10 BII), the mRNA fragment of HCN1 was still detectable using a primer pair targeting more 5' located exons of the gene. When using a primer pair targeting the deleted genomic region, no amplification products were detectable in HCN1<sup>-/-</sup> animals, but in wildtype controls (Fig. 3.10 BIII). To confirm the loss of HCN1 channel proteins in HCN1<sup>-/-</sup> mice, immunofluorescent stainings were performed. The immunofluorescence images showed that the HCN1 protein was completely absent in PHNs from HCN1<sup>-/-</sup> mice (Fig. 3.10 CII). In addition, patch-clamp recordings revealed a shift in the half-maximal activation voltages of the isolated I<sub>h</sub>-channel currents from  $-113.2 \pm 4.24$  mV in wildtype PHNs to  $-128.8 \pm 4.47$  mV in HCN1<sup>-/-</sup> PHNs (Fig. 3.10 D). Thus, a loss of HCN1 lead to a shift of the half-maximal activation voltages from more depolarized potentials to more hyperpolarized potentials.

### ***3.2.3 Electrophysiological characterization of HCN-channel function in RNAi treated***

#### ***PHNs***

Because RNAi robustly reduced HCN-channel transcript and protein levels in HEK293 cells, PHNs, and OHSCs more efficiently than CRISPRi, RNAi-mediated knock-down was used to examine the effects of *hcn* gene knock-down on passive neuronal properties and I<sub>h</sub>-current properties.

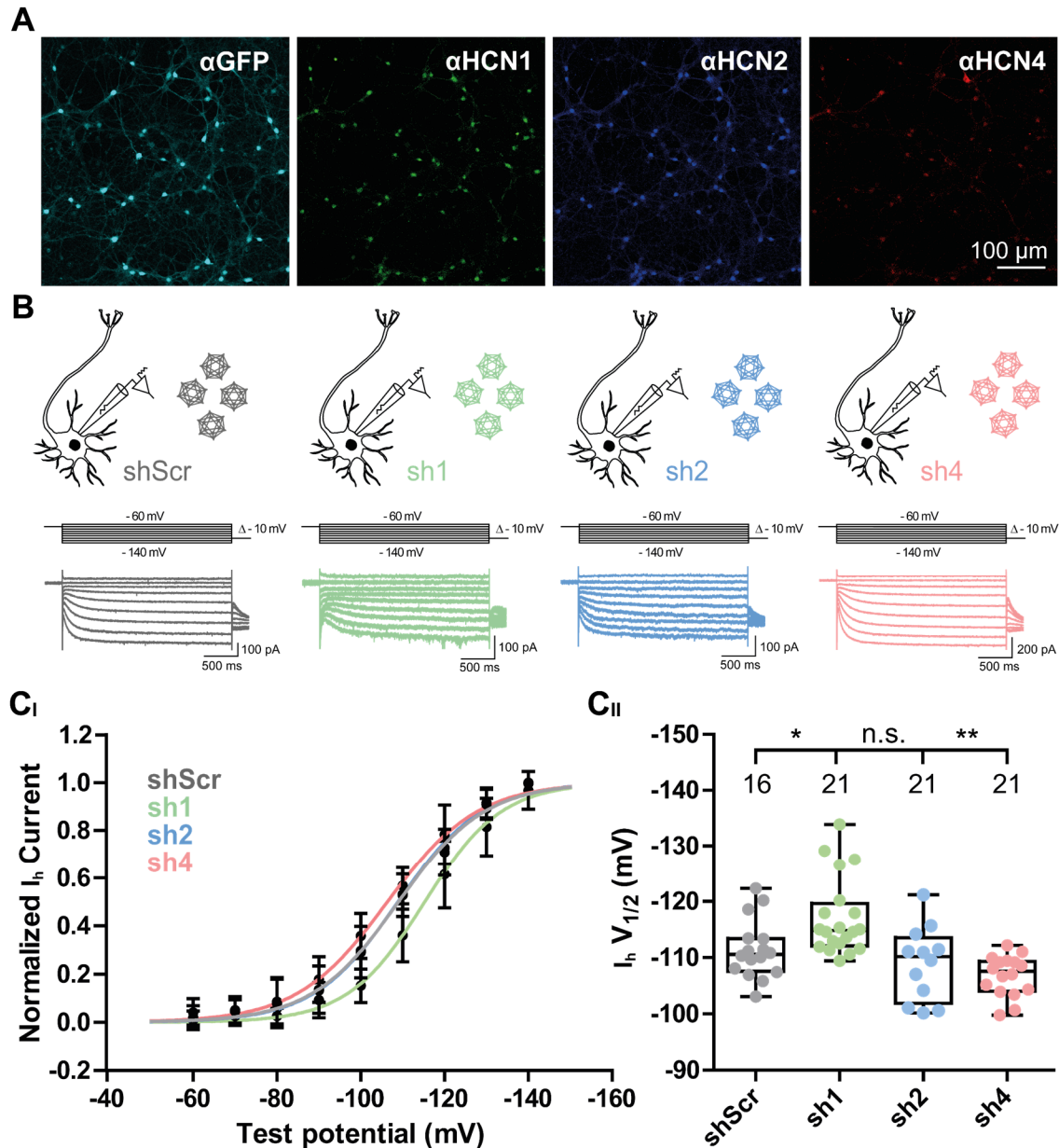


**Figure 3.11: Whole-cell patch-clamp recordings of pharmacologically isolated  $I_h$ -currents in PHNs transduced with RNAi-mediating constructs**

(A) Representative immunofluorescent images showing rAAV9-transduced PHNs expressing the eGFP reporter. EGFP reporter (cyan), HCN-channel isoforms 1 (green), 2 (blue) and 4 (red) were stained using specific antibodies combined with fluorescently labeled secondary antibodies. (B) Representative voltage stimulation protocols and corresponding current traces of whole-cell patch-clamp recordings derived from rAAV9-transduced PHNs expressing shScr (control), sh1 (HCN1 channel knock-down), sh2 (HCN2-channel knock-down), or sh4 (HCN4 channel knock-down) after 15 days *in vitro* (d.i.v.). (BI) Current-voltage relationships recorded from rAAV9-transduced, shRNA expressing PHNs. Currents were calculated from the difference of the instantaneous current and the steady-state current. The continuous lines represent fitted Boltzmann functions of the data. (BII) Half-maximal activation voltages from rAAV9-transduced, shRNA expressing PHNs, calculated from the fitted Boltzmann functions of the whole-cell currents. Results are depicted as boxplots. Statistical significance was assessed using the unpaired two-tailed Student's t test, \* $p < 0.05$ , \*\* $p < 0.01$ .

For recording current-voltage relationships, PHNs were transduced with rAAV9 coding for shScr (control), sh1 (knock-down of HCN1), sh2 (knock-down of HCN2) or sh4 (knock-down of HCN4). In sh1-treated neurons, the half-maximal activation potential ( $V_{1/2}$ ) was shifted to a more hyperpolarized potential of  $-117.1 \pm 6.9$  mV compared to shScr-treated neurons (shScr:  $-111.4 \pm 5.22$  mV). In contrast,  $V_{1/2}$  of sh4-treated neurons shifted to more depolarized potentials of  $-106.8 \pm 3.61$  mV. However,  $V_{1/2}$  of sh2-treated neurons ( $-108.9 \pm 6.55$  mV) was similar to the value obtained for shScr-treated neurons. Thus, a knock-down of HCN1 channels partially reproduced the effect observed in PHNs from HCN1<sup>-/-</sup> mice. Furthermore, a knock-down of HCN4 channels had a strong influence on the activation potential, while a knock-down of HCN2 channels did not influence the activation potential of native  $I_h$ -currents in PHNs.

### 3.2.4 Consequences of HCN channel reduction on basic properties of PHNs

To validate if the HCN1 knock-out or the knock-down of individual HCN channel subtypes is causative for changes in cellular electrophysiological characteristics, basic properties of rAAV-untreated and rAAV-treated neurons were assessed (Fig. 3.12).

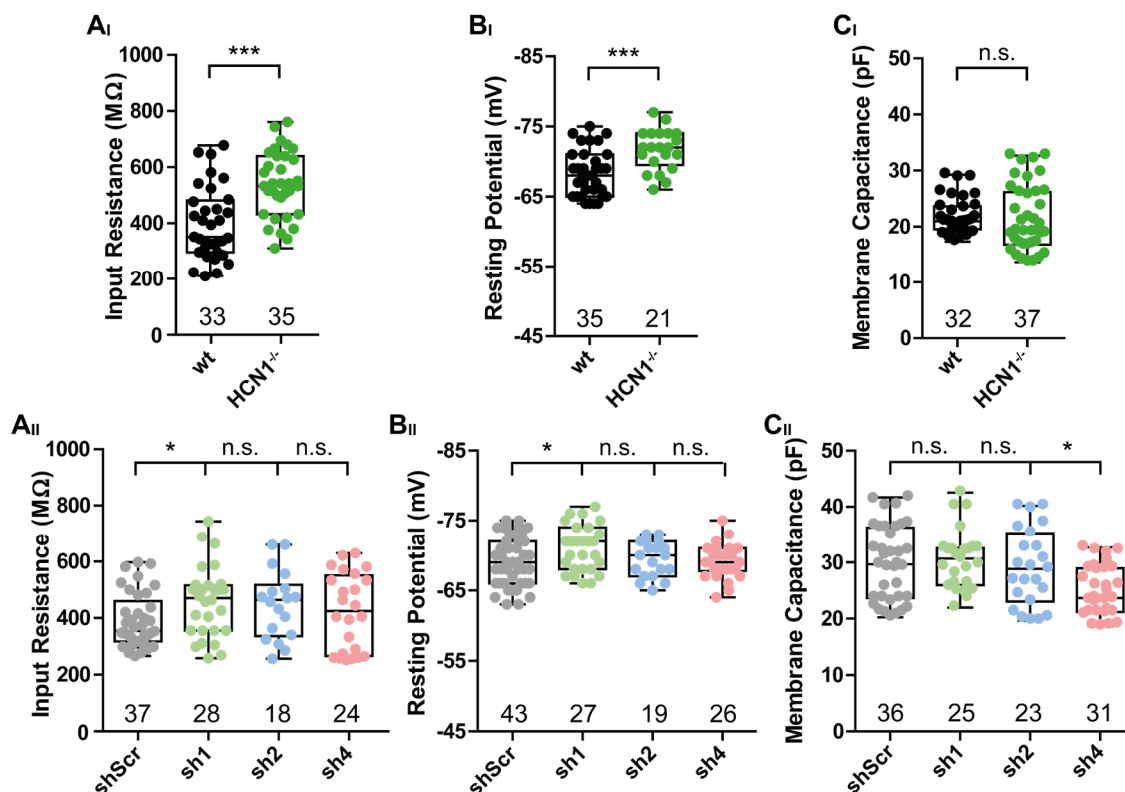


Figure 3.12: Effects of HCN channel knock-out and knock-down on basic parameters of primary hippocampal neurons

Results of whole-cell patch-clamp recordings from wildtype (non-transduced), HCN1 channel knock-out (HCN1<sup>-/-</sup>), or AAV9-shRNA transduced eGFP positive PHNs. (A) Influence of HCN1<sup>-/-</sup>, shScr (control), sh1 (HCN1 channel knock-down), sh2 (HCN2-channel knock-down), or sh4 (HCN4 channel knock-down) on input resistances in PHNs. Input resistances were measured with a single 10 mV hyperpolarizing voltage pulse. (B) Influence of HCN1<sup>-/-</sup>, shScr, sh1, sh2, or sh4 expression on the resting membrane potential of PHNs. Resting membrane potentials were measured approx. 30 s after establishing the whole-cell configuration. (C) Influence of HCN1<sup>-/-</sup>, shScr, sh1, sh2, or sh4 on the membrane capacitance as a measure for the cell sizes of PHNs. Membrane capacitance was measured by the membrane capacitance compensation of the amplifier. Results are depicted as boxplots. Statistical significance was assessed using the unpaired two-tailed Student's t test, \*p<0.05, \*\*\*p<0.001.

As a measure for the ability of a neuron to conduct current across the membrane at resting conditions, the input resistance was measured. In HCN1<sup>-/-</sup> neurons, the input resistance at the resting potential of -70 mV was strongly increased compared to neurons from wildtype mice (wt:  $398.1 \pm 129.6 \text{ M}\Omega$ ; HCN1<sup>-/-</sup>:  $538.6 \pm 115.0 \text{ M}\Omega$ ) (Fig. 3.12 AI). Similarly, when PHNs were transduced with rAAV9 encoding sh1, the input resistance was also increased compared to the controls (shScr:  $389.9 \pm 95.6 \text{ M}\Omega$ ; sh1:  $457.5 \pm 125.1 \text{ M}\Omega$ ). However, knock-down of HCN2 by sh2 or HCN4 by sh4 did not change input resistance of the neurons (sh2:  $447.4 \pm 120.8 \text{ M}\Omega$ ; sh4:  $423.5 \pm 135.6 \text{ M}\Omega$ ) (Fig. 3.12 AII). These results indicated that manipulation of HCN1 channel expression decreased the proportion of open ion channels at the resting membrane potential, and thus, restricted the amount of current crossing the membrane. Moreover, in HCN1<sup>-/-</sup> neurons, the resting membrane potential was more negative compared to neurons from wildtype mice (wt:  $-68.34 \pm 3.23 \text{ mV}$ ; HCN1<sup>-/-</sup>:  $-71.67 \pm 2.9 \text{ mV}$ ) (Fig. 3.12 AII). This decrease was also observed when neurons were transduced with rAAV9 encoding for sh1 ( $-71.0 \pm 3.29 \text{ mV}$ ) compared to neurons transduced with rAAV9 encoding for shScr ( $-69.19 \pm 3.52 \text{ mV}$ ) (Fig. 3.12 BII). This observation is in accordance with previous reports (Matsumoto-Makidono et al., 2016) and is accompanied by the finding that HCN1 channels are partially activated at the resting membrane potential (Fig. 3.8 BI). Thus, it was not surprising that a knock-down of HCN2 and HCN4 (sh2 and sh4), which were almost not activated at the resting membrane potential (Fig. 3.8 BI), did not change the resting membrane potential of the neurons (sh2:  $-69.42 \pm 2.52 \text{ mV}$ ; sh4:  $-69.04 \pm 2.44 \text{ mV}$ ) compared to control neurons (shScr; Fig. 3.12 BII). To rule out that different neuron sizes were causative for the observed effects, the membrane capacitance was measured. Neither in PHNs from HCN1<sup>-/-</sup> mice, nor in PHNs treated with sh1 or sh2 constructs changes occurred in the membrane capacitance compared to control conditions (wt:  $22.27 \pm 3.27 \text{ pF}$ ; HCN1<sup>-/-</sup>:  $21.83 \pm 5.95 \text{ pF}$ ; shScr:  $30.17 \pm 6.69 \text{ pF}$ ; sh1:

$30.81 \pm 5.3$  pF; sh2:  $29.3 \pm 6.84$  pF). However, the knock-down of HCN4 (sh4) caused a decrease of the membrane capacitance ( $25.37 \pm 4.38$  pF) compared to the control condition (shScr). Taken together, these data suggest that HCN1 is the main contributors to basic cellular properties like the input resistance and the resting membrane potential.

### ***3.2.5 Consequences of HCN channel reduction on $I_h$ -current properties***

In addition to the effects of HCN channel knock-down on passive electrical properties of neurons, effects of HCN-channel knock-out and knock-down on the  $I_h$ -current properties were examined. Therefore, amplitudes of isolated  $I_h$ -currents in HEK293 cell-lines and PHNs were measured (Fig. 3.13).

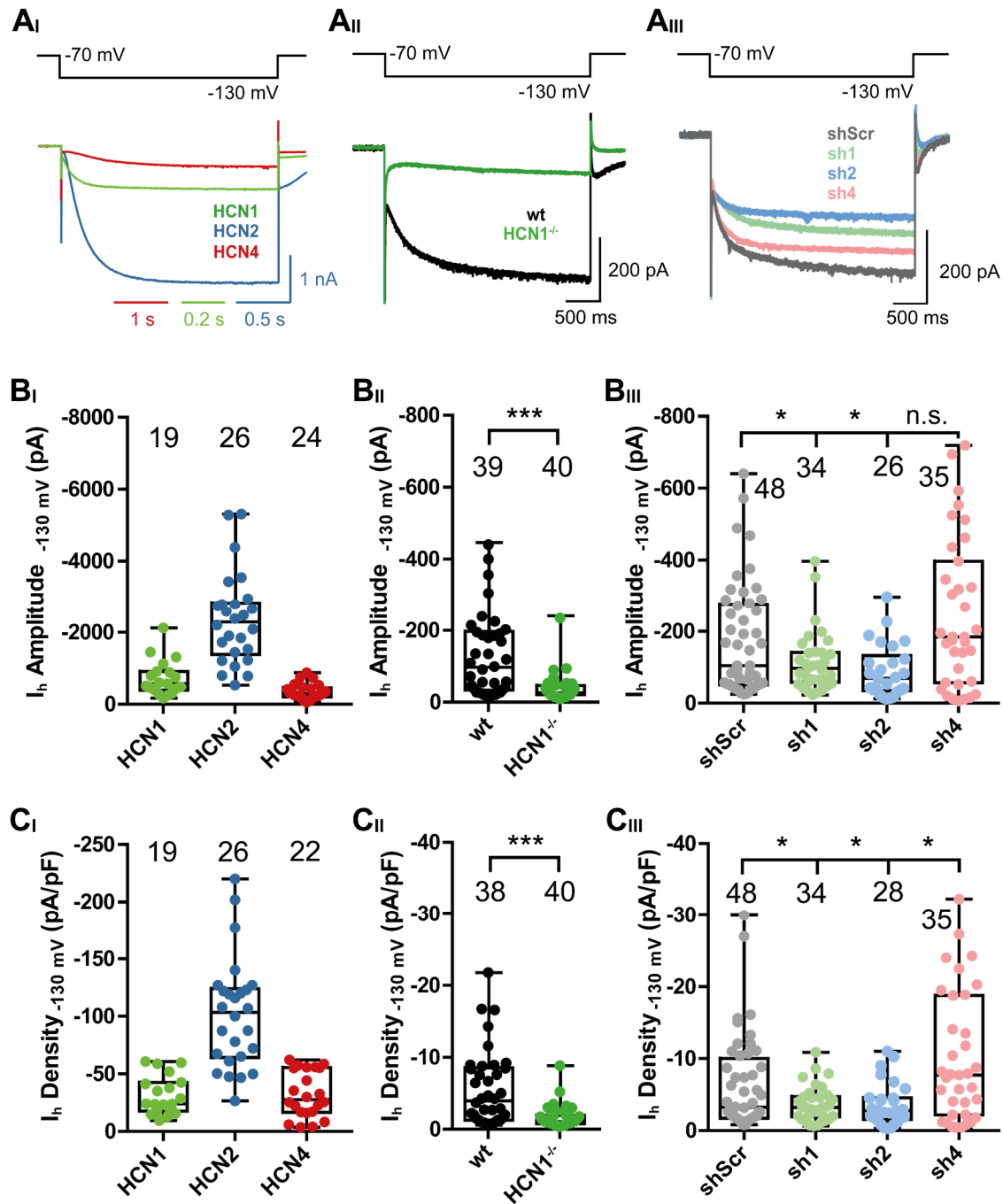


**Figure 3.13: Effects of HCN-channel knock-out and knock-down on current amplitudes of isolated I<sub>h</sub>-currents in HEK293 cell-lines and primary hippocampal neurons**

(A) Representative voltage stimulation and corresponding current traces of whole-cell patch-clamp recordings derived from (A<sub>I</sub>) HEK293 cell-lines constitutively expressing HCN channel subunit 1 (HCN1), HCN channel subunit 2 (HCN2), or HCN channel subunit 4 (HCN4); (A<sub>II</sub>) primary hippocampal neurons (PHNs) from wildtype (wt) or HCN1<sup>-/-</sup> mice, and (A<sub>III</sub>) of PHNs treated with shScr (control), sh1 (HCN1 channel knock-down), sh2 (HCN2-channel knock-down), or sh4 (HCN4 channel knock-down) expressing rAAVs after 15 days *in vitro* (d.i.v.). (B) Current amplitudes of (B<sub>I</sub>) HEK293 cell-lines expressing HCN1, HCN2 or HCN4, (B<sub>II</sub>) PHNs from wt and HCN1<sup>-/-</sup> mice, and of (B<sub>III</sub>) rAAV9-shScr, -sh1, -sh2, or -sh4 transduced eGFP-positive PHNs. Current amplitudes were measured from the difference of the instantaneous current and the steady-state current to the current response of a hyperpolarizing pulse (from -70 mV to -130 mV). (C) Current densities of (C<sub>I</sub>) HEK293 cell-lines expressing homomeric HCN1, HCN2 or HCN4 channels, (C<sub>II</sub>) PHNs from wt and HCN1<sup>-/-</sup> mice, and of (C<sub>III</sub>) rAAV9-shScr, -sh1, -sh2, or -sh4 transduced eGFP-positive PHNs. Current densities were calculated by dividing the current amplitude by

the corresponding membrane capacitance of the cell (Fig. 3.12 C). Results are depicted as boxplots. Statistical significance was assessed using the unpaired two-tailed Student's t test, \* $p < 0.05$ , \*\*\* $p < 0.001$ .

$I_h$ -currents in HEK293 cells were recorded in extracellular solution without addition of blocking substances. Current amplitudes were calculated by the difference of the instantaneous current at the beginning of the test pulse and the steady-state current at the end of each test pulse (from -70 mV to -130 mV) (Fig. 3.13 B). Comparison of the  $I_h$ -current amplitudes recorded in HEK293 cells either expressing HCN1, HCN2, or HCN4 channel subtypes showed that homomeric HCN2 channels produced the highest current amplitudes ( $-2370 \pm 1265$  pA) in comparison to homomeric HCN1 channels ( $-725.7 \pm 491.9$  pA) or homomeric HCN4 channels ( $-341.7 \pm 216.5$  pA) (Fig. 3.13 BI). By dividing the current amplitudes by the corresponding membrane capacitance of the cell (Fig. 3.12 C), current densities were determined to diminish the effects of changes in cell sizes on the current amplitudes (Fig. 3.13 C). Comparison of the  $I_h$ -current densities showed that homomeric HCN2 channels had higher current densities ( $-101.8 \pm 47.81$  pA/pF), while homomeric HCN4 channels ( $-32.27 \pm 20.07$  pA/pF) and homomeric HCN1 channels ( $-31.61 \pm 16.76$  pA/pF) (Fig. 3.13 CI) had lower current densities, respectively. These results are in agreement with a study showing that single-channel parameters of homomeric HCN channels differ from each other. While HCN2 homomeric channels had the highest conductance, HCN1 and HCN4 homomeric channels had lower conductances (Michels et al., 2005). Thus, HCN2 homomeric channels can produce the highest current amplitudes.

To analyze  $I_h$ -current amplitudes and densities in PHNs, currents were recorded in extracellular solution containing blocking substances to isolate the  $I_h$ -current from non-HCN channel currents (see Chapter 2.16). Both,  $I_h$ -current amplitudes and  $I_h$ -current densities in HCN1<sup>-/-</sup> neurons were smaller in comparison to wt neurons (wt:  $-123.5 \pm 112.8$  pA;  $-5.56 \pm 5.22$  pA/pF; HCN1<sup>-/-</sup>:  $-34.28 \pm 38.23$  pA;  $-1.64 \pm 1.56$  pA/pF) (Fig. 3.13 BII and CII). In addition, a knock-down of HCN1 and HCN2 subunits, but not of HCN4 subunits, decreased  $I_h$ -current amplitudes compared to the control (shScr  $-173.5 \pm 157.7$  pA; sh1:  $-107.0 \pm 74.09$  pA; sh2:  $-89.25 \pm 74.08$  pA; sh4:  $-244.5 \pm 208.1$  pA) (Fig. 3.13 BIII). However, while a knock-down of HCN1 and HCN2 subunits also decreased  $I_h$ -current densities compared to the control (shScr  $-6.28 \pm 6.49$  pA/pF; sh1:  $-3.69 \pm 2.43$  pA/pF; sh2:  $-3.64 \pm 2.97$  pA/pF), a

knock-down of the HCN4 subunit even increased  $I_h$ -current densities (sh4:  $-9.92 \pm 8.92$  pA/pF). This increase in  $I_h$ -current density might arise from the knock-down of the subunit with the lowest single-channel amplitude (Michels et al., 2005). Thus, hetero-tetrameric HCN channels present in the neuron's membrane most likely are mainly composed of HCN1 and HCN2 subunits, thus resulting in higher single-channel amplitudes.

To examine effects of HCN-channel knock-out and knock-down on activation kinetics of native  $I_h$ -currents, isolated  $I_h$ -currents in HEK293 cell-lines and PHNs were measured. By recording  $I_h$ -currents at a membrane potential of  $-130$  mV and fitting the data to a mono-exponential function, time constants of activation ( $\tau$ ) were determined.

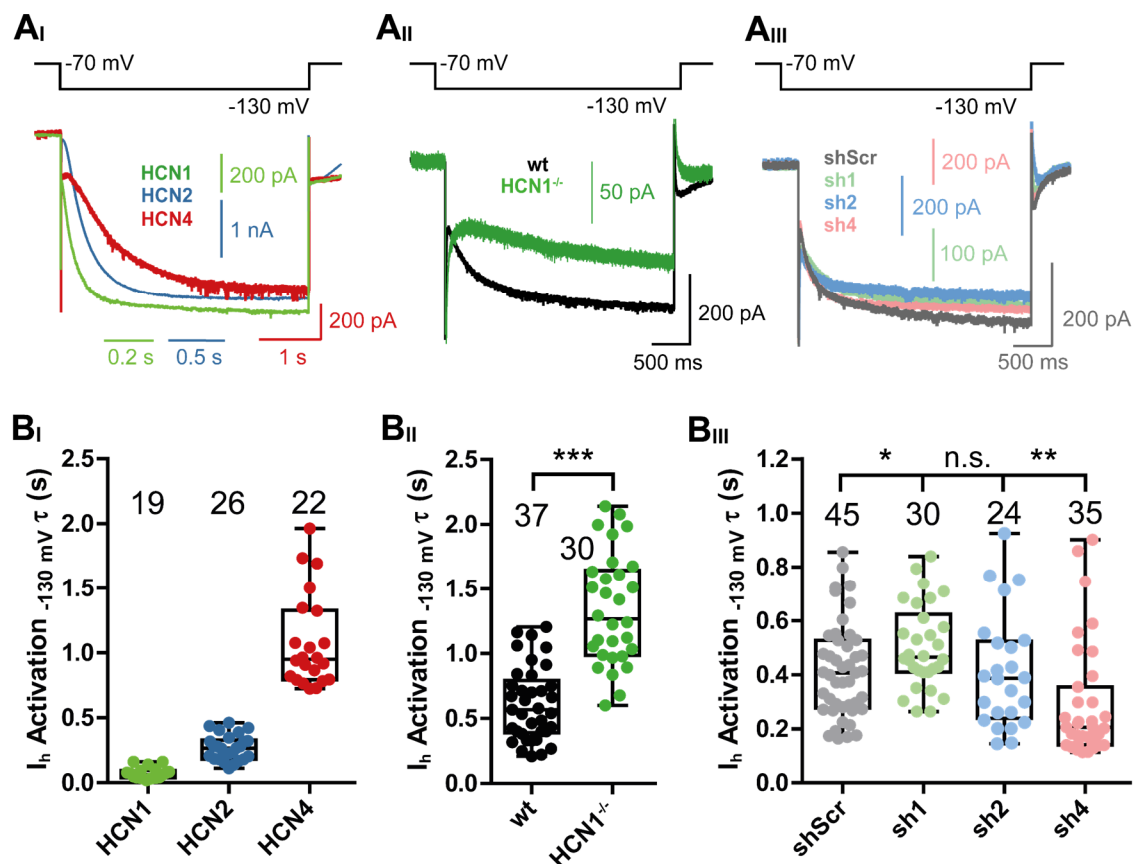


**Figure 3.14: Effects of HCN channel knock-out and knock-down on activation kinetics of isolated  $I_h$ -currents in HEK293 cell-lines and primary hippocampal neurons**

(A) Representative voltage stimulation protocols and corresponding current traces of whole-cell patch-clamp recordings derived from (AI) HEK293 cell-lines constitutively expressing HCN channel subunit 1 (HCN1), HCN channel subunit 2 (HCN2), or HCN channel subunit 4 (HCN4); (AII) primary hippocampal neurons (PHNs) from wildtype (wt) and HCN1<sup>-/-</sup> mice, and (AIII) of PHNs treated with shScr (control), sh1 (HCN1 channel knock-down), sh2 (HCN2-channel knock-down), or sh4 (HCN4 channel knock-down) expressing rAAVs after 15 days *in vitro* (d.i.v.). (B) Activation time constants ( $\tau$ ) of (BI) HEK293 cell-lines expressing HCN1, HCN2 or HCN4, (BII) PHNs from wt and HCN1<sup>-/-</sup> mice, and of (BIII) rAAV9-

shScr, -sh1, -sh2, or -sh4 transduced eGFP-positive PHNs. Activation time constants were calculated by fitting the current response of a hyperpolarizing pulse (from -70 mV to -130 mV) to a mono-exponential function. Results are depicted as boxplots. Statistical significance was assessed using the unpaired two-tailed Student's t test, \* $p < 0.05$ , \*\* $p < 0.01$ , \*\*\* $p < 0.001$ .

Similar to the observed differences in activation potentials of HCN-channel subtypes (Fig. 3.8), also the activation kinetics differed among these subtypes (Fig. 3.14 AI and BI). While homomeric HCN1 channels activated relatively fast with a  $\tau$  value of  $0.072 \pm 0.044$  s, HCN2 and HCN4 homomeric channels activated slower with  $\tau$  values of  $0.27 \pm 0.097$  s and  $1.078 \pm 0.359$  s, respectively. This observation is in line with previous studies, describing differences in activation kinetics of HCN1, HCN2 and HCN4 (Biel et al., 2009). When the fast activating HCN1 subtype was absent in HCN1<sup>-/-</sup> neurons, I<sub>h</sub>-current activation was slowed down compared to native currents in wildtype neurons (HCN1<sup>-/-</sup>:  $1.341 \pm 0.428$  s; wt:  $0.612 \pm 0.284$  s) (Fig. 3.14 AII and BII). Again, this finding is in line with previous reports, demonstrating the strong contribution of HCN1 to the activation kinetics of native I<sub>h</sub>-currents in neurons (Kopp-Scheinflug et al., 2015). Similar to the effects in HCN1<sup>-/-</sup> neurons, I<sub>h</sub>-current activation was also slowed down in PHNs expressing sh1 shRNA. Compared to controls (shScr:  $0.416 \pm 0.176$  s),  $\tau$  in sh1 transduced neurons was  $0.503 \pm 0.156$  s (Fig. 3.14 AIII and BIII). Conversely, I<sub>h</sub>-current activation was accelerated in PHNs expressing sh4 ( $\tau$  value of  $0.289 \pm 0.212$  s) due to the loss of HCN4, which is known to activate slowly. A knock-down of the HCN2 subtype displaying intermediate activation kinetics, however, almost had no effect on I<sub>h</sub>-current activation ( $\tau$ :  $0.412 \pm 0.211$  s) compared to I<sub>h</sub>-currents of control neurons.

Because the I<sub>h</sub>-current is responsible for a prominent inward rectification in the voltage response to a steady hyperpolarizing current pulse called "sag" (Banks et al., 1993), sag half-widths were assessed to monitor effects of changes in HCN subtype expression on these voltage responses (Fig. 3.15).

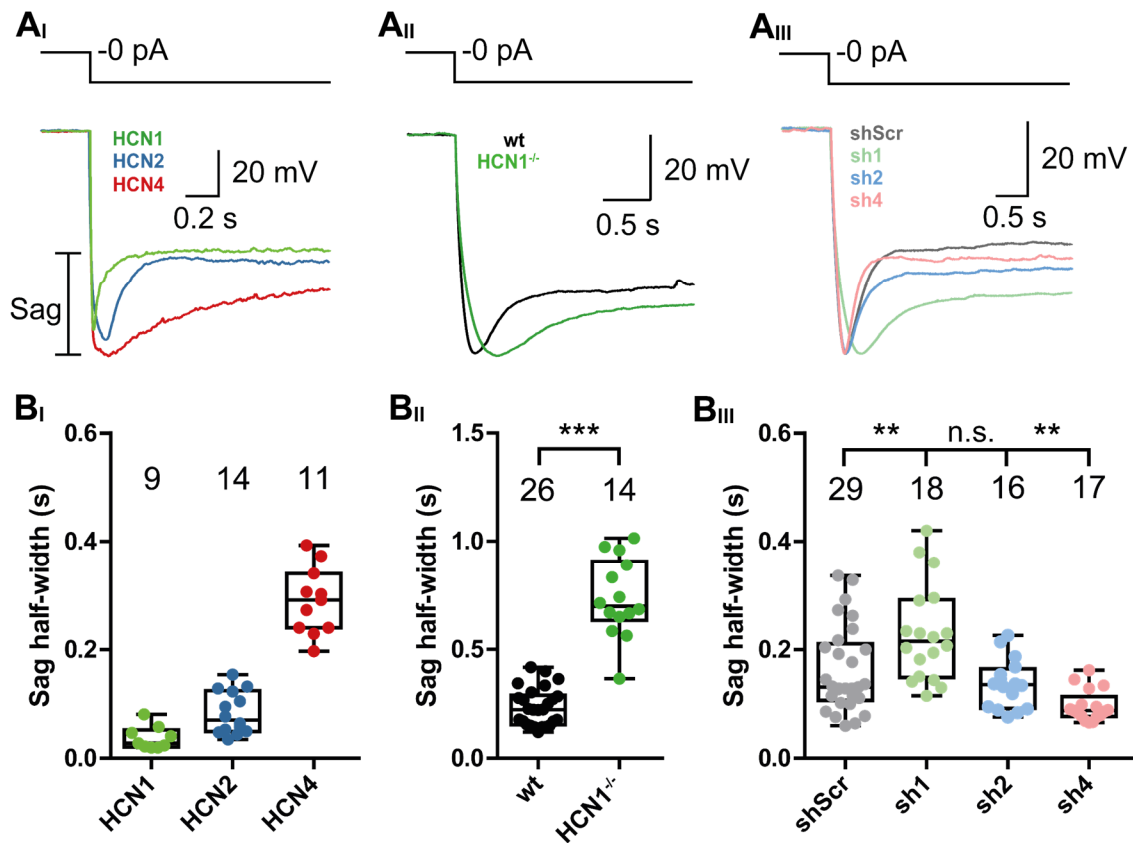


**Figure 3.15: Effects of HCN-channel knock-out and knock-down on the inward rectification (sag) of primary hippocampal neurons**

(A) Representative current stimulation and corresponding voltage traces of whole-cell patch-clamp recordings derived from (AI) HEK293 cell-lines constitutively expressing HCN channel subunit 1 (HCN1), HCN channel subunit 2 (HCN2), or HCN channel subunit 4 (HCN4); (AII) primary hippocampal neurons (PHNs) from wildtype (wt) and HCN1<sup>-/-</sup> mice, and (AIII) of PHNs treated with shScr (control), sh1 (HCN1 channel knock-down), sh2 (HCN2-channel knock-down), or sh4 (HCN4 channel knock-down) expressing rAAVs after 15 days *in vitro* (d.i.v.). (B) Sag half-widths of (BI) HEK293 cell-lines expressing HCN1, HCN2 or HCN4, (BII) PHNs from wt and HCN1<sup>-/-</sup> mice, and of (BIII) rAAV9-shScr, -sh1, -sh2, or -sh4 transduced eGFP-positive PHNs. Sag potentials were evoked by current pulses which hyperpolarize the membrane potential to -130 mV. Results are depicted as boxplots. Statistical significance was assessed using the unpaired two-tailed Student's t test, \*p<0.05, \*\*p<0.01, \*\*\*p<0.001.

Strikingly, sag half-widths recorded in HEK293 cells expressing HCN1, HCN2 or HCN4 homomeric channels were reminiscent of the differences in activation kinetics shown in figure 3.13 AI and BI. Sag potentials recorded in cells expressing HCN1 channels were faster (sag half width:  $0.038 \pm 0.021$  s) in comparison to cells expressing homomeric HCN2 (sag half width:  $0.083 \pm 0.039$  s) or HCN4 channels (sag half width:  $0.299 \pm 0.056$  s), respectively (Fig. 3.14 AI and BI). When the fast activating HCN1 subtype was absent in PHNs obtained from HCN1<sup>-/-</sup>-mice, the sag potential half-width increased compared to wildtype neurons (wt:  $0.235 \pm 0.086$  s; HCN1<sup>-/-</sup>:  $0.778 \pm 0.126$  s) (Fig. 3.15 AII and BII). Similar to the effect of HCN1 knock-out, the knock-down of

HCN1 by sh1 lead to increased sag potential half-widths compared to controls (sh1:  $0.229 \pm 0.038$  s; shScr:  $0.143 \pm 0.059$  s). Conversely, sag potential half-width decreased when HCN4 expression was reduced by sh4 expression ( $0.092 \pm 0.024$  s). Since a knock-down of the HCN2 subtype did not influence  $I_h$ -current activation, the sag potential half-width was not altered in neurons expressing sh2 ( $0.137 \pm 0.045$  s) as well. These results suggest, that a knock-out or knock-down of the fast activating HCN1 subtype in PHNs was responsible for a deceleration in  $I_h$ -current activation, accompanied by an increase in sag potential half-width. Conversely, a knock-down of the slow activating HCN4 subtype was causative for accelerating  $I_h$ -current activation, which was accompanied by a decrease in sag potential half-widths. However, a knock-down of the intermediate activating HCN2 subtype did neither cause a change in  $I_h$ -current activation nor in sag potential half-widths.

### ***3.2.6 Effects of HCN channel blocker ZD7288 on PHNs***

In a variety of studies it was shown that 4-Ethylphenylamino-1,2-dimethyl-6-methylaminopyrimidinium (ZD7288) specifically blocks HCN channels in various configurations (Harris and Constanti, 1995, Green et al., 1996, Gasparini and DiFrancesco, 1997). To analyze effects of ZD7288 on passive electrical properties and  $I_h$ -current-specific properties, wildtype PHNs were perfused with 100  $\mu$ M ZD7288 for at least 5 min prior to electrophysiological recordings (Fig. 3.16 A).

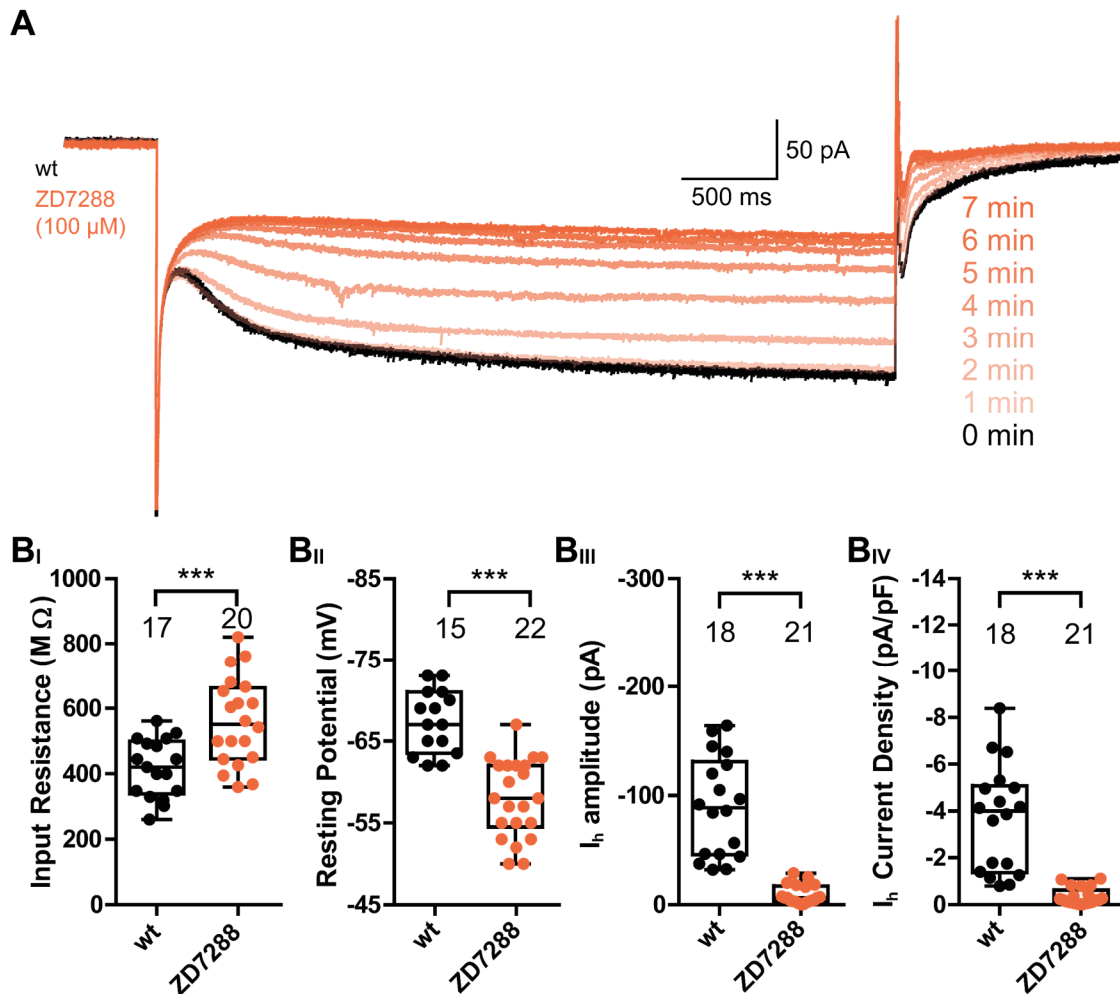


**Figure 3.16: Effects of the HCN channel blocker ZD7288 on HCN channel dependent properties of primary hippocampal neurons**

(A) Representative current traces of the current response to a hyperpolarizing pulse (from -70 mV to -130 mV) of whole-cell patch-clamp recordings obtained from primary hippocampal neurons (PHNs) treated with 100  $\mu$ M ZD7288. Current traces were measured at various timepoints after ZD7288 perfusion. (B) Results of whole-cell patch-clamp recordings from wildtype PHNs treated with 100  $\mu$ M ZD7288. (BI) Influence of ZD7288 on input resistances in PHNs. Input resistances were measured with a single 10 mV hyperpolarizing voltage pulse. (BII) Influence of ZD7288 on the resting membrane potential of PHNs. Resting membrane potentials were measured approx. 30 s after establishing whole-cell configuration or 5 min after ZD7288 perfusion, respectively. (BIII) Influence of ZD7288 on  $I_h$ -current amplitudes of PHNs. Current amplitudes were measured from the difference of the instantaneous current and the steady-state current to the current response of a hyperpolarizing pulse (from -70 mV to -130 mV). (BIV) Influence of ZD7288 on  $I_h$ -current densities of PHNs. Current densities were calculated by dividing the current amplitude by the corresponding membrane capacitance of the cell (Fig. 3.15 C). Results are depicted as boxplots. Statistical significance was assessed using the unpaired two-tailed Student's t-test, \*\*\* $p < 0.001$ .

In comparison to untreated wildtype control neurons, ZD7288 treated neurons showed an increase in input resistance (wt:  $417.2 \pm 88.61$  M $\Omega$ ; ZD7288:  $560.2 \pm 134.4$  M $\Omega$ ), similar to the increase observed in HCN1 knock-out or HCN1 knock-down neurons. Surprisingly, ZD7288 treated neurons had depolarized membrane potentials compared to untreated control neurons (wt:  $-67.37 \pm 3.83$  mV; ZD7288:  $-58.09 \pm 4.76$  mV). As reported

previously (Green et al., 1996), both, the  $I_h$ -current amplitude and density were strongly decreased by treating the neurons with ZD7288 (wt:  $-89.78 \pm 45.28$  pA /  $-3.67 \pm 2.27$  pA/pF; ZD7288:  $-8.92 \pm 8.52$  pA /  $-0.35 \pm 0.36$  pA/pF).

To analyze effects of  $I_h$ -currents on action potential (AP) properties of PHNs, neurons were treated with  $100 \mu\text{M}$  ZD7288 and clamped to  $-70$  mV. Initial APs were evoked by injecting depolarizing currents in  $10$  pA increments until AP threshold was reached (Fig. 3.17).

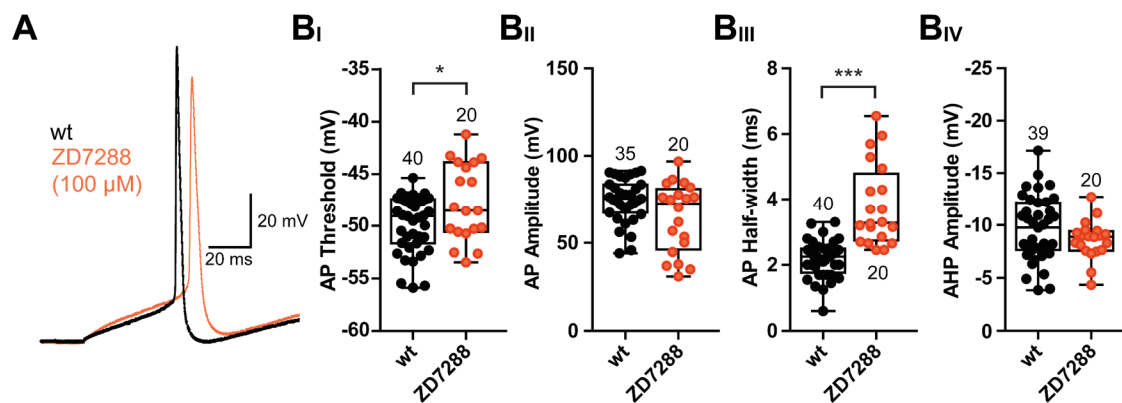


**Figure 3.17: Effects of the HCN channel blocker ZD7288 on action potential properties of primary hippocampal neurons**

(A) Representative voltage traces showing initial action potentials (APs) of whole-cell patch-clamp recordings derived from wildtype (wt) PHNs and PHNs treated with  $100 \mu\text{M}$  ZD7288. The initial APs were evoked by injecting depolarizing currents in  $10$  pA increments until threshold was reached. (B\_I) Influence of ZD7288 on the AP threshold, (B\_II) on the AP amplitude, (B\_III) on the AP half-width, and (B\_IV) on the after-hyperpolarization (AHP) of the AP in PHNs. Results are depicted as boxplots. Statistical significance was assessed using the unpaired two-tailed Student's t-test, \* $p < 0.05$ , \*\*\* $p < 0.001$ .

Application of  $100 \mu\text{M}$  ZD7288 shifted the AP activation threshold to more depolarized potentials compared to APs of wildtype neurons (wt:  $-49.78 \pm 2.69$  mV; ZD7288:  $-47.77 \pm 0.37$  mV). While the application of ZD7288 did not change AP amplitudes (wt:  $73.41 \pm 14.49$  mV; ZD7288:  $64.63 \pm 20.0$  mV), AP half-widths were strongly increased upon application of  $100 \mu\text{M}$  ZD7288 (wt:  $2.175 \pm 0.543$  ms; ZD7288:  $3.81 \pm 1.257$  ms). However, ZD7288 had no effect on the amplitude of the afterhyperpolarization, which occurs after an AP (wt:  $9.623 \pm 3.064$  mV; ZD7288:  $8.589 \pm 1.803$  mV).

Because the effects of ZD7288 on the resting membrane potential were in contrast to what was expected from analysis of  $\text{HCN1}^{-/-}$  animals and HCN1 knock-down experiments shown before (Fig. 3.12), inward and outward currents of PHNs were analyzed (Fig. 3.18).

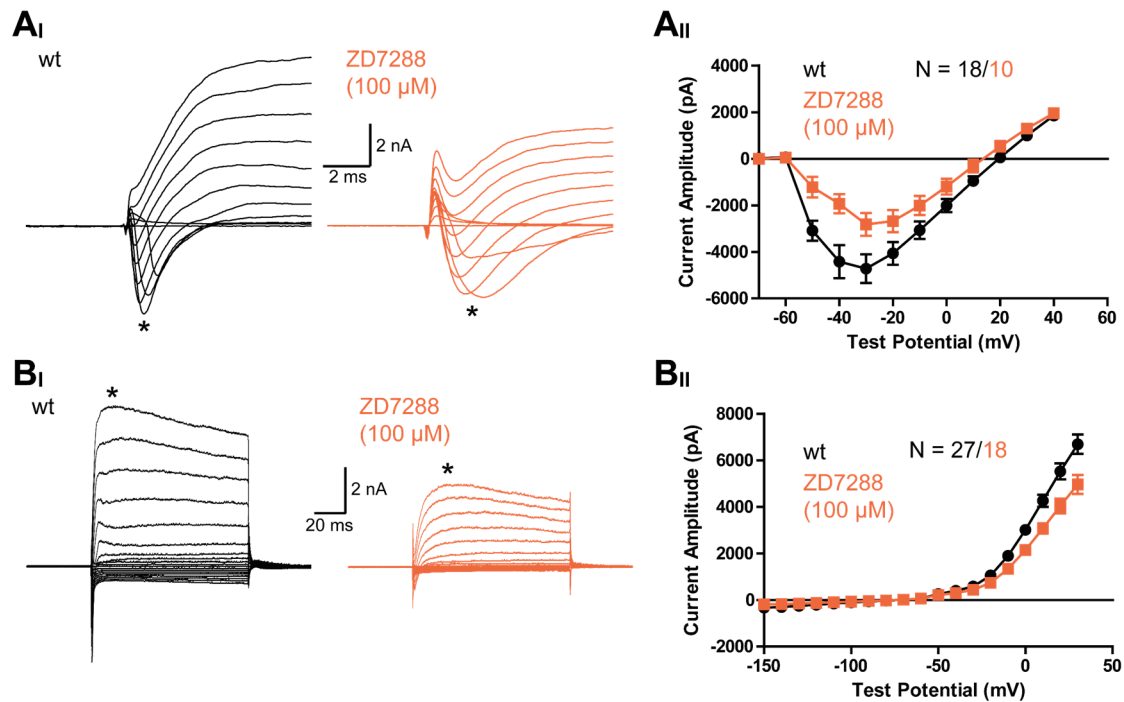


**Figure 3.18: Effects of the HCN channel blocker ZD7288 on inward and outward currents of primary hippocampal neurons**

(A<sub>I</sub>) Representative current traces of whole-cell patch-clamp recordings showing inward currents of wildtype (wt) PHNs and PHNs treated with 100 μM ZD7288. (A<sub>II</sub>) Current-voltage relationships recorded from wt PHNs and PHNs treated with 100 μM ZD7288. Current amplitudes were obtained from the instantaneous inward current indicated with the asterisks. (B<sub>I</sub>) Representative current traces of whole-cell patch-clamp recordings showing inward and outward currents of wildtype (wt) PHNs and PHNs treated with 100 μM ZD7288. (B<sub>II</sub>) Current-voltage relationships recorded from wt PHNs and PHNs treated with 100 μM ZD7288. Current amplitudes were obtained from the instantaneous outward current indicated with the asterisks.

Surprisingly, in addition to the blocking effect on  $I_h$ -currents, the application of 100 μM ZD7288 had a strong blocking effect on PHN inward currents (Fig. 3.18 A) and a strong blocking effect on PHN outward currents (Fig. 3.18 B). Previous studies already reported that ZD7288 can inhibit calcium channels (Felix et al., 2003, Sanchez-Alonso et al., 2008) and even sodium channels with high sensitivity (Wu et al., 2012). However, until now there was no report of blocking effects of ZD7288 on potassium currents, which might explain the reduction in outward currents observed in PHNs treated with ZD7288. Nonetheless, interpretations of HCN channel related properties based on experiments incorporating ZD7288 should be taken with care, since potential side-effects cannot be ruled out.

### 3.2.7 Consequences of HCN2-channel knock-down for neuronal signaling

Since the HCN2-channel subtype showed the highest transcript expression levels in wildtype PHNs (Fig. 3.9), action potential properties of PHNs with a reduced expression of the HCN2 isoform were analyzed (Fig. 3.19 A).

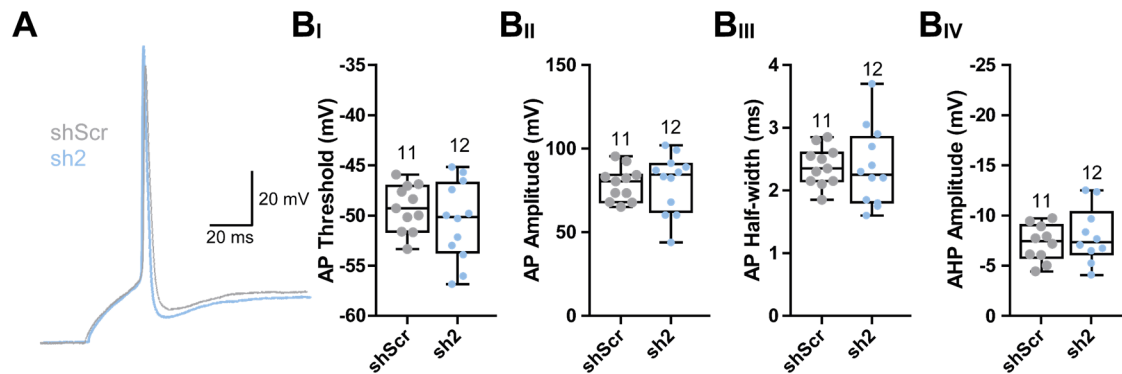


**Figure 3.19: Effects of HCN2-channel knock-down on action potential properties of primary hippocampal neurons**

(A) Representative voltage traces showing initial action potentials (APs) of whole-cell patch-clamp recordings derived from PHNs treated with shScr (control) or sh2 (HCN2-channel knock-down) encoding rAAV9. The initial APs were evoked by injecting depolarizing currents in 10 pA increments until threshold was reached. (B\_I) Influence of HCN2-isoform knock-down on the AP threshold, (B\_II) on the AP amplitude, (B\_III) on the AP half-width, and (B\_IV) on the after-hyperpolarization (AHP) of the AP in PHNs. Results are depicted as boxplots. Statistical significance was assessed using the unpaired two-tailed Student's t-test.

In contrast to the effects observed upon treatment of PHNs with ZD7288, the knock-down of HCN2 had no effect on AP properties in comparison to APs of shScr control-treated neurons. There was neither a difference in AP threshold (shScr:  $-49.27 \pm 2.34$  mV; sh2:  $-50.57 \pm 3.92$  mV), nor in AP amplitude (shScr:  $78.77 \pm 10.04$  mV; sh2:  $79.42 \pm 17.54$  mV), in AP half-width (shScr:  $23.82 \pm 3.10$  ms; sh2:  $23.71 \pm 6.22$  ms) or in AHP amplitude (shScr:  $-7.27 \pm 1.82$  mV; sh2:  $-8.02 \pm 2.79$  mV) (Fi. 3.19 B).

Because HCN channels are known to conduct calcium ions and thereby actively participate in calcium signaling (Yu et al., 2004), calcium-imaging experiments were performed using the genetically-encoded calcium indicator GCaMP6f (Chen et al., 2013).

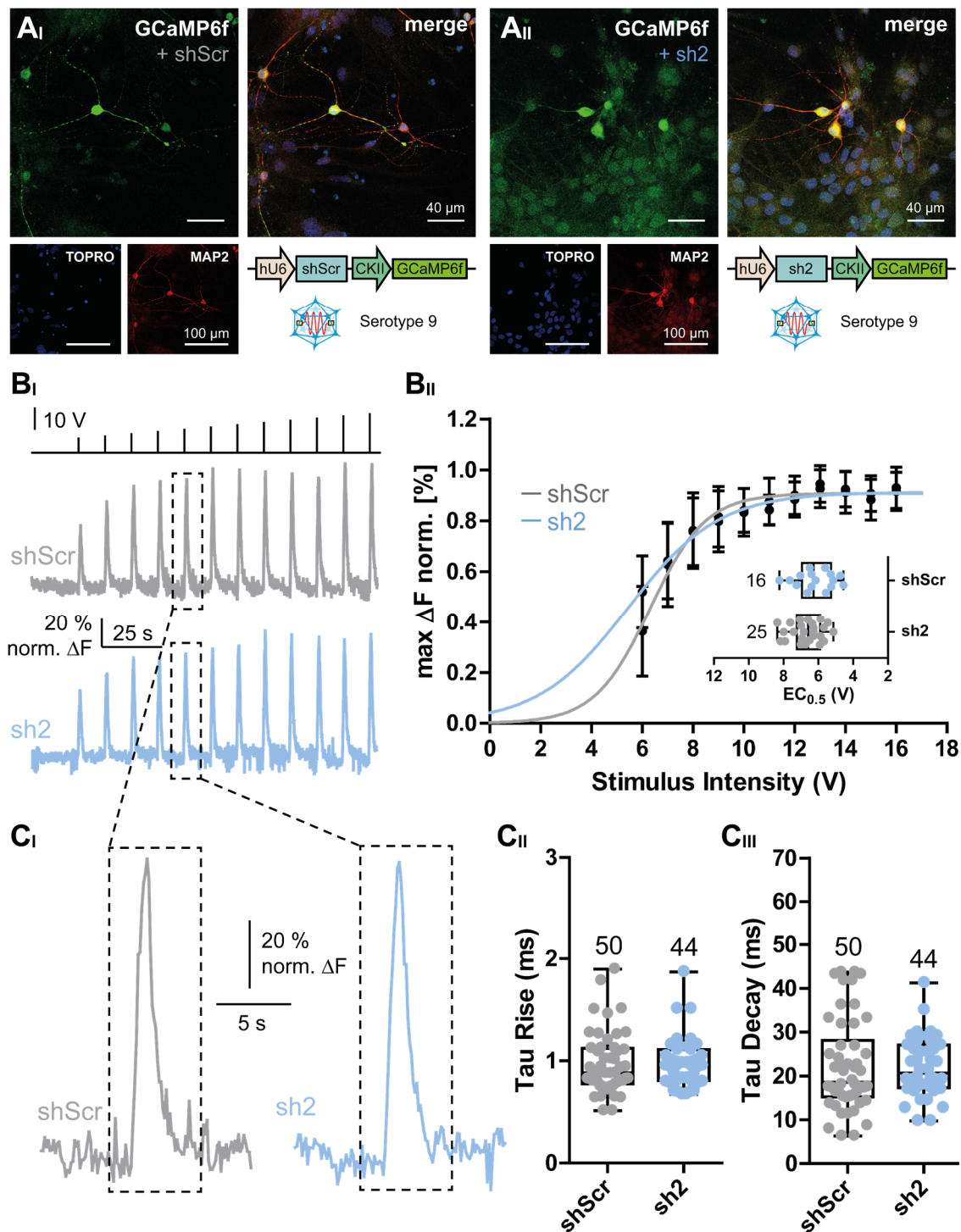


**Figure 3.20: Effects of HCN2-channel knock-down on intracellular calcium responses of primary hippocampal neurons**

(A) Representative immunofluorescent images of wildtype primary hippocampal neurons (PHNs) transduced with rAAV9 encoding GCaMP6f and shScr (A<sub>I</sub>) or GCaMP6f and sh2 (A<sub>II</sub>). GCaMP6f was labeled using an anti-GFP antibody and neurons were stained using a microtubule-associated protein 2 (MAP2) antibody. Primary antibodies were combined with fluorescently labeled secondary antibodies (GFP green; MAP2 red). Nuclei were labeled with TOPRO (blue). Cartoons of the AAV-delivered constructs are displayed below the merged immunofluorescent images. (B<sub>I</sub>) Stimulation protocol and representative fluorescent responses of GCaMP6f in PHNs either transduced with GCaMP6f+shScr or GCaMP6f+sh2 virions. (B<sub>II</sub>) Stimulus intensity was plotted against the normalized fluorescence change. The continuous lines represent fitted Boltzmann functions of the data. Half-maximal activation voltages

were calculated from the fitted Boltzmann functions. (CI) Enlargements showing fluorescence response of PHNs transduced with GCaMP6f+shScr or GCaMP6f+sh2 virions to a stimulus intensity of 10 V for 200 ms. (CII) The rising phase of the fluorescence responses were fitted by an exponential growth equation to determine the rise time, while the decay phase (CIII) was fitted by a one phase decay equation to determine the decay time. Results are depicted as boxplots. Statistical significance was assessed using the unpaired two-tailed Student's t test.

In order to express GCaMP6f in control neurons and HCN2 knock-down neurons, rAAV9 virions were generated expressing GCaMP6f under control of the neuron specific CKII promoter and additionally shScr or sh2 under control of the hU6 promoter (Schilling, 2019). Neurons transduced with shScr-GCaMP6f or sh2-GCaMP6f (Fig. 3.20 A) were stimulated with voltage pulses of varying intensities to evoke changes in the intracellular calcium concentration. By measuring the change in fluorescence intensity of GCaMP6f, which is a result of calcium binding to the calcium-binding domains of calmodulin, calcium influx into the cytoplasm was visualized. Comparison of calcium signals from control neurons (shScr) and HCN2 knock-down neurons (sh2) showed that a knock-down of HCN2 had no influence on the responsiveness of the cells to increasing stimulus intensities (Fig. 3.20 B). No differences were detectable when comparing  $EC_{50}$  values of control and HCN2 knock-down neurons (shScr:  $6.69 \pm 0.88$  V; sh2:  $6.16 \pm 1.06$  V), obtained by fitting the fluorescence changes of GCaMP6f to increasing stimulus intensities to Boltzmann functions. In addition, neither the rise time (shScr:  $0.97 \pm 0.29$  ms; sh2:  $0.98 \pm 0.24$  ms) obtained by fitting the rising phase of a calcium signal to a stimulus of 10 V for 200 ms, nor the decay time (shScr:  $22.43 \pm 10.54$  ms; sh2:  $22.18 \pm 6.63$  ms) obtained by fitting the decay phase of the same signal, varied between the two groups (Fig. 3.20 C).

To examine the consequences of HCN2-isoform knock-down on neuronal transmission, excitatory synaptic currents were recorded in control neurons and HCN2 knock-down neurons. For measuring spontaneous excitatory postsynaptic currents (sEPSCs) neurons were clamped to -70 mV and EPSCs were recorded in the presence of the GABA<sub>A</sub> receptor blocker Bicuculline (25  $\mu$ M) (Fig. 3.21).

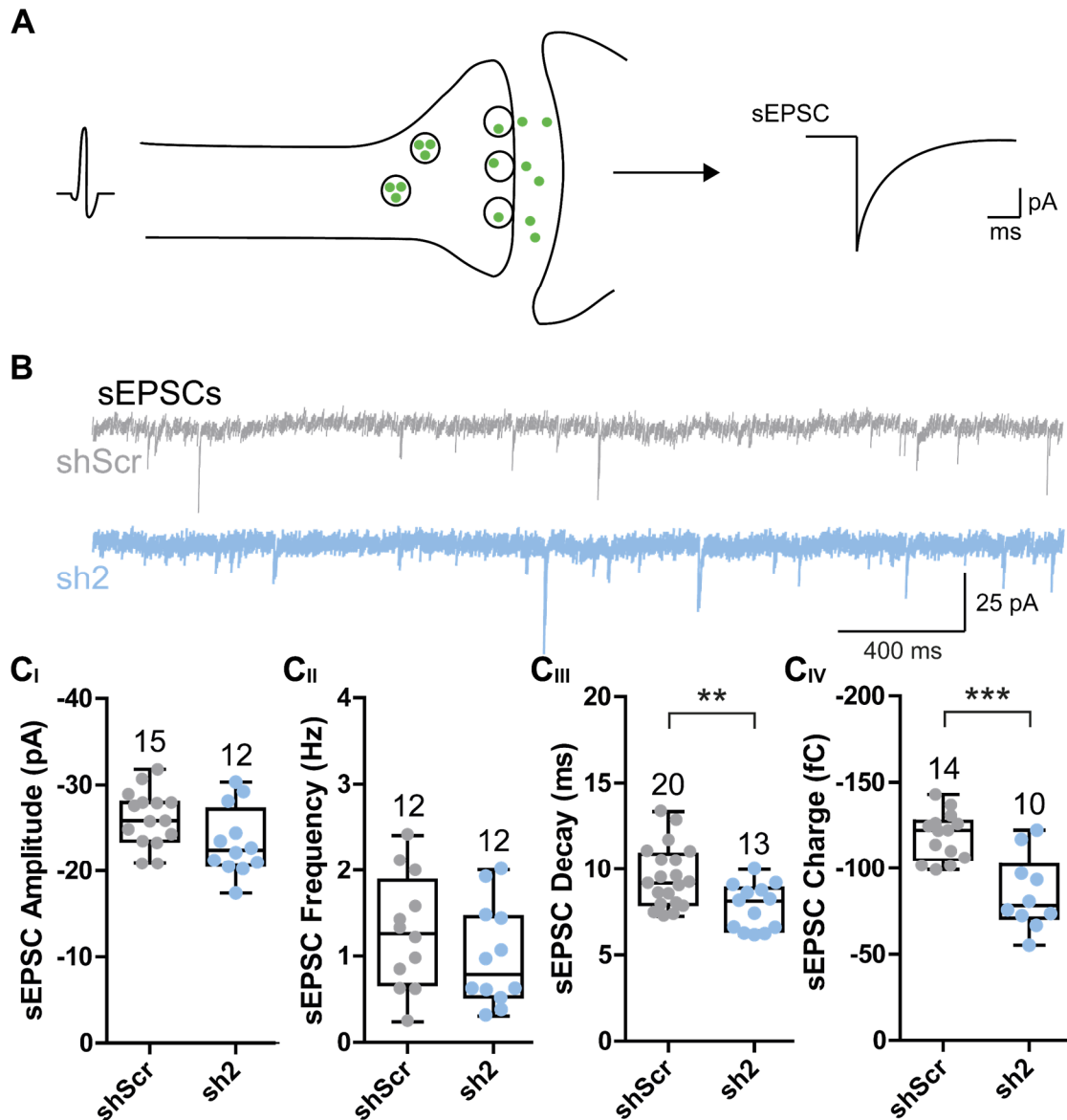


**Figure 3.21: Effects of HCN2-channel knock-down on sEPSCs of primary hippocampal neurons**

(A) Schematic showing spontaneous and action potential induced release of neurotransmitters, evoking spontaneous excitatory postsynaptic currents (sEPSCs). (B) Representative current traces showing sEPSCs in primary hippocampal neurons (PHNs) treated with shScr (control) or sh2 (HCN2-channel knock-down) encoding rAAV9. (C) Influence of HCN2-channel knock-down on (CI) sEPSC amplitude, (CII) sEPSC frequency, (CIII) sEPSC decay time, calculated by fitting the decay phase by a mono-exponential decay equation, and (CIV) on sEPSC charge, calculated by the integral of the synaptic events. Data are depicted as boxplots. Statistical significance was assessed using the unpaired two-tailed Student's t test, \*\* $p < 0.01$ , \*\*\* $p < 0.001$ .

While the knock-down of HCN2 did not affect parameters which might point to a presynaptic role of HCN channels, e.g., sEPSC amplitude (shScr:  $-26.16 \pm 3.25$  pA; sh2:  $-23.42 \pm 3.96$  pA) or sEPSC frequency (shScr:  $1.29 \pm 0.66$  Hz; sh2:  $1.0 \pm 0.59$  Hz), it affected sEPSC decay time (shScr:  $9.56 \pm 1.8$  ms; sh2:  $7.81 \pm 1.32$  ms) and consequently also sEPSC charge transfer (shScr:  $-119.0 \pm 13.78$  fC; sh2:  $-85.47 \pm 21.74$  mV),

suggesting a postsynaptic role of HCN channels. This indicated, that a loss of HCN2 channels might change the dendritic integration processes without affecting presynaptic mechanisms.

In order to eliminate spontaneous activity emerging from the network, action potentials were blocked by application of 2  $\mu\text{M}$  tetrodotoxin (TTX) in addition to the GABA<sub>A</sub> receptor blocker Bicuculline (25  $\mu\text{M}$ ). Neurons were clamped to -70 mV and miniature EPSCs (mEPSCs) were measured, induced by the probabilistic spontaneous release of neurotransmitters from the presynapse (Fig. 3.22).

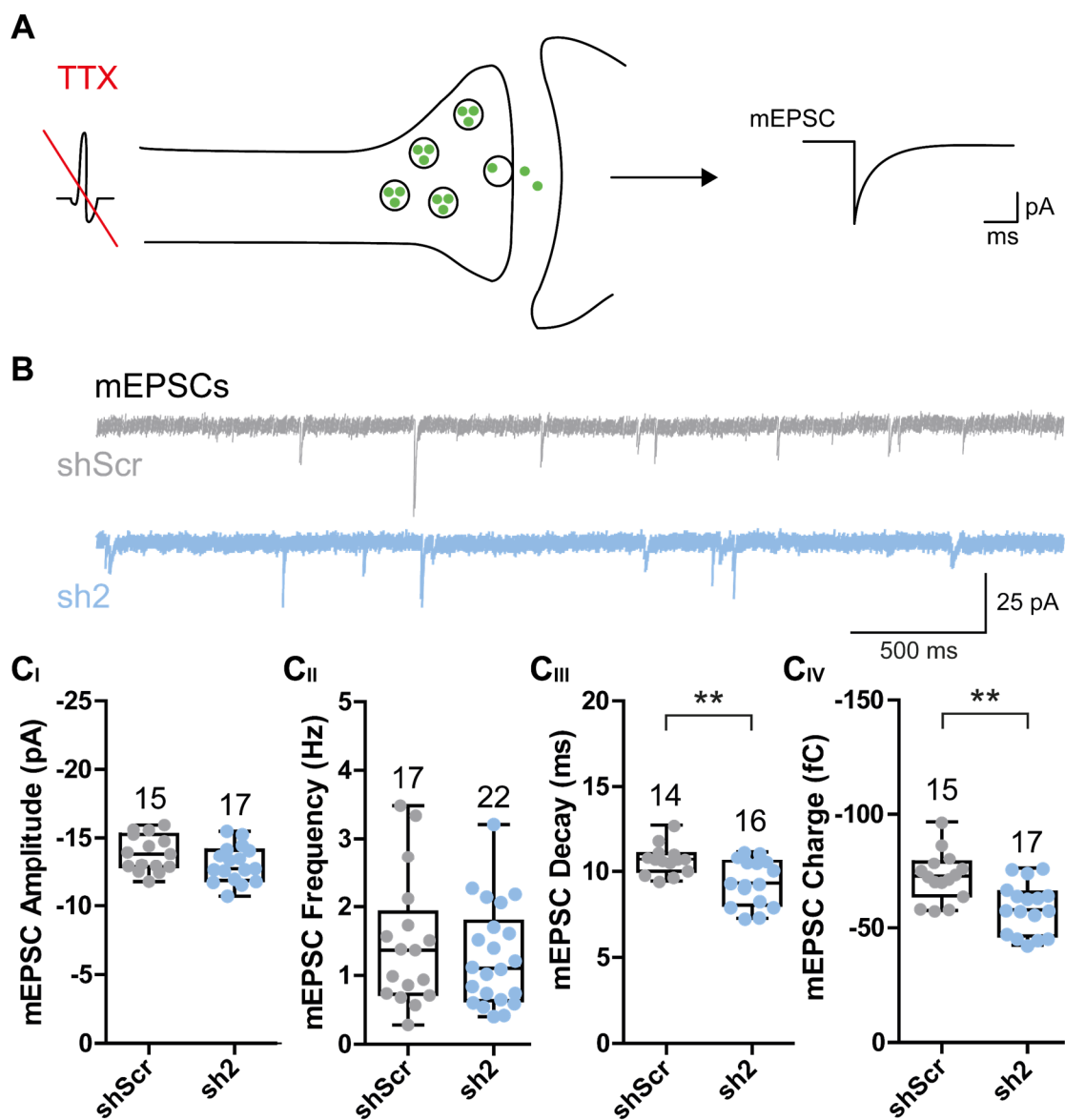


**Figure 3.22: Effects of HCN2-channel knock-down on mEPSCs of primary hippocampal neurons**

(A) Schematic showing action potential independent release of presynaptic neurotransmitters resulting in miniature excitatory postsynaptic currents (mEPSCs). (B) Representative current traces showing mEPSCs

in primary hippocampal neurons (PHNs) treated with shScr (control) or sh2 (HCN2-channel knock-down) encoding rAAV9. (C) Influence of HCN2-channel knock-down on (CI) mEPSC amplitude, (CII) mEPSC frequency, (CIII) mEPSC decay time, calculated by fitting the decay phase by a mono-exponential decay equation, and (CIV) on mEPSC charge, calculated by the integral of the synaptic events. Data are depicted as boxplots. Statistical significance was assessed using the unpaired two-tailed Student's t test, \*\* $p < 0.01$ .

As action potential properties of control PHNs were not altered compared to HCN2 knock-down PHNs (Fig. 3.19), it was not surprising that a loss of HCN2 channels induced similar effects on mEPSCs as previously described for sEPSCs. Thus, the knock-down of HCN2 did not affect mEPSC amplitude (shScr:  $-13.84 \pm 1.35$  pA; sh2:  $-13.06 \pm 1.35$  pA) or mEPSC frequency (shScr:  $0.96 \pm 0.66$  Hz; sh2:  $0.72 \pm 0.44$  Hz). But the knock-down affected mEPSC decay time (shScr:  $10.68 \pm 0.87$  ms; sh2:  $9.37 \pm 1.35$  ms) and consequently also mEPSC charge transfer (shScr:  $-72.28 \pm 10.76$  fC; sh2:  $-58.53 \pm 11.0$  fC). Again, this indicates a role of the HCN2 channel isoform in dendritic integration processes of PHNs.

To test whether the knock-down of HCN2 also affects evoked synaptic responses, (eEPSCs) postsynaptic currents were recorded after local extracellular stimulation using a concentric bipolar electrode. Neurons were clamped to a holding potential of  $-70$  mV and synaptic responses were recorded upon electrical stimulation in the presence of GABA<sub>A</sub> receptor blocker Bicuculline ( $25 \mu\text{M}$ ) (Fig. 3.23).

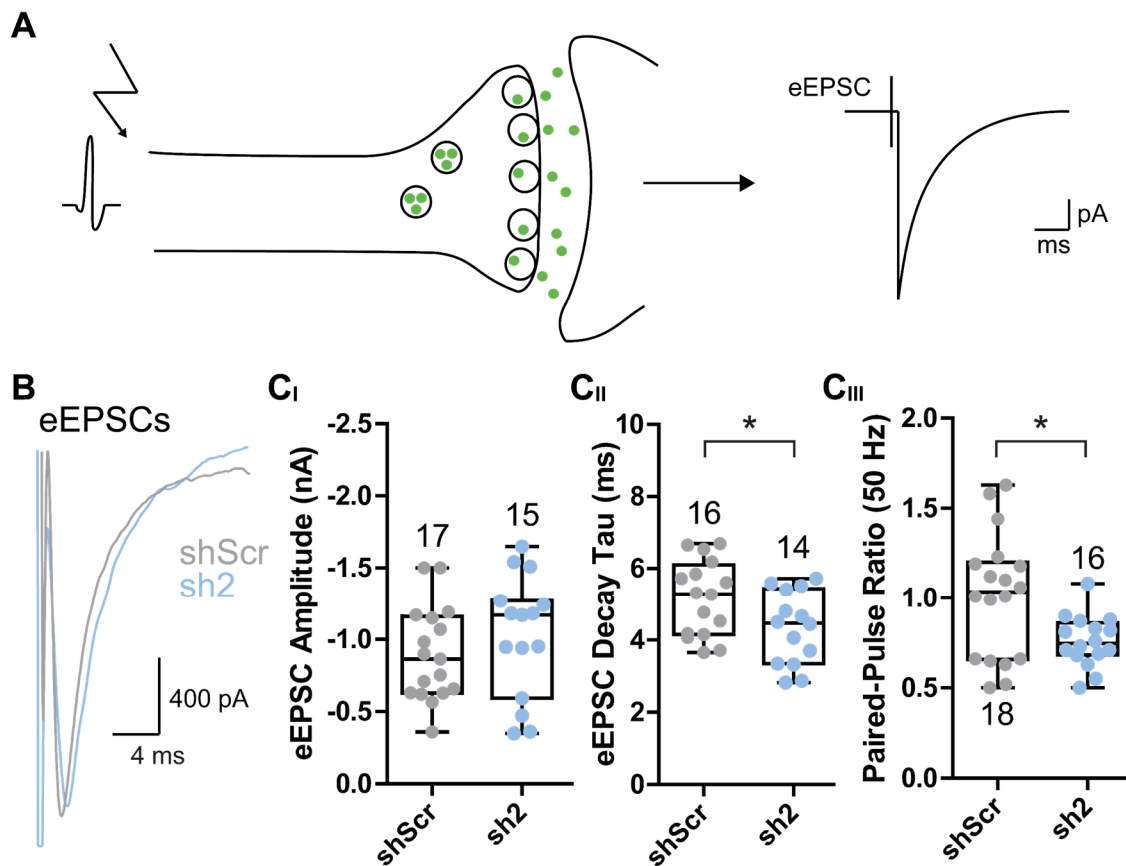


**Figure 3.23: Effects of HCN2-channel knock-down on eEPSCs of primary hippocampal neurons**

(A) Schematic showing stimulated release of presynaptic neurotransmitters evoking excitatory postsynaptic currents (eEPSCs). (B) Representative current traces showing eEPSCs in primary hippocampal neurons (PHNs) treated with shScr (control) or sh2 (HCN2-channel knock-down) encoding rAAV9. (C) Influence of HCN2-channel knock-down on (CI) eEPSC amplitude, (CII) eEPSC decay time, calculated by fitting the decay phase by a mono-exponential decay equation, and (CIII) paired-pulse ratio, evoked with an inter-pulse-interval of 20 ms. Data are depicted as boxplots. Statistical significance was assessed using the unpaired two-tailed Student's t test, \* $p < 0.05$ .

In agreement with the previous results of HCN2-channel knock-down, sh2-treated PHNs showed no changes in the amplitudes of evoked EPSCs (eEPSCs) compared to shScr-treated PHNs (shScr:  $-0.90 \pm 0.33$  nA; sh2:  $-1.02 \pm 0.42$  nA). Furthermore, the knock-down of HCN2 induced a decrease in the decay time constant (shScr:  $5.18 \pm 1.05$  ms; sh2:  $4.34 \pm 1.01$  ms), and additionally induced a depression of the paired-pulse ratio with an inter-pulse interval of 20 ms (shScr:  $1.01 \pm 0.35$  PPR; sh2:  $0.76 \pm 0.14$  PPR). Taken together, these results suggest, that a knock-down of HCN2 most likely influenced the dendritic integration properties of excitatory synaptic inputs of PHNs.

---

The results of the electrophysiological experiments showed that the isoform-specific knock-down by rAAV9-mediated RNAi was capable to induce subtype-specific changes in  $I_h$ -current properties.

The unspecific effects of ZD7288 on additional ion channels indicate, that a knock-out or knock-down of individual HCN channel isoforms is a more reliable strategy to investigate HCN-channel properties in neurons.

However, while the knock-down of the HCN2 channel isoform did not change action potential properties or calcium responses, it altered dendritic integration properties of excitatory synaptic inputs in PHNs.

---

### 3.3 *In vivo* HCN2-channel knock-down by stereotaxic intrahippocampal rAAV injections

#### *injections*

To investigate consequences of a loss of the HCN2 channel isoform on animal behavior, C57BL/6J mice (8 weeks old) were injected with rAAV9 virions encoding shScr (control) or sh2 (HCN2 knock-down) constructs (Fig. 3.24 A). The spatially restricted delivery of the virions was achieved by bilateral stereotaxic injections targeting the dorsal part of the hippocampus (Fig. 3.24 B). Behavioral experiments were chosen to cover some of the most important functions of the hippocampal formation in controlling murine behavior.

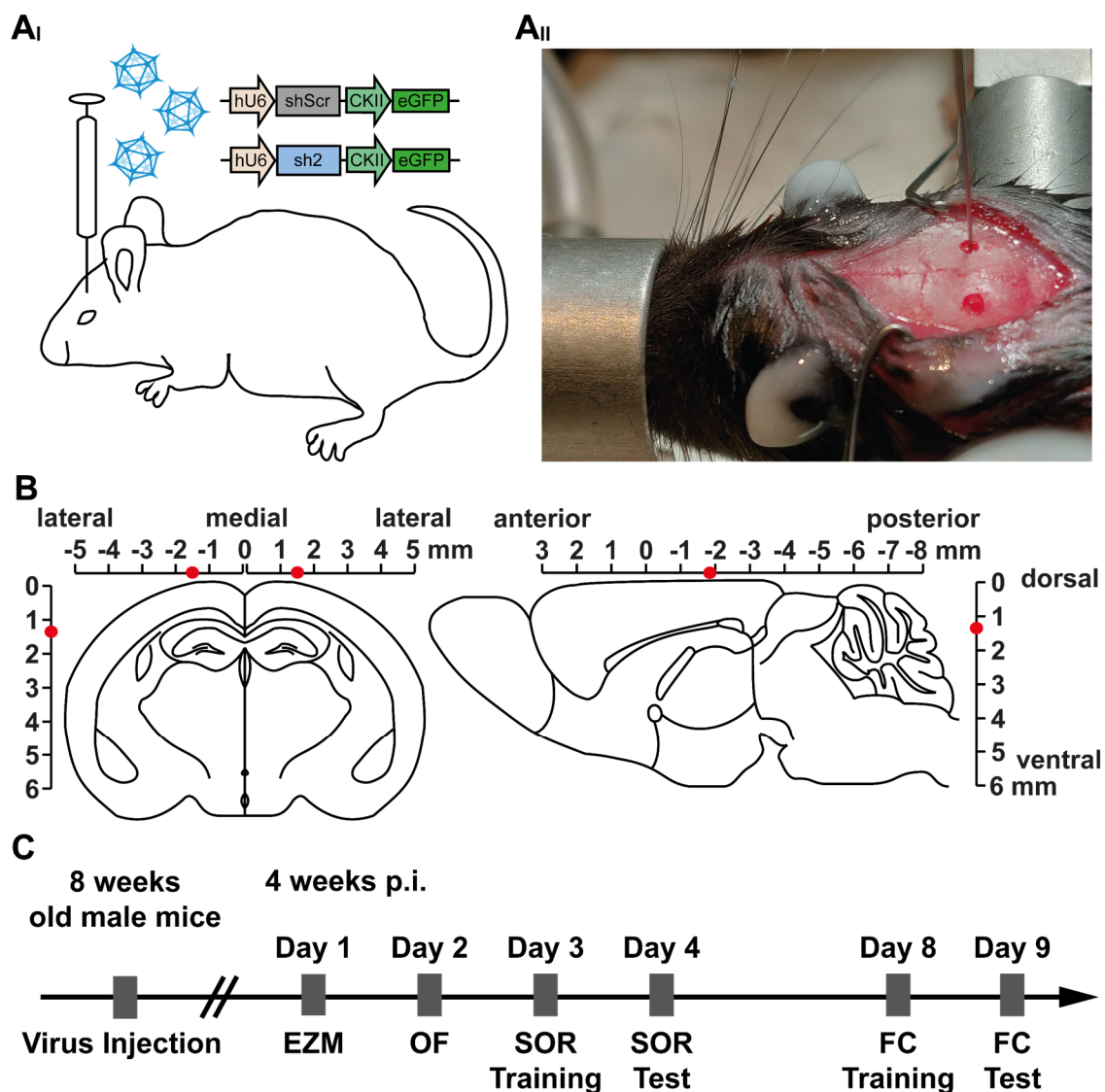


**Figure 3.24: Stereotaxic injection of rAAVs into the hippocampal formation and timeline of behavioral experiments**

(A<sub>I</sub>) Schematic showing bilateral injections of rAAV9 virions coding for shScr or sh2 into the brain of living mice. Cartoons of the AAV-delivered constructs are displayed. (A<sub>II</sub>) Picture showing the mounted head of a subject. The skin was removed and two bilateral holes were drilled according to positions

determined via the bregma into the cranium to facilitate access for the Nanofil injection needle. (B) Stereotaxic coordinates for injection of rAAVs into the mouse hippocampus. The coordinates for injecting into 8 weeks old, male C57BL/6J mice were: -1.9 mm anteroposterior (AP),  $\pm 1.5$  mm mediolateral (ML), and -1.4 mm dorsoventral (DV) relative to the bregma. (C) Timeline of stereotaxic injections and behavioral experiments. After surgery, mice recovered for 4 weeks, before the elevated zero maze (EZM) test was performed. On three consecutive days after the EZM, the open field (OF) test, and spatial object recognition (SOR) training and test sessions were performed. 7 days after the EZM, fear conditioning (FC) training sessions, and 8 days after the EZM, FC test sessions were performed.

### ***3.3.1 Analysis of behavioral changes upon stereotaxic intrahippocampal rAAV***

#### ***injections***

Since the hippocampal-hypothalamic circuit is known to influence innate anxiety behavior (Jimenez et al., 2018), the elevated zero maze (EZM) was used to test for anxiety-related behavioral changes upon HCN2-channel knock-down. During the EZM test, mice were placed onto an elevated arena. The apparatus consisted of a circular boardwalk which contained two non-enclosed, thus open quadrants and two wall-enclosed, thus closed quadrants (Fig. 3.25 A). Usually, mice prefer closed areas over open areas, while their innate curiosity prompts at least partial exploration of the open areas. The EZM test allows analyzing the interplay of these two behaviors by scoring the time spent in open and closed quadrants. Additionally, the overall activity can be quantified by measuring the total distance traveled, the velocity of movement, and the total number of crossings between both areas.

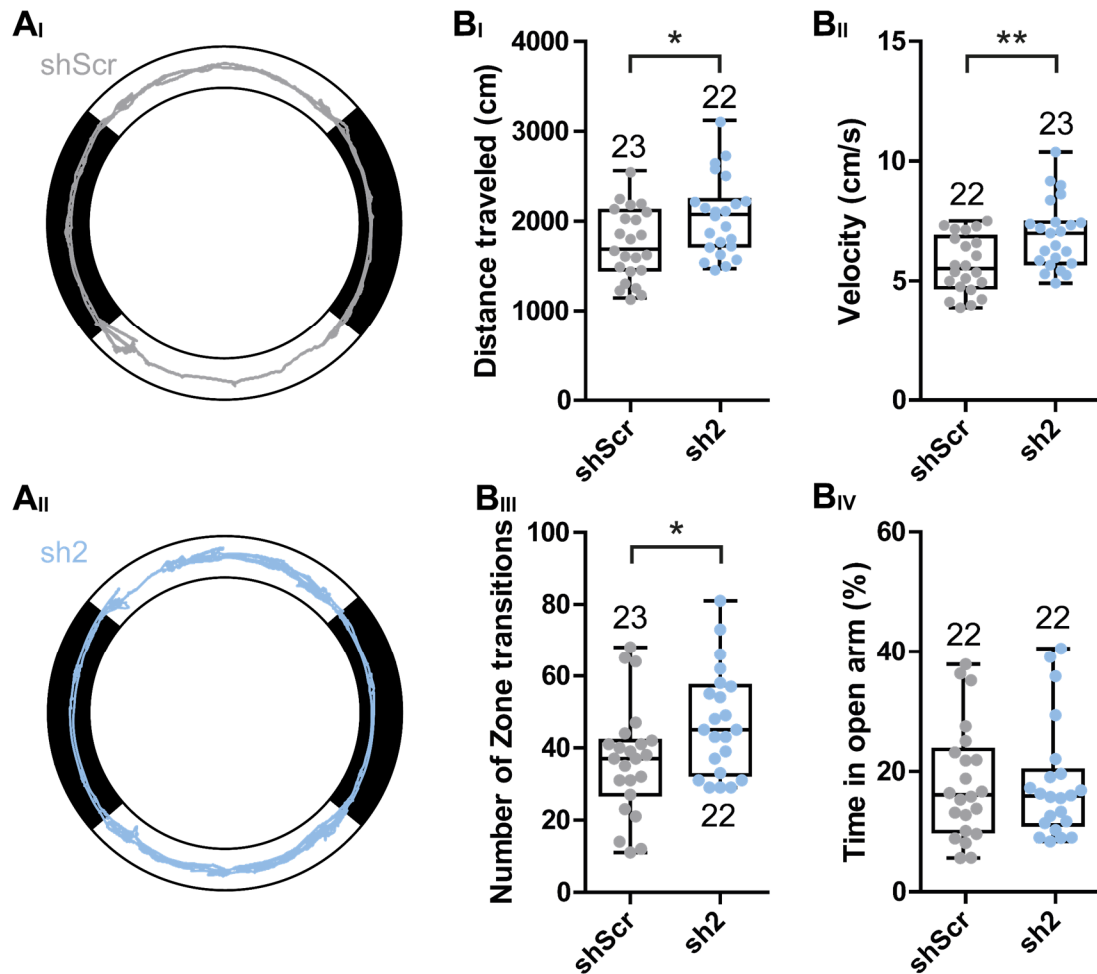


**Figure 3.25: Analysis of elevated zero maze test (EZM)**

(A) Schematic showing the elevated zero maze (EZM) arena and tracks of mice bilaterally injected with rAAV9-shScr (grey) (AI) or rAAV9-sh2 (blue) (AII). The white areas represent the open quadrants of the maze, while the black areas represent the closed quadrants of the maze. (B) Animals were placed for 5 min in the EZM arena and were scored for (BI) distance traveled, (BII) velocity of movement, (BIII) number of zone transitions between open quadrants and closed quadrants of the maze, and (BIV) time spent in the open arm of the maze. Data are depicted as boxplots. Statistical significance was assessed using the unpaired two-tailed Student's t test, \* $p < 0.05$ ; \*\* $p < 0.01$ .

The analysis of the EZM test (Fig.3.25 B) indicated, that mice injected with sh2-expressing virions showed an increase in the distance traveled (shScr:  $1737 \pm 396.2$  cm; sh2:  $2048 \pm 439.0$  cm), in the velocity of movement (shScr:  $5.8 \pm 1.2$  cm/s; sh2:  $6.9 \pm 1.4$  cm/s), and in the number of crossings between open and closed quadrants (shScr:  $36.5 \pm 15.3$ ; sh2:  $47.1 \pm 14.9$ ). Notably, the treatment did not influence the time animals spent in the open arms (shScr:  $18.2 \pm 9.6$  %; sh2:  $18.1 \pm 9.7$  %).

In addition to the EZM test, the open field (OF) test was used to monitor the basal exploratory behavior upon HCN2-channel knock-down. During the OF test, mice freely explored a rectangular enclosed arena (Fig. 3.26 A). Similar to the EZM test, mice prefer the peripheral areas over the central area, while their innate curiosity prompts at least

partial exploration of the central area. This allows analyzing the interplay of these two behaviors by scoring the time spent in peripheral and central areas. Additionally, the overall activity was analyzed by measuring the total distance traveled, the velocity of movement and the number of zone transitions.

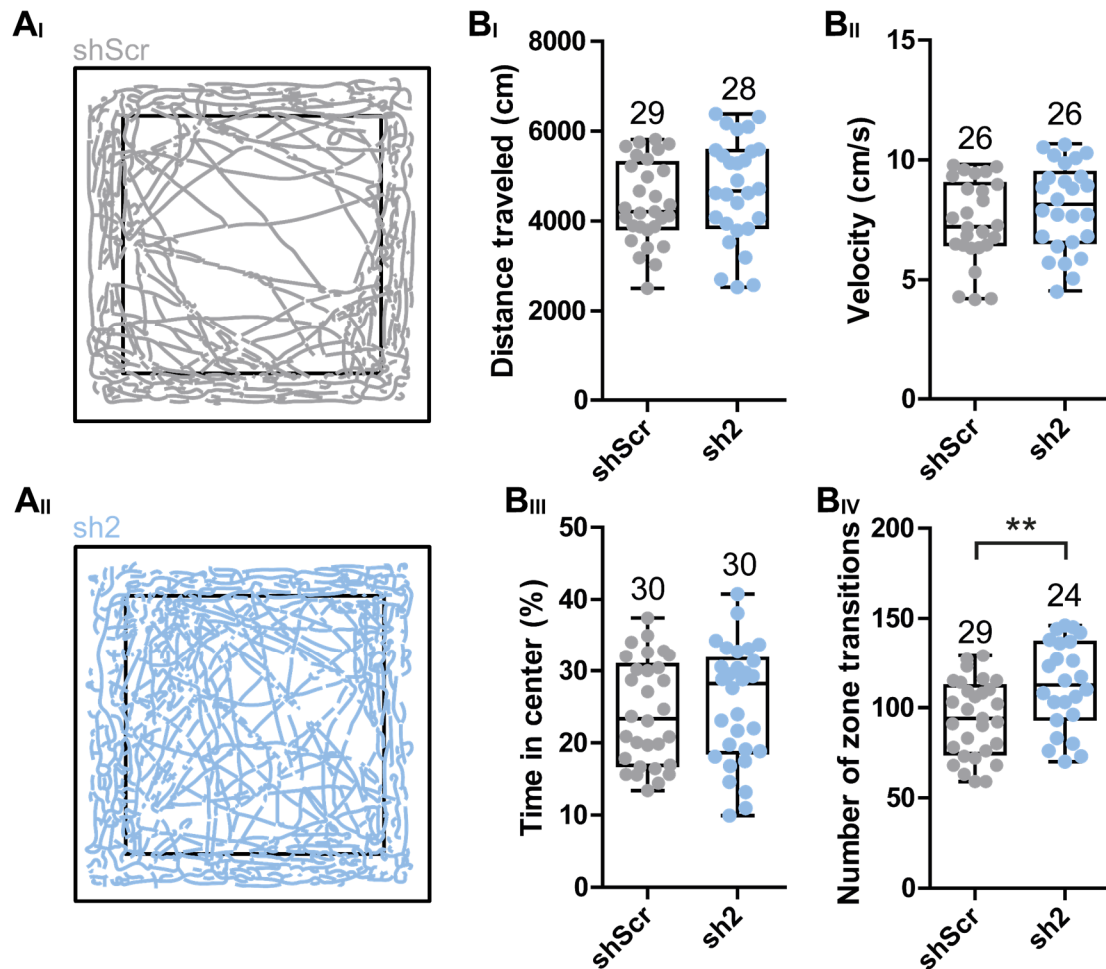


**Figure 3.26: Analysis of open field test (OF)**

(A) Schematic showing the open field (OF) arena and tracks of mice bilaterally injected with rAAV9-shScr (grey) (A<sub>I</sub>) or rAAV9-sh2 (blue) (A<sub>II</sub>). For analysis, the arena is separated into a peripheral and a central area (inner square). (B) Animals were placed for 6 min in the OF arena and their behavior was scored for (B<sub>I</sub>) distance traveled, (B<sub>II</sub>) velocity of movement, (B<sub>III</sub>) time spent in the central area of the arena, and (B<sub>IV</sub>) number of zone transitions between peripheral and central areas of the arena. Data are depicted as boxplots. Statistical significance was assessed using the unpaired two-tailed Student's t test, \*\*p < 0.01.

In contrast to the behavioral changes observed in the EZM test, mice injected with sh2-encoding virions showed no changes in the distance traveled (shScr:  $4407 \pm 914.5$  cm; sh2:  $4687 \pm 1143$  cm) or in the velocity of movement (shScr:  $7.4 \pm 1.7$  cm/s; sh2:  $8.0 \pm 1.8$  cm/s) compared to control mice (Fig.3.26 B<sub>I</sub> and B<sub>II</sub>). However, mice injected with sh2-encoding virions showed an increase in the number of zone transitions compared

to control animals (shScr:  $93.9 \pm 21.2$ ; sh2:  $112.4 \pm 24.6$ ), but there was no change in the time spent in the center of the OF arena (shScr:  $24.2 \pm 7.3$  %; sh2:  $25.4 \pm 8.2$  %) (Fig.3.26 BIII and BIV). Thus, the treatment with sh2-encoding rAAV9s partially affected the overall locomotor activity as seen by an increase in the number of zone transitions, without affecting anxiety-related behavior.

To investigate the interplay of emotions like anxiety or fear with hippocampal-dependent context learning and memory, contextual fear conditioning (FC) was performed in which animals are tested for generating an association between a specific context and an aversive stimulus (Fig. 3.27).

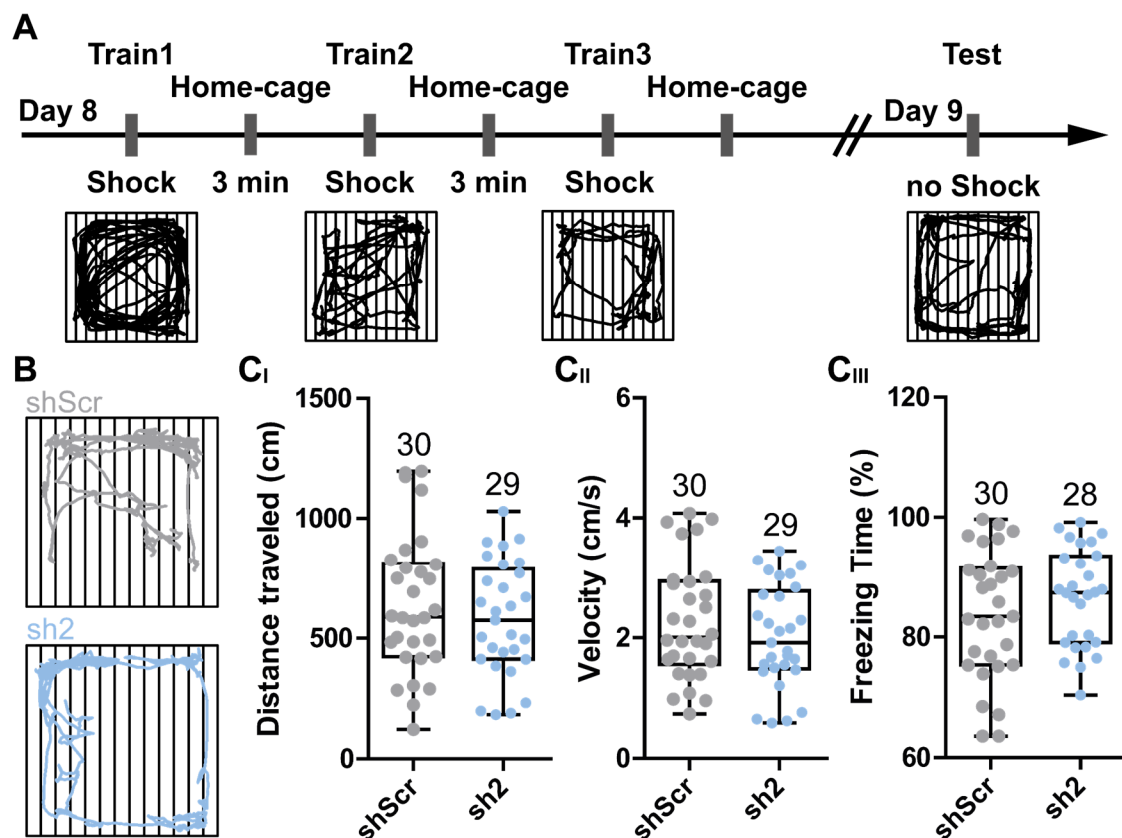


**Figure 3.27: Analysis of fear conditioning test (FC)**

(A) Schematic showing the timeline and arena for the fear conditioning (FC) test. At day eight after mice performed the EZM test (Fig. 3.25) mice were trained to the conditioning context for 148 s, followed by a 2 s 0.75 mA footshock. Animals were removed from the chamber 30 s after receiving a footshock and were placed back to their home cage for 3 minutes between the three consecutive training sessions. After 24 h, animals were tested for memory retention by returning them to the conditioning chamber for a single 5 min context test. (B) Tracks of mice bilaterally injected with rAAV9-shScr (grey) or rAAV9-sh2 (blue) are shown. (C) In the testing sessions, animals were placed for 5 min in the FC arena and scored for (CI) distance traveled, (CII) velocity of movement, (CIII) freezing time. Data are depicted as boxplots. Statistical significance was assessed using the unpaired two-tailed Student's t-test.

Mice were trained three times in a cage with a metal grid ground floor. During the training sessions, mice habituated in the cage before they received a mild aversive stimulus (electrical footshock). Between the training sessions, mice recovered from the treatment in their home-cages for three minutes. One day after training, mice were tested for associative memory retrieval by exposing them to the conditioning context without the aversive stimulus. Freezing behavior, defined as intervals of complete immobility except for breathing, was analyzed as an indicator of fear behavior. Usually, fear memory retrieval results in increased freezing time of the animal. However, injection of sh2-encoding virions did not change the freezing time compared to animals that had received shScr-encoding viruses (shScr:  $83.8 \pm 10.7$  %; sh2:  $86.5 \pm 8.1$  %). The overall activity of sh2-treated animals did not differ from control animals, neither in the distance traveled during the training session (shScr:  $638.7 \pm 289.8$  cm; sh2:  $576.6 \pm 236.6$  cm), nor in the velocity of movement during the training session (shScr:  $2.27 \pm 0.97$  cm/s; sh2:  $2.02 \pm 0.85$  cm/s) (Fig. 3.27 C).

Finally, the spatial object recognition (SOR) test was used to assess changes in hippocampus-related spatial memory and discrimination abilities in mice injected with sh2-encoding virions. The SOR is based on the spontaneous tendency of mice to spend more time exploring an object which has been relocated compared to already known, non-displaced objects. Testing occurred in an open field arena, to which the animals were habituated during the OF test. On the next day, three objects of similar material but different shapes were introduced to the arena. During three training sessions, the animals were allowed to explore the arena and the objects. In order to test the spatial memory reconsolidation after 24h, one of the objects was displaced to a novel position, and mice were allowed to explore the arena again. The object discrimination behavior was recorded during the last training session and the testing session. The overall locomotor activity was recorded solely during the testing session (Fig. 3.28).

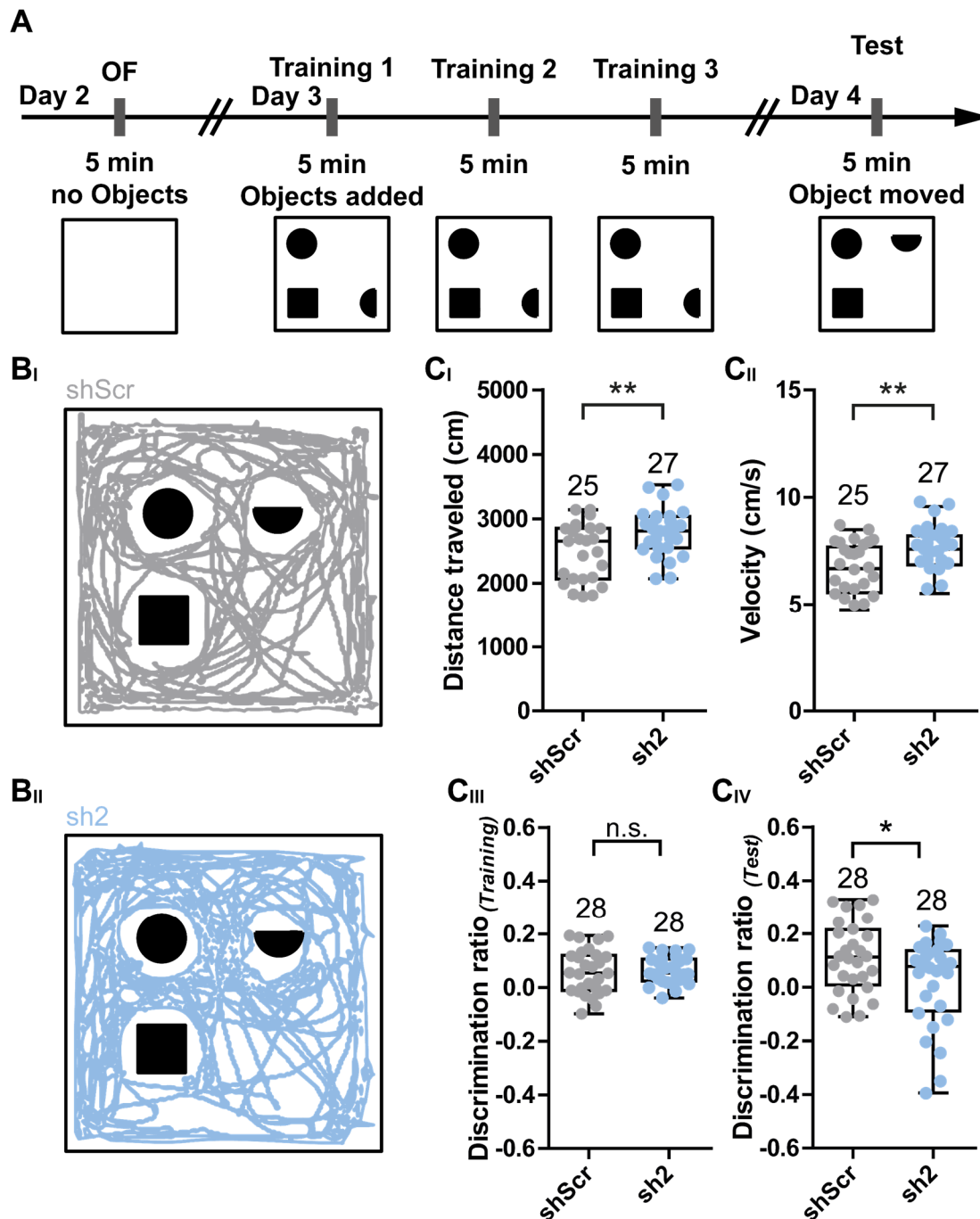


**Figure 3.28: Analysis of spatial object recognition test (SOR)**

(A) Schematic showing the timeline and arena for the spatial object recognition (SOR) test. At day two after mice performed the EZM test (Fig. 3.25), mice were habituated for 5 min to the OF arena (Fig. 3.26). One day later, mice were trained 3 times for 5 min each with a rectangular metal column (square), a half-moon shaped plastic cylinder (half-moon), and a glass bottle (circle) introduced as objects in a defined spatial organization in the OF arena. For the testing session 24h later, the half-moon shaped plastic cylinder was displaced in the arena. Tracks of mice bilaterally injected with rAAV9-shScr (grey) (BI) or rAAV9-sh2 (blue) (BII) are shown for the testing session. (C) In the testing session, animals were placed for 6 min in the SOR arena and scored for (CI) distance traveled, (CII) velocity of movement, (CIII) discrimination ratio between displaced and non-displaced objects during training session, and (CIV) discrimination ratio between displaced and non-displaced objects during testing session. Data are depicted as boxplots. Statistical significance was assessed using the unpaired two-tailed Student's *t* test, \* $p < 0.05$ ; \*\* $p < 0.01$ .

Mice injected with sh2-encoding virions showed an increase in overall locomotor activity compared to mice injected with shScr-encoding virions, resulting in an increase in the distance traveled (shScr:  $2483 \pm 444.4$  cm; sh2:  $2791 \pm 369.8$  cm) and velocity of movement (shScr:  $6.9 \pm 1.2$  cm/s; sh2:  $7.8 \pm 1.0$  cm/s) (Fig. 3.28 CI and CII). Notably, both groups showed no preference for any of the objects during the training session, resulting in a rather low discrimination ratio (shScr:  $0.058 \pm 0.083$ ; sh2:  $0.063 \pm 0.051$ ). However, shScr-treated mice showed an increased discrimination ratio during the testing session (shScr:  $0.11 \pm 0.13$ ), whereas the sh2-treated mice were even worse in discriminating the objects compared to the training session (sh2:  $0.02 \pm 0.16$ ). This suggests, that sh2-treated mice had difficulties to discriminate between familiar, non-displaced objects and the same but displaced objects.

Taken together, the results of the behavioral experiments indicated that the injection of sh2-encoding virions neither influenced anxiety-related behavior, nor fear-related memory retrieval. However, it induced a robust increase in locomotor activity and additionally caused a deficiency in object spatial memory and discrimination abilities.

### ***3.3.2 Biochemical and molecular-biological analyses of injected animals***

In order to analyze changes in transcript expression levels of different target proteins in mice injected with sh2-encoding virions, qRT-PCR was performed on cDNA from shScr- or sh2-injected dorsal hippocampal tissue (Fig 3.29 A and B).

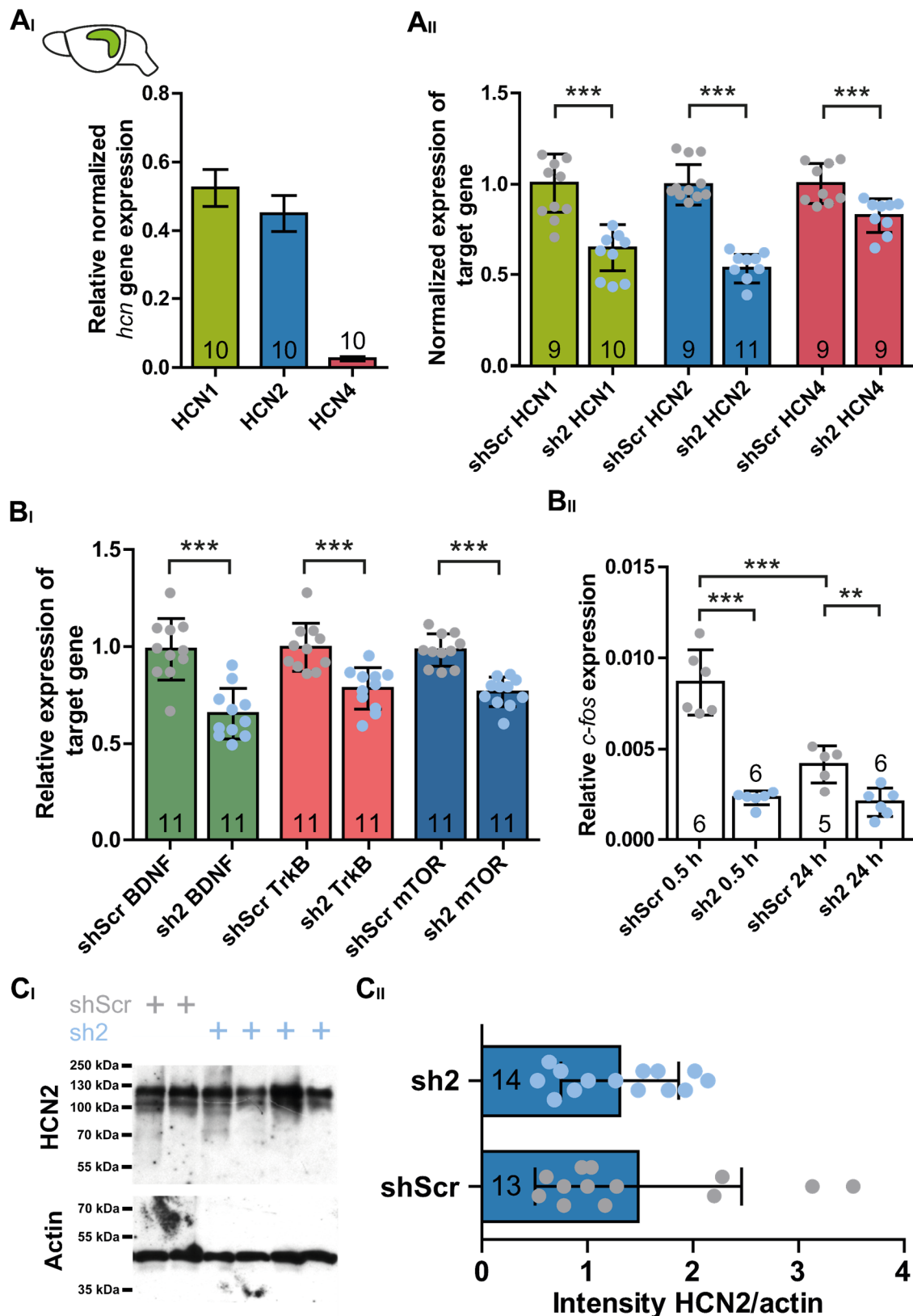


**Figure 3.29: Validation of HCN2-channel knock-down *in vivo***

(A) Quantitative PCR analysis of *hcn1*, *hcn2* and *hcn4* transcript levels in dorsal hippocampal tissue 5 weeks post injection of shScr (AI). Transcript levels of *hcn* genes were normalized to *gapdh* transcript levels. (AII, BI and BII) Mice were injected either with rAAV9-shScr (control, grey dots) or rAAV9-sh2 (HCN2-channel knock-down, blue dots). First-strand cDNA was synthesized on 1  $\mu$ g total RNA isolated from shScr-treated or sh2-treated dorsal hippocampal tissue. Expression levels were calculated and normalized to the shScr-injected control. Quantitative PCR analysis of *hcn1*, *hcn2* and *hcn4* transcript levels

(AII), of transcript levels of different neuronal expressed genes, e.g., *brain-derived neurotrophic factor (BDNF)*, *tropomyosin receptor kinase B (TrkB)* receptor, and *mechanistic Target of Rapamycin (mTOR)* (BI), and of the *cellular oncogene Fos (c-Fos)* (BII) in dorsal hippocampal tissue 5 weeks post injection of rAAV9-shScr or rAAV9-sh2. *C-fos* transcript levels were measured in animals sacrificed 30 min or 24h after performing the fear conditioning task. (C) Quantitative WB analysis of HCN2-channel knock-down in dorsal hippocampal tissue 5 weeks post injection of rAAV9-shScr or rAAV9-sh2. After staining with HCN2 and actin specific antibodies, signals were detected using enhanced chemiluminescence and quantified by densitometry. Data were obtained from indicated numbers of animals. Results are depicted as mean  $\pm$  standard deviation. Statistical significance was assessed using the unpaired two-tailed Student's t test, \*\*\* $p < 0.001$ .

To assess HCN-channel isoform expression under control conditions, HCN-channel transcripts were quantified by qRT-PCR (Fig. 3.29 AI). Examination of transcript numbers showed that *hcn1* and *hcn2* transcripts were almost equally abundant (*hcn1*:  $52.9 \pm 5.4$  %; *hcn2*:  $44.5 \pm 5.3$  %), while *hcn4* transcript expression was lower (*hcn4*:  $2.6 \pm 0.6$  %). Notably, this expression pattern was different to that previously determined in PHNs (Fig. 3.9) and OHSCs (Fig. 3.7).

Because the injection of rAAV9-sh2 was performed to knock-down the expression of the HCN2 channel subtype, transcript levels of *hcn1*, *hcn2*, and *hcn4* in rAAV9-sh2 injected hippocampi and in rAAV9-shScr injected hippocampi were compared (Fig. 3.29 AII). Notably, in sh2-treated animals the *hcn2* transcript level was reduced to  $53.2 \pm 8.0$  % of shScr-treated controls. However, sh2-treatment also reduced *hcn1* and *hcn4* transcript levels to  $64.8 \pm 12.8$  % and  $82.6 \pm 9.3$  % of shScr-treated controls, respectively. To check if this 'unspecific' knock-down effect also occurred in other neuronally expressed genes, transcript levels of *brain-derived neurotrophic factor (BDNF)*, *tropomyosin receptor kinase B (TrkB)* receptor, and *mechanistic Target of Rapamycin (mTOR)* were assessed and analyzed (Fig. 3.29 BI). Notably, also the transcript levels of these target genes were also reduced in hippocampi of mice injected with rAAV9-sh2 compared to control mice injected with rAAV9-shScr (*BDNF*:  $65.3 \pm 13.0$  %; *TrkB*:  $78.3 \pm 10.7$  %; *mTOR*:  $76.5 \pm 7.5$  %). Since learning and memory mediated by hippocampal neurons is associated with increased neuronal activity, expression of the transcription factor *c-fos* in the hippocampal cornu amonis (CA)1 region has been shown to be increased in animals exposed to associative learning tasks (Mahringer et al., 2019). To validate if changes in neuronal activity might account for the reduction in neuronally expressed genes, *c-fos* transcript levels were analyzed in hippocampi of sh2- and shScr-treated mice. *C-fos* transcript levels were measured in animals sacrificed 0.5 h or 24h after performing the FC task (Fig. 3.29 BII). In sh2-injected animals sacrificed 0.5 h after performing the FC test less *c-fos* transcripts were present compared to control animals (shScr:

$0.0086 \pm 0.0018$  *c-fos/gapdh*; sh2:  $0.0023 \pm 0.0004$  *c-fos/gapdh*). However, while shScr-treated animals showed a clear time dependent reduction of the *c-fos* transcript numbers (0.5 h:  $0.0086 \pm 0.0018$  *c-fos/gapdh*; 24h:  $0.0041 \pm 0.0010$  *c-fos/gapdh*), *c-fos* transcript numbers in sh2-treated animals did not change (0.5 h:  $0.0024 \pm 0.0001$  *c-fos/gapdh*; 24h:  $0.0020 \pm 0.0008$  *c-fos/gapdh*). This suggests, that sh2-treated animals had lower neural activity compared to shScr-treated animals and thus expressed less amounts of the transcription factor *c-fos*.

To further validate the HCN2-channel knock-down, western blots of membrane proteins (see Chapter 2.14) from dorsal hippocampal tissue of mice injected with rAAV9-shScr or rAAV9-sh2 were performed (Fig. 3.29 C). The chemiluminescence signal corresponding to the HCN2-subunit specific staining consisted of two bands (Figure 3.29 CI), corresponding to glycosylated and non-glycosylated HCN2 proteins (Much et al., 2003). However, compared to shScr-treated control samples, the intensities of the HCN2 bands were unaffected in sh2-treated samples. This finding was supported by a densitometric analysis and calculation of the HCN2/actin ratio, showing that the relative HCN2-channel expression was similar between both groups (shScr:  $1.48 \pm 0.98$  HCN2/actin; sh2:  $1.31 \pm 0.56$  HCN2/actin) (Fig. 3.29 CII). Taken together, these results indicated that the injection of rAAV9-sh2 induced a general reduction in transcript levels of neuronally expressed genes. Despite a reduction of HCN2-channel transcripts, the HCN2-channel protein level was unaltered.

To verify if the reduction of *hcn1*- and *hcn4*-transcripts observed in sh2-treated animals was due to unspecific binding of the sh2 shRNA to *hcn1* or *hcn4* mRNA, the cross-reactivity of sh2 was re-evaluated in PHNs (Fig. 3.30).

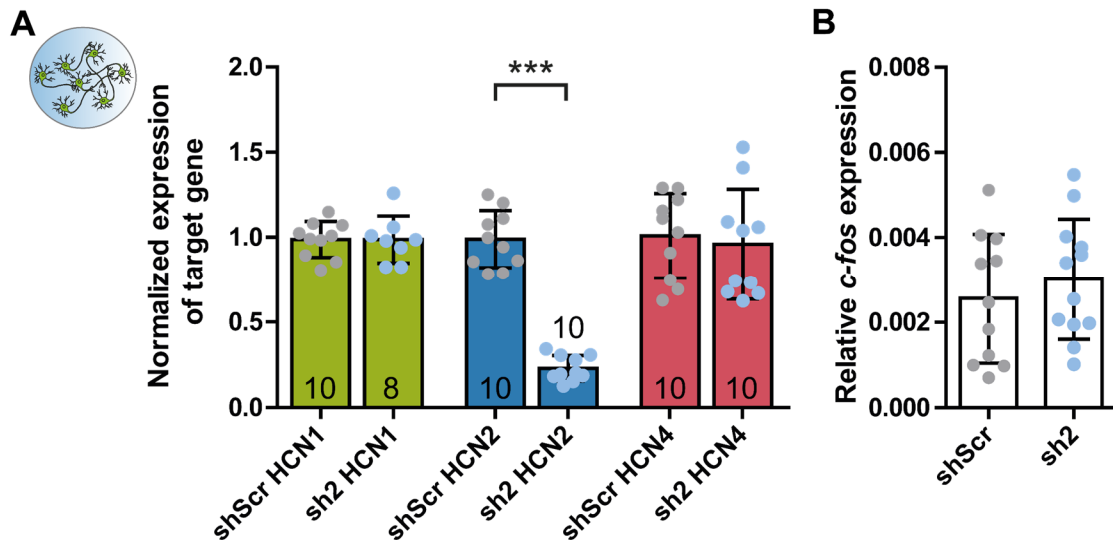


**Figure 3.30: Quantification of HCN2-channel knock-down specificity in PHNs**

(A) Quantitative PCR analysis of *hcn1*, *hcn2*, and *hcn4* transcript levels, and (B) *c-fos* transcript levels in primary hippocampal neurons (PHNs) 2 weeks after transduction either with rAAV9-shScr (control, grey dots) or rAAV9-sh2 (HCN2-channel knock-down, blue dots). First-strand cDNA was synthesized on 500 ng total RNA isolated from shScr-treated or sh2-treated PHNs. Expression levels were calculated and normalized to the shScr-treated control neurons. Data were obtained from indicated numbers of cultures obtained from at least 3 different animals. Results are depicted as mean  $\pm$  standard deviation. Statistical significance was assessed using the unpaired two-tailed Student's t test, \*\*\* $p < 0.001$ .

Notably, the sh2-encoding construct reduced *hcn2* transcript levels in PHNs to  $22.8 \pm 7.4$  % of shScr-treated control neurons. In contrast to the results obtained from injected animals, sh2 did not cause a reduction in *hcn1* or *hcn4* mRNA levels (*hcn1*:  $98.5 \pm 13.9$  % and *hcn4*:  $95.8 \pm 32.3$  % of the shScr-treated control neurons) (Fig. 3.30 A). Furthermore, *c-fos* transcript levels were analyzed in PHNs treated with sh2 or shScr to validate the cross-reactivity of sh2 to other neuronally expressed genes. Again, sh2-treated neurons expressed similar *c-fos* transcript numbers compared to shScr-treated neurons (shScr:  $0.0026 \pm 0.0015$  *c-fos/gapdh*; sh2:  $0.0030 \pm 0.0014$  *c-fos/gapdh*). These results suggest that the reduction in transcript expression levels of non-HCN2 channel genes is not evoked by unspecific binding of sh2 RNA to non-target mRNAs.

### 3.3.3 Immunohistochemical analysis of changes upon stereotaxic intrahippocampal rAAV injections

To visualize the localization of HCN isoforms 1, 2, and 4 in the hippocampus, immunohistochemical stainings of tissue sections from animals injected with rAAV9-shScr or rAAV9-sh2 were performed (Fig. 3.31).

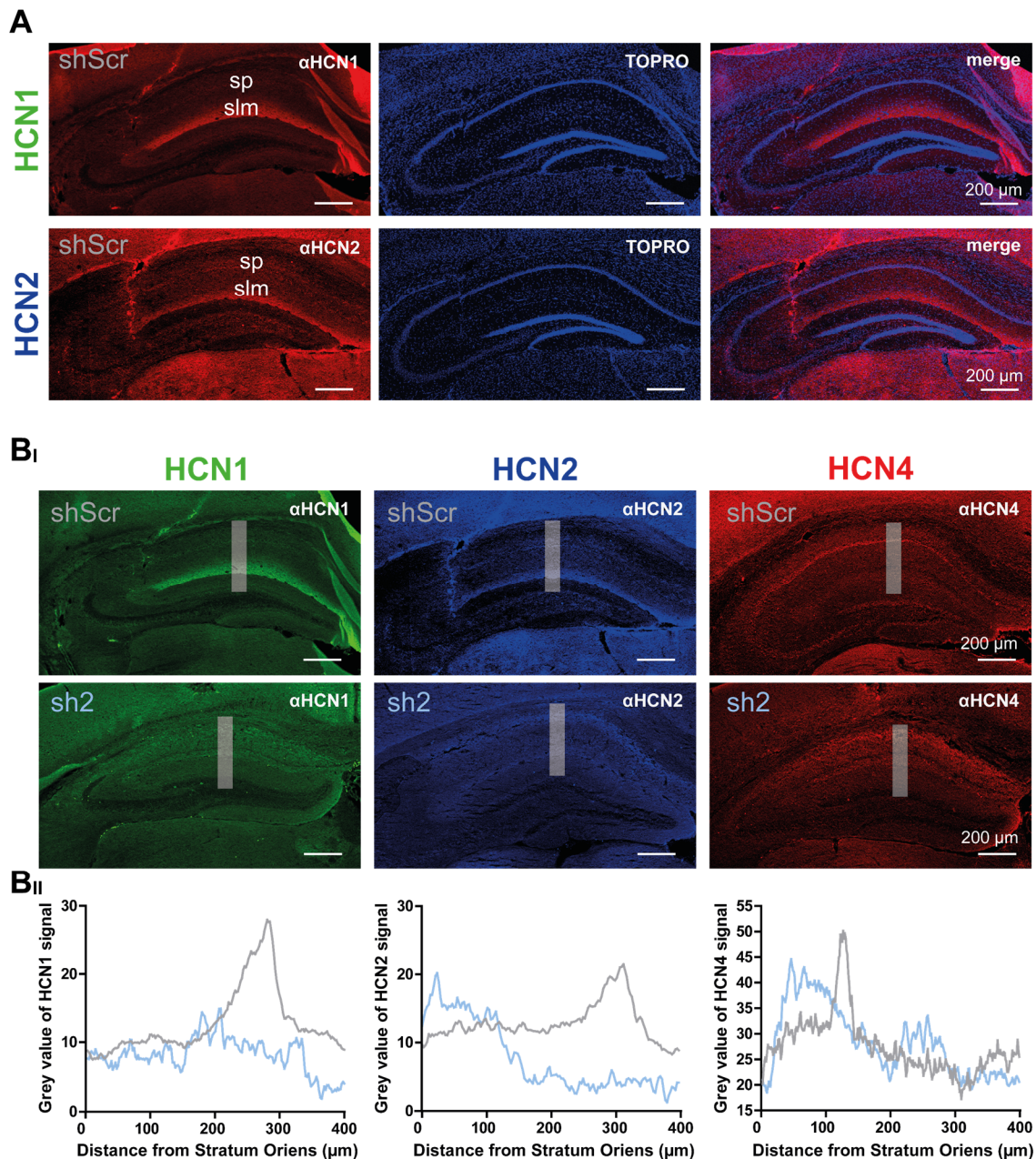


**Figure 3.31: HCN-channel isoform localization in the hippocampus**

(A) Representative immunofluorescent images showing expression of HCN-channel isoforms 1 (upper lane) and 2 (lower lane) in rAAV9-shScr (control) injected hippocampi. Isoforms were stained using subunit-specific antibodies combined with fluorescently labeled secondary antibodies (red). Nuclei were stained with TOPRO (blue). Merged images are shown on the right. sp: stratum pyramidale; slm: stratum lacunosum-moleculare (BI) Representative immunofluorescent images showing expression of HCN-channel isoforms 1 (green), 2 (blue) and 4 (red) in rAAV9-shScr (control, upper lane) or rAAV9-sh2 (HCN2-channel knock-down, lower lane) injected hippocampi. Isoforms were stained using subunit-specific antibodies combined with fluorescently labeled secondary antibodies. Grey bars indicate region for (BII) quantification of immunofluorescence intensities of HCN1-, HCN2-, and HCN4-specific immunofluorescent stainings. Intensities were measured from the stratum oriens of the cornu amonis 1 (CA1) region to the dorsal part of the dentate gyrus (DG) granule cell layer.

Both, expression of HCN1 and HCN2 channel proteins in rAAV9-shScr injected animals was locally restricted to the cornu amonis (CA) subfield 1 (Fig. 3.31 A). Consistent with

previous reports (Magee, 1998, Lörincz et al., 2002), expression of HCN1 and HCN2 is organized as a gradient of increasing intensity along the dendrites of CA1 pyramidal neurons, with a maximum of expression intensity in the stratum lacunosum-moleculare (slm). Expression of HCN4 in rAAV9-shScr injected animals was detected in the granule cell layer of the dentate gyrus (DG) and also in the stratum pyramidale of the CA subfields (Fig. 3.31 B, right panel). However, injection of rAAV9-sh2 dramatically changed the expression patterns of each of the HCN channel subtypes expressed in the hippocampus (Fig. 3.31 B). Both, HCN1 and HCN2 expression was not organized in a gradient 5 weeks after injection of rAAV9-sh2, and HCN4 expression was no longer restricted to the pyramidal cell layer of the CA1 subfield.

Additional immunohistochemical stainings of the fluorescent marker GFP, which was co-expressed with the shRNAs, the neuronal marker NeuN, and the nuclear marker TOPRO were performed to visualize changes in the overall architecture of the hippocampal formation (Fig. 3.32).

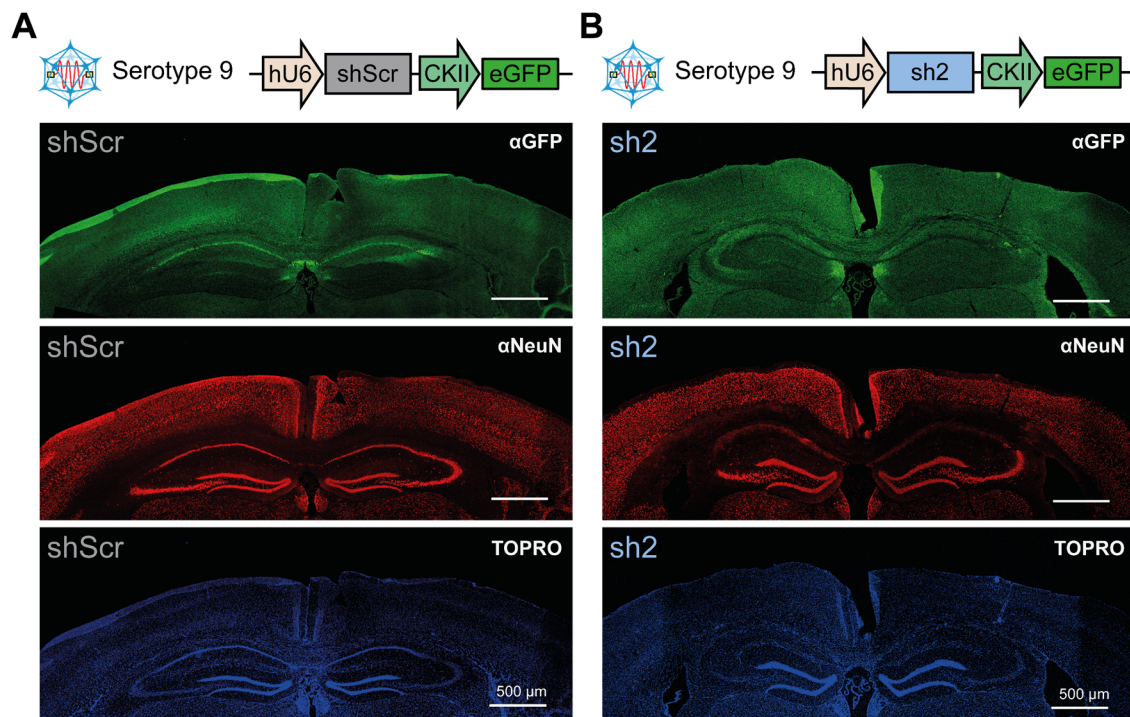


**Figure 3.32: Immunohistochemical analysis of bilateral stereotaxic injections**

(A and B) Representative immunofluorescent images showing expression of the fluorescent reporter eGFP (green), the neuronal marker protein NeuN (red), and the nuclear marker TOPRO (blue) in (A) rAAV9-shScr (control) or (B) rAAV9-sh2 (HCN2-channel knock-down) bilaterally injected hippocampi. Proteins were stained using specific primary antibodies combined with fluorescently labeled secondary antibodies. Cartoons of the AAV-delivered constructs are displayed above the immunofluorescent images.

While rAAV9-shScr injected hippocampi showed a distinct fluorescent signal of GFP in the CA1 subfield, rAAV9-sh2 injected hippocampi showed a diffuse expression of GFP in various regions, including the medial part of the DG (Fig. 3.32 A and B, upper panel). Notably, fluorescent signals of both, the neuronal marker NeuN and the nuclear marker TOPRO, indicated a loss of the neurons in the CA1 subfield of rAAV9-sh2 injected hippocampi compared to rAAV9-shScr injected hippocampi (Fig. 3.32 A and B, lower panels). Enlargements of the fluorescent images of rAAV9-shScr and rAAV9-sh2 injected animals, sacrificed 5 weeks post injection (Fig. 3.33) corroborate the loss of the CA1 pyramidal cell layer.

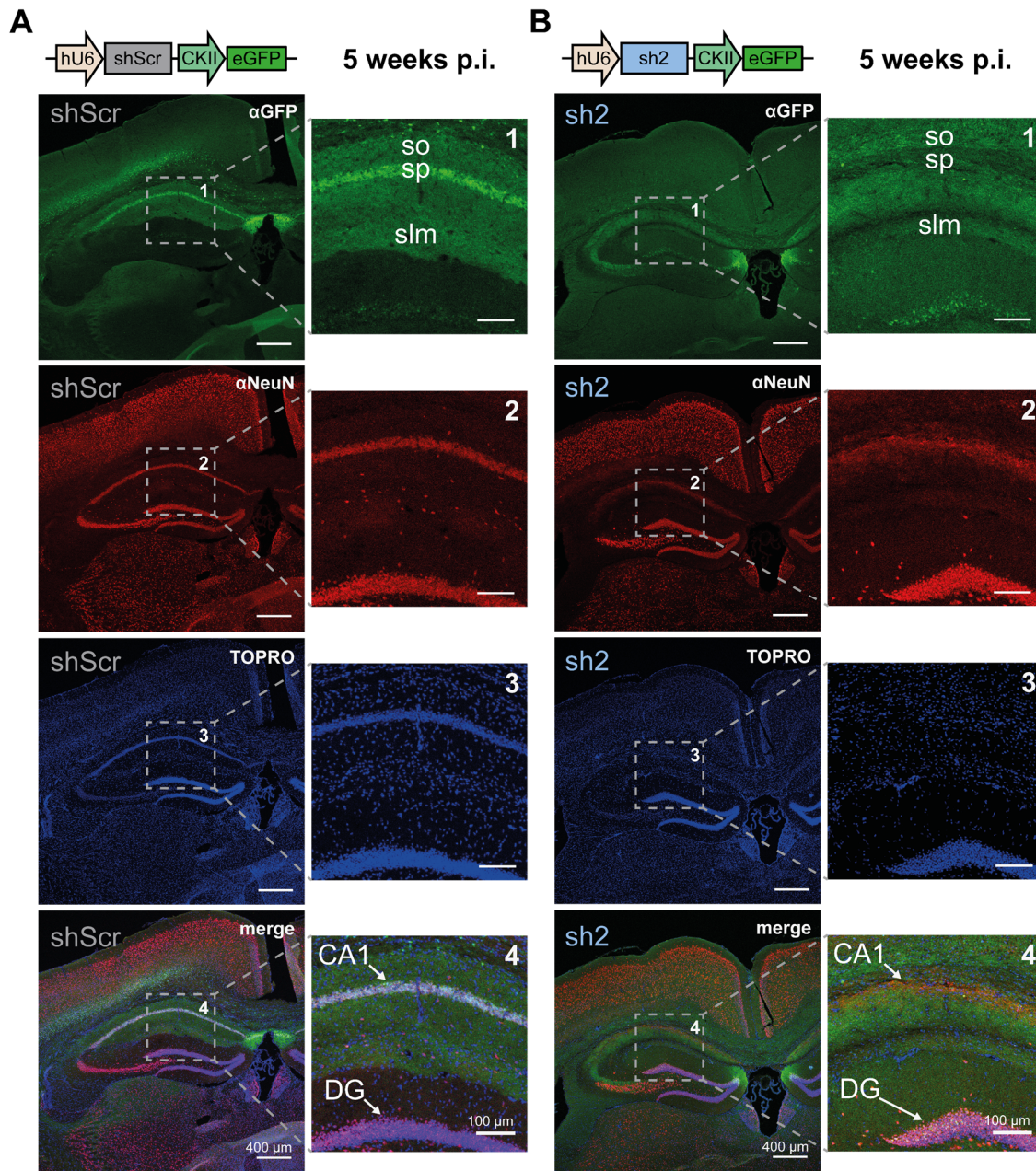


**Figure 3.33: Loss of hippocampal CA1 pyramidal cell layer 5 weeks post injection of sh2-encoding rAAV9**

(A and B) Representative immunofluorescent images showing expression of the fluorescent reporter eGFP (green), the neuronal marker protein NeuN (red), and the nuclear marker TOPRO (blue) in (A) rAAV9-shScr (control) or (B) rAAV9-sh2 (HCN2-channel knock-down) bilaterally injected hippocampi. Animals were sacrificed 5 weeks post injection. Proteins were stained using specific primary antibodies combined with fluorescently labeled secondary antibodies. Enlargements and arrows show the cornu amonis 1 (CA1) pyramidal cell layer and the dorsal part of the dentate gyrus granule (DG) cell layer of the hippocampus. Cartoons of the AAV-delivered constructs are displayed above the immunofluorescent images. so: stratum oriens; sp: stratum pyramidale; slm: stratum lacunosum-moleculare

Injection of rAAV9-shScr into the hippocampus resulted in eGFP fluorescent signals especially in the stratum pyramidale (sp), harboring somata of CA1 pyramidal neurons, in the stratum lacunosum-moleculare (slm), harboring dendrites of CA1 pyramidal

neurons, and in the stratum oriens (so), harboring local branches of the axons of CA1 pyramidal neurons. In contrast, injection of rAAV9-sh2 into the hippocampus resulted in eGFP fluorescent signals completely lacking the stratum pyramidale of the CA1 subfield (Fig. 3.33 A and B, upper panel). In addition, the prominent fluorescent signals showing somata (NeuN) and nuclei (TOPRO) in the stratum pyramidale were completely absent in mice injected with rAAV9-sh2 (Fig. 3.33 A and B). However, rAAV9-sh2 injection had no obvious effects on the gross architecture of the DG.

To verify if the loss of the CA1 pyramidal cell layer in rAAV9-sh2 injected mice is a transient or a permanent effect, fluorescent images of rAAV9-shScr and rAAV9-sh2 injected animals sacrificed 9 weeks post injection were analyzed (Fig. 3.34).

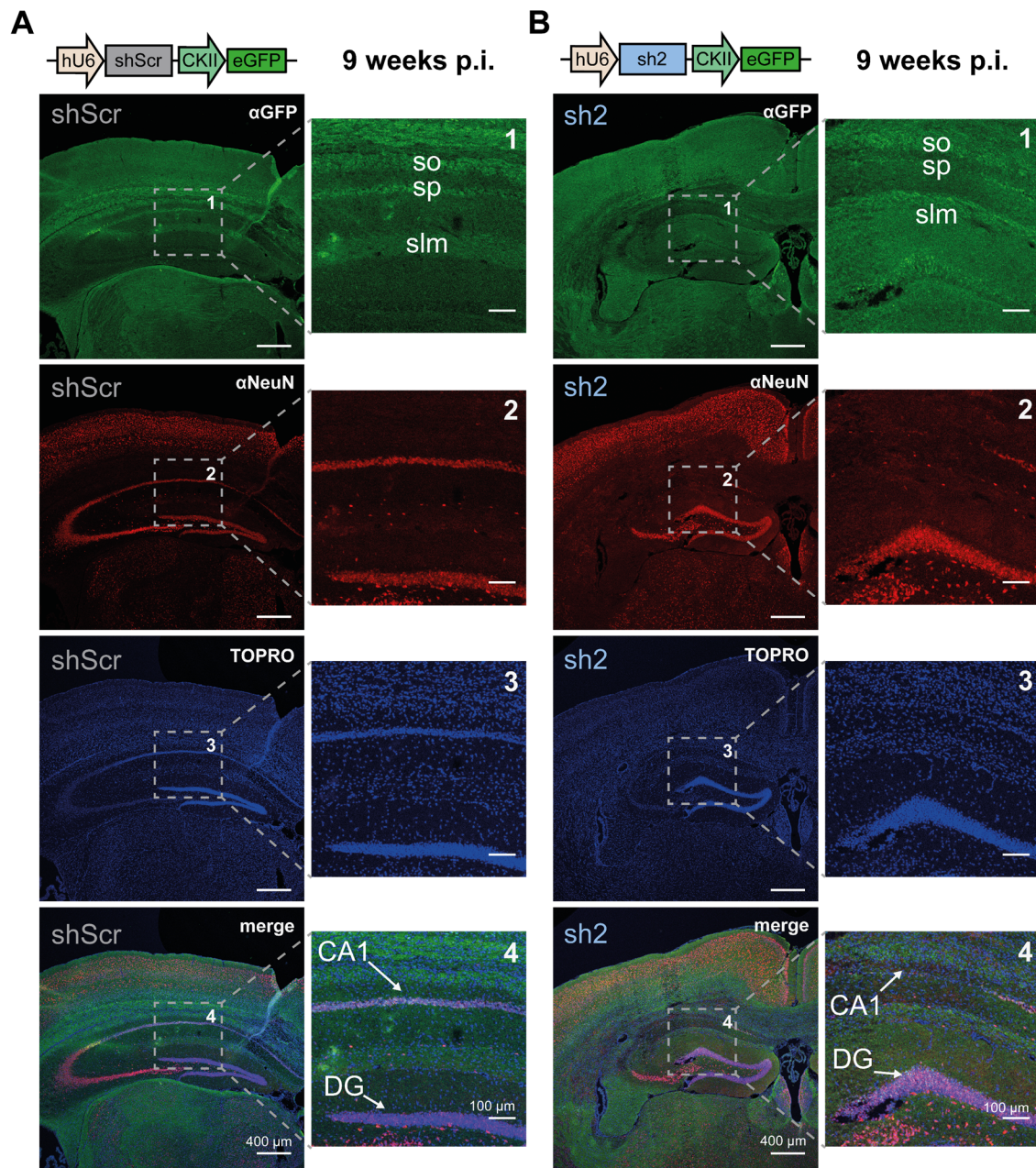


**Figure 3.34: Loss of hippocampal CA1 pyramidal cell layer 9 weeks post injection of sh2-encoding rAAV9**

(A and B) Representative immunofluorescent images showing expression of the fluorescent reporter eGFP (green), the neuronal marker protein NeuN (red), and the nuclear marker TOPRO (blue) in (A) rAAV9-shScr (control) or (B) rAAV9-sh2 (HCN2-channel knock-down) bilaterally injected hippocampi. Animals were sacrificed 9 weeks post injection. Proteins were stained using specific primary antibodies combined with fluorescently labeled secondary antibodies. Enlargements and arrows show the cornu amonis 1 (CA1) pyramidal cell layer and the dorsal part of the dentate gyrus granule (DG) cell layer of the hippocampus. Cartoons of the AAV-delivered constructs are displayed above the immunofluorescent images. so: stratum oriens; sp: stratum pyramidale; slm: stratum lacunosum-moleculare

Similar to the effects observed 5 weeks post injection, fluorescent signals of soma (NeuN) and nuclei (TOPRO) were absent in mice 9 weeks after injection of rAAV9-sh2 (Fig. 3.34

A and B). The loss of CA1 pyramidal neurons, however, did not expand to the granule cells of the DG.

To gain more insight into the mechanism accompanying the loss of the CA1 pyramidal cell layer in rAAV9-sh2 injected mice, active caspase-3 (Caspase) and glial fibrillary acidic protein (GFAP) were used as indicators for the adverse tissue response (Günther et al., 2017) (Fig. 3.35).

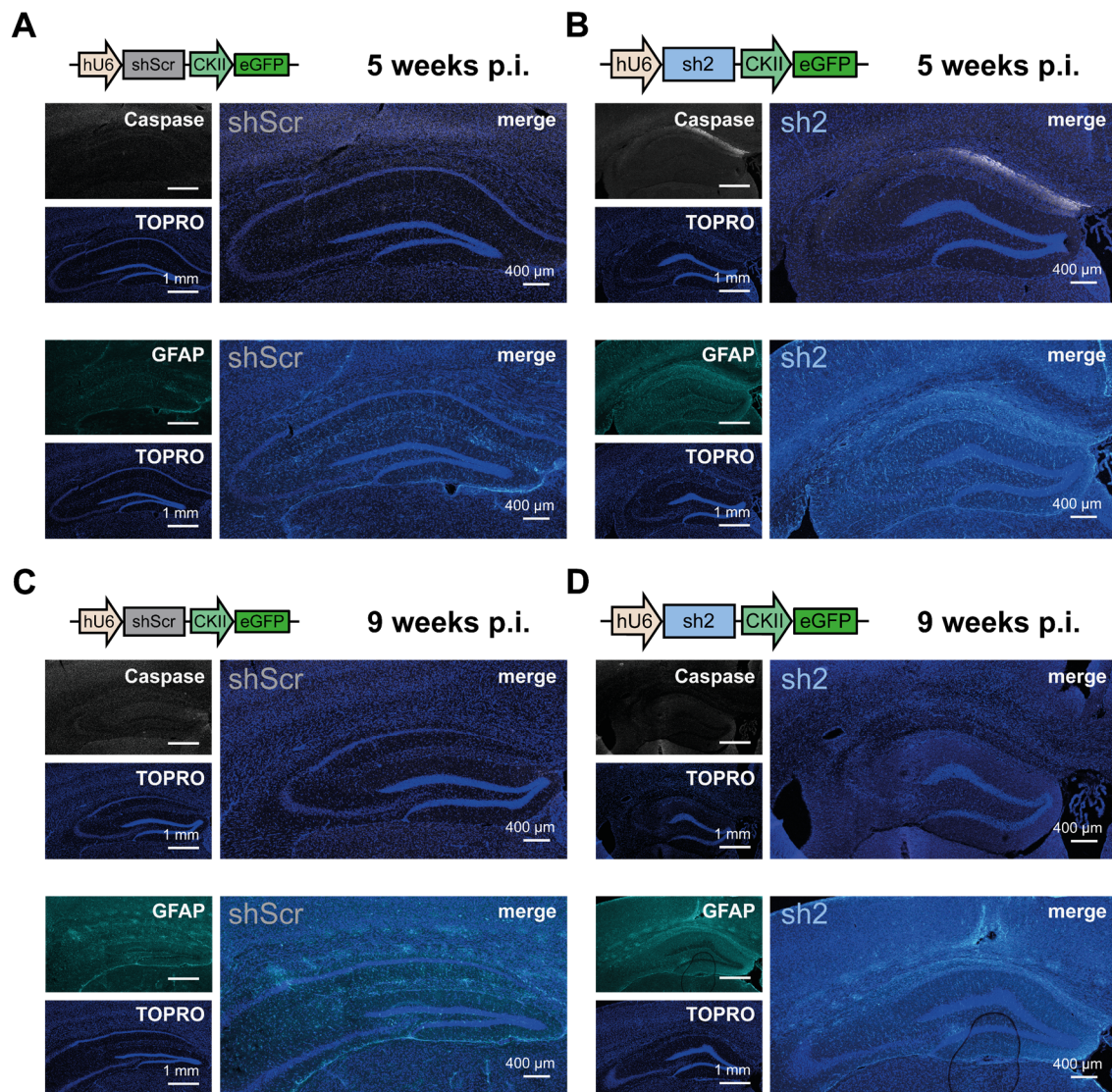


**figure 3.35: Markers of rAAV9-sh2 -induced tissue degeneration in the hippocampal CA1 region**

(A) Representative immunofluorescent images showing expression of the apoptosis marker active caspase-3 (Caspase, grey) and astrogliosis enriched glial fibrillary acidic protein (GFAP, cyan). Animals were injected with (A and C) rAAV9-shScr virions (control) or (B and D) rAAV9-sh2 virions (HCN2-channel knock-down). Animals were sacrificed 5 weeks (A and B) or 9 weeks (C and D) post injection. Proteins were stained using specific antibodies combined with fluorescently labeled secondary antibodies. Nuclei were stained with TOPRO (blue). Cartoons of the AAV-delivered constructs are displayed above the immunofluorescent images.

Fluorescent signals of cleaved (active) Caspase-3, a main component of apoptosis in eukaryotic cells, was higher especially in the CA1 subfield of rAAV9-sh2 injected hippocampi compared to rAAV9-shScr injected hippocampi, 5 weeks post injection (Fig. 3.35 A, upper panel). Notably, Caspase-3 signals of rAAV9-sh2 injected hippocampi were almost indistinguishable from those of rAAV9-shScr injected hippocampi 9 weeks post injection (Fig. 3.35 B, upper panel). Moreover, the GFAP fluorescent signal, a marker for glial scars after injury, increased in the CA1 subfield of rAAV9-sh2 injected hippocampi compared to rAAV9-shScr injected hippocampi, 5 weeks post injection (Fig. 3.35 A, lower panel). The GFAP signals did not decline in rAAV9-sh2 injected animals 9 weeks post injection. However, also rAAV9-shScr injected animals showed similar elevated levels of GFAP expression in the CA1 subfield and in the DG, 9 weeks post injection. This indicates that GFAP expression might increase with aging, independent of the molecular identity of the injected virus.

Taken together, the results of the biochemical analysis of the *in vivo* knock-down experiments indicated, that injection of rAAV9-sh2 caused a degeneration of the CA1 pyramidal neurons. Injection of rAAV9-shScr control virions, however, resulted neither in changes of gene expression levels, protein marker localization, nor overall hippocampal architecture.

---

The results of the stereotaxic bilateral hippocampal injections of rAAVs to achieve *in vivo* HCN2-channel knock-down showed, that the sh2-encoding rAAVs caused a severe but specific loss of the CA1 pyramidal cell layer, without changing the overall hippocampal architecture.

The behavioral experiments showed that rAAV9-sh2 injection did not alter hippocampal functions related to emotional responses. However, rAAV9-sh2 injection altered hippocampus-related spatial memory and discrimination abilities in the SOR test and also increased the overall locomotor activity of the animals.

---

---

# Chapter 4

## Discussion

---

The goal of this thesis was to characterize the consequences of hyperpolarization-activated and cyclic nucleotide-gated (HCN) channel knock-down *in vitro* and *in vivo*. The mammalian genome encodes four HCN subunit isoforms (HCN1 – 4) (Ludwig et al., 1998) which are known to control electrical properties of neurons, for example by determining and stabilizing the resting membrane potential (Kase and Imoto, 2012). In addition, HCN channels play crucial roles in generating rhythmic activity and thereby participate in cardiac pacemaking (DiFrancesco, 1986), as well as in modulating the sleep and wake cycle in the thalamocortical system (McCormick and Pape, 1990).

#### 4.1 Knock-down of HCN-channel isoforms *in vitro*

To uncover the most suitable approach for HCN-channel knock-down *in vitro* and *in vivo*, the specificity and efficacy of two mechanistically independent strategies, i.e. RNA interference (RNAi) (Fire et al., 1998) and “Clustered Regularly Interspaced Short Palindromic Repeats interference” (CRISPRi) (Larson et al., 2013), were evaluated and compared. Because suitable CRISPRi constructs were not available, a modular all-in-one vector was designed providing the core components necessary to induce CRISPRi-mediated knock-down in neuronal and non-neuronal target cells. To induce RNAi- or CRISPRi-mediated knock-down in neurons, recombinant Adeno-associated viruses (rAAVs) were used. Notably, these viruses are known to be non-immunogenic and have been approved for therapeutic applications (Mendell et al., 2017, Russell et al., 2017).

Evaluation and comparison of both approaches in different cell culture systems resulted in three fundamental findings: [1] both strategies induced a gene-specific reduction on the transcript level [2], the knock-down efficiency of RNAi exceeded the efficiency of CRISPRi, and [3] rAAV9 virions were better suited than rAAV2 virions for delivering the cargo into primary hippocampal neurons (PHNs), as well as organotypic hippocampal slice cultures (OHSCs). In recent publications, efficient and specific CRISPRi-based gene inactivation has been described in, e.g., HEK293 cells (Qi et al., 2013), induced pluripotent stemcells (Mandegar et al., 2016), and in neurons *in vivo* and *in vitro* (Zheng et al., 2018). Application of CRISPRi described in this thesis, however, resulted in only moderate reductions (~20 – 40 %) of *hcn* transcript levels in neurons (Fig. 3.6). An explanation for this moderate efficiency at *hcn* gene loci might arise from an imprecise assignment of the transcriptional start site (TSS) regions. The most challenging part in designing CRISPRi experiments is to identify a gene’s TSS and 5’ upstream promoter region to which sgRNA molecules can bind (Radziszewska et al., 2016). Upon binding of the dSaCas9-KRAB-sgRNA complex to the target sequence, KRAB induces heterochromatin formation (Groner et al., 2010) and finally prevents RNA polymerase from initiating transcription. Several online tools are currently available to assist in identifying gene promoters (Radziszewska et al., 2016). It has been shown that sgRNAs should bind in a region covering -50 to + 300 bp around the TSS (Gilbert et al., 2014). To improve the CRISPRi efficacy for *hcn* transcript knock-down, one could re-examine the current TSS annotations with independent prediction algorithms to uncover additional and potentially more favorable sgRNA target sites (Radziszewska et al., 2016).

Alternatively, the TSS could be exactly determined by molecular biological tools, like 5' primer-extension or 5' rapid extension of cDNA ends (RACE) (Frohman, 1994, Beischlag, 1995). These experiments, however, were beyond the scope of the current investigation. Nevertheless, the CRISPRi approach demonstrated its strength in displaying high specificity in transcript knock-down and overcomes potential drawbacks concerning off-target effects, frequently observed in classical CRISPR/Cas approaches (Zhang et al., 2015). Because the sgRNAs applied in CRISPRi exclusively bind to the non-coding promoter regions of target genes, unspecific off-target effects are very unlikely to occur (Gilbert et al., 2014).

In contrast to the results obtained with CRISPRi, RNAi knock-down resulted in robust reduction of *hcn* transcripts in recombinant cell-lines, PHNs as well as OHSCs. Thus, RNAi facilitated a 40 - 80% reduction of *hcn1*, *hcn2* and *hcn4* transcript levels in PHNs (Fig. 3.6). Interfering with transcript levels by RNAi strategies has the advantage that the target site(s) to which shRNA molecules can bind are less restricted. In principle, the entire primary transcript of a gene might serve as a template for shRNA binding (Shan, 2010). However, this makes RNAi, similar to the CRISPR/Cas technique more vulnerable to produce unexpected off-target effects.

To overcome constraints of construct delivery to neurons, rAAVs are widely used as cargo vehicles (Aschauer et al., 2013). AAV serotypes differ in their efficacy to transduce different cell types or tissues, a feature called tropism. While rAAV2 virions are often favored because they are known to have a broad spectrum of cell type infection, rAAV9 virions have been found advantageous when neurons should be transduced.

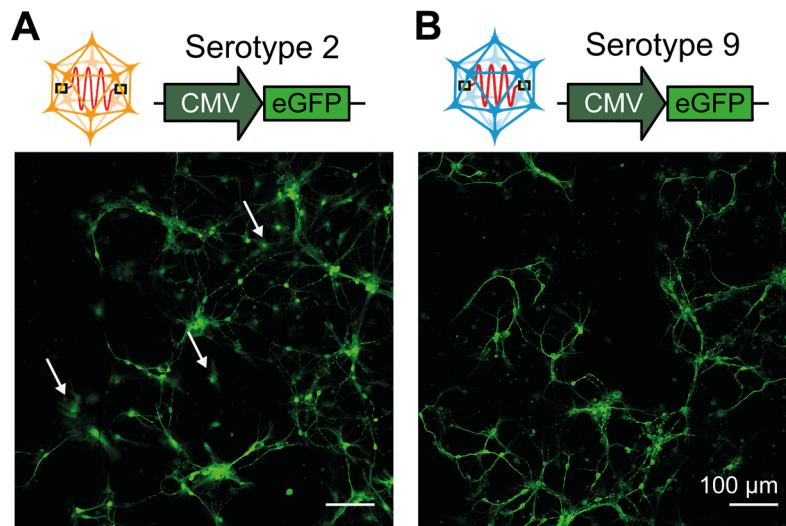


**Figure 4.1: Transduction of primary hippocampal cultures by AAV serotypes 2 and 9**

(A and B) Representative immunofluorescent images showing expression of eGFP fluorescent reporter in primary hippocampal cultures transduced with (A) AAV serotype 2 or (B) AAV serotype 9. Arrows in A indicate eGFP fluorescence in glial cells. Expression of eGFP was controlled by a CMV promoter. The eGFP reporter was immunostained with a specific anti-GFP antibody combined with a fluorescently labeled secondary antibody (green). Cartoons of the AAV-delivered constructs are displayed above the immunofluorescent images.

Here, both serotypes were used to induce RNAi- or CRISPRi-mediated knock-down in neurons. Transduction experiments with AAV2 and AAV9 virions encoding an eGFP fluorescent reporter under the control of the ubiquitously active CMV promoter (Fig. 4.1) suggested that serotype 2 transduced both, neurons and glia cells in mouse primary hippocampal cultures (arrows in Fig. 4.1 A indicate glia cells). However, due to its neuronal tropism, serotype 9 preferably transduced neurons, corroborating its neuronal transduction efficiency (Fig. 4.1 B). In addition, a systematic analysis of AAV serotype abilities to drive transgene expression in different brain regions showed that AAV9 virions also provide higher expression levels in all brain regions compared to AAV2 virions (Aschauer et al., 2013). Because HCN channels are thought to be primarily expressed in neurons (Honsa, 2014), these features make AAV serotype 9 virions more favorable for both, *in vitro* and *in vivo* experiments, compared to AAV serotype 2. Thus, the increased knock-down potential of constructs delivered by rAAV9 might result from AAV serotype 9 being more efficient in transducing neurons compared with AAV serotype 2 (Fig. 3.6).

#### 4.2 Electrophysiological characterization of HCN-channel knock-down in vitro

Since the individual HCN subtypes are capable to form functional homo- and heterotetrameric ion channels, they contribute significantly to the electrical properties of excitable cells. To investigate the effects of HCN-isoform specific knock-down on electrophysiological properties of hippocampal neurons, whole-cell patch-clamp recordings were utilized. To achieve HCN-channel knock-down, RNAi turned out to be advantageous over CRISPRi as discussed previously. Despite the strong reduction of *hcn*-transcript levels in neurons treated with rAAVs (Fig. 3.6), there was a remarkable discrepancy in  $I_h$ -current related properties obtained from AAV-treated neurons vs. neurons from HCN1 knock-out mice (HCN1<sup>-/-</sup>). While the knock-out of the HCN1 subunit resulted in a hyperpolarizing shift in the half-maximal activation potential ( $V_{1/2}$ ) of approximately -15 mV (Fig. 3.10), HCN1 subunit knock-down shifted  $V_{1/2}$  only by approx. -6 mV (Fig. 3.11). Similarly, the knock-out of the HCN1 subunit resulted in a hyperpolarizing shift of the resting membrane potential ( $V_m$ ) of approx. -3.5 mV, whereas HCN1 subunit knock-down shifted  $V_m$  only by approx. -1.8 mV (Fig. 3.12). Notably, the pronounced reduction in current amplitudes and densities observed in PHNs obtained from HCN1<sup>-/-</sup> mice suggested that the loss of the HCN1 isoform resulted in an almost complete loss of the total  $I_h$ -current conductance. These findings become even more surprising with regard to the *hcn1* transcript expression levels of HCN1<sup>-/-</sup> PHNs. The qRT-PCR data showed that approx. 30 % of total *hcn* transcripts originated from *hcn1* gene expression (Fig. 3.9). An explanation for this discrepancy might be that truncated *hcn1* transcripts could be amplified from cDNA samples of HCN1<sup>-/-</sup> mice (Fig. 3.10). Even though the HCN1 antibody did not detect any HCN1 protein in HCN1<sup>-/-</sup> PHNs, expression even of truncated *hcn1* transcripts might lead to the biosynthesis of short versions of HCN1-channel proteins, that may assemble and alter the properties of heteromeric HCN channels. Notably, coimmunoprecipitation experiments of mouse brain lysates (Much et al., 2003) and co-expression experiments in Chinese hamster ovary (CHO) cells (Ukens and Tytgat, 2001), HEK293 cells (Altomare et al., 2003) and *Xenopus laevis* oocytes (Whitaker et al., 2007) confirmed the existence of HCN1/HCN2; HCN1/HCN4 and HCN2/HCN4 heteromeric channels. Especially the co-expression of HCN1 and HCN2 resulted in heteromeric HCN channels with current properties resembling native  $I_h$ -currents recorded in CA1 pyramidal neurons of mice (Santoro et al., 2000, Chen et al., 2001). Thus, PHNs obtained from HCN1<sup>-/-</sup> mice might still form HCN1/HCN2 heteromeric ion channels, although lacking the pore region and the S6

transmembrane domain of the HCN1 subunits. This might lead to non-functional and/or non-conducting ion channels. Such channels would then resemble  $I_h$ -current amplitudes obtained by blocking total  $I_h$ -currents using ZD7288 or cesium chloride (Fig. 3.16). However, both, HCN-channels and the closely related cyclic nucleotide-gated- (CNG) channels oligomerize due to a conserved domain in the C-linker region of the individual subtypes (Zhou et al., 2004). The knock-out of the HCN1 subunit in HCN1<sup>-/-</sup> mice was achieved by a genomic deletion of the exon encoding the pore region and S6 transmembrane domain (Nolan et al., 2003). Thus, it remains elusive, if a truncated HCN1 protein still harbors the heteromerization domain allowing assembly of heteromeric HCN channels that contain truncated HCN1 subunits.

Notably, basal transcript levels of the *hcn1* and *hcn4* genes in PHNs were rather low compared to *hcn2* transcript levels (Fig. 3.9), suggesting that HCN1 and HCN4 isoforms might serve to diversify native  $I_h$ -current properties by forming heterotetrameric channels (Altomare et al., 2003). Electrophysiological recordings of PHNs showed that both, HCN1 and HCN4 had substantial influences on  $I_h$ -current activation potentials and kinetics. For example, while the knock-down of the fast activating HCN1 isoform led to a deceleration of  $I_h$ -current kinetics, knock-down of the slow activating HCN4 isoform led to an acceleration of  $I_h$ -current kinetics (Figs. 3.14 and 3.15). Similarly, the knock-down of HCN1, which is known to activate at depolarized membrane potentials ( $V_{1/2}$ : -96.1 mV), led to a hyperpolarizing shift in  $I_h$ -current activation potential of approx. 6 mV. Vice versa, the knock-down of HCN4, the subunit known to activate at rather hyperpolarized membrane potentials ( $V_{1/2}$ : -119.3 mV), led to a depolarizing shift in  $I_h$ -current activation potential of approx. 4.6 mV (Fig. 3.11). In addition, only the knock-down of HCN1 induced a change in the resting membrane potential (Fig. 3.12). This observation is in accordance with previous reports (Matsumoto-Makidono et al., 2016) and is accompanied by the finding that HCN1 channels are partially activated at the resting membrane potential and thus provide a resting conductance. Therefore, HCN1 expression in PHNs influences both, passive HCN-channel related membrane properties and  $I_h$ -current properties by forming heteromeric functional ion channels with HCN2 and/or HCN4 (Much et al., 2003). Furthermore, HCN4 expression might modulate  $I_h$ -current kinetics and activation potentials by incorporating this subunit into heterotetrameric ion channels. This would introduce the pronounced sensitivity of the HCN4 subunit for cyclic nucleotides, causing a shift of  $I_h$ -current activation to depolarized potentials (Ishii et al., 1999, Chen et al., 2001). Notably, in a previous study

it has been shown that a knock-down of HCN4 channel expression in the dorsal hippocampus of adult mice led to a pronounced anxiogenic effect, presumably due to altered HCN channel sensitivity for cyclic AMP (Günther et al., 2019).

However, the knock-down of HCN2 in PHNs did neither change the resting membrane potential (Fig. 3.12),  $I_h$ -current activation kinetics (Fig. 3.14 and 3.15), nor  $I_h$ -current activation potentials (Fig. 3.11), as previously reported for the HCN2 knock-out mouse model in CA1 hippocampal neurons (Ludwig et al., 2003). At a first glance these observations were surprising since *hcn2* transcript levels were relatively high in PHNs and accounted for approx. 70 % of all *hcn* transcripts (Fig. 3.9). But, HCN2 homomeric channels were reported to have a higher single channel conductance compared to homomeric HCN1 or HCN4 channels (Michels et al., 2005). Indeed, homomeric HCN2-channel currents recorded from transgenic HEK293 cell-lines had much higher  $I_h$ -current amplitudes and densities, compared to homomeric HCN1- or HCN2-channel currents (Fig. 3.13). Therefore, it was not surprising that a knock-down of HCN2 in PHNs led to the strongest reduction in  $I_h$ -current amplitudes and densities compared to the knock-down of HCN1- or HCN4-subunits (Fig. 3.13). Furthermore, the activation kinetics and potentials of native  $I_h$ -currents recorded in wildtype or shScr-transduced neurons were similar to the kinetics and activation potentials of homomeric HCN2-channel currents recorded in transgenic HEK293 cell-lines. Altogether, these observations suggest that HCN2 subunits were the main contributors for heteromeric  $I_h$ -currents in PHNs. Additionally, the formation of HCN2/HCN1 heteromers (Chen et al., 2001, Ulens and Tytgat, 2001), HCN2/HCN4 heteromers (Whitaker et al., 2007), or even HCN1/HCN4 heteromers (Altomare et al., 2003) equip hippocampal neurons with a powerful mechanism to generate a variety of different HCN channels with distinct electrophysiological and biochemical characteristics based on a relatively small number of genes (Much et al., 2003). The existence of a plethora of  $\beta$ -subunits, scaffolding proteins, and regulatory proteins, i.e. TRIP8b, Caveolin-3 or MiRP1, even increase the variability of HCN channels and may further expand the functional properties of these proteins *in vivo* (Sartiani et al., 2017).

For ion channels exerting their functions at sub-threshold membrane potentials, the remarkable plasticity regarding HCN channel's properties raised the question for which processes this plasticity can be utilized. A prominent feature, especially of HCN1 channels, is that they are partially open at the resting membrane potential (Fig. 3.8). Thus, expression of HCN channels induces a permanent depolarization of the resting membrane

potential, due to the inward current conducted by these non-inactivating channels (Doan and Kunze, 1999). In addition, HCN channels can counteract both, hyperpolarizing and depolarizing input, by either producing a depolarizing inward current due to  $I_h$ -current activation, or by inducing membrane hyperpolarization due to  $I_h$ -current deactivation (Biel et al., 2009). Therefore, rather than solely stabilizing the resting membrane potential, HCN channels are perfectly suited to fine-tune a neuron's response to depolarizing or hyperpolarizing external stimuli (Bender and Baram, 2008). These integrating properties were very prominent and well-studied in CA1 hippocampal neurons (Magee, 1998) and neocortical layer 5 pyramidal cells (Berger et al., 2003). In general, integration of excitatory post-synaptic potentials (EPSPs) at the dendrites must be perfectly controlled, both in time and in space, to generate appropriate output at the soma. However, passive dendritic filtering properties cause a deceleration of distal EPSP time courses compared to proximal EPSPs (for review see (Magee, 2000)). Theoretically, this would lead to a localization dependence of EPSP waveforms, accompanied by a localization dependence of temporal summation properties. Repetitive EPSPs generated at distal dendrites would have higher chances to generate action potentials at the soma, compared to repetitive EPSPs generated at proximal dendrites (Biel et al., 2009). As CA1 pyramidal neurons are known to act as coincidence detectors, this would strongly influence their ability to integrate temporal, precisely timed input from different spatial locations (Pavlov et al., 2011). However, in CA1 pyramidal neurons and neocortical layer 5 pyramidal neurons, this localization dependence is not observed (Magee, 1999). This discrepancy in theory compared to experiment is probably solved by the observation that the density of HCN channels in dendrites of these neurons increases with distance to the soma (Lörincz et al., 2002, Harnett et al., 2015). Thus, HCN channels are organized in a gradient, facilitating EPSP time courses which are increasingly shortened with the distance from the soma (Magee, 1999). This prominent function of HCN channels is accompanied by the finding that the removal of HCN1 from entorhinal cortical neurons in HCN1<sup>-/-</sup> mice, led to a deceleration of EPSPs and thus to an increase in the summation ratio (Huang et al., 2009). Additionally, loss of HCN1 led to larger postsynaptic responses in CA1 neurons which further enhanced the induction of perforant path long term potentiation (LTP). A loss of HCN1 thereby enhanced hippocampal dependent learning and memory and thus emphasized a behavioral role for dendritic integration (Nolan et al., 2004). However, impairment of HCN2 subunit expression in CA1 pyramidal neurons did not change postsynaptic responses. In contrast to the HCN1 knock-out, the HCN2 knock-out did not

constrain LTP in the perforant path by modulating dendritic integration in CA1 pyramidal neurons. This is not surprising, since HCN2 channels are not activated at resting membrane potentials (Fig. 3.8). Therefore, HCN2 channels most likely regulate inhibitory inputs, rather than excitatory input and thereby might contribute to the excitation-inhibition balance in hippocampal CA1 neurons (Ludwig et al., 2003, Matt et al., 2011). In accordance with this finding, time courses of EPSCs were not decelerated in PHNs treated with sh2. However, decay time constants of spontaneous EPSCs, miniature EPSCs, and evoked EPSCs were increased compared to control conditions (Figs. 3.21, 3.22 and 3.23). Even though the electrophysiological recordings of sh2-treated PHNs did not show an increase in  $I_h$ -current kinetics, there might be a shift from heteromeric HCN1/HCN2 channels to HCN1 dominating homomeric channels, as described for  $I_h$ -currents in HCN2 knockout mice (Ludwig et al., 2003, Matt et al., 2011). This would lead to an increase in resting HCN1 channel conductance and to an acceleration of EPSPs. These observations might underpin the role of HCN1 and HCN2 heteromeric channels in balancing excitation-inhibition in neurons. Interestingly, knock-down of HCN2 additionally induced paired-pulse depression without altering the initial amplitude of evoked EPSCs (Fig. 3.23). This observation suggested also a presynaptic role of HCN2. Notably, both, HCN1 and HCN2 isoforms were identified in presynaptic locations (Boyes et al., 2007), and presynaptic HCN1 channels were described to regulate calcium channel activity (Huang et al., 2011). Thus, depression of synaptic responses might be explained by decreased calcium influx at the presynapse. Because neurotransmitter release is tightly regulated by calcium, even small activity-dependent changes in calcium influx might lead to presynaptic plasticity mechanisms (Fioravante and Regehr, 2011). Furthermore, HCN channels are known to control resting sodium concentrations in nerve termini. Thus a change in HCN channel activity might affect intracellular sodium concentrations and thereby eventually alters neurotransmitter release from the presynapse (Huang and Trussell, 2014). To what extent the properties of HCN2 channels regulate pre-synaptic neurotransmission and dendritic integration *in vivo* remains elusive. On the one hand, the dendritic distribution of HCN channels in PHNs does not resemble the distal/proximal gradient found in native hippocampal CA1 pyramidal neurons (Noam et al., 2010). This result is in accordance with a previous study showing that the gradient-like distribution of HCN channels is controlled by an activity-dependent mechanism (Shin and Chetkovich, 2007). On the other hand, HCN-channel expression levels in CA1 pyramidal neurons are known to undergo developmental changes (Fig. 4.2).

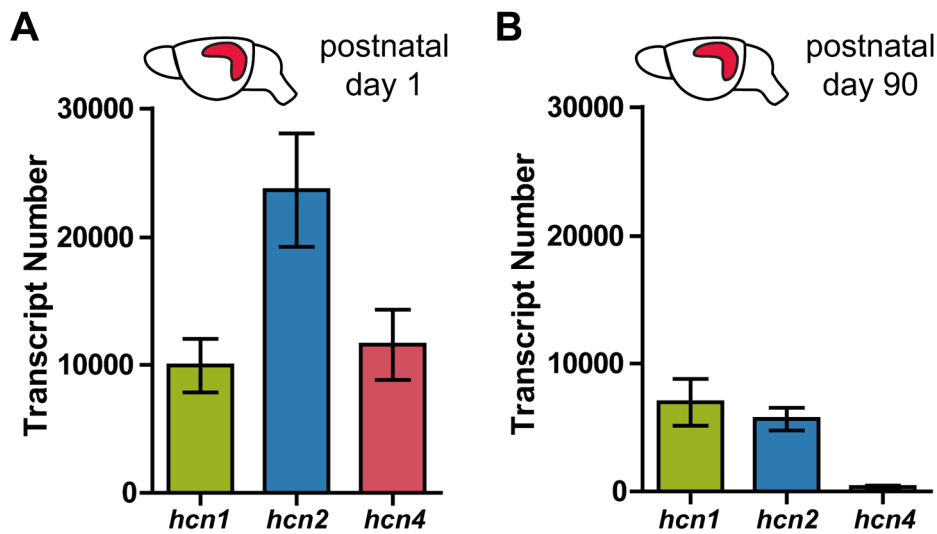


**Figure 4.2: Developmental changes in HCN-channel transcript levels**

(A and B) Quantitative PCR analysis of *hcn1*, *hcn2* and *hcn4* transcript levels in dorsal hippocampal tissue (A) of animals from postnatal day 1 and (B) of animals from postnatal day 90. First-strand cDNA was synthesized on 1  $\mu$ g of total RNA. Data were obtained from at least 5 different of animals. Results are depicted as mean  $\pm$  standard deviation.

These quantitative changes in HCN1, HCN2 and HCN4 isoform expression levels might indicate a ‘molecular switch’ from an early-postnatal slow-activating, cAMP-sensitive  $I_h$ -current (HCN2/HCN4 dominant) to a mature fast-activating, cAMP-insensitive  $I_h$ -current (HCN1 dominant) (Surges et al., 2006, Brewster et al., 2007). Notably, these changes in HCN isoform expression levels correlate with a developmental transition from slow network oscillations in the immature CA1 network towards theta frequency oscillation in the mature CA1 network. Thus, developmental regulation of HCN gene expression might modulate neuronal resonance behavior to shape pyramidal neuron firing frequencies (Bender and Baram, 2008). Since PHNs were prepared from newborn animals and grow for approx. 2 weeks, they might recapitulate the HCN expression level of immature neurons (Fig. 3.9). Based on these findings, PHNs and heterologous expression systems in general, might be limited in their ability to capture the full spectrum of HCN channel dynamics and physiological functions.

### 4.3. *In vivo* HCN2-channel knock-down

To overcome some limitations of hippocampal neurons studied *in vitro* and to investigate the role of the HCN2 isoform *in vivo*, rAAV9 encoding sh2 or shScr were injected into the dorsal hippocampus of adult mice. Previous studies demonstrated that mice with reduced  $I_h$ -currents due to the loss of HCN1, HCN2 or the auxiliary scaffolding protein TRIP8b showed antidepressant-like behavior (Ludwig et al., 2003, Nolan et al., 2004, Lewis et al., 2011, Matt et al., 2011) along with subunit-specific behavioral changes like impaired motor-learning or improved short- and long-term spatial learning and memory (Nolan et al., 2003). Notably, the behavioral changes observed upon injection of AAV9-sh2 did not resemble previous reports. Instead, the injected animals showed no changes in anxiety- or fear-related behaviors. However, the injected animals had deficits in spatial memory and showed increased locomotor activity. Although a knock-down of the HCN2 isoform was detected in sh2 injected mice, this was accompanied by unexpected reductions in the transcript levels of several, even unrelated neuronally expressed genes (Fig. 3.29). These ‘unspecific’ knock-down effects were not detected in sh2 treated PHNs (Fig. 3.30). The immunohistochemical analysis finally shed some light on these inconsistencies. Especially the stainings, including the neuronal marker NeuN, showed that the previously observed phenomena might be explained by neurodegenerative processes, ultimately leading to a loss of the hippocampal CA1 pyramidal cell layer (Fig. 3.32). The loss of these neurons was accompanied by increased levels of active Caspase3 and GFAP expression compared to control conditions (Fig. 3.35), indicating an apoptotic mechanism (Tzeng et al., 2013). Possible explanations for these findings might be unspecific off-target effects of sh2 RNA or a contamination of the sh2-encoding virus batch. However, previous *in silico* and *in vitro* experiments using the same virus batch were inconspicuous and the use of an appropriate scrambled control shRNA ruled out the possibility of cytotoxic effects emerging from the hU6 promoter as previously observed (Günther et al., 2017).

Interestingly, the CA1 pyramidal cell layer was found to express high levels of HCN1 and HCN2 channel isoforms (Fig. 3.31). However, despite the finding that GFP expression, originating from the injected virus, was also found in the dentate gyrus (DG), there were no indications for apoptotic mechanisms in the DG, which expresses only basal levels of HCN isoform genes (Fig. 3.33). Furthermore, even after 9 weeks post injection, there were no indications for further spreading of the neurodegenerative and apoptotic processes (Fig. 3.34). Thus, the degeneration of neurons in the CA1 region might be

attributed to the knock-down of HCN2. Supporting this idea, a recent publication showed that CA1 pyramidal neurons of the dorsal hippocampus (DHC) express more HCN2 subunits compared to CA1 pyramidal neurons of the ventral hippocampus (VHC) (Dougherty et al., 2013). This indicates, that the physiological function of HCN2 might be more relevant to the DHC, than to the VHC. In accordance with this finding, the behavioral changes observed after injection of rAAV9-sh2 into the dorsal hippocampus were mainly attributed to DHC-related defects. While changes in anxiety- or fear-related behaviors were mainly attributed to VHC (Henke, 1990, Bannerman et al., 2003), changes in spatial memory were mainly attributed to DHC (Moser et al., 1995). Moreover, HCN channel expression is not only tightly regulated in space, but also in time (Fig. 4.2) (Bender et al., 2001, Surges et al., 2006, Bender and Baram, 2008). This further emphasizes that any interference with the exquisitely regulated protein expression could lead to dramatic changes in neuronal homeostasis. Even though there are no reports on compensatory up- or downregulations of gene expression in HCN1 or HCN2 knockout animals, the interference with gene expression at a certain timepoint during postnatal stages might cause severe functional implications.

Mechanistically, a knock-down of HCN2 could lead to a disturbance of excitation-inhibition balance. As previously mentioned, HCN channels are regulated by neuronal activity (Shin and Chetkovich, 2007). Thus, the magnitude of somatic  $I_h$ -current is dependent on excitatory synaptic activity, which has been proposed as a homeostatic mechanism for regulating neuronal excitability (van Welie et al., 2004). This mechanism may have an additional homeostatic role by narrowing the time window for coincidence detection during increased neuronal activity. Vice versa, the coincidence detection window would broaden with decreasing synaptic activity (Pavlov et al., 2011). Interfering with this mechanism might cause overexcitation and ultimately could lead to neurodegeneration due to the cytotoxic actions of excessive glutamate (Lewerenz and Maher, 2015). Supporting this idea, propofol, a commonly used anesthetic known to act on both, GABA<sub>A</sub> receptors and HCN channels at clinically relevant concentrations (Cacheaux et al., 2005), induces apoptosis of CA1 pyramidal neurons in mice (Yan et al., 2017). If the neurodegenerative effect of propofol is caused by its direct actions on HCN channels has to be experimentally proven. Additionally, point mutations in the *hcn2* gene were uncovered in patients suffering from febrile seizures (Dibbens et al., 2010) or epilepsy (Tang et al., 2008, DiFrancesco et al., 2011). These mutations were thought to lower the threshold of action potentials and thereby strongly increase excitability.

Another possibility which might seem unreasonable at a first glance, should not be overlooked. There might be other cell-types involved as potential contributors for neurodegeneration (Chang et al., 2019). Notably, HCN channels are not exclusively expressed in neurons. They have been additionally described in reactive astrocytes (Rusnakova et al., 2013, Honsa, 2014) and in microglia (Fig. 4.3). Interestingly, HCN channels in microglia are localized in intracellular compartments, rather than in the plasma membrane, and thus do not give rise to typically  $I_h$ -currents or sag-potentials, which can be measured by whole-cell patch-clamp recordings (Fig. 4.3 C).

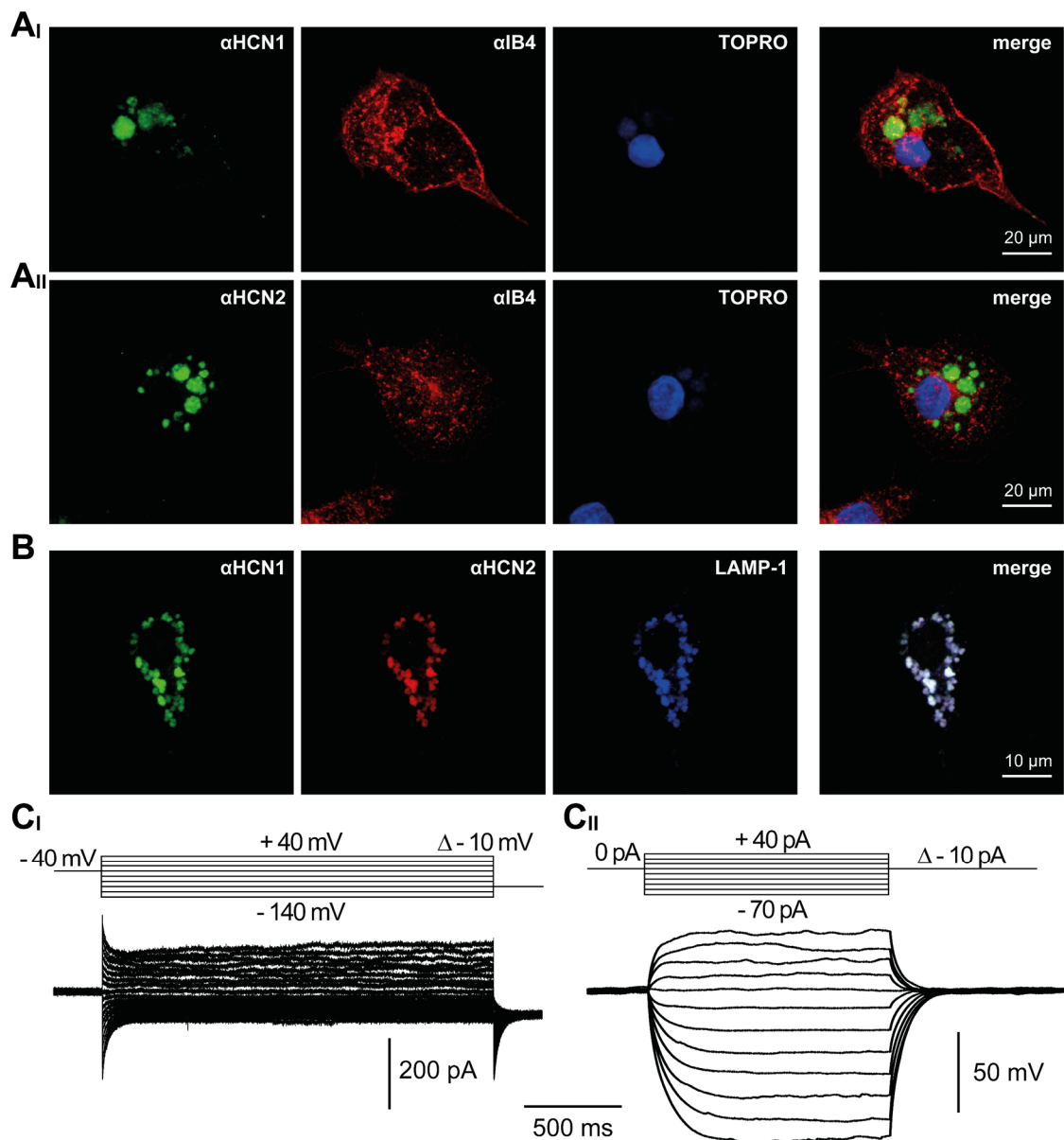


**Figure 4.3: HCN expression in rat microglia**

(A and B) Representative immunofluorescent images showing the expression of (A<sub>i</sub>) HCN1, (A<sub>ii</sub>) HCN2, and (B) colocalization of both proteins in lysosomes of microglia derived from rat cortex. HCN channel isoforms were stained with specific anti ( $\alpha$ )HCN1 and  $\alpha$ HCN2 antibodies. Microglia were stained using the

microglial marker isolectin IB4 ( $\alpha$ IB4). Lysosomes were stained using a lysosomal-associated membrane protein 1 (LAMP-1) antibody ( $\alpha$ LAMP-1). Primary antibodies were combined with fluorescently labeled secondary antibodies and nuclei were stained with TOPRO (blue). (CI) Representative voltage stimulation protocol and corresponding current traces and (CII) representative current stimulation protocol and corresponding voltage traces of whole-cell patch-clamp recordings derived from rat cortical microglia cultured cells.

Both, HCN1 and HCN2 subunits were identified in lysosomes, as indicated by the colocalization of the lysosomal marker protein LAMP-1 (Fig. 4.3 A and B). This observation is supported by data showing that microglia express a splice variant of the auxiliary protein TRIP8b (TRIP8b-1b) (personal communication with Dr. Sabine Vay), targeting HCN channels to intracellular compartments and thereby decreasing the surface expression (Santoro et al., 2004, Santoro et al., 2009). However, the function of HCN channels in lysosomes was not investigated so far, even though there might be a physiological role for  $I_h$ -currents in intracellular vesicles (Calejo et al., 2014). Since AAV serotype 9 virions are known to transduce a proportion of astrocytes and microglia in the hippocampus (Aschauer et al., 2013), this raises the possibility that manipulation of HCN expression in glia cells might be additionally involved in the neurodegenerating processes observed in the CA1 region. However, the function of HCN channels in glial cells, as well as their potential contribution to neurodegenerative mechanisms remains elusive and thus should be experimentally examined.

#### 4.4 Summary and Outlook

In summary, the presented thesis demonstrated the capability of virus-mediated knock-down for examining protein functions in cultured neurons *in vitro* and neuronal networks *in vivo*. This approach facilitated to elaborate on the differential functions of individual HCN channel subunits in contributing to basic electric properties of primary hippocampal neurons. Furthermore, the subunit-specific knock-down enabled to characterize the role of HCN2 in excitatory signal transduction. Unexpectedly, the injection of recombinants evoking a knock-down of HCN2 in the dorsal hippocampus of adult mice resulted in a severe degeneration of the CA1 pyramidal cell layer. If this degeneration is attributed and caused by the loss of HCN2, or provoked by difficult to grasp side-effects remains elusive and is worth for further investigation.

To examine specifically the temporal implications of HCN2 channel functions in CA1 pyramidal cells and to rule out the possibility that non-neuronal cells are engaged in the neurodegenerative mechanism observed upon rAAV9-sh2 injection, alternative experimental strategies may be necessary. A pyramidal neuron-specific temporal controllable deletion of the HCN2 isoform might be a reasonable strategy. Mice harboring a NEX-CreERT2 transgene (Agarwal et al., 2012) induce Cre expression exclusively in pyramidal neurons, which can be temporally controlled by injection of tamoxifen. In such mice, the neuronal helix-loop-helix protein-1 NEX gene promoter (Schwab et al., 2000) was used to drive Cre recombinase expression in pyramidal neurons, while the mutant estrogen receptor (ERT2) ligand binding domain fused with the Cre recombinase was used to temporally control the Cre recombinase activity. Crossing these mice to a strain harboring loxP-flanked exons 2 and 3 of the HCN2 channel gene, would lead to a loss of the HCN2 isoform in pyramidal neurons (Matt et al., 2011) which can be temporally controlled by application of tamoxifen. However, since pyramidal neurons are not exclusively located in the hippocampus, the injection of AAVs encoding the Cre recombinase under control of the NEX promoter into the hippocampus of mice carrying the loxP-flanked exons 2 and 3 of the HCN2 isoform gene, might be more closely related to the experimental conditions described in this thesis. Similar transgenic approaches could also be used to knock-out the HCN2 gene in glial cell-types to further investigate the physiological function of HCN channels in non-neuronal cells. However, because little is known about HCN channels in glial cells, additional *in vitro* experiments might be necessary to gain a basic knowledge of the physiological role of HCN channels in intracellular compartments of non-neuronal cells.

---

# Chapter 5

## Bibliography

---

- Agarwal, A., Dibaj, P., Kassmann, C. M., Goebbels, S., Nave, K. A. & Schwab, M. H. 2012. In vivo imaging and noninvasive ablation of pyramidal neurons in adult NEX-CreERT2 mice. *Cereb Cortex*, 22, 1473-86.
- Altomare, C., Terragni, B., Brioschi, C., Milanesi, R., Pagliuca, C., Viscomi, C., Moroni, A., Baruscotti, M. & Difrancesco, D. 2003. Heteromeric HCN1-HCN4 channels: a comparison with native pacemaker channels from the rabbit sinoatrial node. *J Physiol*, 549, 347-59.
- Araki, T., Ito, M. & Oshima, T. 1961. Potential changes produced by application of current steps in motoneurons. *Nature*, 191, 1104-5.
- Aschauer, D. F., Kreuz, S. & Rumpel, S. 2013. Analysis of transduction efficiency, tropism and axonal transport of AAV serotypes 1, 2, 5, 6, 8 and 9 in the mouse brain. *PLoS One*, 8, e76310.
- Azene, E. M., Xue, T. & Li, R. A. 2003. Molecular basis of the effect of potassium on heterologously expressed pacemaker (HCN) channels. *J Physiol*, 547, 349-56.
- Baghirova, S., Hughes, B. G., Hendzel, M. J. & Schulz, R. 2015. Sequential fractionation and isolation of subcellular proteins from tissue or cultured cells. *MethodsX*, 2, 440-5.
- Banks, M. I., Pearce, R. A. & Smith, P. H. 1993. Hyperpolarization-activated cation current (I<sub>h</sub>) in neurons of the medial nucleus of the trapezoid body: voltage-clamp analysis and enhancement by norepinephrine and cAMP suggest a modulatory mechanism in the auditory brain stem. *J Neurophysiol*, 70, 1420-32.
- Bannerman, D. M., Grubb, M., Deacon, R. M. J., Yee, B. K., Feldon, J. & Rawlins, J. N. P. 2003. Ventral hippocampal lesions affect anxiety but not spatial learning. *Behavioural Brain Research*, 139, 197-213.
- Barker, G. R. & Warburton, E. C. 2011. When is the hippocampus involved in recognition memory? *J Neurosci*, 31, 10721-31.
- Baruscotti, M., Bucchi, A. & Difrancesco, D. 2005. Physiology and pharmacology of the cardiac pacemaker ("funny") current. *Pharmacol Ther*, 107, 59-79.
- Beischlag, T. V., Marchese, A., Meador-Woodruff, J.H., Damask, S.P., O'dowd, B.F., Tyndale, R.F., Van Tol, H.H.M., Seeman, P., Niznik, H.B 1995. The Human Dopamine D5 Receptor Gene: Cloning and Characterization of the 5'-Flanking and Promoter Region. *Biochem.*, 34, 5960-5970.
- Bender, R. A. & Baram, T. Z. 2008. Hyperpolarization activated cyclic-nucleotide gated (HCN) channels in developing neuronal networks. *Prog Neurobiol*, 86, 129-40.
- Bender, R. A., Brewster, A., Santoro, B., Ludwig, A., Hofmann, F., Biel, M. & Baram, T. Z. 2001. Differential and age-dependent expression of hyperpolarization-activated, cyclic

- nucleotide-gated cation channel isoforms 1-4 suggests evolving roles in the developing rat hippocampus. *Neuroscience*, 106, 689-98.
- Berger, T., Senn, W. & Luscher, H. R. 2003. Hyperpolarization-activated current Ih disconnects somatic and dendritic spike initiation zones in layer V pyramidal neurons. *J Neurophysiol*, 90, 2428-37.
- Biel, M. & Michalakis, S. 2007. Function and Dysfunction of CNG Channels: Insights from Channelopathies and Mouse Models. *Molecular Neurobiology*, 35, 266-277.
- Biel, M., Wahl-Schott, C., Michalakis, S. & Zong, X. 2009. Hyperpolarization-activated cation channels: from genes to function. *Physiol Rev*, 89, 847-85.
- Boettcher, M. & Mcmanus, M. T. 2015. Choosing the Right Tool for the Job: RNAi, TALEN, or CRISPR. *Mol Cell*, 58, 575-85.
- Boyes, J., Bolam, J. P., Shigemoto, R. & Stanford, I. M. 2007. Functional presynaptic HCN channels in the rat globus pallidus. *Eur J Neurosci*, 25, 2081-92.
- Brewster, A. L., Chen, Y., Bender, R. A., Yeh, A., Shigemoto, R. & Baram, T. Z. 2007. Quantitative analysis and subcellular distribution of mRNA and protein expression of the hyperpolarization-activated cyclic nucleotide-gated channels throughout development in rat hippocampus. *Cereb Cortex*, 17, 702-12.
- Brown, H. F., DiFrancesco, D. & Noble, S. J. 1979. How does adrenaline accelerate the heart? *Nature*, 280, 235-6.
- Cacheaux, L. P., Topf, N., Tibbs, G. R., Schaefer, U. R., Levi, R., Harrison, N. L., Abbott, G. W. & Goldstein, P. A. 2005. Impairment of hyperpolarization-activated, cyclic nucleotide-gated channel function by the intravenous general anesthetic propofol. *J Pharmacol Exp Ther*, 315, 517-25.
- Calcedo, R., Morizono, H., Wang, L., Mccarter, R., He, J., Jones, D., Batshaw, M. L. & Wilson, J. M. 2011. Adeno-associated virus antibody profiles in newborns, children, and adolescents. *Clin Vaccine Immunol*, 18, 1586-8.
- Calejo, A. I., Jorgacevski, J., Rituper, B., Gucek, A., Pereira, P. M., Santos, M. A., Potokar, M., Vardjan, N., Kreft, M., Goncalves, P. P. & Zorec, R. 2014. Hyperpolarization-activated cyclic nucleotide-gated channels and cAMP-dependent modulation of exocytosis in cultured rat lactotrophs. *J Neurosci*, 34, 15638-47.
- Chang, K., Elledge, S. J. & Hannon, G. J. 2006. Lessons from Nature: microRNA-based shRNA libraries. *Nat Methods*, 3, 707-14.
- Chang, X., Wang, J., Jiang, H., Shi, L. & Xie, J. 2019. Hyperpolarization-Activated Cyclic Nucleotide-Gated Channels: An Emerging Role in Neurodegenerative Diseases. *Front Mol Neurosci*, 12, 141.
- Chen, C. & Okayama, H. 1987. High-efficiency transformation of mammalian cells by plasmid DNA. *Mol Cell Biol*, 7, 2745-52.
- Chen, S., Wang, J. & Siegelbaum, S. A. 2001. Properties of hyperpolarization-activated pacemaker current defined by coassembly of HCN1 and HCN2 subunits and basal modulation by cyclic nucleotide. *J Gen Physiol*, 117, 491-504.
- Chen, T. W., Wardill, T. J., Sun, Y., Pulver, S. R., Renninger, S. L., Baohan, A., Schreiter, E. R., Kerr, R. A., Orger, M. B., Jayaraman, V., Looger, L. L., Svoboda, K. & Kim, D. S. 2013. Ultrasensitive fluorescent proteins for imaging neuronal activity. *Nature*, 499, 295-300.
- Cho, A., Haruyama, N. & Kulkarni, A. B. 2009. Generation of transgenic mice. *Curr Protoc Cell Biol*, Chapter 19, Unit 19 11.
- Cong, L., Ran, F. A., Cox, D., Lin, S., Barretto, R., Habib, N., Hsu, P. D., Wu, X., Jiang, W., Marraffini, L. A. & Zhang, F. 2013. Multiplex genome engineering using CRISPR/Cas systems. *Science*, 339, 819-23.

- Craven, K. B. & Zagotta, W. N. 2006. CNG and HCN channels: two peas, one pod. *Annu Rev Physiol*, 68, 375-401.
- Dibbens, L. M., Reid, C. A., Hodgson, B., Thomas, E. A., Phillips, A. M., Gazina, E., Cromer, B. A., Clarke, A. L., Baram, T. Z., Scheffer, I. E., Berkovic, S. F. & Petrou, S. 2010. Augmented currents of an HCN2 variant in patients with febrile seizure syndromes. *Ann Neurol*, 67, 542-6.
- Difrancesco, D. 1981. A study of the ionic nature of the pace-maker current in calf Purkinje fibres. *J Physiol*, 314, 377-93.
- Difrancesco, D. 1986. Characterization of single pacemaker channels in cardiac sino-atrial node cells. *Nature*, 324, 470-3.
- Difrancesco, D. 2019. Comparing pathways for long-term heart rate modulation by the funny current. *J Gen Physiol*, 151, 1066-1069.
- Difrancesco, D. & Tortora, P. 1991. Direct activation of cardiac pacemaker channels by intracellular cyclic AMP. *Nature*, 351, 145-7.
- Difrancesco, J. C., Barbuti, A., Milanesi, R., Coco, S., Bucchi, A., Bottelli, G., Ferrarese, C., Franceschetti, S., Terragni, B., Baruscotti, M. & Difrancesco, D. 2011. Recessive loss-of-function mutation in the pacemaker HCN2 channel causing increased neuronal excitability in a patient with idiopathic generalized epilepsy. *J Neurosci*, 31, 17327-37.
- Doan, T. N. & Kunze, D. L. 1999. Contribution of the hyperpolarization-activated current to the resting membrane potential of rat nodose sensory neurons. *J Physiol*, 514 ( Pt 1), 125-38.
- Dominguez, A. A., Lim, W. A. & Qi, L. S. 2016. Beyond editing: repurposing CRISPR-Cas9 for precision genome regulation and interrogation. *Nat Rev Mol Cell Biol*, 17, 5-15.
- Doudna, J. A. & Charpentier, E. 2014. Genome editing. The new frontier of genome engineering with CRISPR-Cas9. *Science*, 346, 1258096.
- Dougherty, K. A., Nicholson, D. A., Diaz, L., Buss, E. W., Neuman, K. M., Chetkovich, D. M. & Johnston, D. 2013. Differential expression of HCN subunits alters voltage-dependent gating of h-channels in CA1 pyramidal neurons from dorsal and ventral hippocampus. *J Neurophysiol*, 109, 1940-53.
- Doyle, D. A., Morais Cabral, J., Pfuetzner, R. A., Kuo, A., Gulbis, J. M., Cohen, S. L., Chait, B. T. & Mackinnon, R. 1998. The structure of the potassium channel: molecular basis of K<sup>+</sup> conduction and selectivity. *Science*, 280, 69-77.
- Dreos, R., Ambrosini, G., Perier, R. C. & Bucher, P. 2015. The Eukaryotic Promoter Database: expansion of EPDnew and new promoter analysis tools. *Nucleic Acids Res*, 43, D92-6.
- Elbashir, S. M., Harborth, J., Lendeckel, W., Yalcin, A., Weber, K. & Tuschl, T. 2001. Duplexes of 21-nucleotide RNAs mediate RNA interference in cultured mammalian cells. *Nature*, 411, 494-8.
- Fain, G. L., Quandt, F. N., Bastian, B. L. & Gerschenfeld, H. M. 1978. Contribution of a caesium-sensitive conductance increase to the rod photoresponse. *Nature*, 272, 466-9.
- Felix, R., Sandoval, A., Sanchez, D., Gomora, J. C., De La Vega-Beltran, J. L., Trevino, C. L. & Darszon, A. 2003. ZD7288 inhibits low-threshold Ca(2+) channel activity and regulates sperm function. *Biochem Biophys Res Commun*, 311, 187-92.
- Fioravante, D. & Regehr, W. G. 2011. Short-term forms of presynaptic plasticity. *Curr Opin Neurobiol*, 21, 269-74.
- Fire, A., Xu, S., Montgomery, M. K., Kostas, S. A., Driver, S. E. & Mello, C. C. 1998. Potent and specific genetic interference by double-stranded RNA in *Caenorhabditis elegans*. *Nature*, 391, 806-11.
- Friedland, A. E., Tzur, Y. B., Esvelt, K. M., Colaiacovo, M. P., Church, G. M. & Calarco, J. A. 2013. Heritable genome editing in *C. elegans* via a CRISPR-Cas9 system. *Nat Methods*, 10, 741-3.

- Fröhlich, F. 2016. Microcircuits of the Hippocampus. *Network Neuroscience*.
- Frohman, M. A. 1994. On beyond classic RACE (rapid amplification of cDNA ends). *PCR Methods Appl*, 4, S40-58.
- Gaj, T., Gersbach, C. A. & Barbas, C. F., 3rd 2013. ZFN, TALEN, and CRISPR/Cas-based methods for genome engineering. *Trends Biotechnol*, 31, 397-405.
- Gasparini, S. & DiFrancesco, D. 1997. Action of the hyperpolarization-activated current (I<sub>h</sub>) blocker ZD 7288 in hippocampal CA1 neurons. *Pflugers Arch*, 435, 99-106.
- Gauss, R., Seifert, R. & Kaupp, U. B. 1998. Molecular identification of a hyperpolarization-activated channel in sea urchin sperm. *Nature*, 393, 583-7.
- Gilbert, L. A., Horlbeck, M. A., Adamson, B., Villalta, J. E., Chen, Y., Whitehead, E. H., Guimaraes, C., Panning, B., Ploegh, H. L., Bassik, M. C., Qi, L. S., Kampmann, M. & Weissman, J. S. 2014. Genome-Scale CRISPR-Mediated Control of Gene Repression and Activation. *Cell*, 159, 647-61.
- Gilbert, L. A., Larson, M. H., Morsut, L., Liu, Z., Brar, G. A., Torres, S. E., Stern-Ginossar, N., Brandman, O., Whitehead, E. H., Doudna, J. A., Lim, W. A., Weissman, J. S. & Qi, L. S. 2013. CRISPR-mediated modular RNA-guided regulation of transcription in eukaryotes. *Cell*, 154, 442-51.
- Green, M. E., Edwards, G., Kirkup, A. J., Miller, M. & Weston, A. H. 1996. Pharmacological characterization of the inwardly-rectifying current in the smooth muscle cells of the rat bladder. *Br J Pharmacol*, 119, 1509-18.
- Green, M. R. 2012. *Molecular cloning : a laboratory manual* / Michael R. Green, Joseph Sambrook, Cold Spring Harbor, N.Y, Cold Spring Harbor Laboratory Press.
- Grieger, J. C. & Samulski, R. J. 2005. Packaging capacity of adeno-associated virus serotypes: impact of larger genomes on infectivity and postentry steps. *J Virol*, 79, 9933-44.
- Groner, A. C., Meylan, S., Ciuffi, A., Zangger, N., Ambrosini, G., Denervaud, N., Bucher, P. & Trono, D. 2010. KRAB-zinc finger proteins and KAP1 can mediate long-range transcriptional repression through heterochromatin spreading. *PLoS Genet*, 6, e1000869.
- Günther, A. 2016. *Pacemaker channels in cardiomyocytes, hippocampal neurons, and murine behavior*. Dr. rer. nat., University of Cologne.
- Günther, A., Luczak, V., Abel, T. & Baumann, A. 2017. Caspase-3 and GFAP as early markers for apoptosis and astrogliosis in shRNA-induced hippocampal cytotoxicity. *J Exp Biol*, 220, 1400-1404.
- Günther, A., Luczak, V., Gruteser, N., Abel, T. & Baumann, A. 2019. HCN4 knockdown in dorsal hippocampus promotes anxiety-like behavior in mice. *Genes Brain Behav*, 18, e12550.
- Guzman, R. E., Alekov, A. K., Filippov, M., Hegermann, J. & Fahlke, C. 2014. Involvement of ClC-3 chloride/proton exchangers in controlling glutamatergic synaptic strength in cultured hippocampal neurons. *Front Cell Neurosci*, 8, 143.
- Guzman, R. E., Schwarz, Y. N., Rettig, J. & Bruns, D. 2010. SNARE force synchronizes synaptic vesicle fusion and controls the kinetics of quantal synaptic transmission. *J Neurosci*, 30, 10272-81.
- Halliwell, J. V. & Adams, P. R. 1982. Voltage-clamp analysis of muscarinic excitation in hippocampal neurons. *Brain Res*, 250, 71-92.
- Hamill, O. P., Marty, A., Neher, E., Sakmann, B. & Sigworth, F. J. 1981. Improved patch-clamp techniques for high-resolution current recording from cells and cell-free membrane patches. *Pflugers Arch*, 391, 85-100.
- Harnett, M. T., Magee, J. C. & Williams, S. R. 2015. Distribution and function of HCN channels in the apical dendritic tuft of neocortical pyramidal neurons. *J Neurosci*, 35, 1024-37.

- Harris, N. C. & Constanti, A. 1995. Mechanism of block by ZD 7288 of the hyperpolarization-activated inward rectifying current in guinea pig substantia nigra neurons in vitro. *J Neurophysiol*, 74, 2366-78.
- Heigwer, F., Kerr, G. & Boutros, M. 2014. E-CRISP: fast CRISPR target site identification. *Nat Methods*, 11, 122-3.
- Henke, P. G. 1990. Hippocampal pathway to the amygdala and stress ulcer development. *Brain Res Bull*, 25, 691-5.
- Hermonat, P. L. & Muzyczka, N. 1984. Use of adeno-associated virus as a mammalian DNA cloning vector: transduction of neomycin resistance into mammalian tissue culture cells. *Proc Natl Acad Sci U S A*, 81, 6466-70.
- Hommel, J. D., Sears, R. M., Georgescu, D., Simmons, D. L. & Dileone, R. J. 2003. Local gene knockdown in the brain using viral-mediated RNA interference. *Nat Med*, 9, 1539-44.
- Honsa, P. P., H.; Harantova, L.; Butenko, O.; Kriska, J.; Dzamba, D.; Rusnakova, V.; Valihrach, L.; Kubista, M.; Anderova, M.; 2014. Increased expression of hyperpolarization-activated cyclic nucleotide-gated (HCN) channels in reactive astrocytes following ischemia. *Glia*, 62, 2004-21.
- Huang, H. & Trussell, L. O. 2014. Presynaptic HCN channels regulate vesicular glutamate transport. *Neuron*, 84, 340-6.
- Huang, W. & Li, M. D. 2009. Differential allelic expression of dopamine D1 receptor gene (DRD1) is modulated by microRNA miR-504. *Biol Psychiatry*, 65, 702-5.
- Huang, Z., Lujan, R., Kadurin, I., Uebele, V. N., Renger, J. J., Dolphin, A. C. & Shah, M. M. 2011. Presynaptic HCN1 channels regulate Cav3.2 activity and neurotransmission at select cortical synapses. *Nat Neurosci*, 14, 478-86.
- Huang, Z., Walker, M. C. & Shah, M. M. 2009. Loss of dendritic HCN1 subunits enhances cortical excitability and epileptogenesis. *J Neurosci*, 29, 10979-88.
- Ishii, T. M., Takano, M. & Ohmori, H. 2001. Determinants of activation kinetics in mammalian hyperpolarization-activated cation channels. *J Physiol*, 537, 93-100.
- Ishii, T. M., Takano, M., Xie, L. H., Noma, A. & Ohmori, H. 1999. Molecular characterization of the hyperpolarization-activated cation channel in rabbit heart sinoatrial node. *J Biol Chem*, 274, 12835-9.
- Jarrard, L. E. 1993. On the role of the hippocampus in learning and memory in the rat. *Behavioral and Neural Biology*, 60, 9-26.
- Jiang, W., Bikard, D., Cox, D., Zhang, F. & Marraffini, L. A. 2013. RNA-guided editing of bacterial genomes using CRISPR-Cas systems. *Nat Biotechnol*, 31, 233-9.
- Jimenez, J. C., Su, K., Goldberg, A. R., Luna, V. M., Biane, J. S., Ordek, G., Zhou, P., Ong, S. K., Wright, M. A., Zweifel, L., Paninski, L., Hen, R. & Kheirbek, M. A. 2018. Anxiety Cells in a Hippocampal-Hypothalamic Circuit. *Neuron*, 97, 670-683 e6.
- Jinek, M., Chylinski, K., Fonfara, I., Hauer, M., Doudna, J. A. & Charpentier, E. 2012. A programmable dual-RNA-guided DNA endonuclease in adaptive bacterial immunity. *Science*, 337, 816-21.
- Jinek, M., East, A., Cheng, A., Lin, S., Ma, E. & Doudna, J. 2013. RNA-programmed genome editing in human cells. *Elife*, 2, e00471.
- Joung, J. K. & Sander, J. D. 2013. TALENs: a widely applicable technology for targeted genome editing. *Nat Rev Mol Cell Biol*, 14, 49-55.
- Kaschuba, D. 2010. *Schrittmacherkanäle im olfaktorischen Epithel der Maus*. Dr. rer. nat., University Cologne.
- Kase, D. & Imoto, K. 2012. The Role of HCN Channels on Membrane Excitability in the Nervous System. *J Signal Transduct*, 2012, 619747.

- Kaupp, U. B. & Seifert, R. 2001. Molecular diversity of pacemaker ion channels. *Annu Rev Physiol*, 63, 235-57.
- Kaupp, U. B. & Seifert, R. 2002. Cyclic nucleotide-gated ion channels. *Physiol Rev*, 82, 769-824.
- Klug, A. 2010. The discovery of zinc fingers and their applications in gene regulation and genome manipulation. *Annu Rev Biochem*, 79, 213-31.
- Kopp-Scheinflug, C., Pigott, B. M. & Forsythe, I. D. 2015. Nitric oxide selectively suppresses IH currents mediated by HCN1-containing channels. *J Physiol*, 593, 1685-700.
- Kotterman, M. A. & Schaffer, D. V. 2014. Engineering adeno-associated viruses for clinical gene therapy. *Nat Rev Genet*, 15, 445-51.
- Laemmli, U. K. 1970. Cleavage of structural proteins during the assembly of the head of bacteriophage T4. *Nature*, 227, 680-5.
- Larson, M. H., Gilbert, L. A., Wang, X., Lim, W. A., Weissman, J. S. & Qi, L. S. 2013. CRISPR interference (CRISPRi) for sequence-specific control of gene expression. *Nat Protoc*, 8, 2180-96.
- Lee, C. H. & Mackinnon, R. 2017. Structures of the Human HCN1 Hyperpolarization-Activated Channel. *Cell*, 168, 111-120 e11.
- Leung, R. K. & Whittaker, P. A. 2005. RNA interference: from gene silencing to gene-specific therapeutics. *Pharmacol Ther*, 107, 222-39.
- Lewerenz, J. & Maher, P. 2015. Chronic Glutamate Toxicity in Neurodegenerative Diseases-What is the Evidence? *Front Neurosci*, 9, 469.
- Lewis, A. S., Vaidya, S. P., Blaiss, C. A., Liu, Z., Stoub, T. R., Brager, D. H., Chen, X., Bender, R. A., Estep, C. M., Popov, A. B., Kang, C. E., Van Veldhoven, P. P., Bayliss, D. A., Nicholson, D. A., Powell, C. M., Johnston, D. & Chetkovich, D. M. 2011. Deletion of the hyperpolarization-activated cyclic nucleotide-gated channel auxiliary subunit TRIP8b impairs hippocampal Ih localization and function and promotes antidepressant behavior in mice. *J Neurosci*, 31, 7424-40.
- Liang, P., Xu, Y., Zhang, X., Ding, C., Huang, R., Zhang, Z., Lv, J., Xie, X., Chen, Y., Li, Y., Sun, Y., Bai, Y., Songyang, Z., Ma, W., Zhou, C. & Huang, J. 2015. CRISPR/Cas9-mediated gene editing in human tripronuclear zygotes. *Protein Cell*, 6, 363-372.
- Lipkowitz, M. S., Hanss, B., Tulchin, N., Wilson, P. D., Langer, J. C., Ross, M. D., Kurtzman, G. J., Klotman, P. E. & Klotman, M. E. 1999. Transduction of renal cells in vitro and in vivo by adeno-associated virus gene therapy vectors. *J Am Soc Nephrol*, 10, 1908-15.
- Longo, P. A., Kavran, J. M., Kim, M. S. & Leahy, D. J. 2013. Transient mammalian cell transfection with polyethylenimine (PEI). *Methods Enzymol*, 529, 227-40.
- Lörincz, A., Notomi, T., Tamas, G., Shigemoto, R. & Nusser, Z. 2002. Polarized and compartment-dependent distribution of HCN1 in pyramidal cell dendrites. *Nat Neurosci*, 5, 1185-93.
- Ludwig, A., Budde, T., Stieber, J., Moosmang, S., Wahl, C., Holthoff, K., Langebartels, A., Wotjak, C., Munsch, T., Zong, X., Feil, S., Feil, R., Lancel, M., Chien, K. R., Konnerth, A., Pape, H. C., Biel, M. & Hofmann, F. 2003. Absence epilepsy and sinus dysrhythmia in mice lacking the pacemaker channel HCN2. *EMBO J*, 22, 216-24.
- Ludwig, A., Zong, X., Jeglitsch, M., Hofmann, F. & Biel, M. 1998. A family of hyperpolarization-activated mammalian cation channels. *Nature*, 393, 587-91.
- Ludwig, A., Zong, X., Stieber, J., Hullin, R., Hofmann, F. & Biel, M. 1999. Two pacemaker channels from human heart with profoundly different activation kinetics. *EMBO J*, 18, 2323-9.
- Macri, V., Angoli, D. & Accili, E. A. 2012. Architecture of the HCN selectivity filter and control of cation permeation. *Sci Rep*, 2, 894.

- Macri, V., Proenza, C., Agranovich, E., Angoli, D. & Accili, E. A. 2002. Separable gating mechanisms in a Mammalian pacemaker channel. *J Biol Chem*, 277, 35939-46.
- Magee, J. C. 1998. Dendritic hyperpolarization-activated currents modify the integrative properties of hippocampal CA1 pyramidal neurons. *J Neurosci*, 18, 7613-24.
- Magee, J. C. 1999. Dendritic Ih normalizes temporal summation in hippocampal CA1 neurons. *Nat Neurosci*, 2, 848.
- Magee, J. C. 2000. Dendritic integration of excitatory synaptic input. *Nat Rev Neurosci*, 1, 181-90.
- Mahringer, D., Petersen, A. V., Fiser, A., Okuno, H., Bito, H., Perrier, J.-F. & Keller, G. B. 2019. Expression of c-Fos and Arc in hippocampal region CA1 marks neurons that exhibit learning-related activity changes.
- Mali, P., Yang, L., Esvelt, K. M., Aach, J., Guell, M., Dicarlo, J. E., Norville, J. E. & Church, G. M. 2013. RNA-guided human genome engineering via Cas9. *Science*, 339, 823-6.
- Mandegar, M. A., Huebsch, N., Frolov, E. B., Shin, E., Truong, A., Olvera, M. P., Chan, A. H., Miyaoka, Y., Holmes, K., Spencer, C. I., Judge, L. M., Gordon, D. E., Eskildsen, T. V., Villalta, J. E., Horlbeck, M. A., Gilbert, L. A., Krogan, N. J., Sheikh, S. P., Weissman, J. S., Qi, L. S., So, P. L. & Conklin, B. R. 2016. CRISPR Interference Efficiently Induces Specific and Reversible Gene Silencing in Human iPSCs. *Cell Stem Cell*, 18, 541-53.
- Mangoni, M. E. & Nargeot, J. 2008. Genesis and regulation of the heart automaticity. *Physiol Rev*, 88, 919-82.
- Männikkö, R., Elinder, F. & Larsson, H. P. 2002. Voltage-sensing mechanism is conserved among ion channels gated by opposite voltages. *Nature*, 419, 837-841.
- Matsumoto-Makidono, Y., Nakayama, H., Yamasaki, M., Miyazaki, T., Kobayashi, K., Watanabe, M., Kano, M., Sakimura, K. & Hashimoto, K. 2016. Ionic Basis for Membrane Potential Resonance in Neurons of the Inferior Olive. *Cell Rep*, 16, 994-1004.
- Matt, L., Michalakis, S., Hofmann, F., Hammelmann, V., Ludwig, A., Biel, M. & Kleppisch, T. 2011. HCN2 channels in local inhibitory interneurons constrain LTP in the hippocampal direct perforant path. *Cell Mol Life Sci*, 68, 125-37.
- Mccaffrey, A. P., Fawcett, P., Nakai, H., Mccaffrey, R. L., Ehrhardt, A., Pham, T. T., Pandey, K., Xu, H., Feuss, S., Storm, T. A. & Kay, M. A. 2008. The host response to adenovirus, helper-dependent adenovirus, and adeno-associated virus in mouse liver. *Mol Ther*, 16, 931-41.
- Mccormick, D. A. & Pape, H. C. 1990. Properties of a hyperpolarization-activated cation current and its role in rhythmic oscillation in thalamic relay neurones. *J Physiol*, 431, 291-318.
- Meister, G. & Tuschl, T. 2004. Mechanisms of gene silencing by double-stranded RNA. *Nature*, 431, 343-9.
- Mendell, J. R., Al-Zaidy, S., Shell, R., Arnold, W. D., Rodino-Klapac, L. R., Prior, T. W., Lowes, L., Alfano, L., Berry, K., Church, K., Kissel, J. T., Nagendran, S., L'italien, J., Sproule, D. M., Wells, C., Cardenas, J. A., Heitzler, M. D., Kaspar, A., Corcoran, S., Braun, L., Likhite, S., Miranda, C., Meyer, K., Foust, K. D., Burghes, A. H. M. & Kaspar, B. K. 2017. Single-Dose Gene-Replacement Therapy for Spinal Muscular Atrophy. *N Engl J Med*, 377, 1713-1722.
- Meng, Z. & Lu, M. 2017. RNA Interference-Induced Innate Immunity, Off-Target Effect, or Immune Adjuvant? *Front Immunol*, 8, 331.
- Meyer, R. & Heinemann, S. H. 1998. Characterization of an eag-like potassium channel in human neuroblastoma cells. *J Physiol*, 508 ( Pt 1), 49-56.
- Michels, G., Er, F., Khan, I., Sudkamp, M., Herzig, S. & Hoppe, U. C. 2005. Single-channel properties support a potential contribution of hyperpolarization-activated cyclic nucleotide-gated channels and If to cardiac arrhythmias. *Circulation*, 111, 399-404.

- Mistrik, P., Mader, R., Michalakis, S., Weidinger, M., Pfeifer, A. & Biel, M. 2005. The murine HCN3 gene encodes a hyperpolarization-activated cation channel with slow kinetics and unique response to cyclic nucleotides. *J Biol Chem*, 280, 27056-61.
- Monteggia, L. M., Eisch, A. J., Tang, M. D., Kaczmarek, L. K. & Nestler, E. J. 2000. Cloning and localization of the hyperpolarization-activated cyclic nucleotide-gated channel family in rat brain. *Molecular Brain Research*, 81, 129-139.
- Moser, M. B., Moser, E. I., Forrest, E., Andersen, P. & Morris, R. G. 1995. Spatial learning with a minislab in the dorsal hippocampus. *Proc Natl Acad Sci U S A*, 92, 9697-701.
- Much, B., Wahl-Schott, C., Zong, X., Schneider, A., Baumann, L., Moosmang, S., Ludwig, A. & Biel, M. 2003. Role of subunit heteromerization and N-linked glycosylation in the formation of functional hyperpolarization-activated cyclic nucleotide-gated channels. *J Biol Chem*, 278, 43781-6.
- Noam, Y., Zha, Q., Phan, L., Wu, R. L., Chetkovich, D. M., Wadman, W. J. & Baram, T. Z. 2010. Trafficking and surface expression of hyperpolarization-activated cyclic nucleotide-gated channels in hippocampal neurons. *J Biol Chem*, 285, 14724-36.
- Nolan, M. F., Malleret, G., Dudman, J. T., Buhl, D. L., Santoro, B., Gibbs, E., Vronskaya, S., Buzsaki, G., Siegelbaum, S. A., Kandel, E. R. & Morozov, A. 2004. A behavioral role for dendritic integration: HCN1 channels constrain spatial memory and plasticity at inputs to distal dendrites of CA1 pyramidal neurons. *Cell*, 119, 719-32.
- Nolan, M. F., Malleret, G., Lee, K. H., Gibbs, E., Dudman, J. T., Santoro, B., Yin, D. Q., Thompson, R. F., Siegelbaum, S. A., Kandel, E. R. & Morozov, A. 2003. The hyperpolarization-activated HCN1 channel is important for motor learning and neuronal integration by cerebellar Purkinje cells. *Cell*, 115, 551-564.
- Noma, A. & Irisawa, H. 1976. Membrane currents in the rabbit sinoatrial node cell as studied by the double microelectrode method. *Pflugers Arch*, 364, 45-52.
- Notomi, T. & Shigemoto, R. 2004. Immunohistochemical localization of Ih channel subunits, HCN1-4, in the rat brain. *J Comp Neurol*, 471, 241-76.
- Pape, H. C. 1996. QUEER CURRENT AND PACEMAKER: The Hyperpolarization-Activated Cation Current in Neurons. *Annu Rev. Physiol.*, 58, 299-327.
- Pavlov, I., Scimemi, A., Savtchenko, L., Kullmann, D. M. & Walker, M. C. 2011. I(h)-mediated depolarization enhances the temporal precision of neuronal integration. *Nat Commun*, 2, 199.
- Qi, L. S., Larson, M. H., Gilbert, L. A., Doudna, J. A., Weissman, J. S., Arkin, A. P. & Lim, W. A. 2013. Repurposing CRISPR as an RNA-guided platform for sequence-specific control of gene expression. *Cell*, 152, 1173-83.
- Qiu, S., Adema, C. M. & Lane, T. 2005. A computational study of off-target effects of RNA interference. *Nucleic Acids Res*, 33, 1834-47.
- Radzishenskaya, A., Shlyueva, D., Muller, I. & Helin, K. 2016. Optimizing sgRNA position markedly improves the efficiency of CRISPR/dCas9-mediated transcriptional repression. *Nucleic Acids Res*, 44, e141.
- Ran, F. A., Cong, L., Yan, W. X., Scott, D. A., Gootenberg, J. S., Kriz, A. J., Zetsche, B., Shalem, O., Wu, X., Makarova, K. S., Koonin, E. V., Sharp, P. A. & Zhang, F. 2015. In vivo genome editing using Staphylococcus aureus Cas9. *Nature*, 520, 186-91.
- Rao, D. D., Vorhies, J. S., Senzer, N. & Nemunaitis, J. 2009. siRNA vs. shRNA: similarities and differences. *Adv Drug Deliv Rev*, 61, 746-59.
- Robinson, R. B. & Siegelbaum, S. A. 2003. Hyperpolarization-activated cation currents: from molecules to physiological function. *Annu Rev Physiol*, 65, 453-80.

- Rusnakova, V., Honsa, P., Dzamba, D., Stahlberg, A., Kubista, M. & Anderova, M. 2013. Heterogeneity of astrocytes: from development to injury - single cell gene expression. *PLoS One*, 8, e69734.
- Sanchez-Alonso, J. L., Halliwell, J. V. & Colino, A. 2008. ZD 7288 inhibits T-type calcium current in rat hippocampal pyramidal cells. *Neurosci Lett*, 439, 275-80.
- Santoro, B., Chen, S., Luthi, A., Pavlidis, P., Shumyatsky, G. P., Tibbs, G. R. & Siegelbaum, S. A. 2000. Molecular and functional heterogeneity of hyperpolarization-activated pacemaker channels in the mouse CNS. *J Neurosci*, 20, 5264-75.
- Santoro, B., Grant, S. G., Bartsch, D. & Kandel, E. R. 1997. Interactive cloning with the SH3 domain of N-src identifies a new brain specific ion channel protein, with homology to eag and cyclic nucleotide-gated channels. *Proc Natl Acad Sci U S A*, 94, 14815-20.
- Santoro, B., Liu, D. T., Yao, H., Bartsch, D., Kandel, E. R., Siegelbaum, S. A. & Tibbs, G. R. 1998. Identification of a gene encoding a hyperpolarization-activated pacemaker channel of brain. *Cell*, 93, 717-29.
- Santoro, B., Piskorowski, R. A., Pian, P., Hu, L., Liu, H. & Siegelbaum, S. A. 2009. TRIP8b splice variants form a family of auxiliary subunits that regulate gating and trafficking of HCN channels in the brain. *Neuron*, 62, 802-13.
- Santoro, B., Wainger, B. J. & Siegelbaum, S. A. 2004. Regulation of HCN channel surface expression by a novel C-terminal protein-protein interaction. *J Neurosci*, 24, 10750-62.
- Sartiani, L., Mannaioni, G., Masi, A., Novella Romanelli, M. & Cerbai, E. 2017. The Hyperpolarization-Activated Cyclic Nucleotide-Gated Channels: from Biophysics to Pharmacology of a Unique Family of Ion Channels. *Pharmacol Rev*, 69, 354-395.
- Schilling, K. 2019. *Investigation of Ca<sup>2+</sup> signaling in hippocampal primary neurons*. M.Sc., University of Cologne.
- Schindelin, J., Arganda-Carreras, I., Frise, E., Kaynig, V., Longair, M., Pietzsch, T., Preibisch, S., Rueden, C., Saalfeld, S., Schmid, B., Tinevez, J. Y., White, D. J., Hartenstein, V., Eliceiri, K., Tomancak, P. & Cardona, A. 2012. Fiji: an open-source platform for biological-image analysis. *Nat Methods*, 9, 676-82.
- Schwab, M. H., Bartholomae, A., Heimrich, B., Feldmeyer, D., Druffel-Augustin, S., Goebbels, S., Naya, F. J., Zhao, S., Frotscher, M., Tsai, M. J. & Nave, K. A. 2000. Neuronal basic helix-loop-helix proteins (NEX and BETA2/Neuro D) regulate terminal granule cell differentiation in the hippocampus. *J Neurosci*, 20, 3714-24.
- Seo, H., Seol, M. J. & Lee, K. 2015. Differential expression of hyperpolarization-activated cyclic nucleotide-gated channel subunits during hippocampal development in the mouse. *Mol Brain*, 8, 13.
- Shah, M. M. 2014. Cortical HCN channels: function, trafficking and plasticity. *J Physiol*, 592, 2711-9.
- Shan, G. 2010. RNA interference as a gene knockdown technique. *Int J Biochem Cell Biol*, 42, 1243-51.
- Shin, M. & Chetkovich, D. M. 2007. Activity-dependent regulation of h channel distribution in hippocampal CA1 pyramidal neurons. *J Biol Chem*, 282, 33168-80.
- Shu, X., Lev-Ram, V., Deerinck, T. J., Qi, Y., Ramko, E. B., Davidson, M. W., Jin, Y., Ellisman, M. H. & Tsien, R. Y. 2011. A genetically encoded tag for correlated light and electron microscopy of intact cells, tissues, and organisms. *PLoS Biol*, 9, e1001041.
- Siolas, D., Lerner, C., Burchard, J., Ge, W., Linsley, P. S., Paddison, P. J., Hannon, G. J. & Cleary, M. A. 2005. Synthetic shRNAs as potent RNAi triggers. *Nat Biotechnol*, 23, 227-31.
- Stieber, J., Herrmann, S., Feil, S., Loster, J., Feil, R., Biel, M., Hofmann, F. & Ludwig, A. 2003. The hyperpolarization-activated channel HCN4 is required for the generation of

- pacemaker action potentials in the embryonic heart. *Proceedings of the National Academy of Sciences of the United States of America*, 100, 15235-15240.
- Stieber, J., Stockl, G., Herrmann, S., Hassfurth, B. & Hofmann, F. 2005. Functional expression of the human HCN3 channel. *J Biol Chem*, 280, 34635-43.
- Stieglitz, M. S., Fenske, S., Hammelmann, V., Becirovic, E., Schottle, V., Delorme, J. E., Scholl-Weidinger, M., Mader, R., Deussing, J., Wolfer, D. P., Seeliger, M. W., Albrecht, U., Wotjak, C. T., Biel, M., Michalakis, S. & Wahl-Schott, C. 2017. Disturbed Processing of Contextual Information in HCN3 Channel Deficient Mice. *Front Mol Neurosci*, 10, 436.
- Stoppini, L., Buchs, P. A. & Muller, D. 1991. A simple method for organotypic cultures of nervous tissue. *J Neurosci Methods*, 37, 173-82.
- Sunkara, M. R., Schwabe, T., Ehrlich, G., Kusch, J. & Benndorf, K. 2018. All four subunits of HCN2 channels contribute to the activation gating in an additive but intricate manner. *J Gen Physiol*, 150, 1261-1271.
- Surges, R., Brewster, A. L., Bender, R. A., Beck, H., Feuerstein, T. J. & Baram, T. Z. 2006. Regulated expression of HCN channels and cAMP levels shape the properties of the h current in developing rat hippocampus. *Eur J Neurosci*, 24, 94-104.
- Tang, B., Sander, T., Craven, K. B., Hempelmann, A. & Escayg, A. 2008. Mutation analysis of the hyperpolarization-activated cyclic nucleotide-gated channels HCN1 and HCN2 in idiopathic generalized epilepsy. *Neurobiol Dis*, 29, 59-70.
- Tanguay, J., Callahan, K. M. & D'Avanzo, N. 2019. Characterization of drug binding within the HCN1 channel pore. *Sci Rep*, 9, 465.
- Thakore, P. I., Kwon, J. B., Nelson, C. E., Rouse, D. C., Gemberling, M. P., Oliver, M. L. & Gersbach, C. A. 2018. RNA-guided transcriptional silencing in vivo with *S. aureus* CRISPR-Cas9 repressors. *Nat Commun*, 9, 1674.
- Tzeng, T. T., Tsay, H. J., Chang, L., Hsu, C. L., Lai, T. H., Huang, F. L. & Shiao, Y. J. 2013. Caspase 3 involves in neuroplasticity, microglial activation and neurogenesis in the mice hippocampus after intracerebral injection of kainic acid. *J Biomed Sci*, 20, 90.
- Ulens, C. & Tytgat, J. 2001. Functional heteromerization of HCN1 and HCN2 pacemaker channels. *J Biol Chem*, 276, 6069-72.
- Unniyampurath, U., Pilankatta, R. & Krishnan, M. N. 2016. RNA Interference in the Age of CRISPR: Will CRISPR Interfere with RNAi? *Int J Mol Sci*, 17, 291.
- Vaca, L., Stieber, J., Zong, X., Ludwig, A., Hofmann, F. & Biel, M. 2000. Mutations in the S4 domain of a pacemaker channel alter its voltage dependence. *FEBS Lett*, 479, 35-40.
- Van Welie, I., Van Hoof, J. A. & Wadman, W. J. 2004. Homeostatic scaling of neuronal excitability by synaptic modulation of somatic hyperpolarization-activated Ih channels. *Proc Natl Acad Sci U S A*, 101, 5123-8.
- Wahl-Schott, C. & Biel, M. 2009. HCN channels: structure, cellular regulation and physiological function. *Cell Mol Life Sci*, 66, 470-94.
- Wang, H., Yang, H., Shivalila, C. S., Dawlaty, M. M., Cheng, A. W., Zhang, F. & Jaenisch, R. 2013. One-step generation of mice carrying mutations in multiple genes by CRISPR/Cas-mediated genome engineering. *Cell*, 153, 910-8.
- Whitaker, G. M., Angoli, D., Nazzari, H., Shigemoto, R. & Accili, E. A. 2007. HCN2 and HCN4 isoforms self-assemble and co-assemble with equal preference to form functional pacemaker channels. *J Biol Chem*, 282, 22900-9.
- Wiedenheft, B., Sternberg, S. H. & Doudna, J. A. 2012. RNA-guided genetic silencing systems in bacteria and archaea. *Nature*, 482, 331-8.
- Wu, X., Liao, L., Liu, X., Luo, F., Yang, T. & Li, C. 2012. Is ZD7288 a selective blocker of hyperpolarization-activated cyclic nucleotide-gated channel currents? *Channels (Austin)*, 6, 438-42.

- Wu, Z., Yang, H. & Colosi, P. 2010. Effect of genome size on AAV vector packaging. *Mol Ther*, 18, 80-6.
- Yan, Y., Qiao, S., Kikuchi, C., Zaja, I., Logan, S., Jiang, C., Arzua, T. & Bai, X. 2017. Propofol Induces Apoptosis of Neurons but Not Astrocytes, Oligodendrocytes, or Neural Stem Cells in the Neonatal Mouse Hippocampus. *Brain Sci*, 7.
- Yanagihara, K. & Irisawa, H. 1980. Inward Current Activated during Hyperpolarization in the Rabbit Sinoatrial Node Cell. *Pflugers Archiv-European Journal of Physiology*, 385, 11-19.
- Yu, F. H., Yarov-Yarovoy, V., Gutman, G. A. & Catterall, W. A. 2005. Overview of molecular relationships in the voltage-gated ion channel superfamily. *Pharmacol Rev*, 57, 387-95.
- Yu, J. Y., Deruiter, S. L. & Turner, D. L. 2002. RNA interference by expression of short-interfering RNAs and hairpin RNAs in mammalian cells. *Proc Natl Acad Sci U S A*, 99, 6047-52.
- Yu, X., Duan, K. L., Shang, C. F., Yu, H. G. & Zhou, Z. 2004. Calcium influx through hyperpolarization-activated cation channels (I-h channels) contributes to activity-evoked neuronal secretion. *Proceedings of the National Academy of Sciences of the United States of America*, 101, 1051-1056.
- Zhang, X. H., Tee, L. Y., Wang, X. G., Huang, Q. S. & Yang, S. H. 2015. Off-target Effects in CRISPR/Cas9-mediated Genome Engineering. *Mol Ther Nucleic Acids*, 4, e264.
- Zheng, Y., Shen, W., Zhang, J., Yang, B., Liu, Y. N., Qi, H., Yu, X., Lu, S. Y., Chen, Y., Xu, Y. Z., Li, Y., Gage, F. H., Mi, S. & Yao, J. 2018. CRISPR interference-based specific and efficient gene inactivation in the brain. *Nat Neurosci*, 21, 447-454.
- Zhou, L., Olivier, N. B., Yao, H., Young, E. C. & Siegelbaum, S. A. 2004. A conserved tripeptide in CNG and HCN channels regulates ligand gating by controlling C-terminal oligomerization. *Neuron*, 44, 823-34.

## **Danksagung**

Besonders bedanken möchte ich mich bei Prof. Dr. Arnd Baumann. Einerseits für die Überlassung des vielseitigen Projektes, andererseits für seine unglaublich unermüdliche Bereitschaft wissenschaftliche Probleme, Ergebnisse und Ideen zu diskutieren, so waghalsig sie auch sein mochten.

Bei Sabine Balfanz bedanke ich mich für die intensive Zusammenarbeit. Besonders die vielen Stunden ohne Tageslicht die wir zusammen im Tierhaus verbrachten wären ohne sie nur schwer zu ertragen gewesen.

Neben der Wissenschaft, möchte ich mich auch für die persönliche Unterstützung bei Arnd und Sabine bedanken. Wie wahrscheinlich bei vielen Promotionen zuvor hatte auch meine Promotionszeit Höhen und Tiefen. Daher war euer Zuspruch während der Tiefen und eure Anerkennung während der Höhen unverzichtbar, um diese Zeit halbwegs unbeschadet zu überstehen.

Den Mitgliedern des ICS-4 danke ich für die gute Zusammenarbeit. Besonders Felix danke ich für die sehr angenehme und abwechslungsreiche Zeit in unserem Büro und Thomas danke ich für seine weisen und erheiternden Berliner Erzählungen.

Bei Dr. Sabine Vay und Dr. Carina Stegmayr bedanke ich mich für die gute Zusammenarbeit und die gegenseitige Unterstützung.

Prof. Dr. Christoph Fahlke danke ich für die Finanzierung meiner Stelle und für die Möglichkeit der Nutzung institutsinterner Ressourcen.

Prof. Dr. Guenter Schwarz danke ich für die Begutachtung dieser Arbeit und für die Bereitschaft als Prüfer meine Disputation zu begleiten. Bei Prof. Dr. Sigrun Korsching bedanke ich mich für die Übernahme des Prüfungsvorsitzes.

Abschließend möchte ich mich bei meinen Freunden und besonders bei meiner Familie bedanken, dafür, dass ihr mich so nehmt wie ich bin.

Danke Ira, für die lange und schöne gemeinsame Zeit, danke Charlotte, für deine Aufopferung und Rücksicht und danke an unseren Sohn Caspar, dass du mich daran erinnerst abends früh nach Hause zu kommen.

## **Erklärung**

Ich versichere, dass ich die von mir vorgelegte Dissertation selbständig angefertigt, die benutzten Quellen und Hilfsmittel vollständig angegeben und die Stellen der Arbeit – einschließlich Tabellen, Karten und Abbildungen –, die anderen Werken im Wortlaut oder dem Sinn nach entnommen sind, in jedem Einzelfall als Entlehnung kenntlich gemacht habe; dass diese Dissertation noch keiner anderen Fakultät oder Universität zur Prüfung vorgelegen hat; dass sie – abgesehen von unten angegebenen Teilpublikationen – noch nicht veröffentlicht worden ist, sowie, dass ich eine solche Veröffentlichung vor Abschluss des Promotionsverfahrens nicht vornehmen werde.

Die Bestimmungen der Promotionsordnung sind mir bekannt. Die von mir vorgelegte Dissertation ist von Prof. Dr. A. Baumann betreut worden

## **Teilpublikation**

M. Deutsch, A. Günther, R. Lerchundi, C. Rose, S. Balfanz and A. Baumann, 'AAV-mediated CRISPRi and RNAi based gene silencing in mouse hippocampal neurons' Scientific Reports, in revision

Ich versichere, dass ich alle Angaben wahrheitsgemäß nach bestem Wissen und Gewissen gemacht habe und verpflichte mich, jedmögliche, die obigen Angaben betreffenden Veränderungen, dem Dekanat unverzüglich mitzuteilen.

---

(Datum, Unterschrift)

## Lebenslauf

**Name:** Matthias Deutsch  
**Geburtsdatum:** 22.02.1991  
**Staatsangehörigkeit:** deutsch

### Akademische Ausbildung

<b>Seit 2019</b>	<b>Staatsexamen Medizin, RWTH Aachen</b>
<b>Seit 2016</b>	<b>PhD Kandidat, Forschungszentrum Jülich</b> Institute of Complex Systems, Zelluläre Biophysik (ICS-4)
<b>2013 – 2016</b>	<b>Master in Neurobiological Sciences, Universität zu Köln</b> Masterthesis: Institute Pest Control,
<b>2010 – 2013</b>	<b>Bachelor in Biological Sciences, Universität zu Köln</b> Bachelorthesis: Zoologisches Insitut
<b>2001 – 2010</b>	<b>Friedrich-Spee Gymnasium Trier</b> Abitur

### Forschungstätigkeiten

<b>Seit 02/2016</b>	<b>Wissenschaftlicher Mitarbeiter:</b> Forschungszentrum Jülich, Institute of Complex Systems, Zelluläre Biophysik (ICS-4)
<b>06/2015 – 11/2015</b>	<b>Masterstudent:</b> Bayer AG, Institute Pest Control, Department of Biochemistry
<b>10/2014 – 03/2015</b>	<b>Werkstudent:</b> Bayer AG, Institute Pest Control, Department of Biochemistry
<b>04/2014 – 10/2014</b>	<b>Studentische Hilfskraft:</b> Universität zu Köln, Institut für Biochemie, AG Prof. Dr. G. Schwarz,
<b>02/2014 – 03/2014</b>	<b>Forschungspraktikum:</b> Universität zu Köln, Institut für Entwicklungsbiologie, AG Hammerschmidt,
<b>04/2013 – 05/2013</b>	<b>Forschungspraktikum:</b> Universität zu Köln, Zoologischen Institut, AG Kloppenburg
<b>02/2013 – 04/2013</b>	<b>Laborpraktikum,</b> Klinikum Leverkusen, Institut für Pathologie, Dr. R. Jaussi

### Nebentätigkeiten und Weiterbildung

<b>04/2018</b>	<b>Career and Leadership Development Kurs</b> Senior Lecturer Dr. E. Alpay, University of Surrey
<b>02/2018</b>	<b>49. IFF Spring School: Physics of Life</b> Forschungszentrum Jülich,
<b>10/2017</b>	<b>Scientific Writing Workshop</b> Prof. Dr. U.B. Kaupp, ceasar Bonn
<b>08/2017</b>	<b>Communication and Presentation Skill Development Kurs</b> Senior Lecturer Dr. E. Alpay, University of Surrey
<b>02/2017</b>	<b>Tierexperimenteller Kurs (Kategorie B) (FELASA) Kurs</b> Dr. M. Walberer, Universität zu Köln
<b>12/2016</b>	<b>Research Skill Development Kurs</b> Senior Lecturer Dr. E. Alpay, University of Surrey,

## Stipendien und Auszeichnungen

Seit 06/2016	<b>IHRS BioSoft - International Helmholtz Research School of Biophysics and Soft Matter</b>
Seit 05/2018	<b>e-fellows Fellowship</b>
03/2019	<b>Reiseaward</b> Deutsche Physiologische Gesellschaft
09/2016	<b>Best Poster Award</b> 5. Symposium der jungen Physiologen

## Konferenzbeiträge

05/2019	<b>Posterbeitrag:</b> EMBO Workshop: Cell biology of the neuron: Polarity, plasticity and regeneration, Heraklion, Griechenland
03/2019	<b>Invited Speaker und Posterbeitrag:</b> 7. Symposium der Jungen Physiologen, Nürnberg
03/2019	<b>Posterbeitrag:</b> 13. Göttingen Meeting der Deutschen Neurowissenschaftlichen Gesellschaft, Göttingen
11/2018	<b>Posterbeitrag:</b> 48 <sup>th</sup> Meeting of the Society of Neuroscience, San Diego, USA
11/2018	<b>Posterbeitrag:</b> 20. EMBL PhD Symposium, Heidelberg
02/2018	<b>Mitorganisator:</b> 7. Retreat of Institute of Neuroscience and Medicine (INM) and the Institute of Complex Systems (ICS), Jülich
07/2017	<b>Posterbeitrag:</b> 6. Retreat of Institute of Neuroscience and Medicine (INM) and the Institute of Complex Systems (ICS), Jülich
03/2017	<b>Posterbeitrag:</b> 12. Göttingen Meeting der Deutschen Neurowissenschaftlichen Gesellschaft, Göttingen
09/2016	<b>Posterbeitrag:</b> 5. Symposium der Jungen Physiologen, Jülich
07/2016	<b>Invited Speaker und Posterbeitrag:</b> 5. Annual Retreat of Institute of Neuroscience and Medicine (INM), Jülich

